A Mach-Zehnder interferogram of a Plasma Focus discharge near maximum compression ($\hat{n}_e \sim 5\times10^{19}cm^{-3}$, $T_e \sim 2keV$, exposure time = $1.2\times10^{-9}s$)

The interferometer is set up to produce a series of horizontal lines; on introducing a plasma these lines or 'fringes' are displaced producing a 'contour map'. The implosion of a current-carrying skin produces a conical plasma; A A shows a region of low compression and the cone narrows to B B, a region of high compression (i.e. high density). A series of instabilities can be seen breaking out from the main core.

OPTICAL REFRACTIVITY STUDIES OF PLASMA FOCUS

by

PHILIP DYFRIG MORGAN

Department of Physics
Royal Holloway College

This thesis is submitted for the
Degree of Doctor of Philosophy
in the University of London

January, 1974

ABSTRACT

A study of a Plasma Focus device by optical diagnostic techniques based on plasma refractivity is reported. The device produces at the axis of symmetry of its coaxial electrodes a transient dense plasma filament, of density $\geqslant 10^{19}$ electrons cm^{-3} and electron temperature ~ 2.5keV, by a focusing mechanism.

A review of earlier experimental and theoretical studies of the Plasma Focus permits a detailed description of the four principal phases of the discharge.

The principles of showdowgraphy, schlieren photography and interferometry and their application to plasma diagnostics are discussed in detail. It is shown that in the present study the plasma refractivity is mainly due to free electrons.

The Plasma Focus used in the study is described and the experimental details of using the diagnostic techniques are discussed. A shutter has been developed to produce a pulse of duration one nanosecond from a Q-switched ruby laser and is used to obtain good temporal resolution of the transient plasma.

The refractivity studies lead to a detailed understanding of the Plasma Focus. Interferometry provides the time dependence of the plasma electron-density profile, permitting calculation of the time-dependent plasma line-density and the focusing efficiency. Multiple-exposure shadowgrams lead to values of the velocity and acceleration of the plasma boundary, the dense-filament lifetime and the growth rates of plasma instabilities. An ion temperature is deduced from the damping of acceleration-driven instabilities.

The significance of the results from these original studies is discussed. They are compared with the results from other measurements on the Plasma Focus and with the results of a numerical fluid code. The limitations of the optical techniques used are considered and improvements are suggested. Future studies of the Plasma Focus based on these improved techniques are proposed.

CONTENTS

C O N T E N T S
(continued)

CONTENTS
(continued)

ACKNOWLEDGEMENTS

These experiments were performed in the Culham Laboratory of the United Kingdom Atomic Energy Authority, and I am much indebted to the Laboratory for the use of their Plasma Focus and other experimental facilities.

I gratefully acknowledge research grants provided by the Culham Laboratory and the Science Research Council.

I wish to express my deep gratitude to Dr N.J. Peacock of the Culham Laboratory for the supervision and continual encouragement of this work, and to Dr E.R. Wooding of Royal Holloway College, my director of studies, for much advice and guidance.

I am very grateful to A.H. Jones, F.C. Jones and P.D. Wilcock of the Culham Laboratory for their efforts in maintaining the Plasma Focus in running order.

I wish to express my appreciation of many helpful discussions with numerous people in Experimental Division 'B' of the Culham Laboratory - in particular with D.E. Evans, M.J. Forrest, M.G. Hobby and P.D. Wilcock.

Finally, I thank Ina Godwin for her excellent work in typing this thesis.

CHAPTER I

INTRODUCTION

A study of the electrical discharge in a Plasma Focus, by optical diagnostic techniques based on plasma refractivity, viz. shadowgraphy, schlieren photography and interferometry, is reported in this thesis.

The Plasma Focus consists of two coaxial electrodes, separated at one end by an insulator, in an atmosphere of deuterium at a few torr pressure. A high-current electrical discharge between the electrodes produces a transient dense plasma filament along their axis of symmetry, at the closed inner-electrode end which is remote from the insulator. This filament is the result of an axisymmetric quasi-cylindrical pinch driven by the interaction of the axial current through the plasma with the azimuthal magnetic field induced by this current.

Of all laboratory plasmas produced by rapid magnetic compression, the Plasma Focus dense pinch has one of the highest energy-densities. In addition, the plasma emits fluxes of thermal X-rays and neutrons which are only exceeded in intensity in a nuclear explosion. For a typical Plasma Focus of medium power, taking the parameters of the plasma at maximum compression; with a density greater than 10^{19} electrons cm^{-3} and an electron temperature of about 2.5keV, the energy density of the fully-ionized plasma is greater than 4kJ cm^{-3} and its kinetic pressure is at least 4×10^{4} atmospheres. However, this is achieved at the expense of producing a small volume of plasma, about 10^{-2} cm^{3}, for a short time, about 5×10^{-8} sec. The rate of nuclear fusion reactions between the deuterons is at least 10^{18} sec^{-1}.

The refractivity of a highly-ionized plasma is primarily determined by its electron density. By measuring the refractive index of such a plasma, the electron density can be obtained. Optical measurements of

plasma refractivity consist of propagating a light wave through the plasma, and determining the resultant phase changes in the wavefront. Interferometry measures the plasma refractive index directly, while the schlieren and shadowgraph techniques measure the refractive index gradient and the second derivative of refractive index, respectively. These techniques are capable of high spatial resolution because of the small size of optical wavelengths, while, in the study of a transient plasma, high temporal resolution is achievable by using a light pulse of sufficiently short duration.

When the optical studies reported were begun in mid 1968, the knowledge concerning the Plasma Focus discharge, particularly the transient dense pinch, was superficial only. This was mainly because the diagnostic techniques available at that time, due to insufficient development or lack of full exploitation, did not permit measurements of sufficiently high spatial or temporal resolution. Consequently, it was decided that, by developing a laser light source capable of high temporal resolution, the high potential of the above optical techniques could be exploited fully in a study of the Plasma Focus, to give a better understanding of the discharge.

The thesis is set out as follows:

In Chapter II, a detailed account of the Plasma Focus device and its modus operandi are presented. The two basic types of the device are introduced, and a brief account is given of their development from investigations into metal-walled z-pinches and coaxial plasma guns. From a review of the numerous publications on the Plasma Focus over the past decade, detailed descriptions of the various phases of the discharge are given, viz. the 'run-down', 'collapse', 'dense-pinch' and 'diffuse-pinch' phases. An account is also given of the possible mechanisms responsible for neutron production.

Chapter III is concerned with diagnostic techniques based on plasma optical refractivity. The optical refractivity of a plasma is considered, and it is shown that in the present studies the refractive index is determined by the density of the free electrons. The principles of shadowgraphy, schlieren photography and interferometry are discussed in detail, with particular emphasis on their applications in plasma diagnostics. Finally, the properties of a Q-switched ruby laser are considered, and it is demonstrated that such a laser makes an ideal light source for use with these optical techniques.

Having thus prepared the background, in the fourth chapter the experimental apparatus, the development work and the experimental details of the optical techniques are described. The mechanical construction, vacuum system, capacitor bank, discharge circuit, control and monitoring systems, and operation of the Plasma Focus used are described. An account is given of the development of a suitable laser light source, culminating in a shutter which produced a pulse of about one nanosecond duration from a Q-switched ruby laser. Lastly, experimental details are given of the optical techniques used to study the Plasma Focus.

In the fifth chapter, the photographic records obtained from studies of the Plasma Focus using schlieren photography, interferometry and shadowgraphy are presented.

Chapter VI contains a detailed account of the analysis and interpretation of the records obtained from the optical studies. The significance of the results is discussed, and they are compared with those from other studies of the Plasma Focus.

In the concluding chapter, Chapter VII, the advance in knowledge concerning the Plasma Focus, due to the optical studies, is discussed. The limitations in the experimental methods are considered and suggestions

for improvement are made. This leads to proposals for future studies of the Plasma Focus, based on the improved optical techniques. Finally, the conclusions from the optical studies reported are summarised.

The C G S (e.s.u.) system is used throughout, unless it is otherwise stated. The notation used is given in Appendix 1.

CHAPTER II

THE PLASMA FOCUS

2.1 INTRODUCTION

Filippov et al (1962) and Mather (1964) each developed independently a coaxial-electrode device in which, on discharging a high-energy capacitor bank through the electrodes, a transient dense plasma filament was produced. These devices were the forerunners of the two basic types of Plasma Focus, one or other of which is currently in operation in approximately twenty laboratories in nine countries.

The capacitor bank of a Plasma Focus typically stores energies of 4–500 kJ at 10–40 kV and, on discharge, produces peak currents of 0.1–5.0 MA in 1–3 μsec. When a Plasma Focus is operated with a filling of deuterium at a few torr pressure, the plasma produced emits an intense flux of neutrons from the D–D reaction in addition to soft X-rays. The characteristics of the discharge are dependent on the geometry of the Plasma Focus and on the operating conditions. In general, the parameters of the dense pinch lie in the following ranges: peak electron and ion density 5×10^{18} – 2×10^{20} cm^{-3}, peak electron and ion temperature 0.25–4.0 keV, lifetime 30–100 nsec and radius 0.05–0.2 cm. The neutron yield per discharge is in the range $10^{8} - 2 \times 10^{12}$.

In the Filippov Plasma Focus, shown in Fig.2.1.1, the lid, side wall and ring-shaped base of the chamber (1) form the cathode, which is at earth potential. The high voltage is applied to the inner electrode (2), which is separated electrically from the cathode by a porcelain insulator (3). An azimuthal set of radial pins (4), which are removable, are occasionally used to predetermine the filamentary pattern of the current sheet at the initial breakdown. Item 5 represents the capacitor bank and switching spark gaps. The chamber diameter is 70 cm, that of the anode is 48 cm,

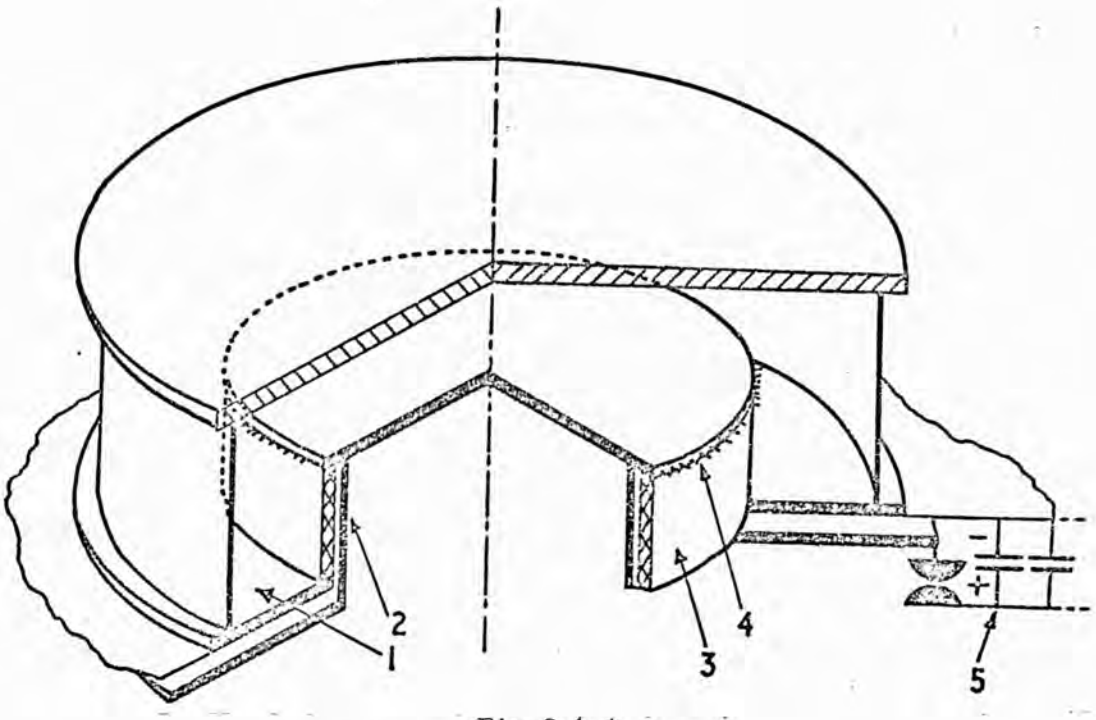

Fig.2.1.1
The Filippov Plasma Focus

the height of the insulator is 12 cm and the axial separation of anode and cathode is 8 cm.

The Mather Plasma Focus, shown in Fig.2.1.2, consists of an outer cathode which is grounded and a centre electrode to which the high voltage is applied. One end of the coaxial gun is closed by a flat pyrex insulator, to which a sleeve covering the first 5 cm of anode is fused, while the open end of the gun projects into a vacuum chamber. A pyrex tube jackets the outer electrode, forming a vacuum seal between the gun assembly and vacuum chamber. The cathode is perforated by a regular array of holes, which improve the performance of the Plasma Focus. The cathode diameter is 10 cm, that of the anode is 5 cm and the overall length of the gun is 25 cm. Also shown in the figure are a current and voltage trace for the initial conditions $C = 94\,\mu F$, $V = 32.5\,kV$ and $p_o = 3.0\,torr\ D_2$. The plasma position at various times is indicated.

The main difference between the two types of Plasma Focus is in the relative electrode sizes. Also, in the Mather device the gun end remote

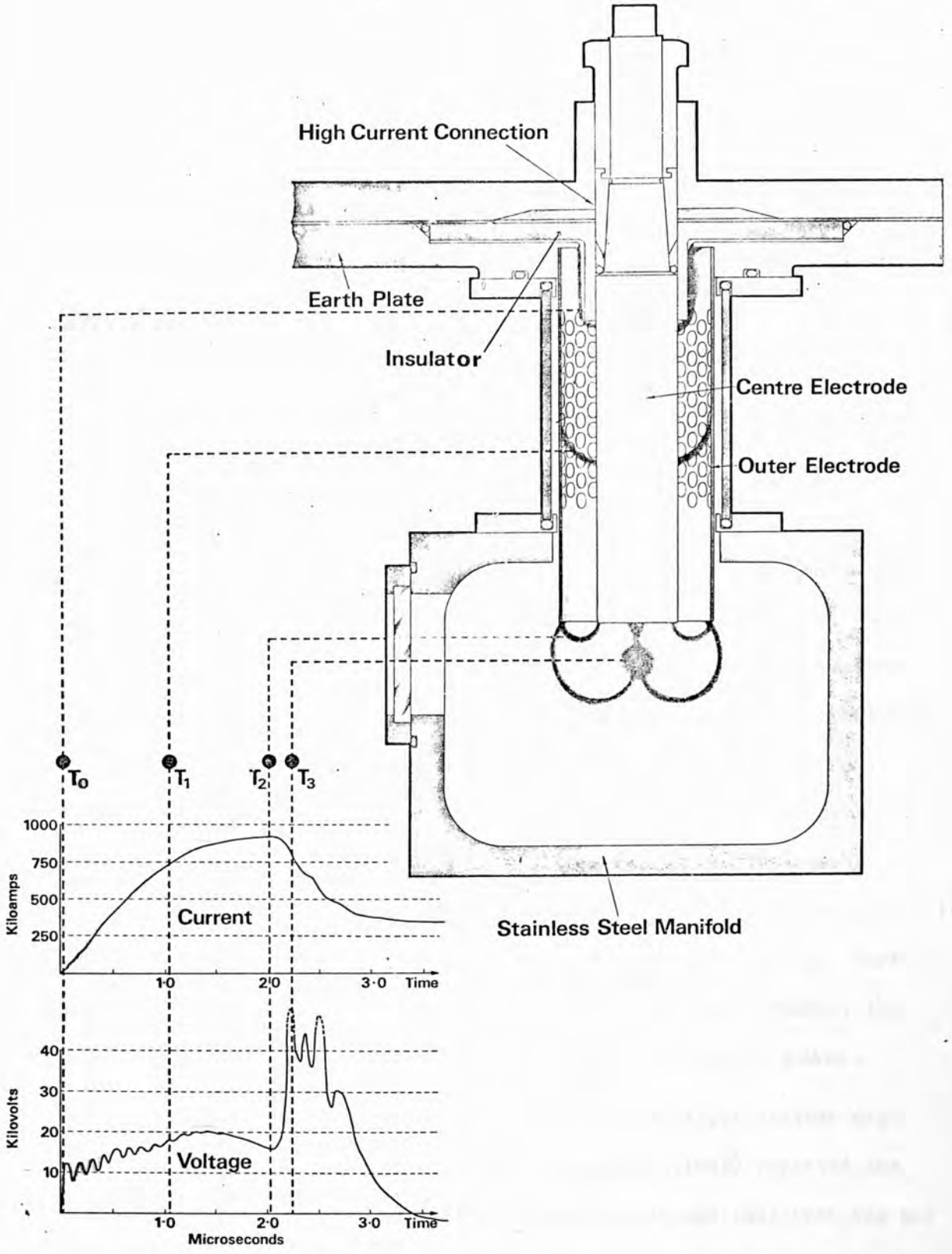

Fig.2.1.2
The Mather Plasma Focus

from the insulator is open, while in the Filippov device the corresponding end is closed by the outer electrode.

2.2 EARLY EXPERIMENTS LEADING TO THE DEVELOPMENT OF THE PLASMA FOCUS

2.2.1 The Filippov Device

Andrianov et al (1960) studied linear discharges in insulated-wall two-electrode chambers at energies up to 500 kJ. It was found that plasma energies at the ceramic wall exceeding 10 J cm^{-2} evaporated sufficient material to contaminate the discharge. Petrov et al (1960) reduced this effect by introducing a copper wall, but found that the character of the discharge was greatly changed.

The latter discharge, instead of initiating between the electrodes then contracting radially, formed between the electrodes and wall, and had a symmetrical rosette-like shape at the anode. The rosette-shaped current sheet contracted into a narrow column, starting at the anode and propagating gradually along the chamber axis. Only the gas volume in an axial region adjacent to the anode was entrained during the compression, unlike the former discharge where the bulk of the gas in the chamber was compressed. Using the copper-walled chamber, an increase in neutron yield by a factor of ~ 100, up to 5×10^9 per discharge, was obtained. Furthermore, the duration of the neutron pulse was reduced from $\sim 3\,\mu$sec, the lifetime of the pinch in the ceramic-walled chamber, to $\sim 0.3\,\mu$sec.

These observations stimulated a detailed investigation into discharges in metal-walled chambers. Filippov et al (1962) reported the results obtained from the first Plasma Focus - although this term was not applied to the device until later. The Plasma Focus was similar to the Filippov device described in section 2.1, although smaller by a factor of ~ 2. The capacitors stored 20 kJ of energy at 32 kV and the device operated with an initial filling of 1 torr of D_2. Several diagnostic

techniques were employed to measure: the plasma temperature and density, the spectrum of protons from D-D reactions, and the gross dynamics and dimensions of the plasma. The measurements showed that a transient dense high-temperature pinch was produced, with the following parameters: electron density $0.7 - 1.2 \times 10^{19}$ cm^{-3}, electron temperature 0.8 - 1.2 keV, neutron pulse duration ≤ 0.25 μsec, radius ~ 0.15 cm and volume $\sim 3 \times 10^{-2}$ cm^3.

2.2.2 The Mather Device

Plasma accelerators were investigated in the late 1950's as a means of injecting plasma into magnetic traps. Marshall (1960) developed a coaxial gun, with pulsed gas operation, which achieved plasma velocities of $\sim 10^7$ cm sec^{-1}. Mather (1964) studied the plasma ejected into a vacuum by such a coaxial gun, with stored energy 5 kJ at 15 kV, and found two distinct modes of operation.

In the first mode, a delay of ~ 140 μsec was used between admitting the deuterium gas, via channels drilled near the muzzle end of the inner electrode (the anode), and discharging the capacitors. The gas was localised in the region of the channels at electrical breakdown, which occurred there. Fast deuterium ions were ejected from the gun with energies ≤ 250 keV. In the second mode, a delay of ~ 380 μsec allowed the gas to diffuse throughout the gun before breakdown, which occurred at the insulator at the breech end. The current sheet produced was accelerated axially between the electrodes, to a velocity of $\sim 2.5 \times 10^7$ cm sec^{-1} at the muzzle, and a high density plasma was subsequently formed on the electrode axis ~ 1 cm from the anode end. Mather identified this second mode of operation with the investigations reported by Filippov et al (1962).

Subsequently, Mather (1965a) studied the second mode in detail using a Plasma Focus similar to the Mather device described in section 2.1,

with a stored energy of 18 kJ at 20 kV and operating with an initial static filling of 0.2 - 1.5 torr D_2. Many of the measurements repeated those of Filippov et al (1962), with similar results.

2.3 MORE RECENT WORK

From 1965 to 1968 the number of groups studying the Plasma Focus grew from two to approximately eleven. During this period, some progress was made in understanding the device, but a number of features remained unexplained. Among these were the apparently-long dense-pinch lifetime, ~50 nsec, when MHD instabilities should have destroyed the pinch in ~5 nsec, and the mechanisms responsible for neutron production.

There were two principal reasons for this slow progress. Firstly, the diagnostic techniques that were currently available did not permit measurements of sufficiently high temporal or spatial resolution on the highly-transient fine-scaled pinch. This was mainly due to insufficient development or lack of full exploitation of those techniques. Secondly, because of the complex nature of the Plasma Focus discharge, a serious analytical study was impossible while, at that time, numerical techniques were not sufficiently advanced for a detailed analysis of the problem.

Since 1968, due to improved diagnostics and the development of numerical techniques, there have been significant advances in understanding the Plasma Focus. In the context of improved diagnostics, the main purpose of this thesis is to report the development and application of optical techniques to study the Plasma Focus, and the resulting advances. With reference to numerical techniques, at this point it is convenient to describe briefly the two most important computational studies of the Plasma Focus - the results obtained are discussed later.

Dyachenko and Imshennik (1969) describe two dimensional, particle in cell, numerical calculations for a Filippov device, assuming azimuthal

symmetry. The plasma is treated as a simple fluid of infinite conductivity, with the only dissipative process being due to viscosity.

A more rigorous approach by Roberts and Potter (1970) and by Potter (1971) describes the Mather device in terms of a two dimensional, two fluid, numerical model. Azimuthal symmetry is assumed and the magnetic field is restricted to the azimuthal direction. Dissipative processes include those due to viscosity, resistivity and bremsstrahlung radiation, and the transport coefficients allow for the effects of cyclotron orbiting and particle collisions. The MHD equations describing the model, which contain the six dependent variables: density, magnetic field, radial and axial velocity, and electron and ion temperature, are coupled with an external LC circuit and are numerically integrated in time on an Eulerian space-mesh.

In particular, the latter numerical study has contributed significantly to knowledge on the Plasma Focus, and is undoubtedly one of the most important, single contributions to the subject.

The remainder of this section contains a concise account of the modus operandi of the Plasma Focus, in terms of current knowledge. Because of geometric differences in each of the basic devices and the wide range of conditions under which they are operated, it is sometimes difficult to make a detailed comparison between results obtained by different groups. Furthermore, the plasma parameters during a discharge are space and time dependent. Hence, averaged values quoted should be treated with caution.

It is convenient to divide the Plasma Focus discharge into four phases:

(a) The run-down phase, in which, in the Mather device, after breakdown at the insulator the current sheet produced is accelerated towards the muzzle end of the gun. This phase is absent in the Filippov device.

(b) The collapse phase, in which the axisymmetric current-sheet, on reaching the inner electrode end in the Mather device or following breakdown in the Filippov device, is rapidly accelerated towards the electrode axis.

(c) The dense-pinch phase, in which the collapsing current-sheet reaches the axis to produce a transient dense pinch.

(d) The break-up and diffuse-pinch phase, in which the dense pinch is disrupted by MHD instabilities, but the broad diffuse plasma column subsequently formed emits a copious burst of neutrons and soft X-rays.

Each of these four phases is discussed in turn. The possible mechanisms responsible for the neutron production are considered separately.

2.3.1 The Run-Down Phase (Mather device only)

Referring to Fig.2.1.2, on applying the high voltage between the electrodes the gas breaks down axisymmetrically across the insulator, and a multi-filamentary current-sheet forms, Mather and Williams (1966), the initial shape of which is prescribed by the insulator. An azimuthal magnetic field, B_θ, is induced by the axial component of current flow, of density j_z. The $\underline{j}_z \times \underline{B}_\theta$ force, acting radially outwards, forces the current sheet away from the inner electrode; an inverse pinch effect. Simultaneously, the $\underline{j}_r \times \underline{B}_\theta$ force drives the current sheet down the gun, and within $\sim 1\,\mu$sec, where typically the transit time down the gun is $2.5\,\mu$sec, the filaments blend together forming a uniform current-sheet.

The uniformity of this blending determines the neutron yield in the dense pinch. Lafferty et al (1968), using a device of energy 250 kJ at ~ 1 torr D_2 pressure, showed that when the current sheet does not become azimuthally symmetric, but instead develops a radial spoke, the neutron yield is very small.

In contrast, Bostick et al (1969) find that the filaments combine into a finite number of radial spokes, which retain their identity throughout the run down and collapse phases until they coalesce to form the dense pinch. However, Bostick's device is operated at a much lower energy, 3.8 kJ , and a higher pressure, ~ 8 torr D_2 , than most other Plasma Foci. The neutron yield per discharge is low, $\sim 10^8$.

The pressure of the azimuthal magnetic field varies as $1/r^2$ between the electrodes ($B_\theta^2/8\pi = I_z^2/200\pi r^2$), and pressure balance across the current sheet is achieved by it taking up a parabolic form. As the current sheet is driven down the gun, it soon forms a shock which snowploughs the gas ahead. A steady-state shock velocity is reached in $\sim 0.5\mu$sec , as predicted by a simple snowplough model, Rosenbluth et al (1954). This model relates the final velocity to the driving electric field strength, E, and the initial mass density, ρ , by

$$v_{sp} = (c^2E^2/4\pi\rho)^{\frac{1}{4}} . \qquad \ldots (2.3.1)$$

The above relationship has been verified experimentally for the Plasma Focus by Mather (1965a) and by Patou et al (1967), and has been demonstrated in the computations of Potter (1971). Shock velocities $\leqslant 2\times 10^7$ cm sec^{-1} have been obtained.

Under the radial $\underline{j}_z \times \underline{B}_\theta$ force, plasma flows outwards along the shock boundary and accumulates at the outer electrode, Potter (1971). Mather and Bottoms (1968) observed the parabolic profile of the axially-travelling shock by means of a perforated outer electrode. They found that the perforations enabled a substantial fraction of the plasma reaching the outer electrode to progress beyond it. Because plasma stagnation at the outer electrode was thus prevented, the quality of the dense pinch and the neutron production were substantially improved.

The shock, as it moves axially, removes the majority of gas initially present in the inter-electrode volume, although substantial plasma accumulation occurs at the outer electrode if it is unperforated. Mather and Bottoms (1968), looking end-on into the gun, observed no secondary electrical breakdown between electrodes after the initial breakdown, even during the collapse phase, when the changing current and plasma inductance induce voltages, $V \propto \frac{d}{dt}(LI)$, several times the applied voltage. From considerations of the time taken for the high voltages induced at the gun muzzle to appear at the breech, they deduced that the fraction of inter-electrode gas remaining was $\leq 10^{-4}$, i.e. a moderate vacuum is produced behind the shock. Bernard et al (1970) observed that when a radial restrike occurred between the electrodes no neutrons were produced during the discharge, due to a large part of the current being shunted in the arc, thus preventing normal compression in the dense pinch. Mather et al (1971) found poor neutron yields when restrike occurred.

The plasma is primarily heated by shock heating of the ions, the electrons obtaining energy from the ions by collisions. At this stage, the temperatures T_e and T_i are rather low (typically a few tens of eV). Hence resistive heating, $\propto T_e^{-\frac{3}{2}}$, further heats the electrons, while viscous heating, $\propto T_i^{\frac{5}{2}}$, does not heat the ions significantly. Thus $T_e > T_i$. Mather and Bottoms (1968) estimated T_e as ~ 60 eV from current-sheet resistivity measurements, in a device for which $C = 90\,\mu F$, $V = 17.3$ kV and $p_o = 1.5$ torr D_2. Potter (1971) computes peak temperatures $T_e = 31$ eV and $T_i = 26$ eV in a device for which $C = 40\,\mu F$, $V = 40$ kV and $p_o = 0.26$ torr D_2. Potter finds peak densities of 1.4×10^{17} cm^{-3}, which represents a compression of ~ 3 above the filling density. The outward flow of plasma parallel to the shock prevents higher compression.

After initial breakdown, the current in the discharge circuit increases sinusoidally as the stored capacitative energy is converted into

magnetic energy. This energy is stored inductively behind the current sheet in the gun, and in the parasitic inductances of the discharge circuit. To optimise the conversion of capacitative energy to plasma energy, the magnetic energy at the start of the collapse phase must be maximised. Thus, if the current sheet reaches the gun muzzle at peak discharge current, maximum energy is subsequently fed into the dense pinch. For a given gun length and operating voltage, the initial gas filling is adjusted until the correct flight-time down the gun is achieved. Fig.2.1.2 schematically shows the current-sheet position at various times during a discharge.

2.3.2 The Collpase Phase

In the Mather device, the leading edge of the current-sheet, because of its parabolic profile, is adjacent to the inner electrode during the run-down phase, and on reaching the electrode end the leading edge remains attached to it, Fig.2.1.2. The current sheet continues moving axially, and the location of its leading edge gradually shifts radially outwards. The profile of the current sheet between its leading edge and the inner electrode is such that the $\underline{j}_z \times \underline{B}_\theta$ force acting on this section is directed radially inwards. Thus, as time progresses, an increasing axial length of current sheet is accelerated towards the gun axis as stored magnetic energy is rapidly converted into plasma kinetic energy.

The Filippov device has no run-down phase. The initial breakdown across the insulator is filamentary, Kolesnikov et al (1966). With reference to Fig.2.1.1, the lower part of the current sheet is pushed away from the insulator to the cathode sidewall by the $\underline{j}_z \times \underline{B}_\theta$ force. On reaching the sidewall, the $\underline{j}_r \times \underline{B}_\theta$ force accelerates the current sheet axially towards the chamber lid, the filaments quickly blending to form a homogeneous current-sheet. As in the Mather device, the $\underline{j}_z \times \underline{B}_\theta$ force now accelerates the section of current sheet between its leading edge and

the inner electrode end radially inwards. For a given electrode geometry and operating voltage, the initial gas filling is optimised to achieve maximum conversion of stored capacitative energy into plasma energy, Agafonov et al (1968).

In both devices, the axisymmetric collapse of the current sheet is non cylindrical, and may be visualised as the formation of a cone by the radial implosion of the walls until an apex is formed adjacent to the inner electrode end. Because of the obliquity of the collapsing current-sheet, there is a strong axial component of plasma flow. The majority of gas particles trapped within the volume encircled by the current sheet are not compressed into the dense pinch, but are ejected axially. MHD calculations show, Agafonov et al (1968) and Potter (1971), that only 10-15% of the particles that could be collected during the collapse phase are gathered in the dense pinch. From interferometry studies, section 6.2.3, the efficiency of the focusing mechanism is seen to be $\sim 5\%$. The loss of this large majority of plasma by axial ejection is the key to the working of the Plasma Focus. The transient hot dense pinch is formed by the available magnetic energy, which is stored inductively, being fed to a relatively small number of particles.

During the collapse, radial velocities from $1\text{-}4\times10^{7}$ cm sec^{-1} have been measured; by photography, Filippov and Filippova (1965) and Patou et al (1967), and by the shadowgraph technique, section 6.3.1. The current sheet, as it is accelerated radially, is perturbed by acceleration-driven instabilities which form at the plasma-vacuum boundary, section 5.3.2 and Filippov et al (1971). The instabilities, because of their relatively slow growth-rate, do not seriously disrupt the current sheet. From measurements of the radial acceleration and the instability growth-rate, a deuterium ion temperature of ~ 70 eV has been estimated, section 6.3.3, in a Mather device with $C = 94\,\mu F$, $V = 30$ kV and $p_o = 2.5$ torr

(D_2 + 4% Ar). Potter (1971) computes peak temperatures $\hat{T}_e = 59$ eV and $\hat{T}_i = 27$ eV, for $C = 40\,\mu F$, $V = 40$ kV and $p_o = 0.26$ torr D_2.

As the current sheet collapses to the axis, the plasma inductance, L, increases sharply. Simplifying to the case of two cylindrical co-axial conductors, the plasma of radius r_p being the inner, and the outer electrode of radius r_o being the return, $L \propto \ell n\,(r_o/r_p)$. Since r_p decreases rapidly during the collapse, L increases correspondingly. This causes the current, I, flowing through the plasma to decrease sharply, Fig.2.1.2. A voltage is transiently induced between the electrodes, $V \propto \frac{d}{dt}(LI)$, which is typically 2-5 times the initial capacitor voltage. Normally, the Plasma Focus is operated with a positive centre electrode, and under the accelerating potential of the induced voltage, $\leqslant 150$ kV, electrons bombard the anode. Severe anode erosion occurs and a high flux of X-rays are produced, of hardness characteristic of the electrode material.

As the collapse progresses, the compression in the shock increases gradually. The mass density in the shock is almost constant, section 6.2.3, due to the majority of particles encountered being swept out axially. Peak electron densities in the range 10^{18}-10^{19} cm^{-3} have been measured, Filippov et al (1971) and section 6.2.1. Potter (1971) calculates values of $\hat{n}_e$ of 2.3×10^{17} cm^{-3} for $C = 40\,\mu F$, $V = 40$ kV and $p_o = 0.26$ torr D_2. When the shock reaches the electrode axis, the electron and ion densities increase rapidly as the dense-pinch phase begins.

The primary mechanism for plasma heating, as in the run-down phase, is shock heating of the ions which heat the electrons collisionally. Further electron heating occurs due to the high plasma resistivity.

2.3.3 The Dense-Pinch Phase

This phase commences when the axisymmetric collapsing current-sheet arrives at the axis. In the Mather device, due to the non-cylindrical nature of the collapse, the current sheet initially reaches the axis adjacent to the inner electrode end. The dense pinch is not formed simultaneously over its whole length but, progressing axially away from the electrode end with time over a distance of 1.5 - 2.5 cm, a short length of dense plasma, ≤ 0.5 cm, is formed and is subsequently disrupted by sausage-type instabilities, in a continuous process, section 5.3.2. There is evidence that in the Filippov device the later stages of the collapse are almost cylindrical in form, Morgan et al (1973), resulting in the dense pinch forming simultaneously over its whole length. In both devices, the dense pinch formed at the electrode axis is due to trapped plasma being strongly compressed by the azimuthal magnetic field, of strength $B_\theta = I/5R \sim 1$ MG, Forrest et al (1973). The name Plasma Focus gives a good description of the device, since it 'focuses' a dense plasma at the end of the inner electrode.

In both devices, electron temperatures from 1-3 keV have been measured under a variety of conditions; mainly from studies on the soft X-ray flux, Filippov et al (1962), Mather (1965a) and Peacock et al (1968). Deuterium ion temperatures in the range 0.7 - 3 keV have been measured at maximum compression by cooperative scattering of laser light, Bernard et al (1971), Peacock et al (1972) and Forrest et al (1973). Introducing $\sim 2\%$ of impurity ions such as argon or neon into the discharge, temperatures of ~ 9 keV have been measured for these highly-stripped ions; by spectroscopy, Peacock et al (1971), and by scattering, Peacock et al (1972). The mechanism responsible for producing such high-energy impurity ions is not clear.

The dense pinch created is of minimum radius 0.05–0.2 cm and of length 0.5 – 2.5 cm. Peak electron densities in the range 10^{19}–10^{20} cm^{-3} have neem measured: from absolute continuum measurements, Filippov et al (1962), Mather (1965a) and Peacock et al (1968); from schlieren studies, Mather (1965b) and Morgan et al (1969); and by interferometry, Morgan and Peacock (1972) and section 6.2.1. The overall lifetime of the dense pinch is 30–100 nsec and its energy density is from 10–100 kJ cm^{-3}, Filippov and Filippova (1965) and Peacock et al (1968). The total thermal energy in the dense pinch is $\leqslant 1\%$ of the initial capacitative energy.

The hot dense pinch is highly radiative; in a discharge in deuterium mainly by bremsstrahlung radiation, and in an impure discharge mainly by recombination and line radiation. The peak intensity of these radiations is between 1 and 15 Å. For a deuterium plasma, the bremsstrahlung radiation power, Glasstone and Lovberg (1960), is

$$P_{br} = 5.35 \times 10^{-31}\ n_e^2\ T_e^{\frac{1}{2}} \quad (W\ cm^{-3}). \qquad \ldots (2.3.2)$$

At an electron temperature of 2keV and a density of 10^{19} cm^{-3}, this gives a power loss of ~ 75 MW cm^{-3}. The soft X-ray burst associated with the dense pinch is $\sim$ 50–100 nsec long. In addition, the dense pinch emits a copious burst of neutrons, of energy 2.45 MeV in a thermal plasma, by the D–D fusion reaction ${}_1^2D + {}_1^2D \rightarrow {}_2^3He + {}_0^1n + 3.27$ MeV. The reaction rate for a thermal plasma, Glasstone and Lovberg (1960), is

$$R_{DD} = 0.5\ n_D^2\ \overline{\sigma v_{DD}}\ (cm^{-3}\ sec^{-1}), \qquad \ldots (2.3.3)$$

where the cross section

$$\overline{\sigma v_{DD}} = \frac{2.33 \times 10^{-14}}{T_D^{\frac{2}{3}}} \exp\left(-\frac{18.76}{T_D^{\frac{1}{3}}}\right)\ cm^3\ sec^{-1}.$$

The neutron pulse associated with the dense pinch is 50–100 nsec long, and the neutron yield, which depends upon the energy and geometry of the device, lies between 10^8 and 2×10^{12} per discharge.

Three heating mechanisms, viz. adiabatic compression, resistive heating and viscous heating, are primarily responsible for the high temperatures achieved in the focus, Potter (1971). During the early stages of the compression, when the electron temperature is relatively low, enhanced resistive heating of the electrons, $\propto T_e^{-\frac{3}{2}}$, occurs. The plasma compressed into the dense pinch by the azimuthal magnetic field is heated adiabatically, the initial and final temperatures being related by $T_f = T_{in} (\rho_f/\rho_{in})^{\gamma-1}$, where ρ is the density. Adiabatic heating raises the plasma temperatures by a factor of $\sim$5-10. In the dense pinch, the ions are heated further by viscous heating, $\propto T_i^{\frac{5}{2}}$, because of their relatively high temperature.

Potter (1971) computes for the dense pinch: a peak density $\sim 10^{19}$ cm^{-3}, radius $\sim$0.1 cm, length $\sim$1.5 cm, lifetime $\sim$50 nsec and equal T_e and T_i, $\sim$1.5 keV, for $C = 40\,\mu F$, $V = 40$ kV and $p_o = 1$ torr D_2. This represents a compression of $\sim$300 above the initial filling density.

2.3.4 The Break-Up and Diffuse-Pinch Phase

In the Mather device, because the dense pinch is not formed simultaneously over its whole length, the pinch is progressively disrupted along its length, beginning at the anode, by sausage-type instabilities, section 5.3.2. Consequently, after the pinch has broken up, the plasma expands without any prescribed form. On the other hand, the dense pinch in the Filippov device is formed simultaneously over its whole length, and subsequently it appears to expand as a body, although its form is distorted by sausage-type instabilities, Morgan et al (1973). In contrast, Gribkov et al (1972) observe that the dense pinch in the Filippov device is violently disrupted by sausage-type instabilities and that the expanding plasma has no prescribed form.

Some 50-150 nsec after the neutron and soft X-ray pulses associated with the dense pinch, in many experiments a further pulse of neutrons and soft X-rays is produced, Maisonnier et al (1971), Peacock et al (1971) and Gribkov et al (1972). In general, the second neutron pulse in Filippov devices is more intense than the first, while in Mather devices the converse is true. Taking soft X-ray photographs at the peak of the second neutron burst, Maisonnier's group observed a uniform diffuse plasma of radius ≥ 1 cm in a Filippov device, with $W = 120$ kJ at 40 kV and $p_o = 1.2$ torr D_2 - hence the term diffuse pinch, Gratreau et al (1971). In the same machine, Morgan et al (1973) measured by interferometry an average electron density of $\sim 2\times10^{17}$ cm^{-3} at this time, over a plasma column of diameter ~ 4 cm. Similar density values have been estimated in other devices, Gribkov et al (1972) and section 6.2.3.

Maisonnier et al (1971) observe that $\sim 80\%$ of the neutron flux during a discharge can be explained by emission from a thermal plasma moving axially away from the anode at $\sim 1.5\times10^{7}$ cm sec^{-1}. Since the second neutron burst is a factor of ~ 4 more intense than the first, to account for the neutron yield from a plasma of density $\sim 2\times10^{17}$ cm^{-3} on a thermal basis, a deuteron temperature of ~ 8 keV is required according to equation (2.3.3), Morgan et al (1973). The attainment of this high temperature in the short time interval between the first and second neutron pulses is not easy to explain.

Maisonnier et al (1972) propose a semi-quantitative model, based on experiment, to account for neutron production in the diffuse pinch. In the model, the dense pinch is disrupted by sausage-type instabilities, and the plasma expands freely. The plasma density decreases and the neutron and soft X-ray fluxes drop to zero. The plasma becomes intermixed with the magnetic field which formerly confined it and stores the magnetic energy internally, since the plasma resistivity is too low to

convert this energy into thermal energy. At a critical radius of expansion, the conditions for the onset of turbulent heating are satisfied, the magnetic energy is rapidly converted into thermal energy, and a pulse of neutrons and soft X-rays are emitted. It is argued that, since the capacitors are discharged at the time of the dense pinch, the only available energy to heat the deuterons is in the magnetic field.

The energy available from the magnetic field is adequate to heat the deuterons to the required temperature, Maisonnier et al (1972). At constant current, the magnetic energy available to a plasma column expanding from radius r_1 to r_2 is

$$W = \tfrac{1}{2} LI^2 = 10^{-9} \ell n(r_2/r_1)\, I^2 \quad (J\ cm^{-1}) .$$

In the dense pinch, of radius r_1, the Bennett relation holds for pressure balance between the confining B_θ field and the plasma kinetic pressure, section 6.2.4. Assuming $T_e = T_i = T_1$

$$I^2 = 400\, N k T_1 ,$$

where N is the line density (cm^{-1}). If the available magnetic energy is fed into $2N$ particles, the new plasma temperature is

$$T_2 = T_1 + W/2Nk .$$

Combining the above three equations, and allowing for the mixed units,

$$T_2 = T_1 \left(1 + 2\, \ell n(r_2/r_1)\right) .$$

Typically the ratio r_2/r_1 is 10 and thus $T_2 \sim 5.6\, T_1$. Since $T_1 \geq 1.5$ keV, there is more than sufficient energy available in the magnetic field to heat the plasma to 8 keV.

The turbulent heating is most probably due to high-frequency electrostatic waves excited by a relative drift between the electrons and ions in the plasma. This drift is driven by current flow normal to the magnetic field lines, through which the plasma column is expanding. The energy in the ordered drift motion is converted into plasma thermal energy by

turbulent scattering off the excited waves. The subject of turbulent heating is complex; a good review is given by Tsytovich (1966).

There are three principal electrostatic instabilities with sufficiently high growth-rate to turbulently heat the plasma on the timescale between the two neutron pulses in the Plasma Focus. These are the two-stream, the ion-acoustic and the electron-cyclotron drift instability. From linear analysis, Lashmore-Davies and Martin (1973) conclude that it is impossible to predict exactly which instability will dominate in a given plasma. However, the dominant instability is largely determined by the ratio of the drift velocity, v_d, to the electron thermal velocity, v_{te}, and also be the ratio T_e/T_i, Wong (1970).

For an electron drift velocity, $v_d = \underline{E}\times\underline{B}/cB^2$, such that $v_d > v_{te} = (kT_e/m_e)^{\frac{1}{2}}$, the two-stream instability is likely to dominate. It has a characteristic frequency of order ω_{pe} and a growthrate $\omega_{ts} \simeq (m_e/m_i)^{\frac{1}{3}}\,\omega_{pe}$, where ω_{pe} is the electron plasma frequency. The drifting electrons are scattered by the wave giving an effective collision time, $\tau_{ts} \sim \omega_{ts}^{-1}$, which is much shorter than that for binary electron-ion collisions. This results in an anomalously-high plasma resistivity.

When $v_{te} > v_d > v_s = (kT_e/m_i)^{\frac{1}{2}}$, where v_s is the ion sound speed, and for $T_e > T_i$, the ion-acoustic instability will probably dominate. This instability has a characteristic frequency of order ω_{pi} and a growth rate $\omega_{ia} \sim (m_e/m_i)^{\frac{1}{2}}\,\frac{v_d}{v_s}\,\omega_{pi}$, where ω_{pi} is the ion plasma frequency. Energy is transferred from those drifting electrons that are resonant with the sound wave to the wave, which then interacts with those ions having velocities close to its phase velocity. The plasma resistivity is enhanced due to electrons scattering off the wave.

Under the conditions $v_d < v_{te}$, $T_e \geq T_i$ and $\omega_{pe} \gg \omega_{ce} = \frac{eB}{m_e c}$, where ω_{ce} is the electron cyclotron frequency, the electron-cyclotron

drift instability probably dominates. It has a characteristic frequency of order ω_{ce} and a growthrate $\omega_{cd} \sim (m_e/m_i)^{\frac{1}{4}}\omega_{ce}$. The instability arises from the resonant coupling of a Doppler-shifted ion mode with the electron cyclotron mode, feeding energy into the electrons.

In the Plasma Focus, if at some stage during the plasma expansion following the dense pinch the density is 10^{18} cm^{-3}, and for $T_i < T_e = 1.5$ keV, the growthrate of the ion-acoustic instability is $\sim 3\times10^{10}$ sec^{-1} for $v_d = 2v_s$. Since this is the slowest growthrate of all three instabilities, each of them could heat the diffuse pinch within the 50-150 nsec time interval between the two neutron pulses. However, the two-stream and the electron-cyclotron drift instability cause electron heating, and, if the plasma is heated by either of these, classical electron-ion collisions cannot account for any energy transfer to the ions. For the plasma conditions $n_e = n_i = 10^{18}$ cm^{-3}, $T_e = 8$ keV and $T_i = 1.5$ keV, the electron-ion collision time is $\sim 33\,\mu$sec , Spitzer (1962). On the other hand, for direct ion heating by the ion-acoustic instability during the time interval between the two neutron pulses, it is necessary that $T_e > T_i$. Measurements on the dense pinch indicate that this is not so, and that $T_e \simeq T_i$. Thus, the ion-acoustic instability is not likely to be triggered during the plasma expansion immediately following the dense-pinch break-up. One possible answer is that initially the electrons are heated by the two-stream or the electron-cyclotron drift instability, the ions being unheated. At a certain ratio of T_e/T_i, the ion-acoustic instability rapidly dominates, heating the ions.

The diffuse-pinch phase, being a relatively new phenomenon, remains one of the least understood aspects of the Plasma Focus discharge. Currently, many investigators are turning their attention to its study.

2.3.5 Neutron Production

A large amount of research on the Plasma Focus, both experimental and theoretical, has been devoted to a study of neutron production. A brief outline of the more important features of the work is given. The following terminology is used: the forward or 0° direction is the direction in which the plasma has an axial component of flow during the collapse phase, the backward and transverse directions being at 180° and 90° to this direction, respectively.

From the many and diverse experimental results, a number of simple models have been proposed to account for neutron production:

(a) The thermal model. The plasma deuterons have a Maxwellian velocity distribution. Fusion reactions are due to close-range thermal collisions. The neutron flux and energy are completely isotropic.

(b) The moving-boiler model. A thermal plasma has a centre of mass velocity, $v_m, \geqslant 10^7 \text{ cm sec}^{-1}$ in the forward direction. The neutron flux and energy increase smoothly from the backward to the forward direction.

(c) The beam-target model. A beam of deuterons is accelerated to energies $\leqslant 150 \text{ keV}$ in the forward direction, to bombard 'stationary' deuterons in the much less energetic plasma. The neutron flux and energy are highly anisotropic, the forward direction being the preferred direction, with both the flux and energy at 90° being almost equal to those at 180°.

In most experiments, the neutron flux and energy are anisotropic, thus discounting the thermal model. However, Bernard et al (1972), using a Mather device of 100 kJ energy at 40 kV, observed an isotropic neutron emission for initial fillings of ~ 17 torr D_2. In contrast, for fillings of 5–15 torr, the neutron emission was anisotropic.

Filippov and Filippova (1965), using a device with $C = 180\ \mu F$, $V = 16 - 26$ kV and $p_o \simeq 1.2$ torr D_2, found an average neutron energy at

0° which exceeded the 2.45 MeV energy at 90° by ≤ 0.3 MeV. The fluxes were isotropic to within 5%. They interpreted the results as agreeing with a moving-boiler model.

Bottoms et al (1968), using a Mather device with W = 67 kJ at 20 kV and p_o = 5 - 10 torr D_2, found a flux anisotropy which increased smoothly from ~ 5% at 45° to ~ 27% at 180°, with respect to the forward direction. The average neutron energy decreased smoothly from ~ 2.77 MeV at 0° to ~ 2.22 MeV at 180°. These results support a moving-boiler model, with $v_m \sim 1.2 \times 10^8$ cm sec^{-1}. However, multiplying the neutron pulse duration of ~ 100 nsec by this velocity gives an apparent pinch length $\geq$ 10 cm. This is far in excess of the 1-2 cm observed length. Also, hard X-rays of energies $\leq$ 100 keV were produced by voltages induced during the collapse phase. Deuterons of such energies should also have been produced, causing very anisotropic neutron emission, in contrast to the results. It was suggested that a mixture of the beam-target and moving-boiler models could explain these conflicting observations.

Meskan et al (1967) used a gun of paraboloidal geometry, with W = 15 kJ at 18 kV and with p_o = 0.7 torr D_2. The average neutron energies at 0° and 180° were 2.7 MeV and 2.1 MeV, respectively. The neutron spectra could be explained by a beam-target model, with beam energy ~ 100 keV.

Using a Filippov device, with W = 120 kJ at 40 kV and with p_o = 1.2 torr D_2, Maisonnier et al (1971) found no single model could explain the observed anisotropy, but that a mixture of moving-boiler and beam-target models could. About 20% of the neutrons could be accounted for by interactions due to a deuteron beam of energy ~ 105 keV, and the remainder by a moving boiler with $v_m \sim 1.5 \times 10^7$ cm sec^{-1}.

Finally, Patou et al (1969), using a Mather device with $W = 15\,kJ$ at 18 kV and with $p_o \sim 2\,torr\,D_2$, found that not even a mixture of moving-boiler and beam-target models could explain the flux anisotropy. However, the energy anisotropy could be explained either by a moving-boiler model with $v_m \sim 1.2 \times 10^8\,cm\,sec^{-1}$, or by a beam-target model with a deuteron beam of energy $\sim 75\,keV$.

In addition to these simple models, more complex models have been proposed to describe neutron production in the dense pinch.

Bernstein (1970) assumes that an initial annular current distribution rapidly contracts in the dense pinch to an arbitrary distribution peaked on axis, due to an increase in plasma resistance caused by an axial plasma loss as the pinch forms. The sudden contraction generates high $\underline{E}_z \times \underline{B}_\theta$ electric fields, and $\leqslant 10\%$ of the deuterons are accelerated up to 600 keV. The orbiting motion of the deuterons in the magnetic field produces an anisotropic distribution of collision velocities. Collisions between these energetic deuterons and 'stationary' ones can account for the observed characteristics of neutron production in the pinch.

Potter and Haines (1971) have developed a computer code which simulates the interaction of 20,000 deuterons immersed in an electron fluid. Initially, the ions have a uniform distribution throughout the pinch and a Maxwellian velocity distribution. If the ion larmor radius is less than the pinch radius, on applying a small axial electric field the ion velocity distribution rapidly obtains a singularity. The deuterons in this high energy tail acquire their energy by a collisionless axial acceleration in orbits which cross and recross the field-free pinch axis. The applied electric field simulates the field which produces runaway electrons in the majority of Focus devices. The energetic deuterons ($\sim 100\,keV$) cause a significant anisotropic neutron emission from the pinch. Neutrons are also produced by a moving boiler with axial velocity $\sim 3 \times 10^7\,cm\,sec^{-1}$.

A completely different approach is adopted by Bostick et al (1969). Using a low-energy Mather device (~ 3.8 kJ), the filamentary structure formed at breakdown is observed to persist until the dense pinch is formed. The filaments are observed to occur in pairs, with opposing magnetic field structure. A model is proposed in which each filament is described by a bundle of helical magnetic lines, of increasing pitch from periphery to axis. The filaments coalesce in the pinch, releasing magnetic energy by the annihilation of oppositely-directed magnetic-field bundles. Intense electric fields generated by the decaying filaments cause neutrons to be produced in a beam-target-like process over a wide range of angles.

It is difficult to draw any firm conclusion from these diverse experimental results. However, this is not surprising, since the characteristics of the neutron emission from a plasma are very dependent upon the parameters of that plasma, and no two Plasma Focus devices produce exactly the same discharge.

An important factor when assessing the significance of beam-target interactions in a deuterium plasma is the product $\omega_{ci}\,\tau_{ii}$, where ω_{ci} is the ion cyclotron frequency and τ_{ii} is the ion self-collision time. If $\omega_{ci}\,\tau_{ii} \gg 1$, the deuterons are essentially collisionless, and an accelerating field in the plasma can cause a high-energy tail in the ion distribution function. Under these conditions, beam-target interactions can be important, resulting in an anisotropic neutron emission. For $\omega_{ci}\,\tau_{ii} \ll 1$, the deuterons are collisional and thermal reactions will dominate.

For the Plasma Focus, considering the dense-pinch phase, a survey of published measurements reveals differences of $\geqslant 5$ in density and $\geqslant 2$ in temperature between extreme values. Hence, $\omega_{ci}\,\tau_{ii}$ could vary by $\geqslant 10$ between the two extremes. In a device of medium stored energy (32kJ), Potter (1971) computes a value of $\leqslant 10$ for $\omega_{ci}\,\tau_{ii}$. Thus, considering

a variation of 10 in $\omega_{ci}\,\tau_{ii}$ between two dense pinches, in one pinch the deuterons could be collisionless while in the other they could be quasi-collisional. This would lead to two different deuteron velocity distributions and two neutron emissions of very different characteristics.

The situation is further complicated, because in each device the mechanisms responsible for neutron production probably differ from the dense pinch to the diffuse-pinch phase, due to the quite different plasma parameters. Also, the proportion of neutrons produced in each phase differs from one device to another.

Before the problem of neutron production in the Plasma Focus can be resolved fully, it is evident that plasma parameters such as density, temperature and magnetic field have to be known accurately at many points in the discharge throughout its lifetime. Hence, diagnostic techniques are required which are capable of determining such parameters with a high degree of spatial and temporal resolution. Although optical techniques are now sufficiently advanced to measure electron density to the above requirements, e.g. see Chapter VI, there is much work needed if temperature and magnetic field are to be determined with the same precision. The problem of neutron production presents a stimulating challenge to those engaged in studying the Plasma Focus.

CHAPTER III

DIAGNOSTIC TECHNIQUES BASED ON PLASMA OPTICAL REFRACTIVITY

3.1 INTRODUCTION

The refractive index of a highly-ionized plasma is primarily a function of its electron density. In general, the effects due to the presence of ions and a small number of unionized particles are negligible. By measuring the refractive index of such a plasma, its electron density can be determined.

The refractive index of a plasma may be determined optically by propagating a light beam through it and measuring the consequent changes induced in the beam's wavefront. The path of an individual light ray is traced through the plasma, Fig.3.1.1. Without the plasma, the ray would have reached the point P on the screen S, at a time t and made an angle θ with an arbitrary direction. In the presence of the plasma, the ray arrives at the point P′ at a time t' and makes an angle θ'. The insertion of appropriate optical equipment into the light path will display on S either a record of the phase lag $\tau = t' - t$, the deflection $\epsilon = \theta' - \theta$, or the displacement $d = PP'$.

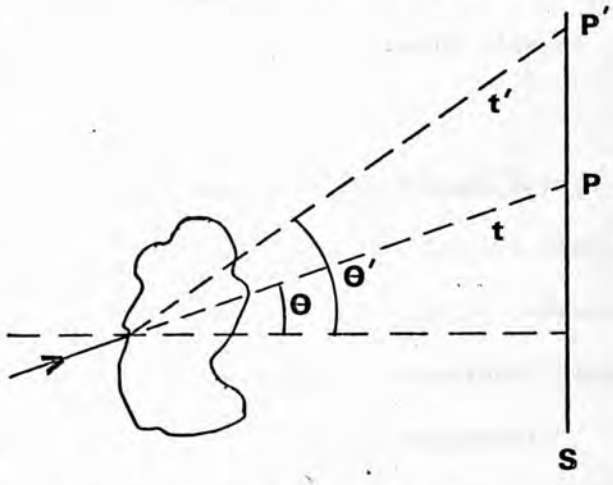

Fig.3.1.1
Path of a light ray through a plasma

There are three principal optical techniques for measuring the refractive index of a plasma :

(a) Interferometry, which records phase changes, measures the refractive index, n, directly.

(b) Schlieren photography, which records deflections, measures the gradient of the refractive index, i.e. dn/dx.

(c) Shadowgraphy, which records displacements, measures the second derivative of the refractive index, i.e. d^2n/dx^2.

Probing a laboratory plasma with a light beam is an invaluable diagnostic technique because, generally, the interaction between the electromagnetic wave and the plasma is weak, due to the wave frequency being much higher than any characteristic frequency of the plasma. Thus, the plasma characteristics are not appreciably altered by the passage of the wave. However, for the same reason, the technique has limited sensitivity and, usually, optical refractivity measurements are restricted to plasmas of density $\geq 10^{14}$ cm^{-3}. A further advantage of optical probing is that high spatial resolution is possible because of the small size of optical wavelengths.

Optical techniques are well suited to a study of the Plasma Focus discharge, because the electron density is sufficiently high and the electron density gradients are sufficiently steep to cause appreciable refractive effects. Also, because of the small size and highly-transient nature of the dense pinch, radius ~ 0.05 cm and lifetime ~ 50 nsec, diagnostic techniques capable of high spatial and temporal resolution are required. Using a pulsed ruby laser as a short-duration light source, optical refractivity techniques fulfil these requirements, and are the basis of the studies described later in the thesis.

3.2 THE OPTICAL REFRACTIVITY OF A PLASMA

3.2.1 General Considerations

In general, a plasma consists of a mixture of: free electrons; ions in various stages of ionization from single to complete, in the ground state and in excited states; residual neutral atoms in the ground state and in excited states; and, finally, if dissociation is incomplete, molecules. The overall refractivity of a plasma may be considered as the sum of the refractivities of its constituent components, i.e.

$$n - 1 = \sum_j K_j \, n_j \, ,$$

where K_j is the specific refractivity of a particle of type j and n_j is the density of such particles.

The refractivities of the various components of a plasma are considered in turn.

3.2.2 The Refractivity of Free Electrons and Fully-Stripped Ions

The refractivity due to the free electrons and fully-stripped ions in a plasma may be obtained by deriving the dispersion relation for an electromagnetic wave propagating through a plasma. In this relation, the wave frequency and propagating wave number are related by the complex dielectric constant.

For an e.m. wave propagating through a fully-ionized collision-dominated plasma, in which a steady magnetic field is applied parallel to the direction of propagation, the plasma refractive index, Appendix 2, is

$$n = \left\{ \tfrac{1}{2}\left(1 - \frac{\omega_{pe}^2}{\omega} \cdot \frac{\omega \pm \omega_{ce}}{(\omega \pm \omega_{ce})^2 + \nu^2}\right) + \tfrac{1}{2}\left(\left[1 - \frac{\omega_{pe}^2}{\omega} \cdot \frac{\omega \pm \omega_{ce}}{(\omega \pm \omega_{ce})^2 + \nu^2}\right]^2 + \left[\frac{\omega_{pe}^2}{\omega} \cdot \frac{\nu}{(\omega \pm \omega_{ce})^2 + \nu^2}\right]^2 \right)^{\frac{1}{2}} \right\}^{\frac{1}{2}}, \quad \ldots \ (3.2.1)$$

where ω is the wave frequency, ω_{pe} the electron plasma frequency, ω_{ce}

the electron cyclotron frequency and ν the electron-ion collision frequency. In the above equation, the refractivity is entirely due to the electrons. This is because the mass of an ion is at least ~ 1840 times greater than the mass of an electron, and thus the ions are much less influenced by the oscillating electric field of the wave.

When the applied magnetic field is transverse to the direction of wave propagation, and provided the magnetic field has a component perpendicular to the wave electric field, the dispersion relation has a smaller correction factor due to the magnetic field, ω^{-2} instead of ω^{-1}, than for the case of longitudinal propagation. Therefore, for the case of a static magnetic field applied in an arbitrary direction, the longitudinal field component is dominant in modifying the dispersion relation.

Equation (3.2.1) is examined, with a view to simplification. As a first step, the peak values of the plasma frequencies in the equation are estimated for a Plasma Focus discharge in deuterium. In the dense pinch, realistic upper values of density and temperature, section 2.3.3, are: $n_e = n_i = 5 \times 10^{19}$ cm^{-3} and $T_e = T_i = 2.5$ keV.

The electron plasma frequency is given by

$$\omega_{pe} = (4\pi n_e e^2/m_e)^{\frac{1}{2}}.$$

Using the above value of density, $\omega_{pe} = 4.0 \times 10^{14}$ sec^{-1}.

To estimate the electron cyclotron frequency, it is necessary to know the strength, B, of the plasma internal magnetic field. An upper limit for B may be deduced using the following model: The dense pinch is assumed to consist of uniform plasma, to have no internal magnetic field and to be confined by an azimuthal magnetic field, of strength B_θ. At the boundary between the plasma and magnetic field, the magnetic pressure, $B_\theta^2/8\pi$, exactly balances the plasma kinetic pressure, $2\, n_e\, kT_e$. Thus,

$$B_\theta = (16\pi n_e kT_e)^{\frac{1}{2}}.$$

Using the above peak values of density and temperature, $B_\theta = 3.2\times10^6$ G. From this value of magnetic field,

$$\omega_{ce} = eB/m_e c = 5.6\times10^{13}\ \text{sec}^{-1}.$$

In practice, the plasma temperature and density are not constant over the pinch radius, and the azimuthal field penetrates into the confined pinch, decreasing smoothly until it is zero at the axis. At any point in the plasma there is balance between the $j_z \times \underline{B}_\theta$ force and the radial gradient of kinetic pressure. Hence, the value of ω_{ce} estimated above may be regarded as the upper limit.

The electron-ion collision frequency is estimated using the relaxation time, τ_{ei}, for the 90^0 total deflection of an electron due to distant encounters with ions, Spitzer (1962).

$$\tau_{ei} = \frac{3 m_e m_i k^{\frac{3}{2}}}{8(2\pi)^{\frac{1}{2}} n_i Z^2 e^4 \ell n \Lambda_{ei}} \cdot \left(\frac{T_e}{m_e} + \frac{T_i}{m_i}\right)^{\frac{3}{2}},$$

where

$$\Lambda_{ei} = \frac{3}{2e^3 Z}\left(\frac{4.2\times10^5 k^3 T_e^2}{\pi n_e}\right)^{\frac{1}{2}}.$$

The electron-deuteron collision frequency is $\nu = \tau_{ei}^{-1} = 6.6\times10^6\ \text{sec}^{-1}$.

In the case of the Focus discharge being illuminated with ruby laser light of wavelength 6943 Å, as in the studies reported in Chapters IV and V, the angular frequency of the wave is

$$\omega = 2\pi c/\lambda = 2.7\times10^{15}\ \text{sec}^{-1}.$$

Comparing the above values of frequency, ω is $\gg \nu, \omega_{ce}$ and $\omega > \omega_{pe}$. Equation (3.2.1) reduces to

$$n = 1 - \frac{\omega_{pe}^2}{2\omega^2}. \qquad \ldots (3.2.2)$$

Substituting the constants into the above equation

$$n = 1 - 4.48\times10^{-14}\lambda^2 n_e. \qquad \ldots (3.2.3)$$

From the above, for a given plasma at a fixed wavelength of illumination, an increase in electron density causes a decrease in refractive index and conversely, i.e. $n-1 \propto -n_e$.

3.2.3 The Refractivity of Non-Electron Species (Excluding fully-stripped ions)

During a Plasma Focus discharge, the temperature and density of the plasma are sufficiently high for it to be fully ionized. However, during the collapse phase, some unionized particles are present within the volume enclosed by the collapsing conical current-sheet. Probing the plasma with a light beam perpendicular to the Focus axis, the beam would pass through ionized particles in the sheet and neutral particles within the cone. Furthermore, in the studies reported in Chapters IV and V, $\sim 2\%$ of argon is added to the deuterium filling. Even in the dense pinch, the majority of argon ions are incompletely ionized, He-like argon ions predominating, Peacock et al (1971). Thus, the refractivity due to the non-electron species in the discharge must be assessed.

(a) The refractivity of unexcited neutrals

For bound electrons in the ground states of like neutral particles, the refractivity is

$$n = 1 + \frac{2\pi e^2 n_e}{m_e} \sum_k \frac{f_k}{\omega_k^2 - \omega^2} . \qquad \ldots (3.2.4)$$

In the above, n_e is the bound electron density, f_k is the oscillator strength for transitions between the ground state and energy level k, and ω_k is the frequency corresponding to the energy difference between the two levels. Equation (3.2.4) may be derived following a procedure similar to that for equation (3.2.1), Born and Wolf (1970).

When $\omega \sim \omega_k$, the formulation leading to equation (3.2.4) breaks down because the effect of dissipation has been neglected. These values of ω_k are the frequencies at which anomalous dispersion occurs. Because

the resonance frequencies of neutrals are almost entirely higher than optical frequencies, anomalous dispersion is unimportant when calculating optical refractivity. Equation (3.2.4) is then approximated by a two-term Cauchy formula

$$n = 1 + A(1 + B/\lambda^2)\, n_n \,, \qquad \ldots (3.2.5)$$

where n_n is the density of the like neutrals and A and B are empirically-determined coefficients.

The coefficients A and B are tabulated for a variety of gases, e.g. Allen (1963). Values for the gases used in the Plasma Focus studies reported later are tabulated below:

Table 3.2.1

Gas	$A \times 10^{-24}$	$B \times 10^{-11}$ (λ in cm)
D_2	5.07	7.52
D	4.17	6.2
Ar	10.42	5.6
Ne	2.49	2.4

Over the visible spectrum, from equation (3.2.5), n is almost independent of λ, since $B/\lambda^2 \ll 1$.

(b) <u>The refractivity of unexcited partially-stripped ions</u>

Martellucci (1967) has estimated the refractivities of unexcited partially-stripped ions from calculations of the polarisabilities of various species. For each species, the refractivity at optical wavelengths can be represented by a two-term Cauchy formula, as equation (3.2.5). The coefficient A is defined

$$A = 2\pi\alpha \,, \qquad \ldots (3.2.6)$$

where α is the polarisability of that species. Now

$$\alpha = \frac{4}{9a_o} \sum_i \left[\overline{r_i^2}\right]^2 , \qquad \ldots (3.2.7)$$

where $a_o = \hbar^2/m_e e^2$ is the Bohr radius and $\overline{r_i^2}$ is the mean of the square of the distance of the i^{th} electron from the nucleus.

Martellucci obtained values of A of the same order of magnitude as, but systematically less than, the values for neutrals.

(c) The refractivity of excited atoms and partially-stripped ions

The refractivity of these species at optical wavelengths can also be represented by equation (3.2.5). The coefficients A are estimated from polarisability calculations. From equation (3.2.7), α, and hence the refractivity, scales approximately as the fourth power of the mean distance of the excited electron from the nucleus.

The number of atoms or ions of any species with an electron excited to a high-lying state will be small. The majority have electrons excited to the inner low-lying levels. Hence, the refractivity of the bulk of excited atoms and ions is again less than that of unexcited neutrals, Martellucci (1967). The combined effect of those species with large polarisabilities is negligible due to their small concentration.

3.2.4 Discussion

At the ruby laser wavelength, $\lambda = 6943 \text{Å}$, the electron refractivity of a plasma, from equation (3.2.3), is

$$n = 1 - 2.16 \times 10^{-22} n_e .$$

Thus, the specific refractivity of electrons at 6943Å is -2.16×10^{-22}. For the purposes of comparison, the absolute value of this quantity is used. In section 3.2.3, it was demonstrated that, of all the non-electron species present in a plasma, unexcited neutrals have the largest specific refractivity. From equation (3.2.5) and Table 3.2.1, the specific refractivity of argon atoms, which is the highest of all the neutrals used in the Plasma Focus studies reported in Chapters IV and V, is ~ 20 less than that of electrons at 6943Å.

The majority of Plasma Focus discharges studied in the present work had $\sim 2\%$ added argon. Thus, in the plasma, the refractivity of the argon

ions would be $< 0.1\%$ of that of the electrons. The refractivity of the argon and deuterium neutrals in the plasma is negligible because of their extremely low concentration. During the collapse phase, when neutrals are trapped within the imploding shock, the specific refractivity of deuterium particles is a factor of ~ 43 less than that of electrons, Table 3.2.1. Although at this stage the electron refractivity should be sufficient to justify neglecting that of the deuterium neutrals, it is necessary to evaluate the total number of each species, as a check.

Thus, in general, during a Plasma Focus discharge the electron refractivity at optical wavelengths is dominant, and the effects due to other species can be neglected.

3.3 THE OPTICAL DIAGNOSTIC TECHNIQUES

The optical techniques of shadowgraphy, schlieren photography and interferometry, and their application to the study of a plasma, are discussed in turn. The properties of a Q-switched ruby laser, as a suitable light source for use with these techniques, are considered separately.

An excellent review of optical plasma diagnostic techniques is given by Jahoda and Sawyer (1971).

3.3.1 The Shadowgraph Technique

(a) General principles

Shadowgraphy is extremely simple in principle. A uniform parallel light beam passes through the test object and falls onto a screen or detector. For a test object of uniform refractive index the screen is uniformly illuminated. If there is a constant refractive-index gradient transverse to the beam, all light rays suffer equal deflection with no change in the screen illumination. However, if the first derivative of the refractive index varies transverse to the beam, all light rays are not equally displaced at the screen, resulting in variations in illumination.

Consider a parallel monochromatic light beam propagating parallel to the z axis of a Cartesian coordinate system, and encountering a system in which the refractive index $n(x,y,z)$ is a function of position. Initially, it is supposed that there is a constant refractive index gradient, $\partial n/\partial x$, in the x direction. Deviations in the x z plane only are considered, Fig.3.3.1, and are greatly exaggerated for the sake of clarity.

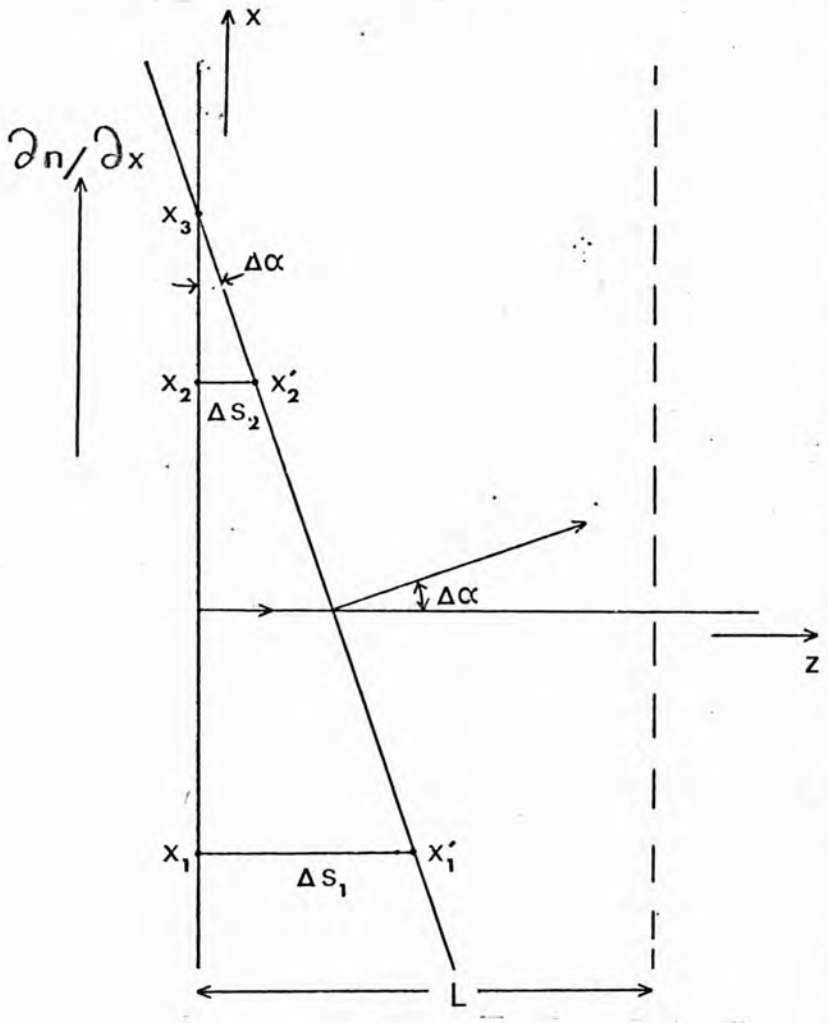

Fig.3.3.1
Angular deviation of a wavefront due to a refractive index gradient

Two sections of the plane wave arrive simultaneously at x_1 and x_2, on the boundary of the system. In a subsequent time interval, Δt, the sections travel distances ΔS_1 and ΔS_2 to positions x_1' and x_2', respectively. If the refractive indices at x_1 and x_2 are n_1 and n_2, respectively, then $\Delta S_1/\Delta S_2 = n_1/n_2$. Hence,

$$\Delta S_1 - \Delta S_2 = \Delta S_1(1 - n_1/n_2) .$$

Now n_1 and n_2 are related by

$$n_2 = n_1 + \frac{\partial n}{\partial x}(x_2 - x_1) .$$

Denoting $x_2 - x_1$ by Δx and combining the above two equations

$$\Delta S_1 - \Delta S_2 = \frac{\Delta S_1}{n_2} \frac{\partial n}{\partial x} \Delta x . \qquad \ldots (3.3.1)$$

The line joining x_1' and x_2' represents the advancing wavefront, the normal to which makes an angle $\Delta\alpha$ with the z axis. A continuation of the new wavefront intersects the old one at position x_3, making an angle $\Delta\alpha$. Thus $\Delta S_1 = (x_3 - x_1)\,\Delta\alpha$ and $\Delta S_2 = (x_3 - x_2)\,\Delta\alpha$. Hence

$$\Delta S_1 - \Delta S_2 = \Delta\alpha . \Delta x .$$

Substituting the above into equation (3.3.1),

$$\Delta\alpha = \frac{1}{n_2} \frac{\partial n}{\partial x} \Delta S_1 .$$

Since $n_2 \simeq n_1$ and $\Delta S_2 \simeq \Delta S_1$, we may write

$$\Delta\alpha = \frac{1}{n} \frac{\partial n}{\partial x} \Delta S . \qquad \ldots (3.3.2)$$

This is the incremental deflection $\Delta\alpha$ of the beam in travelling an incremental length ΔS in the disturbance of thickness L.

The intensity distribution of the beam on a screen placed a distance ℓ, in the z direction, beyond the refractive disturbance will be changed by its presence. Referring to Fig.3.3.1, the light flux incident on the increment Δx at the boundary, as a consequence of travelling a distance ΔS into the disturbance, is spread from a position $x_1 + \ell . \Delta\alpha$ to a position $x_2 + \ell . \Delta\alpha$, on the screen. Hence, the incremental length illuminated on both screen and boundary is the same, and the disturbance causes no change in screen intensity.

However, if the refractive index gradient is changing linearly, the flux on the screen is spread from a position $x_1 + \ell . \Delta\alpha$ to a position $x_2 + \ell\,(\Delta\alpha + \Delta x . \partial\Delta\alpha/\partial x)$, i.e. the screen intensity is changed. For a refractive index gradient changing linearly in the y direction, an illumination of an increment Δy at the disturbance boundary gives a similar result. The area illuminated at the boundary is $\Delta x . \Delta y$. The area illuminated on the screen is

$$\left[x_2 + \ell\left(\Delta\alpha_x + \Delta x \frac{\partial \Delta\alpha_x}{\partial x}\right) - \left(x_1 + \ell \,.\, \Delta\alpha_x\right)\right] . \left[y_2 + \ell\left(\Delta\alpha_y + \Delta y \frac{\partial \Delta\alpha_y}{\partial y}\right) - \left(y_1 + \ell \,.\, \Delta\alpha_y\right)\right]$$

$$\simeq \Delta x \,.\, \Delta y\left(1 + \ell \frac{\partial}{\partial x} \Delta\alpha_x + \ell \frac{\partial}{\partial y} \Delta\alpha_y\right),$$

ignoring the product of small quantities. If A is the area illuminated at the boundary, the change in area illuminated on the screen, due to deviations in an incremental thickness ΔS of the disturbance, is

$$\Delta A = \ell \,.\, \Delta x \,.\, \Delta y \left(\frac{\partial}{\partial x} \Delta\alpha_x + \frac{\partial}{\partial y} \Delta\alpha_y\right) .$$

This change in area will result in an equivalent fractional change in illumination $\Delta I/I$, i.e.

$$\frac{\Delta I}{I} = \frac{\Delta A}{A} = \ell\left(\frac{\partial}{\partial x} \Delta\alpha_x + \frac{\partial}{\partial y} \Delta\alpha_y\right) .$$

Substituting for $\Delta\alpha_x$ and $\Delta\alpha_y$ in the above, from equation (3.3.2),

$$\frac{\Delta I}{I} = \ell \left[\frac{1}{n}\left(\frac{\partial^2 n}{\partial x^2} + \frac{\partial^2 n}{\partial y^2}\right) \Delta S\right] .$$

In the limit of small deflections from the z direction, the total fractional change in intensity at a point on the screen, due to the light beam traversing the whole thickness L of the refractive disturbance is, letting $\Delta S \to 0$ in the above,

$$\frac{\Delta I}{I} = \ell \int_0^L \frac{1}{n(x,y,z)} \left(\frac{\partial^2}{\partial x^2} n(x,y,z) + \frac{\partial^2}{\partial y^2} n(x,y,z)\right) dz \quad \ldots \quad (3.3.3)$$

The shadowgraph technique records the line integral of the second derivative of the refractive index. The derivation of the above result has assumed linearity in the change of the refractive index gradients in the transverse directions.

(b) Practical aspects of shadowgraphy

The ideal system described in the previous section is free of imperfections. The restrictions imposed by using a real system are now considered.

In a real system, the light beam used to illuminate the test section, i.e. the region containing the refractive disturbance, diverges from true

parallelism by the angle θ. The beam is usually obtained using a condenser to focus a light source onto a pinhole of aperture d, which is itself at the focus of a lens of focal length $+f$. Then $\theta = d/f$. To resolve inhomogeneities of dimension δ in the object, the maximum values of ℓ, the screen to object distance, and θ are restricted, Weinberg (1963).

At the screen, light rays having passed through the same point in the test section are spread up to a distance $S = \ell\theta$ apart, due to the beam divergence. Hence, S is the minimum object dimension resolvable at the screen. The resolution may be improved by decreasing either ℓ, θ or both. But, the sensitivity of the system is proportional to ℓ, equation (3.3.3). If ℓ' is the minimum separation at which adequate sensitivity is achieved, to resolve inhomogeneities of dimension δ

$$\theta \leqslant \delta/\ell'. \qquad \ldots (3.3.4)$$

It is impossible to resolve infinitesimally small objects by reducing θ indefinitely, for two reasons: Firstly, reducing θ implies reducing the source aperture d. Because the light flux at the screen is proportional to d^2, the sensitivity of the screen or detector sets a lower limit to d, and hence θ. Secondly, diffraction at the object limits the maximum resolution achievable at the screen. An inhomogeneity of dimension δ causes a deflection of order λ/δ to light of wavelength λ. To produce a shadowgraph effect larger than the diffraction effect, thus detecting but not necessarily resolving the inhomogeneity, a refractive deflection ϵ is needed, such that $\epsilon > \lambda/\delta$, or

$$\epsilon\delta > \lambda . \qquad \ldots (3.3.5)$$

Thus, if the above criterion is satisfied, the inhomogeneity produces a detectable shadow effect.

The dimension of the inhomogeneity as recorded on the screen could, however, by misleading. To resolve an inhomogeneity of dimension δ in

the test section, at the screen, the diffractive displacement of light rays at the screen must not exceed δ, i.e. $\delta \geq \ell'\lambda/\delta$, or

$$\delta \geq \sqrt{\ell'\lambda} \, . \qquad \ldots (3.3.6)$$

Therefore, a small inhomogeneity of dimension $\ll \delta$, in which there are strong second derivatives of n, will be detected as a shadow on the screen if criterion (3.3.5) is satisfied, but the shadow will be broadened to dimension δ.

Occasionally, it is necessary to situate the screen closer to the refractive disturbance than is possible. For example, to avoid mechanical and thermal damage to a window when studying a transient hot plasma, a minimum separation must be maintained, thus restricting the minimum plasma-to-screen distance. This may be overcome by using the focused shadowgraph technique, in which a convex lens is placed between the screen and test section to focus it at a distance S in front of the screen. The principle of operation is unchanged. In equation (3.3.3), ℓ is replaced by S/m, where m is the magnification introduced by the lens.

Finally, good quality optical components, e.g. lenses and windows, are needed to prevent spurious intensity fluctuations, which could be attributed to the test object, being introduced, particularly if quantitative results are required. For example, if the difference in the path lengths of two rays passing through a common point is $> \lambda/4$, interference will occur, causing intensity fluctuations. The limitations imposed by diffraction and finite beam divergence must be considered when assessing the quality of optical components needed.

(c) Application to the study of a plasma

When the refractive disturbance being studied is a plasma, and when n is not a function of z, equation (3.3.3) reduces to

$$\frac{\Delta I}{I} \propto L\ell\left(\frac{\partial^2}{\partial x^2} n_e(x,y) + \frac{\partial^2}{\partial y^2} n_e(x,y)\right) ,$$

since for a plasma at optical wavelengths $n \simeq 1$ and $n - 1 \propto n_e$, equation (3.2.3). Hence, the local change in screen illumination is proportional to the second derivative of the electron density.

In principle, it is possible to obtain values of n_e from a plasma in which $\nabla^2 n_e \neq 0$ by suitably integrating the observed intensity changes, according to equation (3.3.3). However, extracting quantitative values of density from shadowgrams depends on having a uniform or very simple z dependence for the density, so that the necessary double integration may be performed. Also, the two constants of integration involved must be obtained by other measurements, usually one by the schlieren technique and the other by interferometry. This is a serious disadvantage.

Furthermore, quantitative results are only obtainable if the displacement of a ray from its undisturbed position on the screen is sufficiently small to avoid confusion by the overlapping of rays from various source locations. Since the sensitivity of any shadowgraph system is proportional to ℓ, the object-to-screen distance, occasionally, by suitably choosing ℓ, large variations in screen intensity can be displayed without any overlapping. However, in a plasma in which large variations in $\nabla^2 n_e$ occur, it is not usually possible to display the weaker phenomena and to avoid this overlapping.

Generally, the above two restrictions on the plasma are not satisfied, and shadowgraphy is infrequently used for quantitative purposes. Usually, it is used to locate the positions of rapidly-varying density gradients. The technique is well suited to a study of shocks, as described in Chapters V and VI, for example, and of turbulence in plasmas, Ascoli-Bartoli et al (1963).

The minimum detectable second derivative of electron density, using shadowgraphy, may be estimated. If n_e has no z dependence,

from equations (3.3.3) and (3.2.3),

$$\left(\underline{\nabla}^2 n_e(x,y)\right)_{min} = -\left(\frac{\Delta I}{I}\right)_{min} \frac{1}{4.48\times10^{-14}\lambda^2 L\ell'} \quad \ldots (3.3.7)$$

Consider the Plasma Focus dense pinch, of diameter $L = 0.2$ cm and with fine-scale structure $\delta = 0.01$ cm, illuminated with light at $\lambda = 6943$ Å. Using criterion (3.3.6), the optimum value of ℓ' is obtained. Inserting the above values into equation (3.3.7), and assuming that a 5% change in light intensity is the minimum detectable, $\left(\underline{\nabla}^2 n_e(x,y)\right)_{min} \simeq 8.0\times10^{20}$ cm^{-5}.

The main attraction of studying a plasma by the shadowgraph technique is its relative simplicity, compared with schlieren photography and interferometry. Furthermore, in plasmas in which strong variations of electron density gradients occur, the other two techniques cannot always be used because various plasma regions act as lenses and cause distortions to the images produced.

3.3.2 The Schlieren Technique

(a) General principles

The basic principle of the technique is that part of the light deflected by a refractive index gradient in the test section is intercepted before reaching the screen or detector, so that the field regions which the intercepted light has traversed appear darker on the screen.

A basic schlieren system is shown in Fig.3.3.2, Liepmann and Roshko (1957). A monochromatic light beam is produced using a suitable source S at the focus of a collimating lens L_c. This source is usually a rectangular aperture (typical dimensions 0.1 cm in the x direction by 1.0 cm in the y direction) placed at the focus of a lamp-condenser system. The beam passes through the test section TS, and is focused by the schlieren lens L_s. A screen placed at the focus of L_s would display the source image, S′. Otherwise, the light passes through to an objective

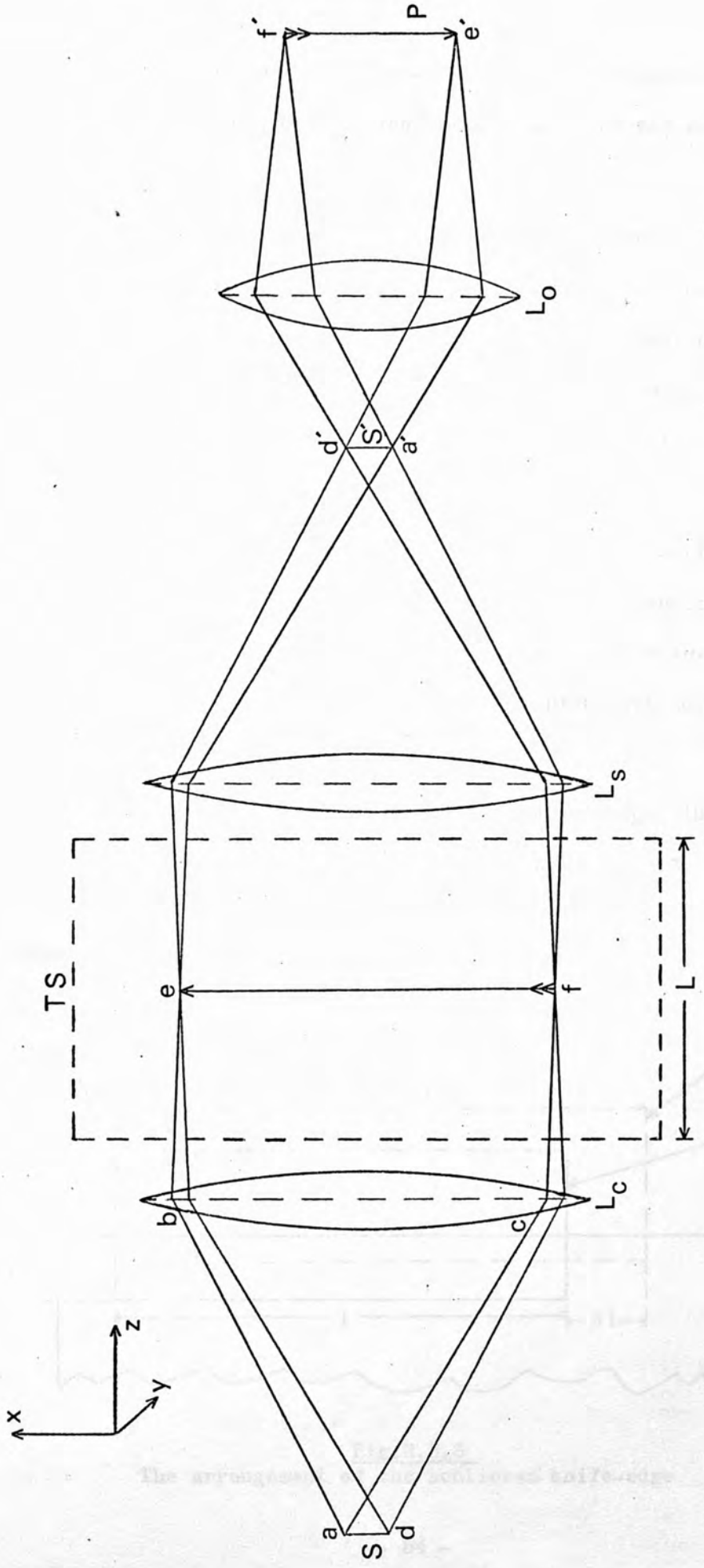

Fig.3.3.2
A basic schlieren system

L_o, which focuses the plane of interest in the test section onto a screen P. Hence, the system has two focal planes, one for the source and the other for the test section.

A point a in the source emits a pencil of light a b c which is focused at a′ in the source image plane. Similarly, other points in the source are focused to form the source image. Each light pencil, originating from a source point, is focused by L_c to form a parallel beam completely filling the test section. Hence, each point in the source image receives light from every point in the test plane ef.

The light reaching point e in the test plane travels within the pencil a e d. This light is transmitted within the pencil e d′ a′, completely filling the source image, to the conjugate point e′ on the screen. Similarly, other points in the test plane are focused onto the screen to form the test-plane image.

Suppose an opaque cut-off having a straight edge, the knife-edge (K), is introduced into the beam at the focus of L_s, Fig.3.3.3. The edge is

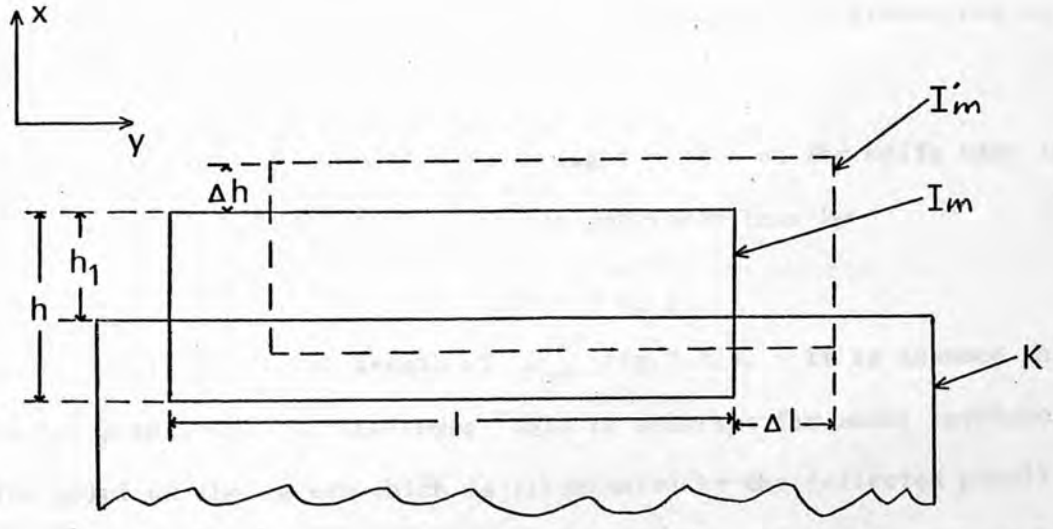

Fig.3.3.3
The arrangement of the schlieren knife-edge

set parallel to the long side of the source image Im, of length ℓ and height h, leaving a portion h_1 uncovered. All light pencils passing through the source image are equally affected, resulting in a uniform decrease of illumination over the test-plane image at the screen. The image has a general illumination, I, proportional to h_1.

If one of the light pencils is deflected at the test section, due to refractive index gradients, by α_x in the x direction and α_y in the y direction, at the focal plane of L_s this pencil forms a displaced image I'm, Fig.3.3.3. Let the displacement at the knife-edge be Δh in the x direction and $\Delta\ell$ in the y direction. All the rays originating from a common point in the test plane will, in the absence of the knife edge, arrive at the conjugate point on the screen, regardless of deviations in the test section. The image on the screen is, therefore, sharp. In the presence of the knife edge, the conjugate point on the screen is brighter than the rest of the field. This is because the light pencil is displaced upwards by Δh at the source image, and less light is intercepted by the knife edge. The displacement $\Delta\ell$ in the y direction causes no change at the screen because the amount of light intercepted is unchanged. Hence, only the refractive index gradient transverse to the knife edge is detected.

The displacement Δh of the light pencil at the knife edge is related to the deflection α_x at the schlieren lens by

$$\Delta h = f\,\alpha_x ,$$

where f is the focal length of L_s, Fig.3.3.4. It is assumed that f is the path length of the rays; this is accurate for small apertures. The point on the screen which is illuminated by the deflected pencil has an additional illumination, ΔI, proportional to Δh, above the background level I. Since $I \propto h_1$, the contrast is defined

$$\Delta I/I = \Delta h/h_1 .$$

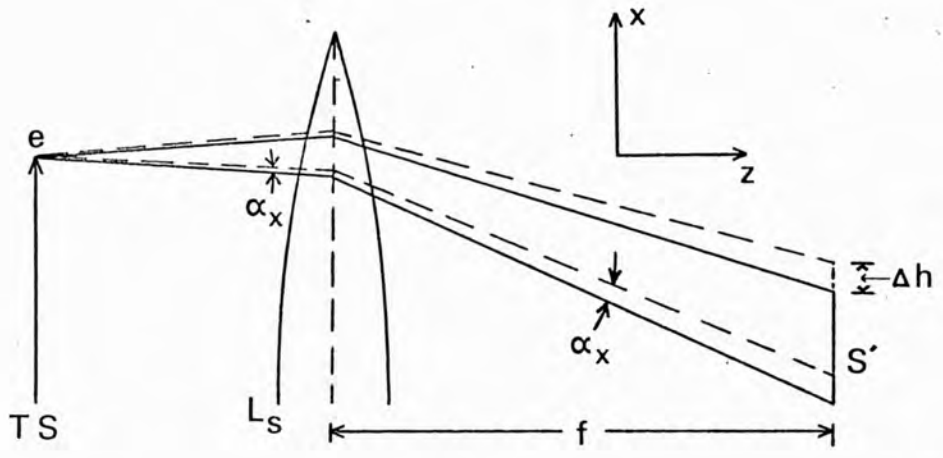

Fig.3.3.4
Displacement of part of the light at the source image due to a deviation α_x produced in the test section

Combining the above two equations

$$\Delta I/I = f\,\alpha_x/h_1 \,. \qquad \ldots (3.3.8)$$

The angular deviation α_x, caused by the refractive index gradient in the x direction, is given by equation (3.3.2). For a non-constant gradient, the derivation of this equation can be generalised by a limiting process to

$$d\alpha_x = \frac{1}{n}\,\frac{\partial n}{\partial x}\,dS \,.$$

Over an object of length L in the z direction, for small deflections from that direction

$$\alpha_x = \int_0^L \frac{1}{n(x,y,z)}\,\frac{\partial}{\partial x}\,n(x,y,z)\,dz \qquad \ldots (3.3.9)$$

Combining the above equation with equation (3.3.8)

$$\frac{\Delta I}{I} = \frac{f}{h_1}\int_0^L \frac{\partial}{\partial x}\,\ell n(x,y,z)\,dz \,. \qquad \ldots (3.3.10)$$

The schlieren technique thus measures the line integral of the refractive index gradient normal to the knife edge.

To observe refractive index gradients in the y direction, both the knife edge and source aperture are rotated through 90°.

(b) Requirements of a system for quantitative analysis

A parameter which measures the performance of the schlieren system is the sensitivity S, defined as the screen contrast for unit angular deflection, normal to the knife edge, at the test section, i.e.

$$S = \frac{\Delta I/I}{\alpha} = f/h_1 .$$

Thus, as $h_1 \to 0$ so $S \to \infty$. The case of infinite sensitivity is where the knife edge completely covers the source image, and the screen is completely black in the absence of deviations in the test section. In this case, only deflections off the knife edge are recorded, deflections onto the obstruction give no increase in screen brightness. For equal ranges for deflections onto and off the knife edge, it must bisect the source image, i.e. $h_1 = h/2$.

According to the last equation, S can be made large by using a small value of h_1. In practice, there are restrictions on the minimum size of h_1 when quantitative measurements are to be made. Firstly, h_1 must be sufficiently large to give adequate illumination at the screen so that $\Delta I/I$ can be determined accurately. Note that ΔI is independent of h_1. Secondly, h_1 must not be so small that the source image is deflected completely onto or off the knife edge, or further deflections in the same direction do not produce further changes in screen intensity, and the system is non linear. However, for qualitative work these restrictions need not be satisfied.

Diffractive effects have to be considered when examining the intensity patterns on the screen. Even in the absence of perturbations in the test section, the image of the source at the knife edge is blurred by diffraction, Ascoli-Bartoli and Martellucci (1963). If d is the aperture of the schlieren lens, the source image is altered by an amount $\Delta \simeq \lambda f/d$. A blurred halo of dimension $a = \Delta/2$ is thus added to the

contour of the light-source image. Thus, h_1 cannot be smaller than a or the system's response becomes non-linear, i.e. $h_1 \geqslant \lambda f/2d$. When $h_1 = a$, maximum sensitivity is achieved. The system must be arranged so that all deflections are off the knife edge, to preserve linearity. Inhomogeneities in the test section, of dimensions $\delta \ll d$, cause much more distortion, by diffraction, to the source image than the finite aperture effects. The restriction on the dimension of h_1 is $h_1 \geqslant \lambda f/2\delta$. For maximum sensitivity

$$h_1 = \lambda f/2\delta . \qquad \ldots (3.3.11)$$

The same criteria as for shadowgraphy apply to the quality of optical components used for quantitative work, section 3.3.1(b). In addition, the apertures and knife edges used must be precision made and accurately adjustable. Under some conditions, an irregularity of $\sim 25\mu$ in the knife edge can cause intensity changes of $\sim 16\%$ at the screen, Beams (1955).

(c) Application to the study of a plasma

The schlieren technique is of limited use for quantitative purposes in the case of a very inhomogeneous plasma. For large variations in the electron density gradients, various plasma regions act as either convex or concave lenses on the incident light. The rays passing through these regions are no longer focused at the knife edge, producing Fresnel fringe patterns on the screen. A simple requirement for quantitative measurements is that linear displacements at the focus of the schlieren lens, due to this defocusing, are negligible compared with the minimum detectable schlieren displacement, Ascoli-Bartoli et al (1964). For a light beam traversing a plasma in the z direction, and encountering an inhomogeneity of dimensions d in the x and y directions, the criteria are

$$\frac{\partial n_e}{\partial x} \geqslant 100\, d\, \frac{\partial^2 n_e}{\partial x^2} \quad \text{and} \quad \frac{\partial n_e}{\partial y} \geqslant 100\, d\, \frac{\partial^2 n_e}{\partial y^2} .$$

Provided the above criteria are satisfied, together with the restrictions discussed in the previous section, the schlieren technique can be used to obtain quantitative values of electron density in a plasma, for the case of a simple or no dependence of n_e in the direction of the light beam. For n_e having no z dependence, from equations (3.3.10) and (3.2.3), at $\lambda = 6943\,\text{Å}$,

$$\frac{\Delta I}{I} = -\ 2.16 \times 10^{-22}\ \frac{fL}{h_1} \frac{\partial}{\partial x}\, n_e(x,y)\ .$$

The electron density profile may be obtained by integration of the above equation, provided the absolute electron density is known in at least one point in the plasma. This information may be obtained using interferometry.

The minimum gradient of n_e detectable by the schlieren technique may be estimated. If n_e has no z dependence, from equations (3.3.10) and (3.2.3),

$$\left(\frac{\partial}{\partial x}\, n_e(x,y)\right)_{\min} = -\left(\frac{\Delta I}{I}\right)_{\min} \cdot \frac{h_1}{4.48 \times 10^{-14} L f \lambda^2}\ . \qquad \ldots\ (3.3.12)$$

Consider the Plasma Focus dense pinch, of diameter $L = 0.2\,\text{cm}$ and with fine-scale structure $\delta = 0.01\,\text{cm}$, illuminated with light at $\lambda = 6943\,\text{Å}$. Using criterion (3.3.11), the optimum value of h_1 is obtained for maximum sensitivity. Inserting the above values into equation (3.3.12), and assuming a 5% light intensity change is the minimum detectable,

$$\left(\frac{\partial}{\partial x}\, n_e(x,y)\right)_{\min} \simeq 4.0 \times 10^{18}\ \text{cm}^{-4}\ .$$

The schlieren technique is used to indicate the regions of steep refractive index gradient in a plasma. Alcock et al (1968) exploited the technique fully to obtain multiple exposures of an expanding laser-produced plasma, using a multi-pulse laser as light source. Schlieren photography is useful for quantitative purposes when the density gradients are sufficiently steep to distort the fringe patterns produced using the interferometric technique, which would lead to inaccuracies during numerical evaluation.

3.3.3 Interferometry

(a) General principles

The basic principle of interferometry is that two coherent monochromatic light beams are made to interfere to produce a series of equidistant parallel fringes on a screen. Introducing a refractive disturbance into the path of one of the beams alters the fringe pattern so that each displaced fringe is a contour of constant integrated refractive-index change.

Consider two such light beams interfering at a screen. A dark fringe occurs at each point where the difference in the optical path lengths of the two beams, i.e. the product of refractive index n and geometric path length ℓ, is an odd number of half wavelengths of the light. Assuming for simplicity that over each path travelled n is a constant, the condition for dark fringes to occur is

$$|n_1\ell_1 - n_2\ell_2| = (2N+1)\,\lambda/2 \qquad \text{for } N = 0,1,2, \ldots$$

Similarly, a bright fringe occurs where this difference is an even multiple of $\lambda/2$.

In general, the pattern on the screen consists of a number of parallel equidistant dark fringes, separated by bright bands. Each fringe is the locus of a constant optical path-difference which is an odd multiple of $\lambda/2$, i.e. $(2N+1)\,\lambda/2$ = constant, for $N = 0,1,2,\ldots$. The integer N, which gives the number of half-wavelengths' difference between the two paths, is the fringe order. This differs by unity between two adjacent fringes.

Suppose the refractive index is increased by an amount Δn over a length L of the geometric path of one of the beams. The optical path length of this beam is increased by $\Delta\ell = \Delta n \,.\, L$. This is equivalent to an increase in optical path of s wavelengths. Hence,

$$s = \Delta n \cdot L/\lambda \ . \qquad \ldots (3.3.13)$$

If s is an integer J, at each point on the screen where a fringe of order M was formerly located, the fringe order changes to $M \pm J$, depending on whether the optical path difference between the two beams is increased (+ sign) or decreased (- sign). Hence, due to the increase in refractive index, a shift of $\pm J$ fringes is observed on the screen.

Generally, s is not an integer, and by observing the fringe shift at the screen the refractive index change may be calculated. From equation (3.3.13)

$$\Delta n = s\lambda/L.$$

If Δn is not constant over L, but is a function of position, equation (3.3.13) may be written

$$s(x,y) = \frac{1}{\lambda} \int_0^L \Delta n(x,y,z)\, dz \ , \qquad \ldots (3.3.14)$$

where the test beam is parallel to the z axis. The displaced fringes on the screen are contours of constant integrated refractive-index change, i.e. $\int_0^L \Delta n \cdot dz = \text{constant}$.

This is the principle of measuring refractive index changes by interferometry.

(b) The Mach-Zehnder interferometer

(i) General description

The Mach-Zehnder interferometer (MZI) is the most widely used interferometer in plasma applications, as it fulfils most of the requirements of practical experiments:

(a) The fringes can be localised at any desired position; usually in the test object so that a camera focused there records a combined interference-photograph. Deflected rays originating from points in the test plane are thus imaged at the conjugate points in the camera's focal plane, i.e. a 1:1 mapping is preserved.

This minimises, but does not entirely eliminate, errors due to deflections.

(b) The mirrors of the MZI can be placed far apart, with wide separation of the test and reference beams. Optical components can therefore be situated at safe distances from hot test objects, and large pieces of laboratory apparatus can be spanned or by-passed with relative ease.

(c) The test beam makes one pass only through the test object, so that quantitative analysis is not complicated by two or more passes.

(d) The interferometer can be made with a reasonably large field of view.

The main disadvantages of the MZI are that, being a high precision instrument, it is very expensive and it is not easy to align, because of its high sensitivity to changes in beam direction.

One possible arrangement of the MZI is shown in Fig.3.3.5. An effective point source LS is situated at the focus of a collimating lens L_c. BS1 and BS2 are 50% reflecting beam-splitters of equal thickness, M1 and M2 are fully-reflecting mirrors and L_o is an objective which focuses a point P in the test section TS onto a screen S at the conjugate point P′. It may be necessary to enclose the test section using two glass windows. These increase the test beam's optical path, and to compensate for this an identical pair of windows (termed compensating plates) are located at CP.

The MZI is a two-beam device working by the principle of division of amplitude. The parallel monochromatic light beam incident on BS1 is split into two beams of equal intensity. These beams travel separate paths, the test beam passing through TS on path BS1-M2-BS2 and the

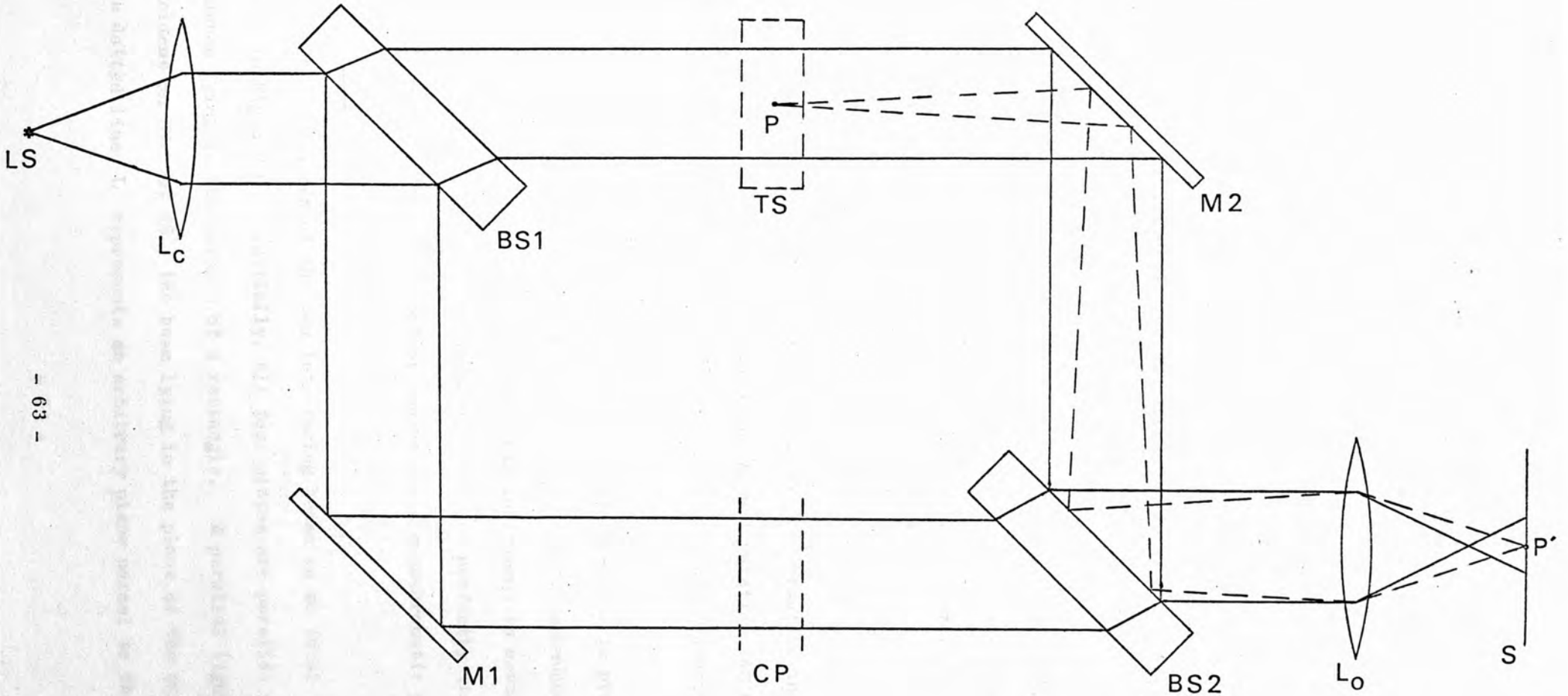

Fig.3.3.5
Optical arrangement of the Mach-Zehnder interferometer

reference beam travelling path BS1-M1-BS2, and recombine at the reflecting surface of BS2.

In the basic adjustment, the four plates occupy the corners of a rectangle and are parallel. The light beam falling on BS1 is at 45° incidence. The two wavefronts emerging from BS2 are parallel, resulting in an infinite fringe width. A disturbance, small compared with the field of view, introduced into the test section, produces fringes which are closed contours of constant optical path.

It is convenient to introduce a number of parallel background fringes into the field of view; against these, fractional fringe shifts may be estimated. Such fringes may be produced by a small rotation of any one of the four plates.

(ii) Theory of fringe formation

A detailed account of the theory of fringe formation in the M Z I is given by Kinder (1946). In addition, a configuration for maximum ease of operation and a method of alignment for fringe production are given.

In this section, a simplified theory of the M Z I is presented, which illustrates the basic principles of the device, Ladenburg and Bershader (1955). The concept of an ideal instrument is used. Such an instrument has infinitely thin beam-splitters and perfectly flat reflecting surfaces, and is used with perfect lenses and a monochromatic point light source.

A ray diagram of the two interfering beams in an ideal M Z I is shown in Fig.3.3.6. Initially, all four plates are parallel with their centres lying on the corners of a rectangle. A parallel light beam is incident on BS1 at 45°, the beam lying in the plane of the mirror centres. The dotted line L represents an arbitrary plane normal to the beam, and

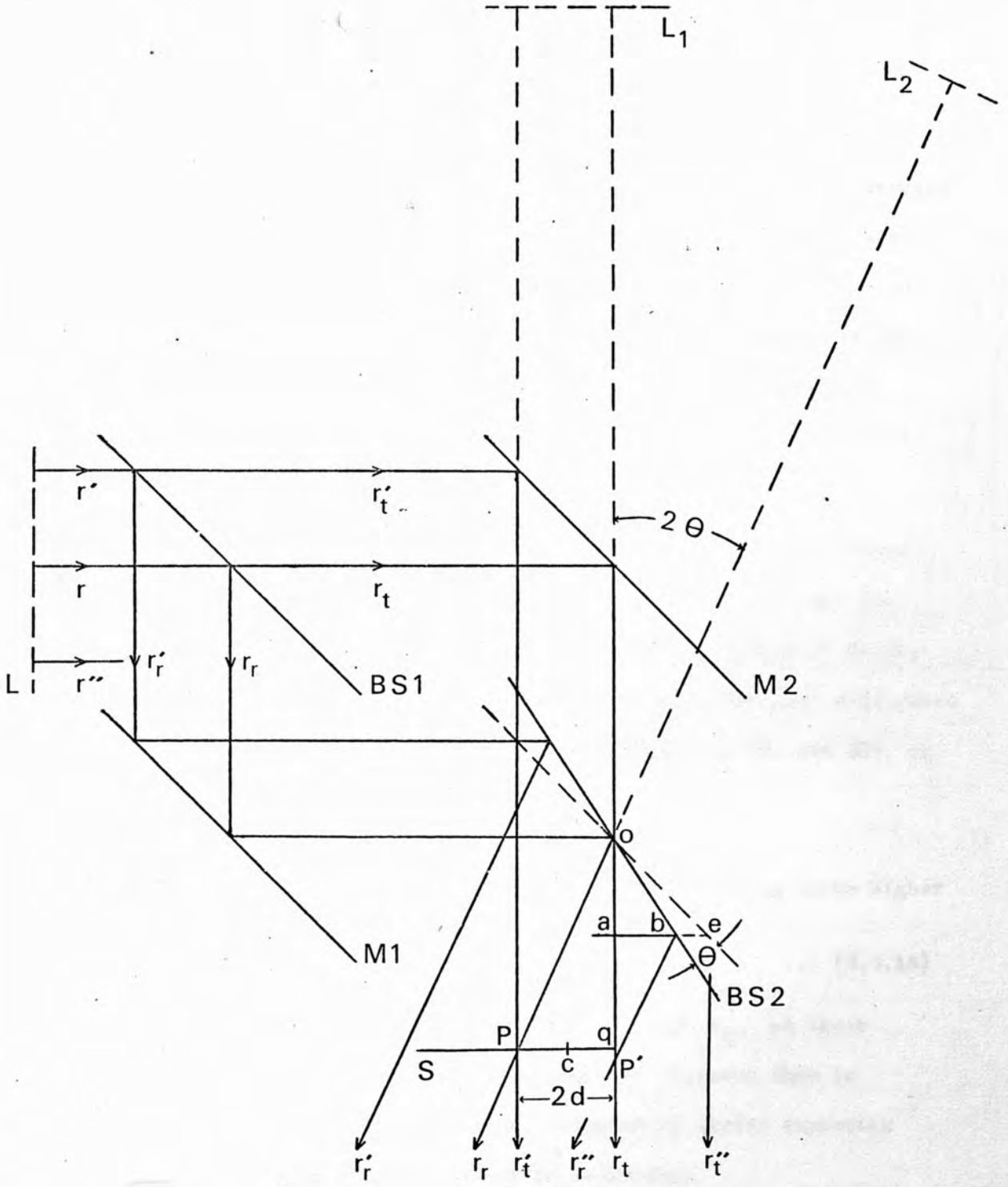

Fig.3.3.6

Ray diagram of two interfering beams in an ideal Mach-Zehnder interferometer

is used as a reference phase plane. Rays from any two points in L can be made to interfere, since light at all points in it is in phase.

Plate BS2 is rotated through a small angle θ, about an axis through the plate centre normal to the plane of centres, producing fringes on a screen S which is located beyond BS2 and is normal to undeviated rays. Three rays are shown emerging from L, and the paths of r and r' are traced fully through the system. The ray r is central in the plane of centres, with r' and r'' being equidistant on either side. Subscripts t and r refer to those fractions transmitted and reflected by BS1, respectively.

The phase difference between rays r_r and r'_t, which interfere at point P on the screen, is obtained by comparing optical paths PL_1 and PL_2. These distances represent the alternate paths from P to L. By construction, oL_1 and oL_2 are equal. Therefore, the path difference ℓ at P is oP-oq. Denoting Pq by 2d, $\ell = 2d\ (\text{cosec } 2\theta - \cot 2\theta)$, or

$$\ell = 2d \left(\frac{1 - \cos 2\theta}{\sin 2\theta} \right).$$

Using the series expansions for sin and cos, and neglecting terms higher than second order,

$$\ell = 2\theta d . \qquad \ldots (3.3.15)$$

Considering interference between rays r''_r and r_t, at their point of intersection P', the path difference ℓ' between them is $\ell' = bP' - aP' - be$. After simplification, followed by series expansion in sin and cos to second order, it can be shown that

$$\ell' = - 2\theta d .$$

Taking a point moving in a straight line from P' to P, the path difference at that point varies linearly from $-2\theta d$ to $2\theta d$, respectively, and is zero on the bisector of $P\hat{o}P'$. At this point, the zeroth-order bright fringe is located. Since θ is very small, to a good

approximation the point c, at the midpoint of Pq, is also on the bisector of $P\hat{o}P'$. If $\ell = N\lambda$, there are N fringes between P and c; likewise for cq, since $|\ell'| = \ell$. Thus, $N = \ell/\lambda$. From equation (3.3.15)

$$N = 2\theta\, d/\lambda .$$

There are N fringes spread out over a distance d, giving a fringe width

$$w = d/N = \lambda/2\theta .$$

The above two equations are for the case of rotation of BS2 alone. More generally, for an angle φ between the interfering beams ($\varphi/2$ being the sum of the angles of rotation of the four plates about axes normal to the plane of centres) we may write

$$N = \varphi\, d/\lambda \qquad \ldots (3.3.16)$$

and

$$w = \lambda/\varphi . \qquad \ldots (3.3.17)$$

The number of fringes within the field of view can thus be controlled by varying φ.

Using an ideal M Z I, fringes occur everywhere in the field of overlap of the two beams. Since the above treatment has been confined to two dimensions, the interference phenomena will be identical in planes parallel to the plane of centres. The fringes appear as bands normal to this plane, i.e. parallel to the axes of rotation.

In addition to rotation about the axis normal to the plane of centres ($\perp$ axis), each plate can be rotated about an axis in the plane of centres, which is also in the plane of the plate ($\parallel$ axis). For small rotations about $\parallel$ axes, fringes are produced parallel to the plane of centres. Because in this case the beams are incident at 45° to the axes, a rotation of a plate through β turns the reflected rays through $\sqrt{2}\,\beta$.

For a M Z I in its basic adjustment, a small rotation of one of the plates through α about the $\perp$ axis and β about the $\parallel$ axis results in an overall plate rotation of $\gamma = \sqrt{\alpha^2 + \beta^2}$. This causes a beam

deflection of $\theta = \sqrt{4\alpha^2 + 2\beta^2}$. The resultant axis of rotation is in the plane of the mirror, at an angle δ to the normal to the plane of centres, given by $\cos\delta = \alpha/\gamma = \alpha/\sqrt{\alpha^2 + \beta^2}$. The fringes produced are parallel to the resultant axis, enabling the desired fringe orientation to be achieved. Normally, the fringes are set either parallel or perpendicular to the plane of centres.

As previously mentioned, an important feature of the MZI is its ability to produce fringes at any desired location. Usually, the fringes are focused in the interferometer test section. Thus, a camera focused on a refractive disturbance is also focused on the fringes it produces. At this point, it is convenient to introduce the linear representation of the MZI. Fig.3.3.7(a) shows a MZI in which BS1 and BS2 have small rotations θ_1 and θ_2, respectively, about $\perp$ axes. The two interfering beams combine at an angle $\varphi = 2(\theta_1 + \theta_2)$, focusing the fringes at plane P. Planes L, L_1 and L_2 have their previous significance. Fig.3.3.7(b) is a linear representation of the same situation. To an observer beyond BS2, unaware of the geometric layout, this is how the instrument appears.

Fringes may be focused at the test section by suitable $\perp$ rotations of BS1 and BS2, Fig.3.3.7(c). Such fringes produced within the instrument are virtual, since the interfering beams do not combine before BS2. However, to an observer the beams appear to intersect at P and, since the fringes are produced at the beams' plane of intersection, a camera focused on this plane produces a real image of the fringes.

Having established interference by rotating two plates, as in Fig.3.3.7, a further rotation of any plate changes the fringes' location and structure (spacing and orientation). In general, having focused the fringes at a given location, any further adjustment to alter the fringe structure results in a defocusing. It is then necessary to refocus and afterwards to readjust the structure, and so on by successive adjustments,

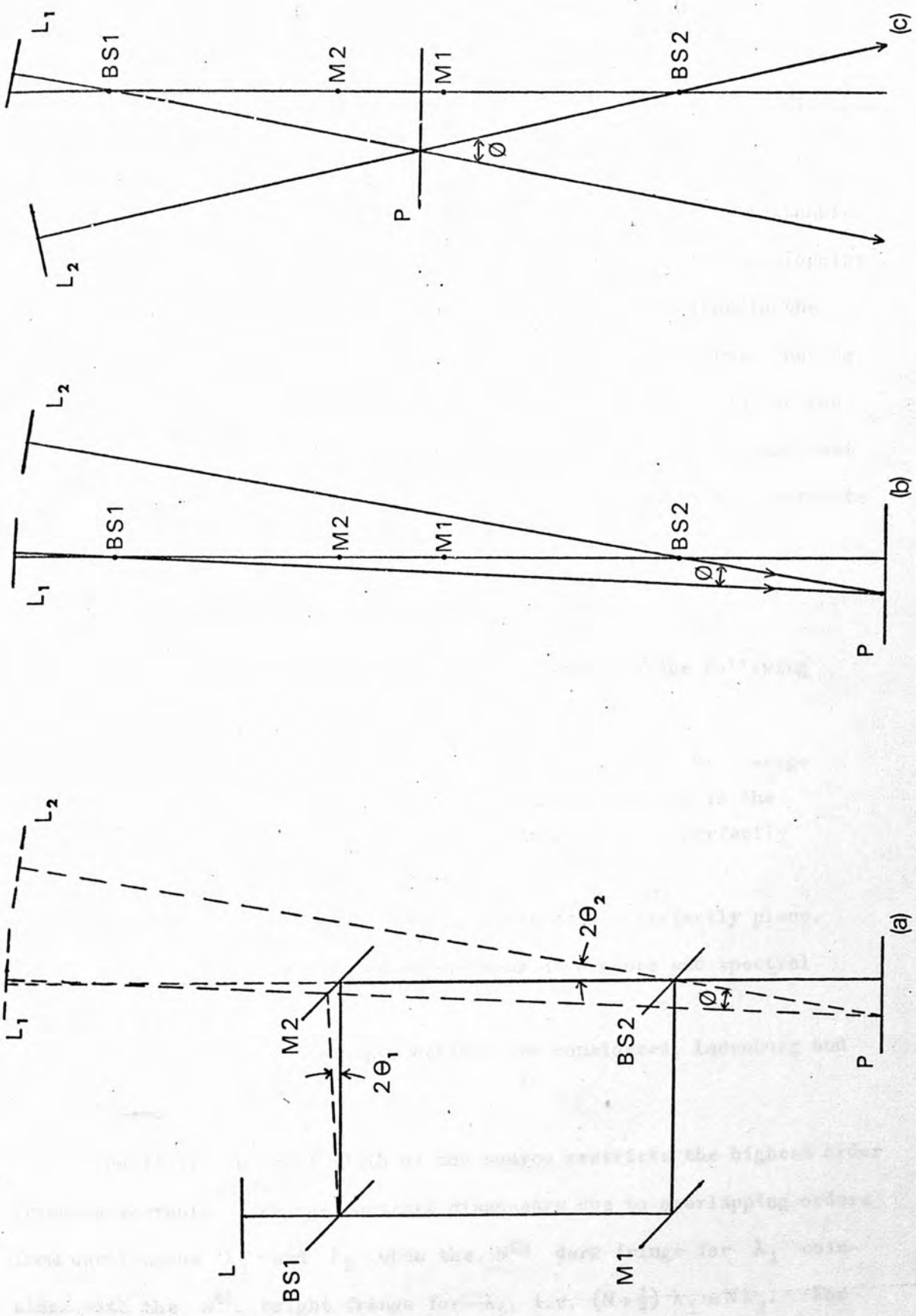

Fig.3.3.7
Focusing of fringes in a Mach-Zehnder interferometer

until both the focusing and structure are as required. However, when the fringes are located at the axis of rotation of one of the plates, that plate may be adjusted to change the fringe structure without loss of focus.

Kinder (1946) proposes a configuration which gives such single-plate control. Referring to Fig.3.3.5, the dimensions of the rectangle are changed so that BS2-M1 = 2.BS2-M2, with the test plane at the midpoint of BS1-M2. The optical paths from M1 and from the test plane to the screen are equal, hence both planes are simultaneously in focus. Having focused the fringes at M1 using BS1 and BS2, their structure may be controlled by M1 without defocusing. The use of a MZI in this arrangement is far simpler than in any other arrangement where successive adjustments are required.

(iii) Limitations imposed by the instrument and associated auxiliaries

No MZI is ideal, and in practice the system has the following defects:

(a) Both beam splitters are of finite thickness, the average for each being different, with inhomogeneities in the glass. The faces of a beam splitter are not perfectly parallel.

(b) None of the four reflecting surfaces are perfectly plane.

(c) The light source has finite beam divergence and spectral width.

The effects of these imperfections are considered, Ladenburg and Bershader (1955).

The finite spectral width of the source restricts the highest order fringe detectable. Fringe contrast disappears due to overlapping orders from wavelengths λ_1 and λ_2 when the N^{th} dark fringe for λ_1 coincides with the N^{th} bright fringe for λ_2, i.e. $(N+\frac{1}{2})\,\lambda_1 = N\lambda_2$. For $\lambda_2 - \lambda_1 = \Delta\lambda$ and $\lambda_1 \simeq \lambda_2 = \lambda$,

$$N = \lambda/2\Delta\lambda \ . \qquad \ldots (3.3.18)$$

Thus, for a source with $\lambda = 5,000\,\text{Å}$ and a wavelength spread $\Delta\lambda = 1\,\text{Å}$, the last fringe visible on either side of the central fringe is $N = 2,500$. Equation (3.3.18) may be used to determine the maximum allowable inequality of geometric paths in the two arms of a MZI. When the path difference is sufficiently large that the minimum order fringe in the image plane is $\geqslant N$, overlapping of fringes of different wavelength destroys the contrast. The maximum permissible path difference $\Delta\ell$, the coherence length, is thus $\Delta\ell = N\lambda$. From equation (3.3.18)

$$\Delta\ell = \lambda^2/2\Delta\lambda \ . \qquad \ldots (3.3.19)$$

Using a light source with $\lambda = 5,000\,\text{Å}$ and $\Delta\lambda = 1\,\text{Å}$, the coherence length $\Delta\ell$ is ~ 0.13 cm. Thus, to observe fringes using this light source, the difference between the geometric paths in the MZI must be $\leqslant 0.13$ cm.

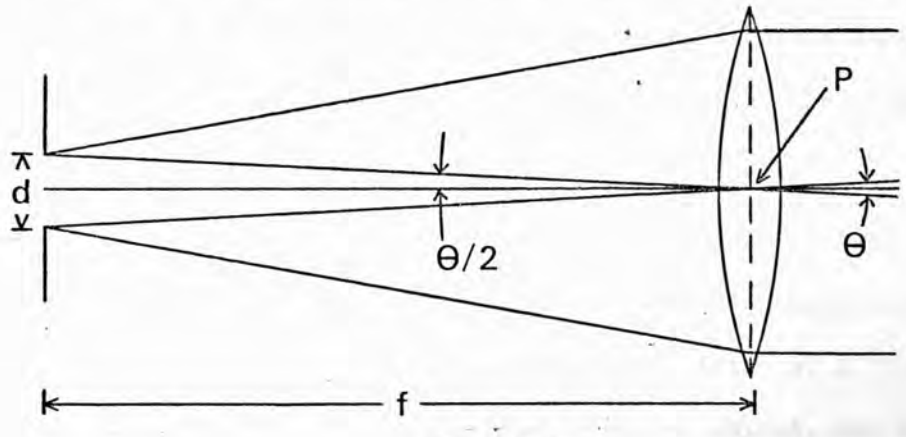

Fig.3.3.8
Effect of a finite-aperture source

The restriction on the maximum permissible beam divergence of the source is that the diverging rays passing through any object point are $< \lambda/4$ out of phase. Fig.3.3.8 represents a source consisting of an illuminated pinhole of aperture d at the focus of a lens of focal length +f. The source divergence is $\theta = d/f$. At point P, the path difference between rays arriving from the centre and edge of the pinhole must be $< \lambda/4$, i.e. $(f/\cos(\theta/2) - f) < \lambda/4$. Thus,

$$d < 2f \cos^{-1}[f/(f+\lambda/4)]. \qquad \ldots (3.3.20)$$

For a source of wavelength 5,000 Å used with a 50 cm collimating lens, the pinhole aperture must be < 0.07 cm to satisfy the above criterion. In addition, auxiliary optical components such as lenses and windows must be of sufficiently high quality not to introduce any path differences $> \lambda/4$.

The MZI is very sensitive to misalignment. Therefore, the plates must be rigidly mounted with provisions for rotation by small angles about the $\perp$ and $\parallel$ axes. Also, plate BS2 is usually mounted on a carriage with movements parallel and normal to either incident beam, allowing equalisation of the two paths. Consider a device with plates of dimensions 10×10 cm used with a light source of wavelength 5,000 Å. For a fringe of 'infinite width', i.e. the fringe-width just filling the plate aperture, from equation (3.3.17) the misalignment φ of the two beams must be $< 5 \times 10^{-6}$ radians. Thus, the total mirror misalignment $\varphi/2 < 2.5 \times 10^{-6}$ radians. To obtain a background of 50 fringes over the plate aperture, $\varphi/2$ must be $< 1.3 \times 10^{-4}$ radians.

Inhomogeneities in the beam splitters, non-planar reflecting surfaces, imperfect lenses, etc., cause spurious shifts in background fringes used for reference purposes. If an accuracy of 1/10th of a fringe is required when measuring fringe shifts due to a test object, the total spurious shift due to optical imperfections in the system must be $< 1/10$th. Thus, in an otherwise perfect system, for a beam of wavelength 5,000 Å incident at 90° on a glass window of refractive index 1.5, a gradual change in its thickness by $\sim 3.3 \times 10^{-6}$ cm over a certain length produces a fringe shift of 0.1 over that length.

Finally, the finite thickness of the beam splitters causes spurious fringe-shifts for a divergent light beam, since different portions of the beam have different optical paths through the glass, Weinberg (1963). In

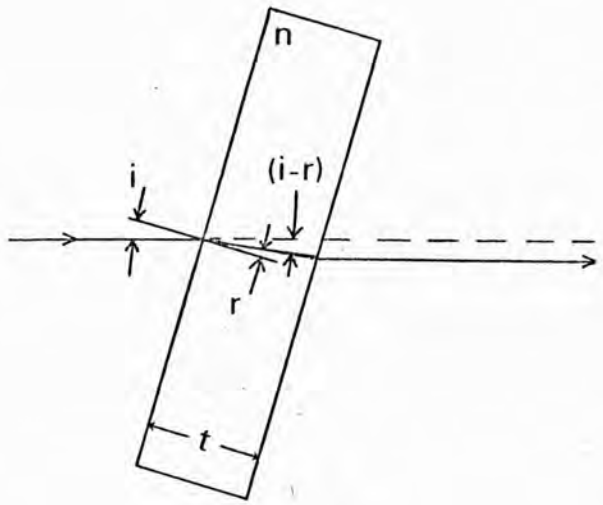

Fig.3.3.9
Deflection of a light ray by a glass slab of finite thickness

Fig.3.3.9, a ray travelling through vacuum is incident at an angle i on a glass slab of thickness t and refractive index n. The increase in optical path due to the slab is $\ell = t[n - \cos(i-r)]/\cos r$. Expanding, and using the relations $\sin i = n \sin r$ and $\cos r = \sqrt{1 - \sin^2 r}$, one obtains

$$\ell = t(\sqrt{n^2 - \sin^2 i} - \cos i) .$$

Differentiating the above,

$$d\ell = t \sin i \left(1 - \frac{\cos i}{\sqrt{n^2 - \sin^2 i}}\right) di .$$

For a beam of wavelength 5,000 Å incident at 45° on a slab of thickness 2 cm and refractive index 1.6, $d\ell = 0.72\,di$. Hence a change in the angle of incidence of $\sim 7.5 \times 10^{-5}$ radians causes a displacement of one fringe.

Suppose the test object deflects the test beam by ~ 1 mrad, due to refractive index gradients. If the beam subsequently passes through a beam splitter, under the same conditions as in the above example, a shift of ~ 14 fringes results. This shift could be incorrectly attributed to the test object's refractivity. Where deflections of the test beam are likely to occur, the MZI should be set out as in Fig.3.3.5. In this way, the test beam does not pass through BS2 after passing through the test section, thus avoiding the above difficulty.

(c) Application to the study of a plasma

When the refractive disturbance studied is a plasma, the fringe shifts produced in an interferometry experiment are proportional to the electron density. From equation (3.2.3), the refractive index change,

relative to vacuum, produced by a plasma is

$$\Delta n(x,y,z) = -\,4.48 \times 10^{-14} \lambda^2 n_e(x,y,z).$$

Using this in equation (3.3.14), the fringe shift caused by a plasma of length L is

$$s(x,y) = -\,4.48 \times 10^{-14} \lambda \int_0^L n_e(x,y,z)\, dz.$$

Interferometry thus measures the line integral of the electron density in a plasma. The displaced fringes are contours of constant $\int_0^L n_e \, d\ell$. At $\lambda = 6943\,\text{Å}$, the above equation becomes

$$s(x,y) = -\,\frac{1}{3.2\times10^{-17}} \int_0^L n_e(x,y,z)\, dz \,. \qquad \ldots (3.3.21)$$

For a plasma in which n_e is independent of z, equation (3.3.21) may be written

$$n_e(x,y) = -\,3.2 \times 10^{17}\, s(x,y)/L \,. \qquad \ldots (3.3.22)$$

Thus, the plasma electron density may be calculated from the observed fringe shifts. The measurement by interferometry of the electron density in a θ-pinch plasma is described by Jahoda et al (1964).

If the minimum detectable fringe-shift is - 0.1, in a 1 cm long plasma the minimum detectable electron density is, from the above equation, $n_e(x,y)_{min} \simeq 3.2\times10^{16}\ \text{cm}^{-3}$. The maximum measurable electron density, at the ruby laser wavelength, may also be estimated from equation (3.3.22). Assuming that a shift of - 30 fringes is the maximum number resolvable, larger shifts being unresolvable due to fringe crowding, for a plasma of centimetre length $n_e(x,y)_{max} \simeq 10^{19}\ \text{cm}^{-3}$.

If there are steep refractive index gradients in a plasma, light traversing it is deflected. The varying curvature of the deflected rays results in spurious variations of optical path, and, in an interferometry study, a correction to the observed fringe shifts is necessary to compensate for this. In the case of severe bending, the fringe pattern can be washed out by overlapping fringes.

The first order correction is calculated for the case of a linear variation of n_e transverse to the light beam, Jahoda and Sawyer (1971). In Fig.3.3.10, a ray incident at A is deflected over a length L to emerge at B′ instead of A′. A camera focused on the plane P determines the fringe shift along path AB′, but appears to determine the fringe shift along BB′. The error in the fringe shift assigned to path BB′ is due, therefore, to the optical path difference between AB′ and BB′.

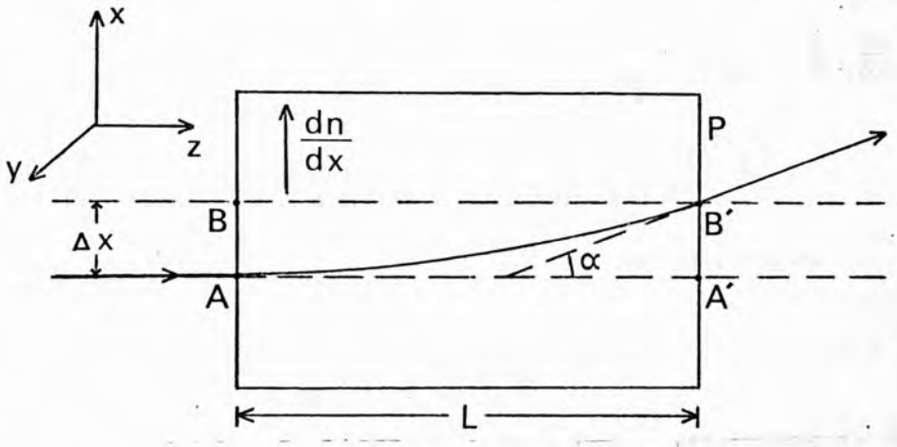

Fig.3.3.10
Deflection of a light ray by a transverse refractive-index gradient

Using equation (3.3.14), the path difference is

$$\delta = \frac{1}{\lambda}\left[\int_A^{B'} n_{AB'}\, ds - \int_B^{B'} n_{BB'}\, dz\right], \qquad \ldots (3.3.23)$$

where $ds = (dx^2 + dz^2)^{\frac{1}{2}} = dz(1 + (dx/dz)^2)^{\frac{1}{2}}$. Now $dx/dz = \alpha$, and from equation (3.3.2)

$$\frac{dx}{dz} = \frac{\partial n}{\partial x} \cdot z , \qquad \text{since } n \simeq 1 .$$

Integrating the above equation yields

$$x = \frac{1}{2}\,\frac{\partial n}{\partial x}\, z^2 .$$

Over the plasma length L, the displacement Δx is

$$\Delta x = \frac{1}{2}\,\frac{\partial n}{\partial x}\, L^2 .$$

Now,

$$ds = dz\ (1 + (dx/dz)^2)^{\frac{1}{2}} \simeq dz(1 + \tfrac{1}{2}(\partial n/\partial x)^2\ z^2)\ .$$

The refractive index along BB' is

$$n_{BB'} = n_{AA'} + \Delta x\ \frac{\partial n}{\partial x} = n_{AA'} + \tfrac{1}{2}\left(\frac{\partial n}{\partial x}\right)^2 L^2\ .$$

Likewise, the refractive index at any point along AB' is

$$n_{AB'} = n_{AA'} + x\ \frac{\partial n}{\partial x} = n_{AA'} + \tfrac{1}{2}\left(\frac{\partial n}{\partial x}\right)^2 z^2\ .$$

Substituting the above three equations into equation (3.3.23)

$$\lambda\delta = \int_0^L \left[\, n_{AA'} + \frac{1}{2}\left(\frac{\partial n}{\partial x}\right)^2 z^2\right] . \left[1 + \frac{1}{2}\left(\frac{\partial n}{\partial x}\right)^2 z^2\right] dz - \int_0^L \left[n_{AA'} + \frac{1}{2}\left(\frac{\partial n}{\partial x}\right)^2 L^2\right] dz$$

$$\simeq \frac{1}{6}\left(\frac{\partial n}{\partial x}\right)^2 L^3 + \frac{1}{6}\, n_{AA'} \left(\frac{\partial n}{\partial x}\right)^2 L^3 - \frac{1}{2}\left(\frac{\partial n}{\partial x}\right)^2 L^3\ ,$$

neglecting 4th order terms. Since $n_{AA'} \simeq 1$, we may write

$$\delta \simeq -\frac{1}{6\lambda}\left(\frac{\partial n}{\partial x}\right)^2 L^3\ . \qquad \ldots (3.3.24)$$

The observed fringe shift, N, relative to vacuum, attributed to the refractive index along BB' is

$$N = (n_{BB'} - 1)\ L/\lambda\ .$$

Combining the above two equations and substituting from equation (3.2.3) for $n - 1$

$$\frac{\delta}{N} = 7.5 \times 10^{-15}\ \lambda^2\ \frac{L^2}{n_e}\left(\frac{\partial n_e}{\partial x}\right)^2\ . \qquad \ldots (3.3.25)$$

If δ/N is greater than the minimum detectable fringe shift, then the observed fringe shifts must be corrected to allow for the effects of ray bending.

3.3.4 The Properties of a Q-Switched Ruby Laser as a Light Source

The requirements of a suitable light source for use with the optical techniques discussed, to study a transient plasma, are :

(a) Sufficient intensity to overcome the plasma self-luminosity.

(b) Narrow spectral width.

(c) Low beam divergence.

(d) Short pulse duration to arrest the plasma motion.

When the only light sources available were of the high-current arc or electric spark type, the optical techniques discussed, although well known in the field of aerodynamics, were seldom used to study high-density plasmas. This was because, in general, such sources could not simultaneously satisfy the above requirements. However, with the advent of the laser, because of the unique properties of laser light, these optical techniques have become standard in the study of plasmas for which $n_e \geqslant 10^{14}$ cm^{-3}.

Consider a typical high-power ruby laser, consisting of a Q-switched oscillator and an amplifier. The output has the following characteristics: energy 10 J in a pulse of half-width 20 nsec, beam diameter 2 cm with full beam divergence 3 mrad and spectral width 0.1 Å at 6943 Å. The average power for the duration of the pulse is, thus, 500 MW.

Usually, a beam of larger diameter than 2 cm is required to probe a plasma. Using an inverted telescope, as in Fig.3.3.11, the beam is

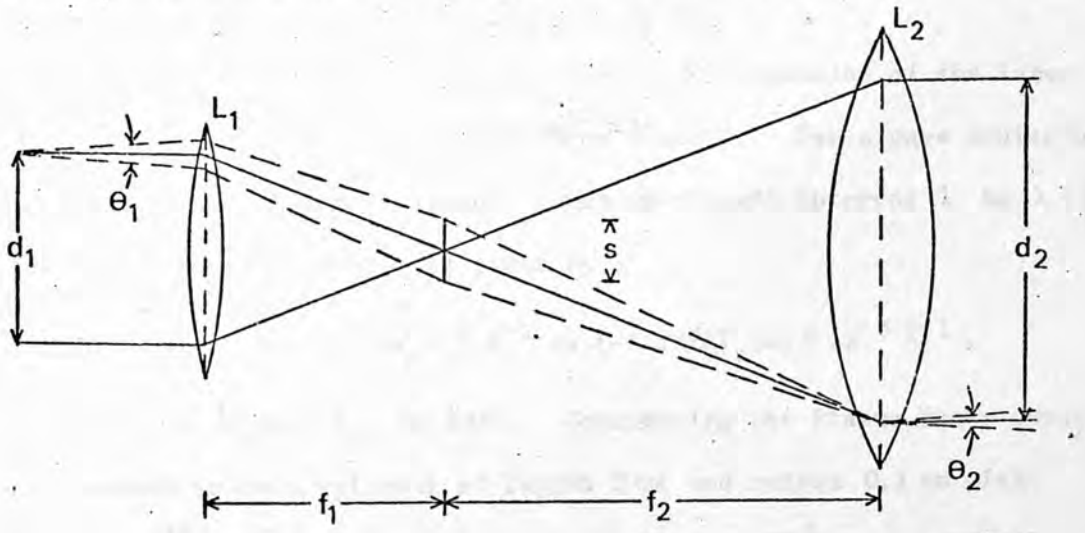

Fig.3.3.11
Expansion of a light beam of finite divergence using an inverted telescope

expanded in the ratio f_2/f_1. The beam divergence is reduced in the same ratio. For a beam expansion of 5X, the beam divergence in the expanded beam is 0.6 mrad for the laser considered. To satisfy criterion (3.3.20), that for a source for interferometry the path difference at a point between extreme rays is $< \lambda/4$, the spot size s must be < 0.08 cm for $f_2 = 50$ cm. Since $f_1 = 10$ cm for 5X expansion, $s = f_1\theta_1 = 0.03$ cm. This is well under the maximum permissible spot size.

The coherence length of the laser beam, from equation (3.3.19), is $\Delta\ell = \lambda^2/2\Delta\lambda \simeq 2.4$ cm. Thus, when using a Mach-Zehnder interferometer, it is only necessary to equalise the two arms of the instrument to within 2.4 cm to enable fringes to be produced. The spectral width of the laser output is sufficiently narrow that fringes of high order number can be produced with a MZI. From equation (3.3.18), $N = \lambda/2\Delta\lambda \simeq 34{,}700$. Thus, with a background spacing of ~ 10 fringes/cm, all fringes in the field of view are of high contrast.

The laser brightness B may be defined for an expanded beam, with reference to Fig.3.3.11, by

$$B = P \cdot \left(\frac{2}{d_2}\right)^2 \frac{1}{\pi} \cdot \frac{4\pi f_2^2}{\pi\left(\frac{s}{2}\right)^2 4\pi} = \frac{P \cdot 16\ f_2^2}{\pi^2 s^2 d_2^2}\ \text{W cm}^{-2}\ \text{str}^{-1}\ ,$$

where P is the power of the output. For a 5X expansion of the laser output, with $f_2 = 50$ cm, $B \approx 2.3\times10^{13}$ W cm^{-2} str^{-1}. For a pure deuterium plasma, the bremsstrahlung emission in the wavelength interval λ to $\lambda + d\lambda$, Glasstone and Lovberg (1960), is given by

$$P_{br} = 6.0\times10^{-30}\, n_e^2\, T_e^{-\frac{1}{2}}\, \lambda^{-2}\, \exp(-12.4/\lambda T_e)\, d\lambda\ \text{W cm}^{-3}\ \text{Å}^{-1}\ ,$$

where λ is in Å and T_e in keV. Considering the Plasma Focus dense pinch, assumed to be a cylinder of length 2 cm and radius 0.1 cm with density 5×10^{19} cm^{-3} and temperature 2.5 keV, in a 20 Å pass band centred on 6943 Å (typical of the interference filters used to discriminate against

plasma light) $P_{br} \approx 250\,W$. This corresponds to a plasma brightness of $\sim 50\,W\,cm^{-2}\,str^{-1}$, which is negligible compared with that of the laser.

Finally, the 20 nsec pulse duration is sufficiently short to 'freeze' the motion of all but the most transient plasmas. In the case of the Plasma Focus dense pinch, various techniques can be used to obtain a pulse of duration $\leqslant 1$ nsec from a ruby laser. These are discussed in Chapter IV.

The Q-switched ruby laser makes an excellent light source for use with the shadowgraph, schlieren and interferometric techniques in studying a high-density transient plasma.

CHAPTER IV

APPARATUS, DEVELOPMENT WORK AND EXPERIMENTAL TECHNIQUES

In the first part of this chapter, the mechanical construction, vacuum system, capacitor bank, discharge circuit, control and monitoring systems, and operation of the Plasma Focus used are described. Next, the development of a ruby laser system, for producing one nanosecond duration exposures of the plasma, is described. Lastly, experimental details of the optical techniques are given.

4.1 THE PLASMA FOCUS

The Plasma Focus studied consisted of a two-electrode coaxial gun, of length ~25 cm and electrode radii 2.5 and 5 cm, connected by approximately 200 coaxial cables to a capacitor bank of stored energy 42 kJ at 30 kV. Eight spark-gap switches, which were triggered in parallel using a Blumlein cable, were used to initiate the discharge. The end of the gun projected into a vacuum chamber, of diameter 24 cm and length 18 cm, equipped with eight ports through which the discharge could be studied. A pulse generator and a system of delays were used to synchronise the triggering of the discharge, the laser used to illuminate the plasma, and the recording oscilloscopes.

4.1.1 The Mechanical Construction

The mechanical arrangement of the gun, current feed plates and vacuum chamber is shown in Fig.4.1.1. The device was, clearly, a Mather type. The gun centre electrode, which was the anode, was basically a solid copper cylinder of diameter 5 cm. At the lower electrode end a plug of heavy metal (95% W + 5% Cu) was inserted to reduce erosion due to electron bombardment. This plug proved to be inadequate and was replaced by a heavy-metal cap of depth 3 cm. Over a length of 21 cm the electrode was a true cylinder. The remainder consisted of a length tapered to a

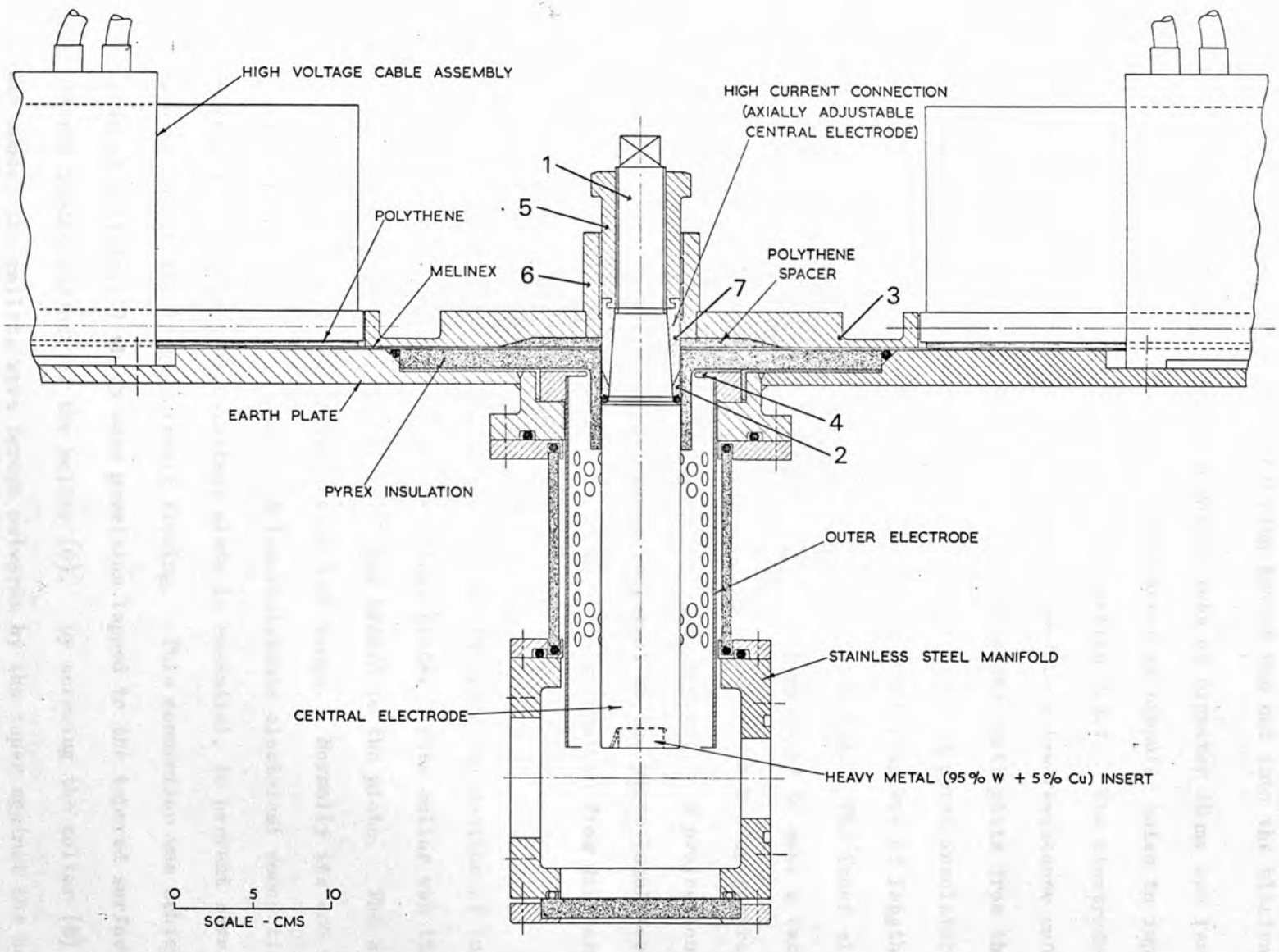

Fig.4.1.1
Plasma Focus. Arrangement of the gun, current feed plates and vacuum chamber

diameter of ~3.3 cm and a cylindrical length (1) which was threaded. At the larger end of the taper a stainless steel collar (2) was shrunk fit. Immediately below the collar an O-ring groove was cut into the electrode.

The outer electrode was a copper tube of diameter 10 cm and length 23 cm. It was perforated by a regular array of circular holes to improve the focusing mechanism, as discussed in section 2.3.1. The electrode was bolted firmly to the brass earth-plate to produce a low-resistance connection. Polythene and Melinex sheets insulated the earth plate from the brass high-voltage plate (3) immediately above it. A pyrex insulator, consisting of a 25 cm diameter disc to which a tubular sleeve of length 5 cm was fused, was used to close the breech end of the gun. The inner electrode passed through this sleeve, and an O-ring was used to make a vacuum seal between them. A second vacuum seal was made by an O-ring compressed between the edge of the pyrex disc and the earth plate. A projection (4) from the outer electrode to the inner, adjacent to the pyrex insulator, provided consistent electrical breakdown at this location from discharge to discharge.

A brass collar (5) was screwed over the threaded section of inner electrode to attach it to the high-voltage plate. This collar was itself screwed into a brass holder (6) which was brazed to the plate. The anode position was axially adjustable over a 5 cm range. Normally its end was flush with that of the cathode. A low-resistance electrical connection between the anode and high-voltage plate is essential, to prevent severe burning due to the large currents flowing. This connection was achieved by using collets (7) which were precision lapped to the tapered surface and the inside surface of the holder (6). By screwing the collar (5) down the anode, the collets were forced outwards by the taper against the holder to give a tight fit between all four contact surfaces.

The gun muzzle projected into a stainless-steel vacuum chamber, which is not drawn to scale in Fig.4.1.1. Internally, the chamber was a cylinder, 18 cm in length and 24 cm in diameter, coaxial with the gun. Externally, the chamber was octagonal in cross section in a plane normal to its axis. The top and bottom surfaces were parallel to this plane. Six of the flat side faces had 2" ports bored in them, the remaining two were directly opposite each other and had 3" ports. The top and bottom chamber faces had 4" ports. O-ring grooves, concentric with the ports, provided a means of making vacuum seals between the chamber faces and connectors to the ports. The eight side ports could be used to study the discharge by connecting various diagnostics or attaching windows. A 60 cm long tube was attached to the lower port to trap material eroded from the electrodes and chamber walls at its bottom. This prevented the accumulated debris from being disturbed during a discharge and damaging any high-quality glass windows used to close the ports. The cathode was jacketed by a pyrex tube, which sealed against O-rings in the lower surface of the earth plate and the top surface of the vacuum chamber.

4.1.2 The Vacuum and Gas Filling Systems

The vacuum chamber and gun assembly were evacuated through one of the 3" ports via a T piece, so as not to lose the use of that port. A single-stage rotary oil pump, of capacity ~450 litres/minute at 100 torr, served as backing to a 6" diameter, oil diffusion pump. The latter pump incorporated a water-cooled baffle to reduce oil vapour pressure in the vacuum chamber. The pressure was further reduced by a refrigerated baffle fitted between the diffusion pump and chamber. A valve, which was remotely operated, was situated adjacent to this baffle and was used to isolate the vacuum chamber.

A background pressure of $\sim 5 \times 10^{-6}$ torr was usually achieved. The pressure in the system was measured on one of two gauges. A Pirani gauge was used in the range 100 torr to 10^{-3} torr, and an ionization gauge at

lower pressures. With the diffusion pump at working temperature, the pressure in the system could be reduced from 2.5 torr (typical operating pressure) to $< 10^{-5}$ torr in ~ 3 minutes.

Gas was introduced into the system by means of valves of the hot-wire leak type. Two such valves were used: one to admit deuterium, and the other to admit an impurity, usually argon or neon, if needed.

4.1.3 The Capacitor Bank and Discharge Circuit

The capacitor bank had a capacity of 94 μF and consisted of 32 capacitors, each of nominal capacity 3 μF. The maximum working voltage was 40 kV, but the bank was usually operated in the range 25 to 35 kV. The capacitors were charged by a power supply consisting of a step-up transformer and half-wave rectifier, in conjunction with a voltage-doubling circuit. A maximum current of 200 mA at 50 kV could be delivered by the supply.

The capacitor bank was divided into four modules, each of which was further divided into two circuits. Each circuit was switched into the gun by a 3-electrode spark-gap switch. The capacitor bank fed the high-voltage and earth plates of the gun, through the spark gaps, via 216 coaxial cables of 50 Ω impedance. Using many parallel cables ensures a low source inductance, so that the capacitor energy can be rapidly delivered to the gun. Likewise, using eight parallel switches results in a switching inductance which is 1/8 of that of a single switch. However, a compromise must be reached between achieving an extremely low source inductance and keeping the cost and complexity of the discharge circuit at a reasonable level. The measured source inductance was 26 nH. The cables were connected to the gun collector plates in four symmetrical groups, the cable braids being at earth potential.

A Blumlein cable charged to ~35kV triggered the eight spark gaps in parallel. The cable was itself switched by a master spark-gap, which was triggered by a 15kV pulse from a thyratron valve unit. The slave spark-gaps proved extremely reliable when used in the range 25 - 35kV, each handling peak currents of ⩽125kA for several thousand shots without maintenance. The typical break-down time for a spark gap, from when the trigger pulse was applied to the trigger electrode to the time at which the main gap began to conduct, was 25nsec. Typical shot-to-shot jitter was 5nsec. Thus, on the timescale of the discharge circuit, of quarter period ~2.5 μsec, the eight spark gaps were well synchronised.

4.1.4 The Control System

The control system for synchronising the triggering of the capacitor bank, the laser used for diagnostics and the recording oscilloscopes is shown schematically in Fig.4.1.2. The system consisted of an arrangement of electronic delay units and thyratron units triggered by a pulse generator, all from the Harwell 2000 series.

Each delay unit consisted of a monostable multivibrator incorporating a diode arrangement to suppress the leading edge of the rectangular pulse triggered by the -50V input pulse. The output was the differentiated trailing edge of the rectangular pulse. By varying the width of this pulse, the delay between the input and output pulses from the unit could be varied. The delay was continuously variable from ~0.2μsec to 100msec, coarse control being achieved using a switched range of capacitors and fine control by a variable resistor. Each thyratron unit consisted of a thyratron valve triggered by a +200V input pulse and giving an output pulse of +250V. Because the unit was relatively insensitive to the input pulse amplitude and the loading on the output, the unit was used as buffer between the more sensitive delay unit and the device to be

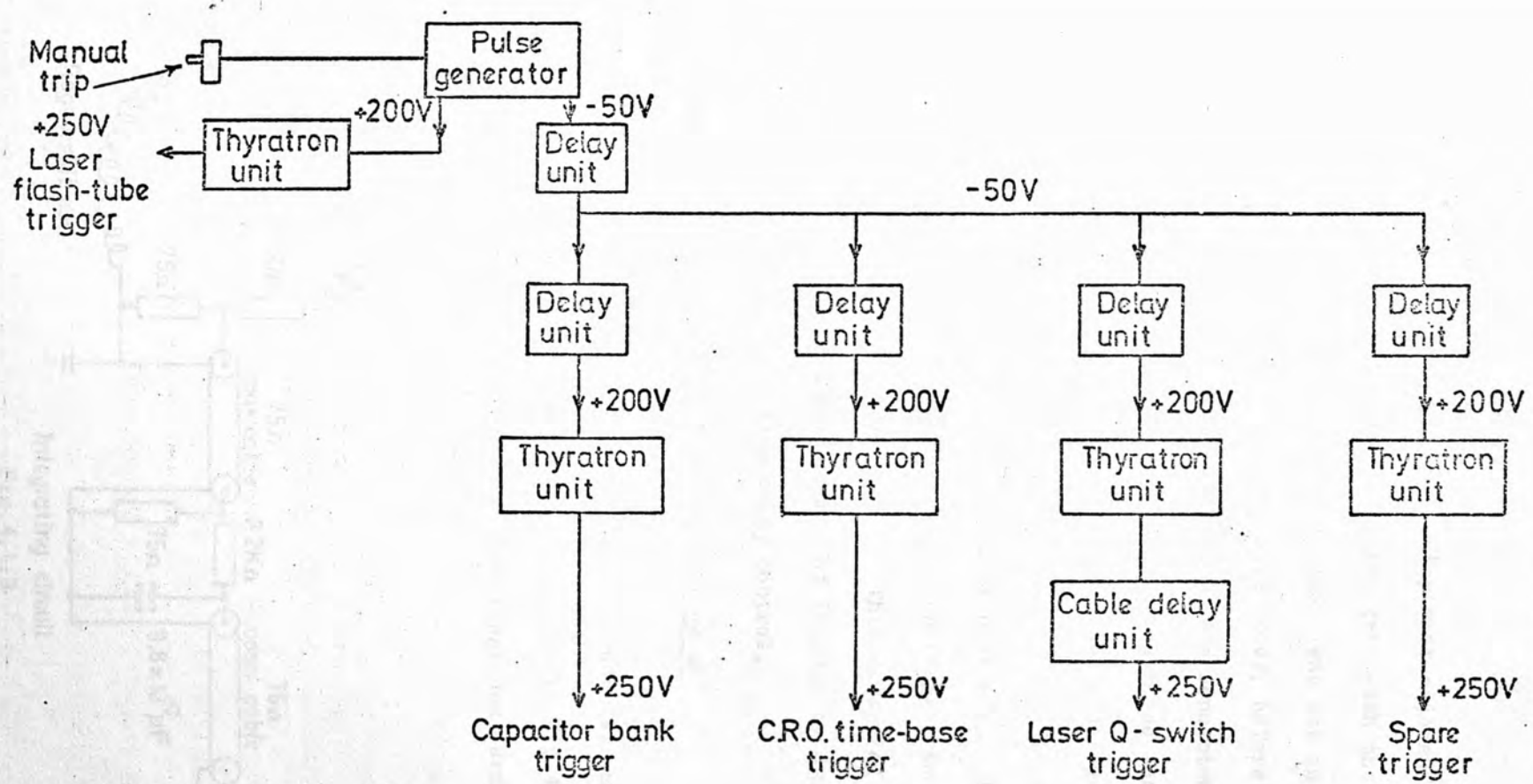

Fig.4.1.2

Schematic diagram of the control system for triggering the capacitor bank and recording devices

triggered. The pulse generator was a monostable multivibrator of fixed rectangular-pulse width.

Referring to Fig.4.1.2, the delay unit adjacent to the pulse generator controlled the timing of all the triggers with the exception of the laser flash-tubes'. A delay of ~1.5 msec was set on this unit to achieve optimum population inversion in the laser rods, before the remaining triggers activated the devices to which they were connected. The remaining delay units each operated on a separate trigger, so that each trigger could be delayed independently. Thus, using suitable delays, the laser could illuminate the plasma at any desired stage of the Plasma Focus discharge, and the oscilloscopes could be tripped accordingly. In addition to being controlled by an electronic delay unit, the trigger to the laser Q-switch was also controlled by a cable delay. This consisted of a number of lengths of cable giving a delay range of 10 nsec to 1 μsec in steps of 10 nsec, i.e. this was for fine delay control.

4.1.5 Monitoring of the Current and Voltage at the Gun, and the Neutron Output

The current flowing between the electrodes was measured using a Rogowskii coil coupled to an integrating circuit, Fig.4.1.3. The coil was looped around the gun between the high-voltage and earth plates, so that

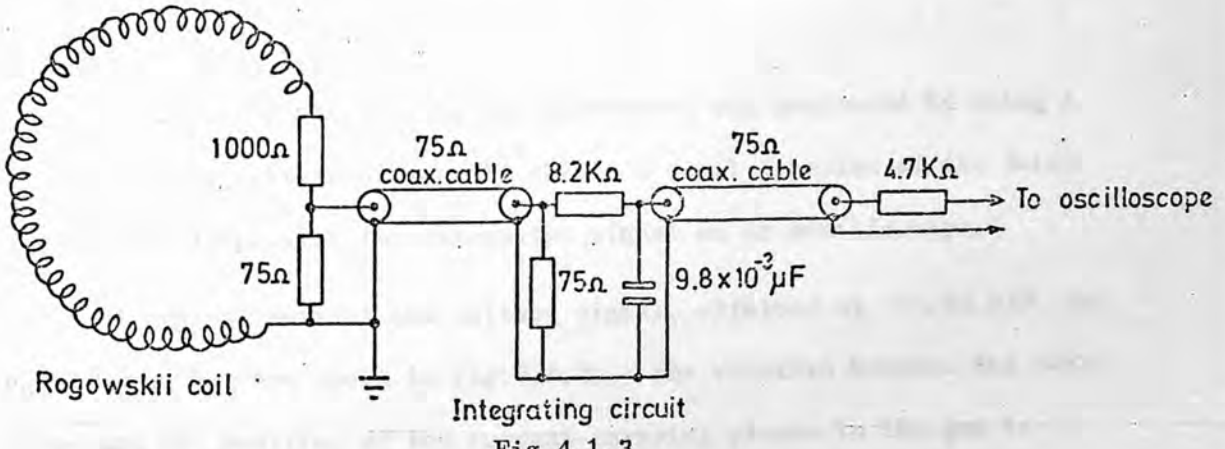

Fig.4.1.3
Schematic diagram of the current-measuring circuit

the current flow threaded the coil. A voltage, $\propto dI/dt$, was induced in the coil, and by means of a potential divider a fraction of this voltage was fed to the integrating circuit. The time constant of the circuit, $RC \sim 80\mu sec$, was much longer than the quarter period of the discharge circuit, $\sim 2.8\mu sec$, so that the integrated signal displayed on the oscilloscope was proportional to I.

The system was calibrated by discharging the capacitor bank with short-circuiting plates connected across the feed plates to the gun. With the plates in position, the discharge circuit was very lightly damped and the current waveform was oscillatory with period $\tau = 2\pi\sqrt{LC} = 11.2\mu sec$, C being the capacity of the bank and L the circuit inductance. The capacity C was found to be $94\mu F$ using an a.c. bridge circuit. From the above values, the total circuit inductance was calculated as being $\sim 34 nH$. By measuring the amplitude of successive peaks of the current waveform, from the oscilloscope traces, the logarithmic decrement of the waveform was obtained. Thus, the amplitude, a_o, that would be observed on the traces in the absence of damping could be determined. The corresponding peak undamped current, $\hat{I}$, could be calculated, since $\hat{I} = V\sqrt{C/L}$, where V is the bank voltage. Hence, the calibration factor was $\hat{I}/a_o$, i.e. the current per unit deflection of the trace. With the shorting plates in position, the current in the discharge circuit at first maximum was $\sim 1.2MA$ for a bank voltage of $25kV$.

The voltage between the gun electrodes was monitored by using a high-impedance voltage divider to obtain a small fraction of the total signal, and displaying the attenuated signal on an oscilloscope.

A typical current and voltage signal, obtained at $V = 32.5kV$ and $p_o = 3.0$ torr D_2, are shown in Fig.2.1.2. The relation between the waveforms and the position of the current-carrying plasma in the gun is

indicated. During the collapse phase, the plasma inductance increased sharply, section 2.3.2, causing the circuit current to decrease correspondingly. A high voltage was induced between the electrodes, $\propto d/dt\ (LI)$, up to five times the magnitude of the initial bank voltage. Neutrons were always produced during a discharge having such waveforms. Occasionally, the current waveform did not exhibit the usual breakaway from a sinusoidal form prior to the focus, and no high-voltage spikes were observed on the voltage waveform. No neutrons were produced during such discharges.

The neutron yield per discharge was monitored using a silver-activation technique. A Geiger-Müller counter with a thin silver window was embedded in a block of Polythene, which moderated the neutrons, of energy ~ 2.45MeV, produced by D-D reactions in the plasma. The thermalised neutrons activated the silver which decayed by β emission with a half-life of ~ 2.4 minutes. An amplifier-scalar system recorded the number of pulses produced by the counter, due to the β particles, during the 100 second interval immediately following each discharge. The system was calibrated using nuclear emulsions, and one count was found to be equivalent to $\sim 3 \times 10^6$ neutrons. For the operating conditions $V = 30$kV and $p_o = 2.5$ torr (D_2 + 4% Ar), the average neutron yield per discharge was $\sim 10^{10}$.

4.1.6 Operation of the Device and Auxiliaries

The operational procedure to produce a plasma was as follows:

(a) The vacuum chamber and gun were pumped for 2-3 minutes until the background pressure was $\leqslant 5 \times 10^{-5}$ torr.

(b) The chamber and gun were isolated from the vacuum pumps by closing the baffle valve.

(c) Using the hot-wire leaks, the appropriate gas filling was introduced into the vacuum chamber and gun - usually 2.5 torr (D_2 + 4% Ar).

(d) The Blumlein trigger cable was charged to 35kV.

(e) The capacitor bank was charged to a voltage in the range 25-35 kV.

(f) Using the control system described in section 4.1.4, the discharge was initiated.

(g) Finally, the recorded voltage and current waveforms were examined, and the neutron count obtained, to establish whether or not the discharge was satisfactory.

When operating the Plasma Focus, either at a fixed bank voltage or filling pressure, it was important to maximise the energy transfer from the capacitors to the dense pinch. Optimum energy transfer occurred when the collapse phase commenced at the time of the first current maximum in the discharge circuit, section 2.3.2. Monitoring the current waveform shot by shot, either the bank voltage or filling pressure was varied, as appropriate, until the characteristic dip in the waveform occurred at peak current.

Having optimised the energy transfer, such active diagnostic devices as a pulsed laser or a framing camera were synchronised to the discharge phase under investigation. When using a laser, a small fraction of its output was monitored using a photo-diode connected to a split-beam oscilloscope, such as a Tektronix 551, which also monitored the current waveform. By adjusting the delays controlling the Q-switch trigger, the laser pulse could be synchronised with any reproducible feature of the current waveform, such as the point of break-away from a sinusoidal form.

It was found that the addition of 4% of argon to the deuterium filling made the discharge more reproducible from shot-to-shot. Consequently, the jitter between the probing laser pulse and the discharge stage being studied was reduced from $\sim \pm$ 50 nsec, when using deuterium only, to $\sim \pm$ 8 nsec. This jitter was the combination of jitters in the delay units, thyratron units, spark gaps, gun and the laser. The improved

reproducibility was probably due to enhanced plasma stability caused by two effects: Firstly, during the final part of the collapse, the dense-pinch phase and the break-up phase, the viscosity of the argon ions was likely to be high compared to that of the deuterium ions. Secondly, the presence of the argon ions increased the radiative-cooling rate by at least two orders of magnitude, Peacock et al (1968), resulting in a less energetic plasma.

Adding a significantly higher percentage of argon resulted in a poor neutron yield and a low plasma energy-density, because of the unacceptably high, radiative cooling. With less argon that $\sim 4\%$, the shot-to-shot jitter became too large.

4.2 DEVELOPMENT OF A LASER SOURCE FOR OPTICAL STUDIES OF THE PLASMA FOCUS

When the optical study which forms the kernel of this thesis was started in mid 1968, no definitive optical investigation of a Plasma Focus had been made, due to difficulty in obtaining adequate temporal resolution. It follows that, during the course of this study, a significant amount of the time was spent in developing a laser source capable of 'freezing' the motion of the plasma, on any optical record produced.

4.2.1 Initial Investigations

From the work of Long et al (1967), during the late stages of the collapse phase and the dense-pinch phase radial velocities in excess of 10^7 cm sec^{-1} had been observed using the Plasma Focus that is described in section 4.1. Thus, it was clear that, at these discharge times, exposures of ≤ 5 nsec were needed for good temporal resolution in any optical study. However, the discharge was initially studied, using the shadowgraph technique, with a Q-switched laser of pulse duration ~ 30 nsec as light source, for two reasons: Firstly, the laser was simple to operate and very reliable. Thus, it was a convenient light source with which to investigate

such initial problems as the reproducibility of the discharge, and the ease of synchronising laser and discharge. Secondly, it was quite possible that after the break-up of the dense pinch such exposures would be adequate.

The laser used was a Barr and Stroud ruby oscillator, type LU 3, which was quarter-wave switched using a Kerr cell (i.e. the cell rotated the plane of polarisation of the light it transmitted by 45° in a single pass). The laser pulse-shape was monitored by using a pellicle beam-splitter to deflect a fraction of the laser output onto an ITT photodiode connected to a Tektronix 519 oscilloscope, the system having a rise-time of 0.35 nsec. Neutral density filters were placed over the photodiode to achieve a suitable input light intensity. Simultaneously, the energy in the remainder of the output was measured using a TRG 107 ballistic thermopile calorimeter coupled to a Keithley 150A microvoltmeter. These checks were made periodically to confirm that the laser output remained satisfactory.

The pulse duration proved to be too long to obtain sharp shadowgrams at any time during the collapse, dense pinch or break-up phases. Some hundreds of nanoseconds after the dense-pinch phase, however, material was spalled from the centre electrode with a velocity of $\sim 10^6$ cm sec^{-1}. The laser pulse duration was sufficiently short to enable sharp shadowgrams of this phenomenon to be obtained.

4.2.2 Further Investigations, and Development

From the above investigation, it was apparent that exposures of < 5 nsec, and preferably as short as 1 nsec, would be needed to obtain good temporal resolution in any optical study of the discharge. Furthermore, since a Q-switched ruby laser is inherently limited to producing a light pulse of minimum duration ~ 10 nsec, it was clear that an alternative type of laser source was needed.

The principles of a Q-switched ruby oscillator are outlined: Typically, an oscillator cavity consists of two reflectors, a ruby rod, an electro-optic rotator and a polariser. The rod is situated between the reflectors with its axis normal to both reflecting surfaces. The reflectivity of the output reflector is ~ 25%, the rear reflector being 100% reflecting. A helical xenon flash-tube is wound around the rod to optically pump it. The rotator, either a Kerr or Pockels cell, is mounted between the rod and rear reflector.

When a current is discharged through the flash tube, the emitted light flux excites the chromium atoms in the rod, and a population inversion starts building up, the inversion increasing with increasing pumping. After excitation, a number of atoms decay spontaneously to the ground state, resulting in a continuous photon flux from the ruby. This flux is returned to the ruby by the reflectors, and will stimulate further depopulation from the meta-stable state of the excited atoms, unless the Q of the cavity is spoiled. The light emitted by the ruby is plane polarised, and if this polarisation plane is rotated by 90° the amount of emission the light can stimulate is drastically reduced. Hence, by electrically stressing the rotator, so that in a single pass the plane of polarisation of the light it transmits suffers 45° rotation, photons returning to the ruby from the rear reflector cause little stimulated emission, having passed twice through the rotator. A polariser, such as a Glàn-Thompson, is mounted between the ruby and rotator and increases the extinction ratio of the system by deflecting these photons out of the cavity.

After ~ 1 msec , typical of the time taken to reach peak flash-tube current, the population inversion is optimum. The voltage stressing the rotator is now quickly removed, consequently it causes no rotation of the light and permits full transmission by the polariser. The cavity thus has a high Q, and the photon flux from the ruby rapidly increases, due to

an avalanche process involving stimulated emission during many transists of the active medium. Lasing occurs and a giant pulse is output. However, the typical delay between initiating the Q-switch and the pulse appearing is 100 nsec, the time taken for the giant pulse to build up. During this build-up time, light leaks through the output reflector, making it impossible to produce a Q-switched pulse of half-width less than ~10 nsec.

At the beginning of the optical study, there were two techniques in common use for producing a pulse of duration < 5 nsec from a ruby laser:

(a) The first method was to operate a ruby oscillator in the pulsed transmission mode, Vuylsteke (1963) and Hook et al (1966). The technique involves double switching of the electro-optic rotator in an oscillator of the type described above, except that both reflectors are 100% reflecting. The first switching, which removes the stressing voltage from the rotator, produces a Q-switched pulse in the usual way, but no output can occur from the cavity. At peak lasing intensity the stressing voltage is reapplied, in two passes rotating the plane of polarisation of the light by 90°. The light is no longer transmitted by the Glan-Thompson polariser, but is dumped out of the cavity off the polariser interface. For instantaneous PTM switching, the half width of the output pulse is twice the cavity transit time for a photon, $t = 2L/c$. The finite time taken to PTM switch broadens the output pulse. With a cavity of length 45 cm a pulse of duration ~4 nsec could be expected.

(b) The second method consisted of mode locking a ruby oscillator and selecting, by means of an electro-optic rotator and a Glan-Thomspon polariser, one pulse out of the train of ultra-short pulses produced. Mode locking consists of using a saturable absorber, e.g. cryptocyanine in methanol for ruby, to passively Q-switch the oscillator and, at the same time, to phase lock the simultaneously-occurring axial modes in the cavity,

Mocker and Collins (1965). From Fourier analysis, the interference of N integrally related and phase-locked frequencies, of equal intensity I and frequency separation ν, gives a repetitive pulse train of pulse width $\Delta t = 1/N\nu$, peak intensity N^2I and repetition period $T = 1/\nu$. Placing the saturable absorber adjacent to the rear reflector, the output intensity is modulated with the fundamental cavity frequency, $\nu_o = (2L/c)^{-1}$. Typically, the output consists of a train of pulses, each of duration $\sim 5\times10^{-11}$ sec and separated by intervals $t = 1/\nu_o$, within the envelope of the Q-switched pulse of half width ~ 50 nsec. To select a single pulse, an electro-optic rotator and Glan-Thompson polariser are added to the cavity, Alcock and Richardson (1968). The principle is very similar to that of PTM switching, the cavity energy being dumped out by the polariser in a single ultra-short pulse.

Unfortunately, the first technique was not suited to studying all phases of the Plasma Focus discharge, while the second technique could not be applied at all. To obtain a pulse of duration 2.5 nsec by PTM switching, the oscillator cavity must not be longer than 15 cm allowing 1 nsec for switching. Into this short length, a ruby rod, Pockels cell and Glan-Thompson polariser have to be packed. Clearly, pulses of duration 1 nsec were unobtainable using this technique, and 2.5 nsec was probably the best resolution achievable. The unsuitability of the second technique was due to the large shot-to-shot jitter in the appearance of the mode-locked pulses. Even under carefully controlled conditions, in a mode-locked oscillator the jitter between the initiation of pumping and the appearance of the output pulses is $\pm 10\,\mu$sec, Carman et al (1970). The Plasma Focus required $\sim 2.5\,\mu$sec from the initiation of the discharge to the production of the dense pinch. Thus, the discharge could not have been initiated by the mode-locked train itself, because its lifetime of ~ 50 nsec would have been far too short to have illuminated the pinch.

Statistically, the chance of lasing occurring within a particular 100 nsec interval during the discharge was < 1 in 50. Hence, the technique was not considered as being worth using as it stood.

In an attempt to reduce the jitter inherent in the second technique, a combination of active Q-switching using a Pockels cell and mode-locking using cryptocyanine dye was used. The jitter was reduced to an acceptable level, $\sim \pm 10$ nsec , but a very irregular train of mode-locked pulses, varying considerably in form from shot to shot, was produced. To obtain a regular well-defined train of pulses it is essential that the Q of the oscillator cavity, after Q-switching, is only marginally greater than unity. This is achieved most simply by passively Q-switching using a saturable absorber of suitable strength. However, the system is now very sensitive to the statistical fluctuations in the spontaneous-decay rate of the excited atoms in the active medium, resulting in the very large jitter in the output from shot-to-shot.

An example of a Q-switched pulse and two mode-locked pulses are shown in Fig.4.2.1. The Barr and Stroud oscillator previously described was used, the Kerr cell being replaced with a Pockels cell. The first frame of the figure shows the normal Q-switched pulse, of half width ~ 27 nsec. To obtain a mode-locked output, a dye cell was placed adjacent to the rear reflector and the concentration of cryptocyanine dye was increased until mode-locking with 100% modulation was observed. Frame 2 shows a mode-locked pulse train obtained with only the reflector surfaces in the cavity being parallel. The pulses at the start of the train were subnanosecond in duration with separation ~ 4 nsec , while those at the end were ~ 1.5 nsec in duration with little separation. For 1 shot in ~ 10, a well-defined train of pulses was obtained. The remainder, however, were irregular, as in frame 2. The energy content of a mode-locked train was

Fig.4.2.1
Q-switched and mode-locked pulses from a ruby laser

~0.2J. Finally, the third frame of Fig.4.2.1 is typical of the mode-locked train obtained with all optical surfaces in the oscillator cavity being parallel.

Because of the irreproducibility of the mode-locked train from shot-to-shot, no attempts were made at selecting a single pulse out of it. Instead, the mode-locked oscillator, producing pulse trains similar to that shown in frame 2 of Fig.4.2.1, was used as a light source for schlieren studies of the Plasma Focus. Each pulse in the train, being of duration $\leq$1.5 nsec, produced a sharp image of the plasma on the film, although successive pulses caused an overlapping of different images, which led to difficulties in interpretation.

4.2.3 Development of a Nanosecond Light Source

For the reasons discussed in the previous section, the techniques of PTM switching and the selection of a single mode-locked pulse were not pursued further. Instead, an electro-optic shutter was developed for use external to a Q-switched ruby oscillator to clip its output to a pulse of ~1 nsec duration.

The shutter consisted of a Pockels cell and a Glan-Thompson polariser. When the oscillator lased, its output passed through the unstressed Pockels cell and was incident on the polariser. The plane of polarisation of the output did not permit transmission by the polariser. Instead, the output was rejected at the polariser interface onto a spark gap. This gap was triggered by the light flux, applying a voltage step of nanosecond rise-time to the Pockels cell. The voltage step rotated the plane of polarisation of the laser light passing through the Pockels cell, resulting in a transient transmission by the polariser to an amplifier.

(a) Apparatus

A schematic diagram of the apparatus used is shown in Fig.4.2.2. The Korad K-1500 ruby laser was basically a Q-switched oscillator and an amplifier, giving typically a pulse of half width ~17 nsec and energy 10 J. The oscillator output was plane polarised in a direction normal to the plane of the diagram. A polariser was added to the oscillator, adjacent to the output reflector, to suppress light plane polarised at 90° to the output due to the ruby birefringence.

On Q-switching the oscillator, the output passed through the unstressed KD*P (potassium di-deuterium phosphate) Pockels cell, with no rotation of the polarisation plane, and was incident on the Glan-Thompson polariser. The cell was a z-cut longitudinal modulator of aperture 1 cm. It required a modest voltage, ~5 kV, to rotate the plane of polarisation of the ruby light through 90° (the half-wave voltage $V_{\lambda/2}$). The polariser prevented transmission to the amplifier, and deflected the beam onto a laser-triggered spark gap (LTSG) similar to that described by Bradley et al (1969).

The LTSG consisted of two brass electrodes 100 μ apart, open to the atmosphere and separated by a 50 μ Melinex sheet. A static voltage of ~14 kV was maintained across the gap. Triggering was achieved by puncturing the dielectric with the laser beam, which was focused by a 5 cm lens onto one electrode through a 0.1 cm hole in the other. The Melinex was replaced after each shot. Voltages ≥ 15 kV could be switched by the LTSG with nanosecond jitter and delay. With the arrangement shown the threshold for breakdown was ~1 MW.

At one end of a Blumlein cable, Wilkinson (1946), of length 2L, the inner conductor was connected to one electrode of the LTSG, while the outer conductor was connected to the other. The Blumlein was made of

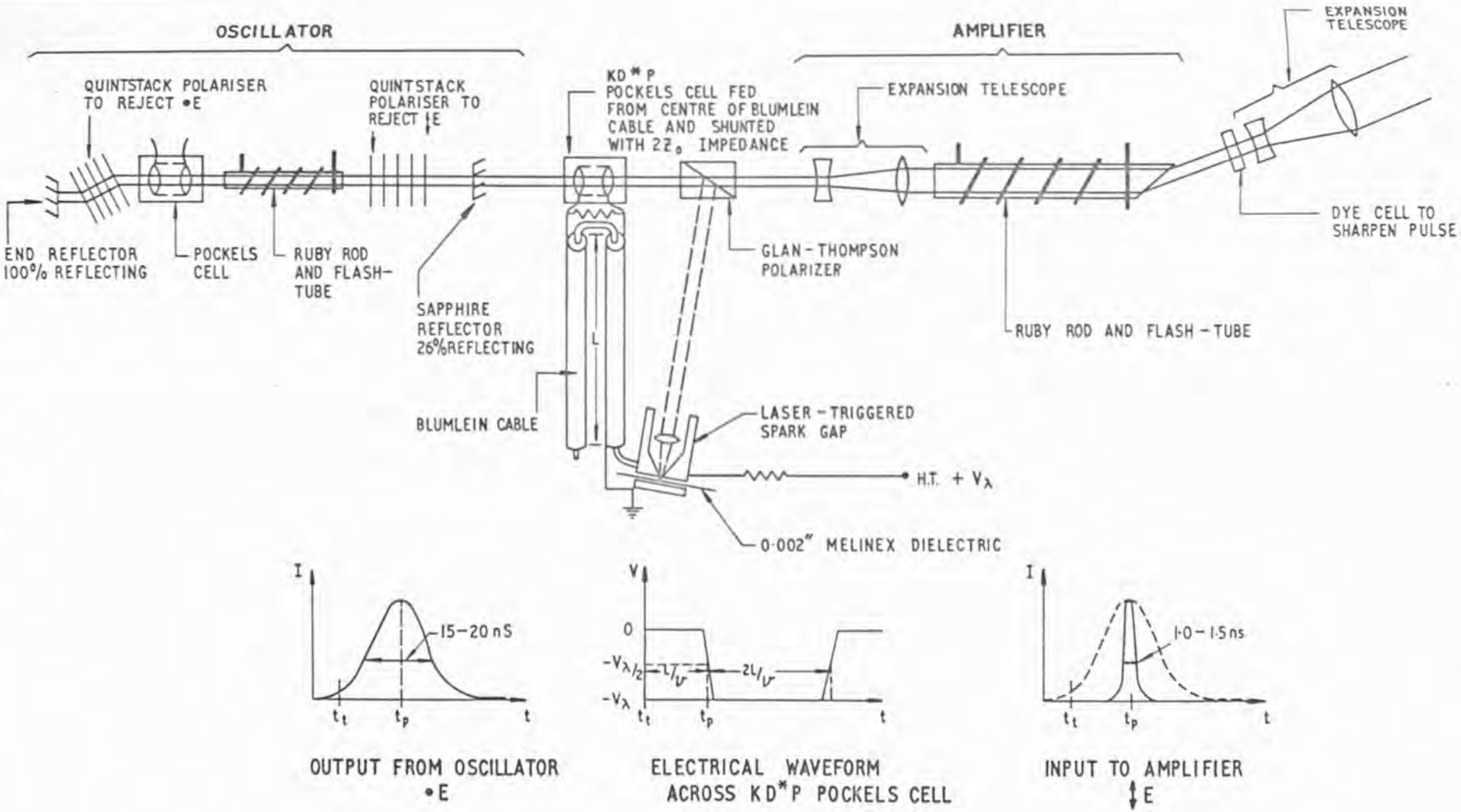

Fig.4.2.2

SCHEMATIC DIAGRAM OF NANOSECOND OPTICAL PULSE GENERATOR

Uniradio 67 coaxial cable of characteristic impedance $Z_o = 50\Omega$. The Blumlein inner conductor was charged to a voltage $V_\lambda = 2V_{\lambda/2}$, the outer conductor being earthed. At the midpoint of the Blumlein cable, the Pockels cell in parallel with a resistor of magnitude $2Z_o$ was connected as a load across a short break in the outer conductor. The Blumlein end remote from the LTSG was open circuit.

(b) Mode of operation

With reference to the waveforms in Fig.4.2.2, the triggering of the LTSG at time t_t launched a voltage step of magnitude $-V_\lambda$ into the cable towards the load. After a delay of L/v, where v is the propagation velocity in the cable, a rectangular pulse of amplitude $-V_\lambda$ and duration $2L/v$ appeared across the load. The clipping action of the shutter was entirely associated with the leading edge of this pulse. As the voltage across the Pockels cell increased from zero to $-V_\lambda$ volts, so the plane of polarisation of the light passing through it was rotated progressively further, up to 180°. The rotation was linearly proportional to the voltage.

At the voltage level $-V_{\lambda/2}$, the Pockels cell had rotated the plane of polarisation of the light passing through it by 90°. This light could now pass through the polariser to the amplifier, with negligible attenuation. However, as the voltage level dropped to $-V_\lambda$, so less light was transmitted by the polariser, until it was all rejected at the interface. Thus, the shutter only admitted light to the amplifier over a portion of the electrical-pulse leading-edge centred at the level $-V_{\lambda/2}$. The duration of the electrical pulse was sufficient to block the remainder of the Q-switched pulse.

By choosing a Blumlein of suitable length and by adjusting the intensity of the light incident on the LTSG, the time of arrival of the electrical pulse at the Pockels cell could be made to coincide with the

time of maximum lasing intensity, t_p. Hence, the clipped pulse transmitted to the amplifier was of maximum intensity. Because of mismatching and losses, the static voltage on the Blumlein needed to be ~ 2.5 kV higher than the pulsed voltage required at the Pockels cell.

The technique described is known as full-wave clipping.

(c) Results and discussion

The waveform of the electrical pulse across the load is shown in Fig.4.2.3. A low-inductance resistive voltage divider coupled to a Tektronix 519 oscilloscope was used to monitor the pulse, the system risetime being ~ 0.9 nsec. The pulse had a risetime of 2.5 nsec which was ~ 2.2 τ, where $\tau = 1.1$ nsec was the 1/e time. Fig.4.2.4 shows the waveform of the optical pulse after 15X amplification and passage through a cryptocyanine dye cell. The dye improved the signal to noise ratio by absorbing the background light due to slight leakage of the Q-switched pulse through the polariser. The optical pulse was monitored on an ITL (HCBI) photodiode which, together with the 519 oscilloscope, had an overall risetime of ~ 0.35 nsec. The pulse had a half width of 1.2 nsec and a risetime of 0.8 nsec.

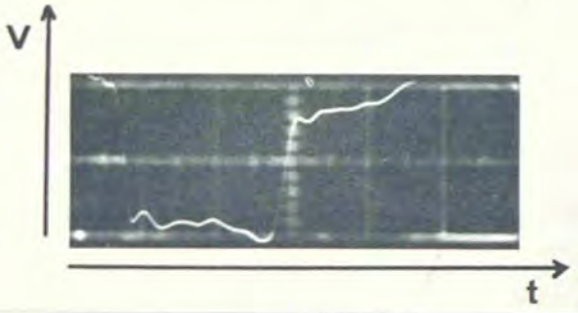

Fig.4.2.3
Waveform of electrical pulse across Pockels cell. Horizontal scale 10 nsec/major division. Vertical scale 5.7 kV/major division

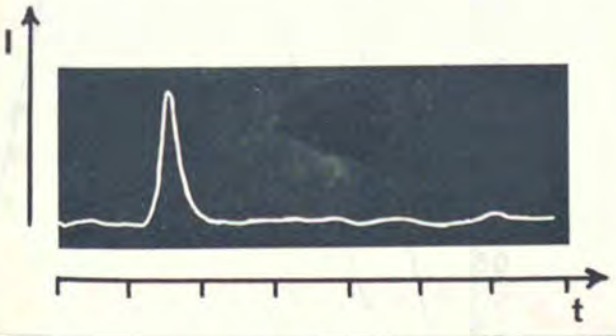

Fig.4.2.4
Waveform of optical pulse after amplification (retouched for clarity). Time scale 5 nsec/division

Operating a Pockels cell, mounted between crossed polarisers, in the longitudinal mode, the transmitted light intensity, I_V,

expressed in terms of the applied volts, V, is

$$I_V/I_o = \sin^2 (\pi/2 \,.\, V/V_{\lambda/2}) \,, \qquad \ldots (4.2.1)$$

where I_o is the inceident light intensity. For any voltage waveform of peak amplitude $-V_\lambda$, the half-intensity points of the Pockels cell's transmission correspond to 25% and 75% of peak amplitude, i.e. $I_V/I_o = 0.5$ when $V = -V_\lambda/4$ or $V = -3V_\lambda/4$. Thus, the half-width of the optical pulse produced is the time required for the voltage to decrease from $-V_\lambda/4$ to $-3V_\lambda/4$. For an exponential waveform, i.e. $V_t = -V_\lambda[\exp(-t/\tau) - 1]$, where τ is the 1/e time, the time required to reach $-V_\lambda/4$ is $0.29\,\tau$ and that to reach $-3V_\lambda/4$ is $1.39\,\tau$. The half width of the optical pulse is, thus, $\Delta t = 1.1\,\tau$. Now, the measured value of τ was 1.1 nsec and that of Δt was 1.2 nsec. Hence, the measured ratio of $\Delta t/\tau$ was ~ 1.1, which agrees with the calculated ratio.

Using a Fabry-Perot interferometer, of etalon spacing $d = 1$ cm, the line width of the amplified clipped pulse was measured. Fig.4.2.5 shows a typical interferogram produced using the clipped pulse. The free spectral range of the interferometer, $\Delta\lambda = \lambda_o^2/2d$, was 0.24 Å for $\lambda_o = 6943$ Å, giving the spectral width of the pulse as ~ 0.075 Å. A lower limit to the minimum pulse line-width, $\Delta\lambda$, obtained by careful mode selection, was given by the pulse duration. This was due to the uncertainty relationship between the pulse width and the spectral width, in terms of frequency $\Delta t \approx 1/\Delta\nu$. Thus, the minimum spectral width was $\Delta\lambda \approx \lambda_o^2/c.\Delta t$. For $\Delta t = 1.2$ nsec and

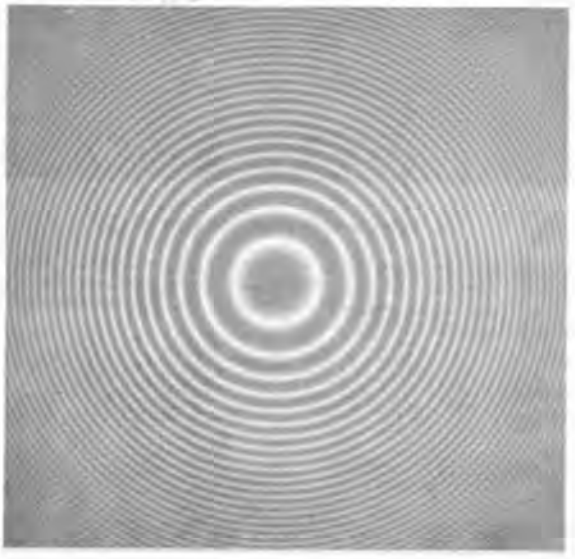

Fig.4.2.5
Fabry-Perot interferogram of light in amplified clipped pulse. Free spectral range 0.24 Å

$\lambda_o = 6943\text{Å}$, $\Delta\lambda = 0.013\text{Å}$, i.e. a continuous beam of ruby laser light of vanishingly small line-width would be broadened to 0.013Å if chopped into pulses of duration 1.2nsec. However, in the case of the system used, the total line-width of 0.075 Å was dominated by mode-coupling in the oscillator cavity, and pulse clipping did not increase the line width significantly. The line width corresponded to a coherence length, equation (3.3.19), of 3.2 cm.

The energy in the amplified pulse was measured, using a calorimeter, as being 30 mJ. The beam divergence was not measurably greater than that of the normal Q-switched pulse, 90% of the beam energy being contained in a 3 milliradian cone. The divergence was measured by focusing the laser beam to a spot of diameter d on a piece of blackened Polaroid film, using a lens of focal length of ≥ 100 cm. To a good approximation, the beam divergence was d/f.

Contemporaneous with the development of full-wave clipping, similar techniques were being developed elsewhere, e.g. Michon et al (1969) and Alcock and Richardson (1970). In principle, all of these techniques were similar, but the latter two employed half-wave clipping. Thus, a rectangular pulse of amplitude $V_{\lambda/2}$ was applied to the Pockels cell, the leading edge of the pulse opening the shutter and the trailing edge closing it. The half width of the electrical pulse defined the half width of the optical pulse produced. Morgan and Peacock (1971) discuss the relative merits of full-wave and half-wave clipping.

The electro-optic shutter described in this section, when used with a ruby oscillator-amplifier system, produced a pulse of sufficiently short duration, 1.2 nsec, of sufficient energy, 30 mJ, of sufficiently narrow line-width, 0.08 Å, and of sufficiently low beam divergence, 3 milliradians, to be an extremely useful light source for the optical study of the Plasma Focus.

4.3 OPTICAL TECHNIQUES APPLIED TO THE PLASMA FOCUS

In this section, the experimental details of the optical techniques used to study the Plasma Focus are given. The principles of these techniques have been discussed in Chapter III.

4.3.1 The Shadowgraph Technique

The basic optical layout used is shown in Fig.4.3.1. Initially, the system was used with the simple Q-switched oscillator as light source, but later the nanosecond laser light source was used. The laser output was expanded 5 X by a telescope and the parallel beam passed into the discharge chamber, in a direction normal to the gun axis, through a glass window. An area 2.5 cm wide by 3 cm in length was illuminated at the gun axis. This area was centred on the gun axis and extended from the inner electrode edge away from the gun.

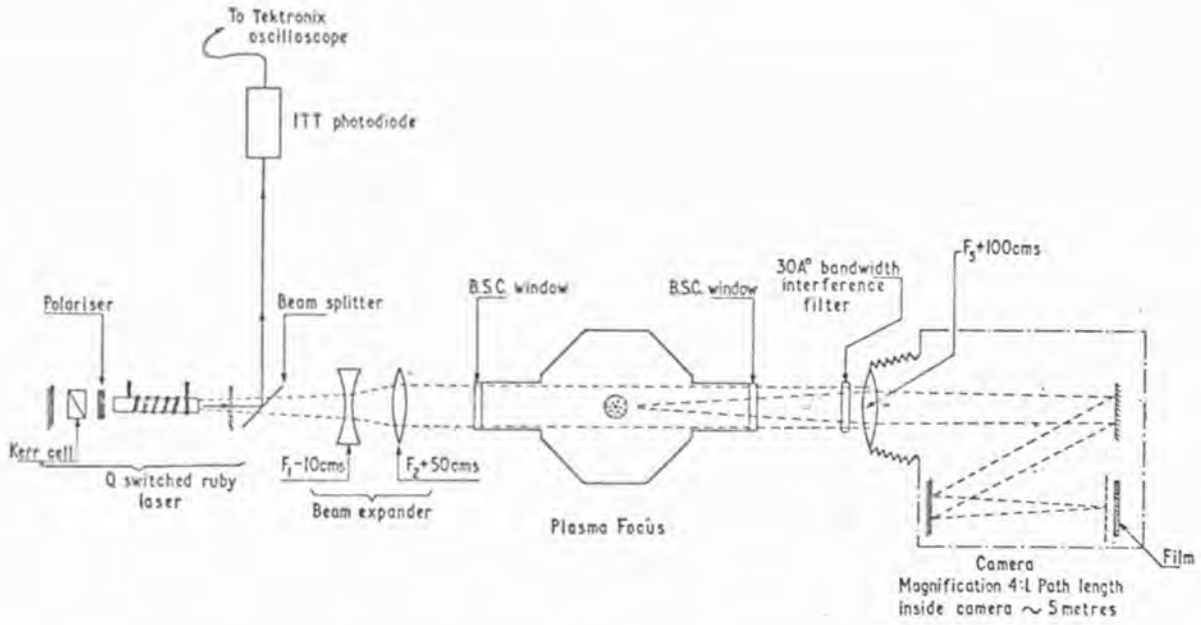

Fig.4.3.1

Schematic diagram of shadowgraph optics used on Plasma Focus

The beam passed out of the chamber through a second window and was collected by a camera lens of focal length +100 cm and aperture ~ f 25. The lens focused the plane which contained the gun axis, and was normal

to the beam, at a plane which was ~0.5 cm in front of the film plane. Two types of film were used for this and the other optical studies; Polaroid type 57 for initial results and, for results where a high resolution film was needed, Kodak SO-243. This latter film was a high definition aerial film, with a resolution capability of ~500 lines/mm and a speed of ~3ASA at 6943 Å. The camera had a field of view covering an area ~1.8×2.4 cm at the gun axis. To discriminate against the light emitted by the plasma, mainly by line and recombination radiation, a narrow-band interference filter with pass band centred on 6943 Å was used to cover the camera input.

The end windows could not be placed closer than ~100 cm to the plasma, because of the risk of damage by debris eroded from the inner electrode and chamber walls. This resulted, typically, in the minimum object distance to the camera lens being ~120 cm. Because of the small dimensions of the dense pinch, it was desirable to obtain a magnified image on the film. A 4X magnification required a camera of optical path ~500 cm, which was too unwieldy to be constructed as a straight-line system. Instead, a folded light path was employed inside the camera, as shown in Fig.4.3.1, by using a pair of plane mirror. The overall camera length was ~200 cm.

Coarse adjustments to the level of illumination on the film were made by varying the pumping voltage to the laser flash-tube. For optimum contrast, fine adjustments to the light level were made by means of neutral density filters, added to or subtracted from a holder in front of the camera lens.

The shadowgraph system described proved very satisfactory in use, and good definition shadowgrams were obtained when using the nanosecond light source. For a 4X magnification and an effective object to film length of 0.5 cm, at 6943 Å the minimum resolvable object size by the

system, assumed to be perfect, was, from equation (3.3.6), $\delta \geq \sqrt{S\lambda / m} = 3 \times 10^{-3}$ cm.

During the collapse phase, the location of the imploding shock showed a measure of irreproducibility in space and time and the growth of instabilities at the plasma-vacuum boundary was random in position and time, from shot-to-shot. After the dense-pinch phase, the plasma was highly irreproducible from shot-to-shot due to MHD instabilities disrupting the plasma column. Thus, in order to measure the plasma collapse and expansion velocities and to study the development of instabilities it was necessary to make multiple exposures, each at a different time, during the same discharge.

Three exposures, each at a different time during the same discharge, were obtained using the apparatus shown schematically in Fig.4.3.2. In essence, the pulse from the nanosecond laser source was divided into three beams of equal intensity, using partially-reflecting mirrors of suitable reflectivity, Basov et al (1967). Each beam was directed through a common plasma volume. The desired time separations between the three beams arriving at the plasma were obtained by making appropriate differences between the three path lengths - 1 nsec delay being obtained for every 30 cm difference. The three beams were inclined at small angles to one another so that three separate images could be obtained on three separate cameras. Each camera had a +75 cm lens, produced a 1:1 image ~0.2 cm from the film plane and covered a field of view of 2.7 cm wide by 3.8 cm at the electrodes. A narrow-band interference filter was placed in front of each camera input.

Using this system, many time sequences of shadowgrams of good definition were obtained at a variety of times throughout the discharge.

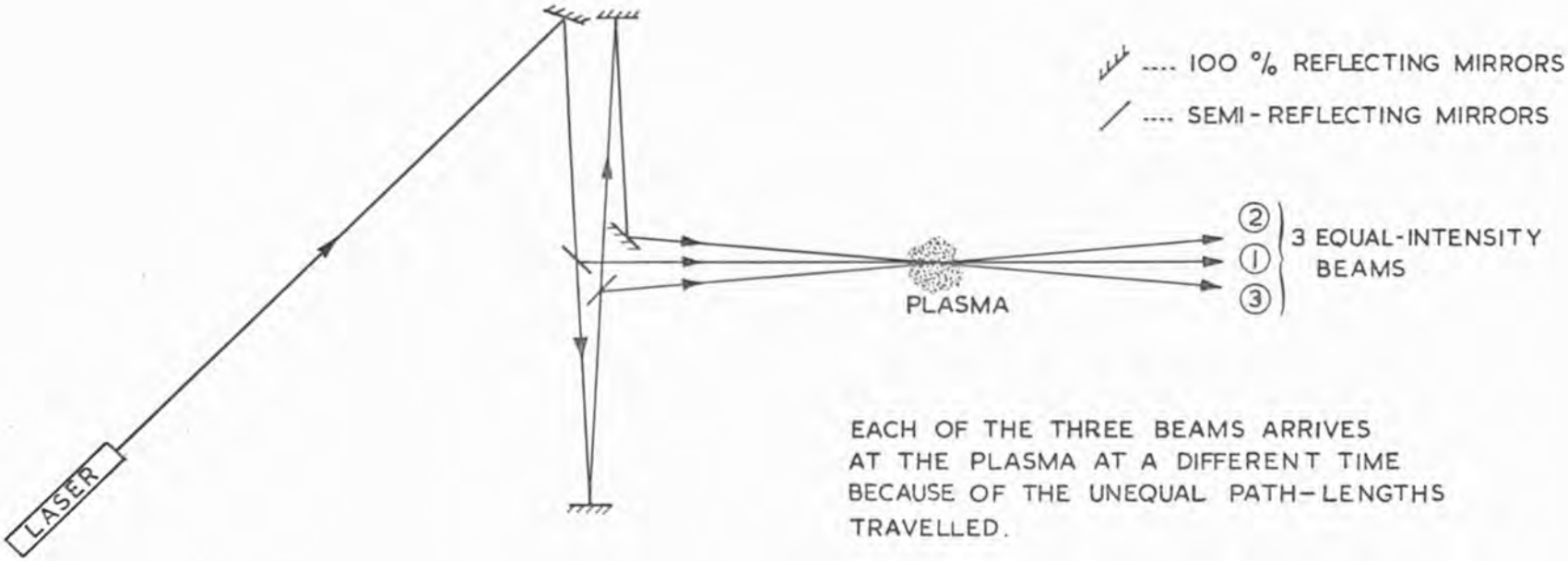

Fig.4.3.2

SCHEMATIC DIAGRAM OF OPTICAL TIME-DELAY SYSTEM

4.3.2 The Schlieren Technique

A schematic diagram of the system used is shown in Fig.4.3.3. The light source initially used was the mode-locked oscillator, followed later by the nanosecond laser source. Up to the point where the laser beam was incident on the schlieren lens, the general arrangements were as described in section 4.3.1. In the absense of the obstacle, the camera lens focused through the schlieren lens the plane which contained the gun axis, and which was normal to the laser beam, onto the film. The same principles of design applied to the camera as discussed in the previous section. The plane mirror was used to avoid a physical obstruction.

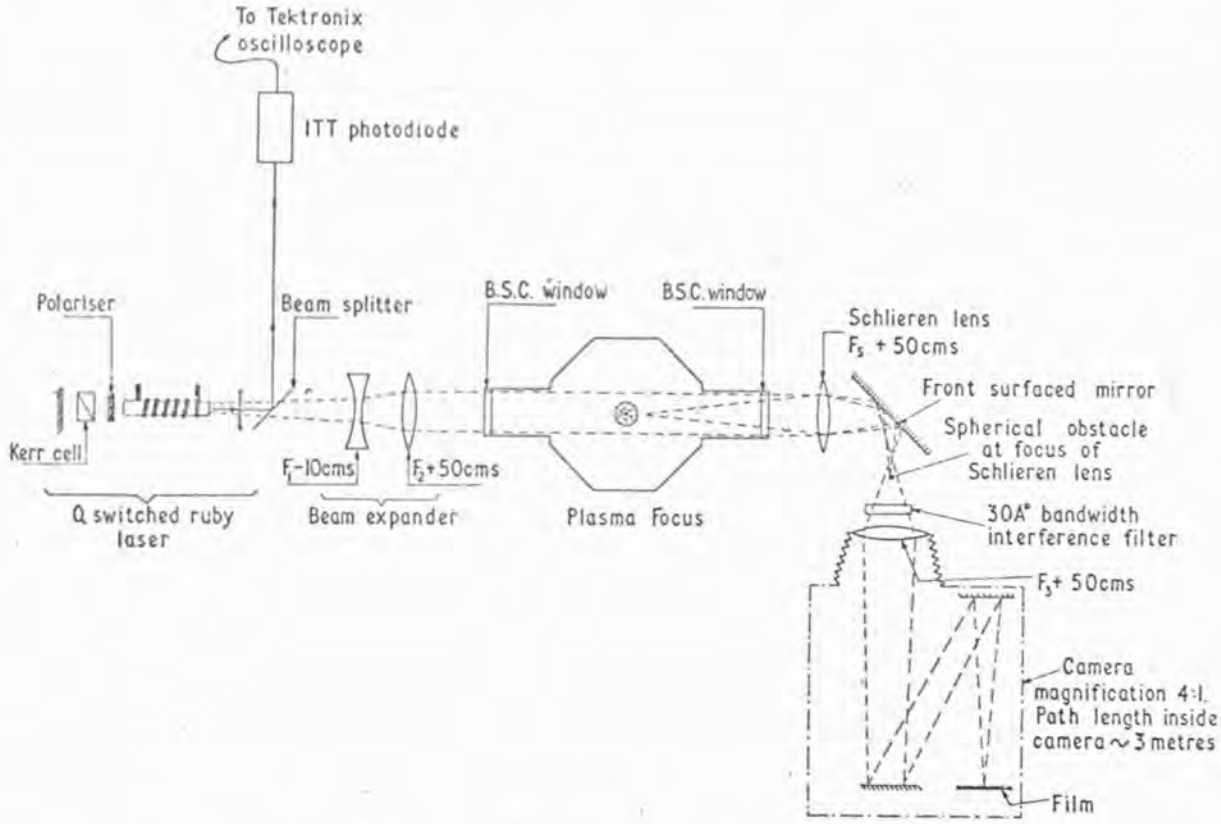

Fig.4.3.3

Schematic diagram of schlieren optics used on Plasma Focus

With the obstacle present at the focus of the schlieren lens, and in the absence of the plasma, no laser light reached the film. In the presence of the plasma, any refractive index gradients normal to the beam caused displacement of some rays at the focal plane of the schlieren lens.

For sufficiently large displacements of these rays, they were not obstructed by the spherical obstacle and were recorded on the film. This technique was sensitive to electron density gradients in any direction in a plane normal to the incident laser beam.

The diameter of the schlieren obstacle set a lower limit to the angle through which the laser light could be deflected by the plasma, and still be recorded on the film. By progressively increasing the obstacle size, the regions of the film which were still exposed corresponded to regions of steeper and steeper density gradients in the plasma. Eventually, all laser light was cut off from the film at an obstacle diameter d_m. The maximum deflection caused by the plasma was then $\alpha_m = d_m/2f_s$, f_s being the schlieren lens' focal length.

With this system, schlieren photographs of the Plasma Focus discharge at different times were taken.

4.3.3 Interferometry

A Mach-Zehnder interferometer was used in the layout shown schematically in Fig.4.3.4. The instrument was set up in the configuration of Kinder, section 3.3.3(b)(ii), with distances M1-BS1 and BS2-M2 being half of distances M1-BS2 and BS1-M2. The plasma was produced at the midpoint of M1-BS2. A field of view of 2.7 cm wide by 3.8 cm, at the gun axis, was covered by the camera, which gave a magnification of ~ 3.8 at the film. The surfaces of the end windows on the discharge chamber were flat to $\lambda/10$ and parallel to 2 arc minutes, so as not to introduce large spurious fringe shifts. A similar pair of windows were used as compensating plates in the reference arm of the interferometer. Similarly, the optical finish of the lenses used was high. The laser used was the system giving nanosecond light pulses.

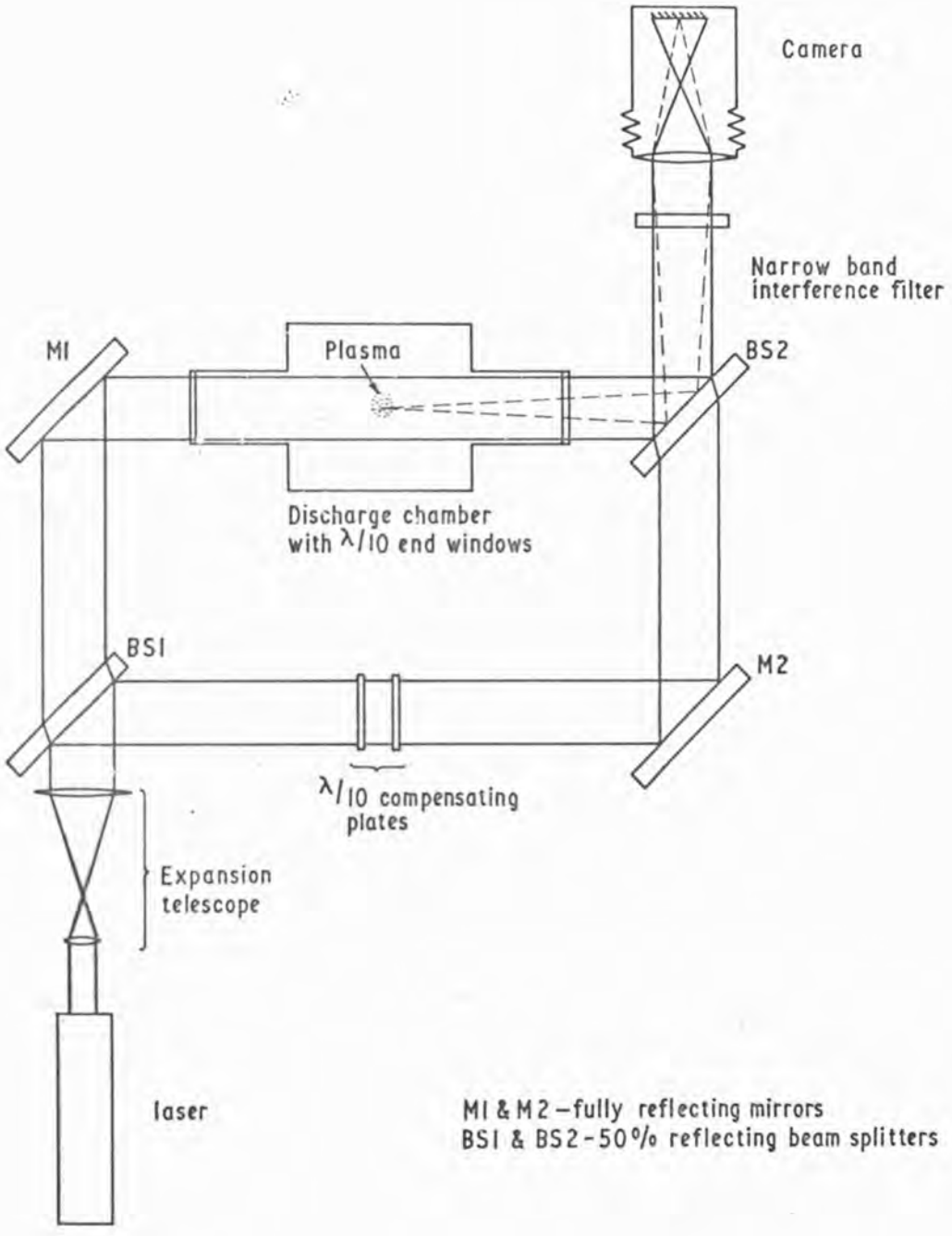

The distances M1 - BS2 & BS1 - M2 are twice the distances M1 – BS1 and BS2 – M2. Hence the plasma is virtually located on M2. Thus, when fringes are focused in the plasma by means of BS2, their spacing and orientation can be changed by M2 without loss of focus.

Fig. 4.3.4

Schematic diagram of interferometric optics used on Plasma Focus

For setting-up and alignment purposes, a helium-neon laser was positioned so that its beam travelled the same path as that taken by the ruby laser beam. The interferometer plates were positioned to be at the corners of a rectangle, of 2:1 aspect ratio as mentioned, and were set at 45° to the direction of the laser beam incident on BS1, using a protractor. Plate BS2 was mounted on a carriage having movements parallel and normal to any of the beams in the interferometer, in the plane of Fig.4.3.4. Measuring lengths using a piece of string, the two paths in the instrument were made as near equal as possible, maintaining the 2:1 aspect ratio by making adjustments to the carriage.

When aligning the instrument, having equalised the two paths, the two pairs of beams coming from BS2, each pair consisting of one reflected and one transmitted beam, were viewed on two screens a few metres distance from BS2. One pair, called pair 1, were parallel to beam BS2-M2, and the other pair, pair 2, were parallel to beam M1-BS2. Initially, the two beams of pair 1 were made to overlap exactly on the appropriate screen, by adjusting plate M2. Then, the two beams of pair 2 were overlapped on the other screen, by adjusting BS2. These steps were repeated in order, the amount of adjustment needed decreasing step-by-step. However, if the amount of adjustment needed increased, the order of adjustment was reversed. After ten or so adjustments, fringes were observed on both screens. The fringe spacing was made as large as possible by adjusting plates BS2, M2, M1 and BS1 in turn, repeating the process if necessary, until a fringe width filling the plate aperture was achieved.

Both screens were removed, and the camera was brought into position and focused on the gun electrode axis. The fringes were viewed on the camera screen, and by adjusting plate BS2 they were brought into focus, i.e. they were located on plate M2. Plate M2 was then adjusted, without changing the focusing, until the desired fringe spacing and orientation

were obtained. Usually, M2 was adjusted so that between 30 and 50 fringes, perpendicular to the gun axis, were present in the field of view. These background fringes were used as a reference against which fringe displacements were measured.

The interferometric system described proved satisfactory for obtaining many good definition integerograms of the Plasma Focus discharge at various times.

CHAPTER V

RESULTS

The photographic records of the Plasma Focus discharge, obtained by schlieren photography, interferometry and shadowgraphy, are now presented and discussed qualitatively. The conditions under which the experiments were carried out are recorded, but the quantitative analyses are postponed until the following chapter.

5.1 SCHLIEREN PHOTOGRAPHY

5.1.1 Initial Results

The schlieren system used to obtain the records is described in section 4.3.2. The mode-locked ruby oscillator, section 4.2.2, was used as light source, and the Plasma Focus was operated under the initial condition $V = 30\,kV$ and $p_0 = 2.5\,torr$ $(D_2 + 4\%\ Ar)$.

A time sequence of five schlieren photographs, obtained using a spherical obstacle of diameter 0.16 cm at the focus of the 50 cm schlieren lens, is shown in Fig.5.1.1. Each frame of the figure was taken during a separate discharge, at the location represented by the position of the middle frame relative to the inner electrode, of diameter 5 cm. For convenience, the remaining four frames are shown in displaced positions. This representation is used to display all optical records of the discharge.

The time at which the current waveform sharply broke away from a quasi-sinusoidal form, Fig.2.1.2, was found to be a convenient reference point for timing the laser pulse relative to the Focus discharge. This time was found to coincide with the maximum compression of the pinch adjacent to the inner electrode, and is designated $t = 0$. All other times are given relative to this reference time, in this and the other optical studies, with earlier and later times having - and + signs, respectively.

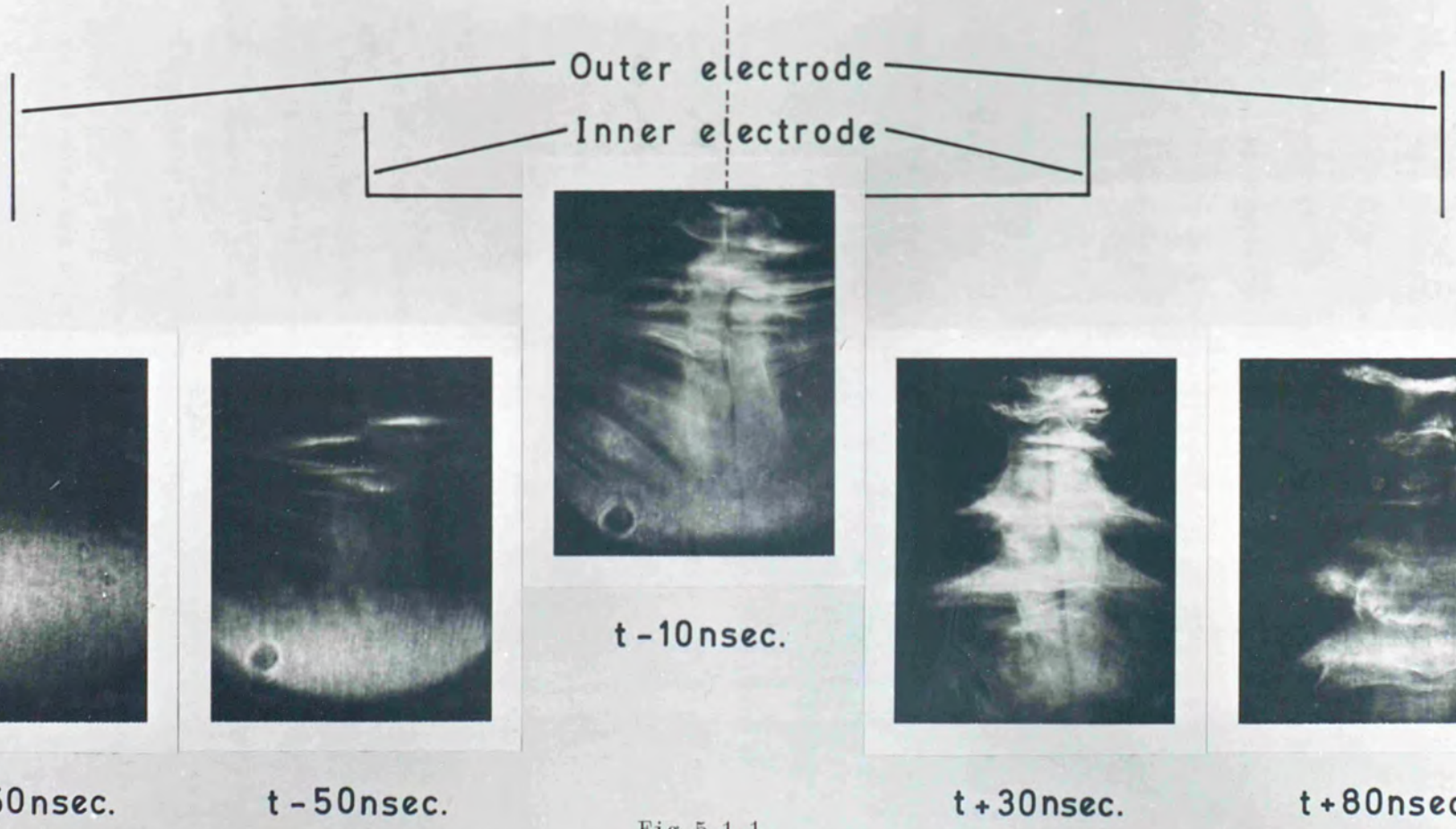

Fig.5.1.1

Time sequence of schlieren photographs during a discharge. Inner electrode diameter 5 cm. Initial conditions V = 30 kV, p_o = 2,5 torr (D_2 + 4% Ar)

The first frame of Fig.5.1.1, at $t = -150$ nsec, shows the leading edge of the current sheet during the collapse phase, i.e. the edge which is furthest away axially from the inner electrode. Frame 2, taken 100 nsec later, shows that the leading edge has moved ~ 0.6 cm axially during this time. A faint outline of the plasma column beginning to form can be seen. The intense horizontal streaks suggest plasma loss in a radial direction. In Frame 3, at $t = -10$ nsec, the plasma column is well formed with mean diameter ~ 0.5 cm. There is a strong suggestion of a radial loss of plasma and, down the centre of the column, a well-defined line of diameter ~ 0.05 cm can be seen. The schlieren technique is sensitive to the refractive index gradients in a plasma, and this line is probably due to a core with steep electron-density gradients. Frame 4, at $t = +30$ nsec, exhibits two prominent flutes. These can be accounted for by the growth of sausage-type instabilities, as the plasma column is disrupted, coupled with an axial movement away from the anode, during the 30-40 nsec duration of the laser pulse. The final frame, at $t = +80$ nsec, shows a completely disrupted plasma column in the centre of the photograph while, further away from the anode, there is again evidence of the presence of sausage-type instabilities.

It was difficult to extract much quantitative information from the schlieren results, because of the superposition of ~ 15 separate images of the plasma, all at different times over a 30-40 nsec interval, on each photograph. However, it was possible to estimate the lifetime of the plasma column, less than 100 nsec, and to obtain the scale length of gradients of n_e during the dense pinch phase, ~ 0.05 cm. Also, it was possible to estimate the axial velocity of the current sheet, $\sim 6 \times 10^6$ cm sec^{-1}.

The effect of using larger schlieren obstacles is shown in Fig.5.1.2. The three frames were obtained at $t \simeq 0$, with obstacles of diameter 0.32,

1

2

3

Fig.5.1.2
Schlieren photographs at $t \simeq 0$, for various obstacle sizes. Inner electrode diameter 5 cm. Initial conditions V = 30 kV, p_o = 2.5 torr (D_2 + 4% Ar)

0.64 and 1.27 cm, respectively. In each frame, a central core structure is much in evidence. It can be seen that as the obstacle diameter, d, was increased, only the plasma regions of increasingly-steep electron density gradients were recorded.

A necessary condition for the film to record light was that some rays had to be deflected through an angle $\alpha \geq d/2f$ by the plasma, where f is the focal length of the schlieren lens. In Cartesian coordinates, with the incident beam propagating along the z axis, the deflection α was the resultant of deflections in the x and y directions due to density gradients in those directions, i.e. $\alpha = (\alpha_x^2 + \alpha_y^2)^{\frac{1}{2}}$, where $\alpha_x = \int_0^L \frac{\partial}{\partial x} \ell n\, n(x,y,z)dz$ etc, using the notation of section 3.3.2(a). In the final frame of Fig.5.1.2, only the plasma central core of diameter ~ 0.05 cm is recorded. In this core, the steepest gradients of n_e exist or, more correctly, the sum $\left(\int_0^L \frac{\partial}{\partial x} \ell n\, n(x,y,z)dz\right)^2 + \left(\int_0^L \frac{\partial}{\partial y} \ell n\, n(x,y,z)dz\right)^2$ is the largest.

Using an obstacle of diameter 2.54 cm, faint images of the pinch core were sometimes recorded at $t \simeq 0$. Increasing the obstacle diameter even further to 2.86 cm, no laser light was recorded on the film. Hence, the maximum beam deflection due to the plasma was ~ 25 mrads. From this observation of the maximu beam deflection, it was possible to estimate the peak plasma electron density.

5.1.2 Results Using the Nanosecond Light Source

Although interferometric and shadowgraph records were obtained which were superior to the schlieren records, it is interesting to present some of the latter obtained using the 1 nsec laser source, section 4.2.3. The schlieren system was as described in section 4.3.2, and the Plasma Focus was operated under the initial conditions $V = 30$ kV and $p_o = 2.5$ torr (D_2 + 4% Ar).

In Fig.5.1.3, a schlieren photograph obtained at $t = -10$ nsec is

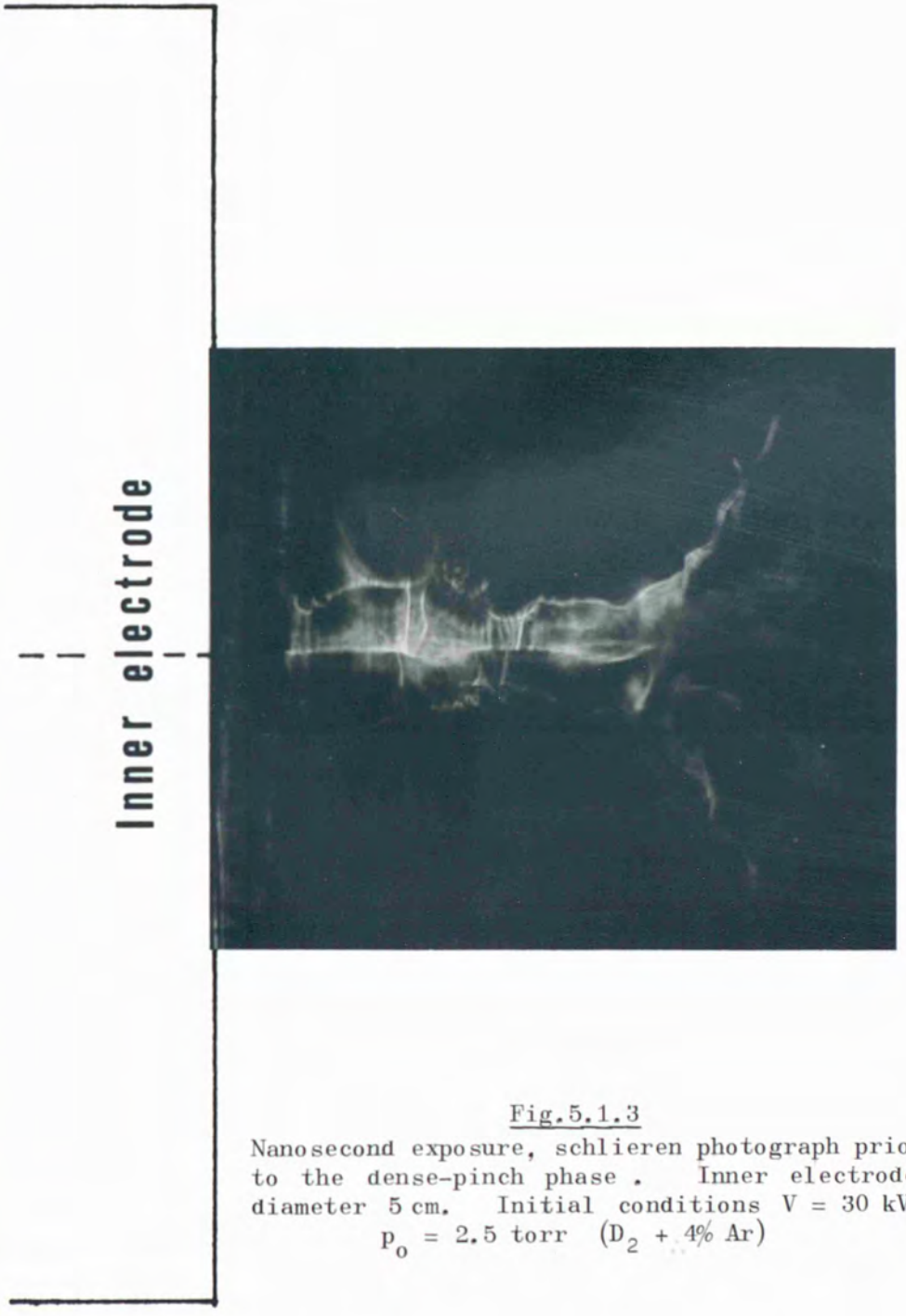

Fig.5.1.3

Nanosecond exposure, schlieren photograph prior to the dense-pinch phase . Inner electrode diameter 5 cm. Initial conditions V = 30 kV, p_o = 2.5 torr (D_2 + 4% Ar)

shown, for which a schlieren obstacle of diameter 0.32 cm was used. The plasma-vacuum boundary is clearly outlined at this late stage in the collapse phase, and it can be seen that sausage-type instabilities are beginning to develop in the plasma column. A central core structure of diameter ~0.05 cm is visible. Thus, the regions of steepest density gradients in the plasma column are at the plasma-vacuum boundary and at the axis.

Increasing the size of the obstacle until it obstructed all of the laser light, a maximum deflection of ~16 mrads by the plasma was calculated. This value is ~35% less than that obtained in the previous schlieren study, with identical initial conditions. The most probable explanation of this discrepancy is that the cavity in the anode end, produced by intense electron bombardment, was quite different in size in the two studies. It is known that the state of the inner electrode affects the performance of the Plasma Focus, in terms of the energy-density of the dense pinch.

5.2 INTERFEROMETRY

The interferometric system used to obtain the optical records is described in section 4.3.3. The laser system producing a pulse of 1 nsec duration was used as a light source, and the Plasma Focus was operated under the initial conditions $V = 30\,kV$ and $p_o = 2.5\,torr$ $(D_2 + 4\%\ Ar)$.

A time sequence of three interferograms, taken during the collapse of the current sheet to the axis, the dense-pinch phase and the break-up of the pinch, is shown in Fig.5.2.1. The first frame shows clearly the oblique nature of the collapsing current-sheet at $t = -30\,nsec$. Outside the current sheet, the fringes form an undisturbed background pattern. The second frame, at $t = 0$, is shown in an enlarged form in Fig.5.2.2. The upper third of the plasma column has pinched to a narrow filament, ~0.2 cm in diameter, which is being disrupted by sausage-type instabilities.

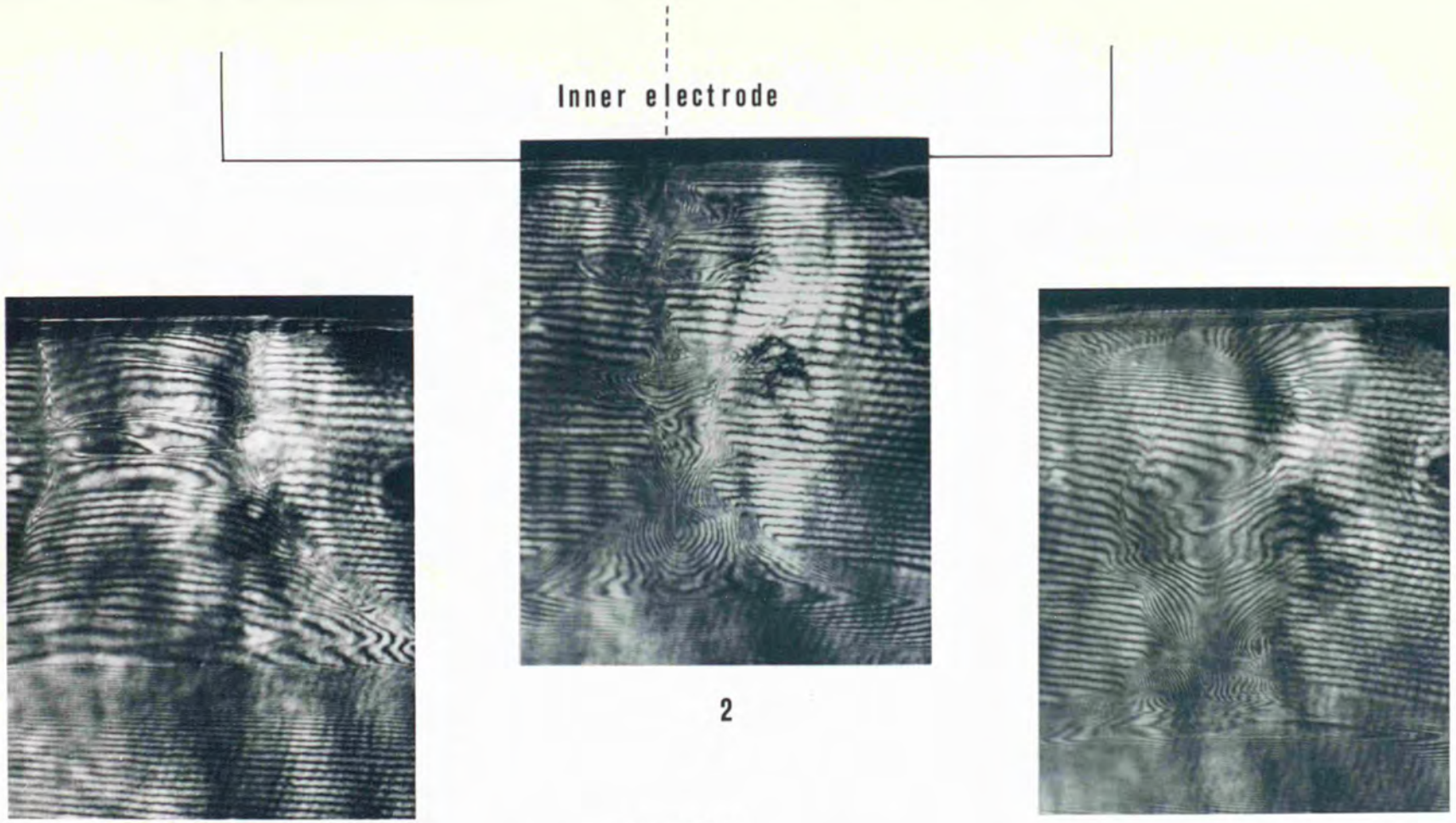

Fig.5.2.1

Time sequence of interferograms at $t = -30$, 0 and $+30$ nsec. Inner electrode diameter 5 cm. Initial conditions V = 30 kV, p_o = 2.5 torr (D_2 + 4% Ar)

Fig.5.2.2

Interferogram of discharge at t = 0. Initial conditions
V = 30 kV, p_o = 2.5 torr (D_2 + 4% Ar)

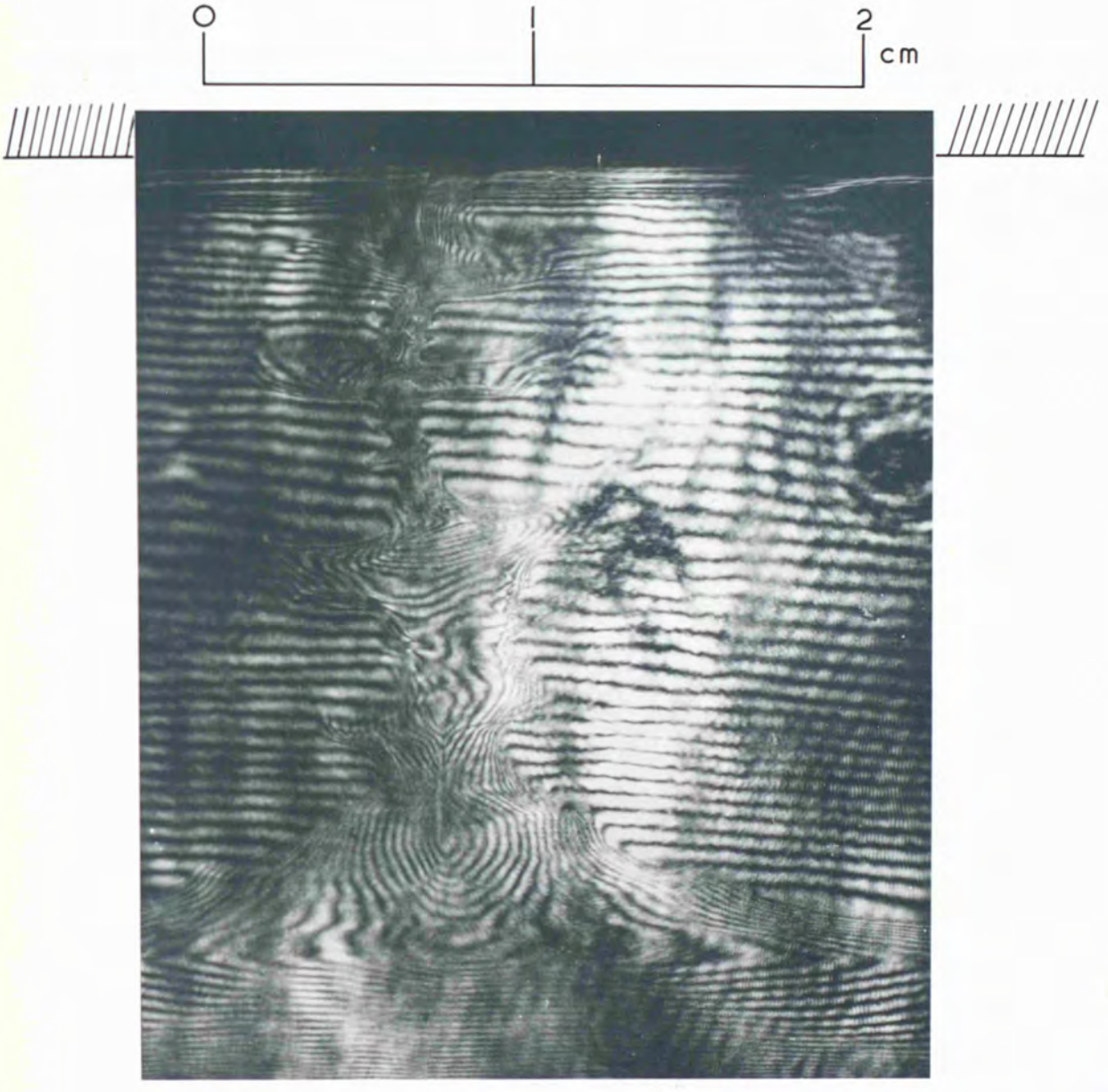

In some parts of the filament the fringes cannot be observed clearly, possibly due to fringe crowding or plasma motion. The whole plasma column exhibits the early stages of a kink-type instability. In the third frame of Fig.5.2.1, the dense pinch has completely broken up at $t = +30$ nsec. Near the electrode surface, the pinch has become very diffuse, while further away there appears to be no plasma. The lower third of the frame shows a plasma column apparently unaffected by the disruption of the upper portion, and still undergoing compression.

Each frame of this time sequence was obtained on a separate discharge. The sequence is representative of the interferograms obtained under the initial conditions given above. Approximately 20 interferograms were obtained at many times during the interesting stages of the discharge. Several interferograms were taken using the widest field of view possible; that permitted by the output aperture of the discharge chamber. No new phenomena were observed using this field of view of 4.3 cm wide by 4 cm.

Attempts were made to obtain interferograms using a pure deuterium filling in the Plasma Focus. However, the shot-to-shot jitter was $\sim \pm 50$ nsec, and many unrewarding exposures were made.

By analysing the fringe shifts on interferograms taken at different times during the discharge, it was possible to obtain values of n_e throughout the plasma lifetime.

5.3 SHADOWGRAPHY

5.3.1 Preliminary Results

The system used to obtain the shadowgrams is described in section 4.3.1. Using the simple Q-switched ruby oscillator, described in section 4.2.1, as light source, no shadowgrams of good definition could be obtained at any time during the life of the rapidly-moving plasma. However, some

hundreds of nanoseconds after the disruption of the dense pinch, electrode material crossed the field of view sufficiently slowly to permit shadowgrams of good resolution to be taken, during the 30 nsec exposure. This material was spalled from the anode by electron bombardment.

Figure 5.3.1 shows a time sequence of three shadowgrams, each taken during a separate discharge. The initial conditions were $V = 30\,kV$ and $p_o = 2.5\,torr$ $(D_2 + 4\%\ Ar)$. The shadowgrams were taken at the times $+160$, $+350$ and $+890\,nsec$, respectively. The movement of the spallation front across the field of view can be seen.

It is a simple matter to calculate the spallation velocity of the electrode material. In the 540 nsec time interval between frames 2 and 3, the material has moved axially $\sim 0.3\,cm$. Thus, the axial velocity of the front is $\sim 5.3 \times 10^5\,cm\,sec^{-1}$.

5.3.2 Results Using the Nanosecond Light Source

Using the nanosecond light source, many shadowgrams of the discharge were obtained under the initial conditions $V = 30\,kV$ and $p_o = 2.5\,torr$ $(D_2 + 4\%\ Ar)$. Fig.5.3.2 shows a shadowgram taken at $t = 0$. The outline of the plasma-vacuum boundary is very sharp, indicating that at this location there is a steep change in the electron density gradient. Diffraction patterns can be seen at the boundary in some parts of the photograph. Near the anode surface, the plasma has pinched to a narrow filament of diameter $\sim 0.1\,cm$ while, further away, the plasma column is $\sim 0.5\,cm$ in diameter and exhibits the early stages of the development of MHD instabilities.

Because of the irreproducibility of the discharge from shot-to-shot, it was impossible to study the dynamics of the plasma column with sufficient precision using a composite time-sequence, i.e. a sequence in which each frame was obtained during a separate discharge. This was overcome by using a system which permitted three exposures, each at a different

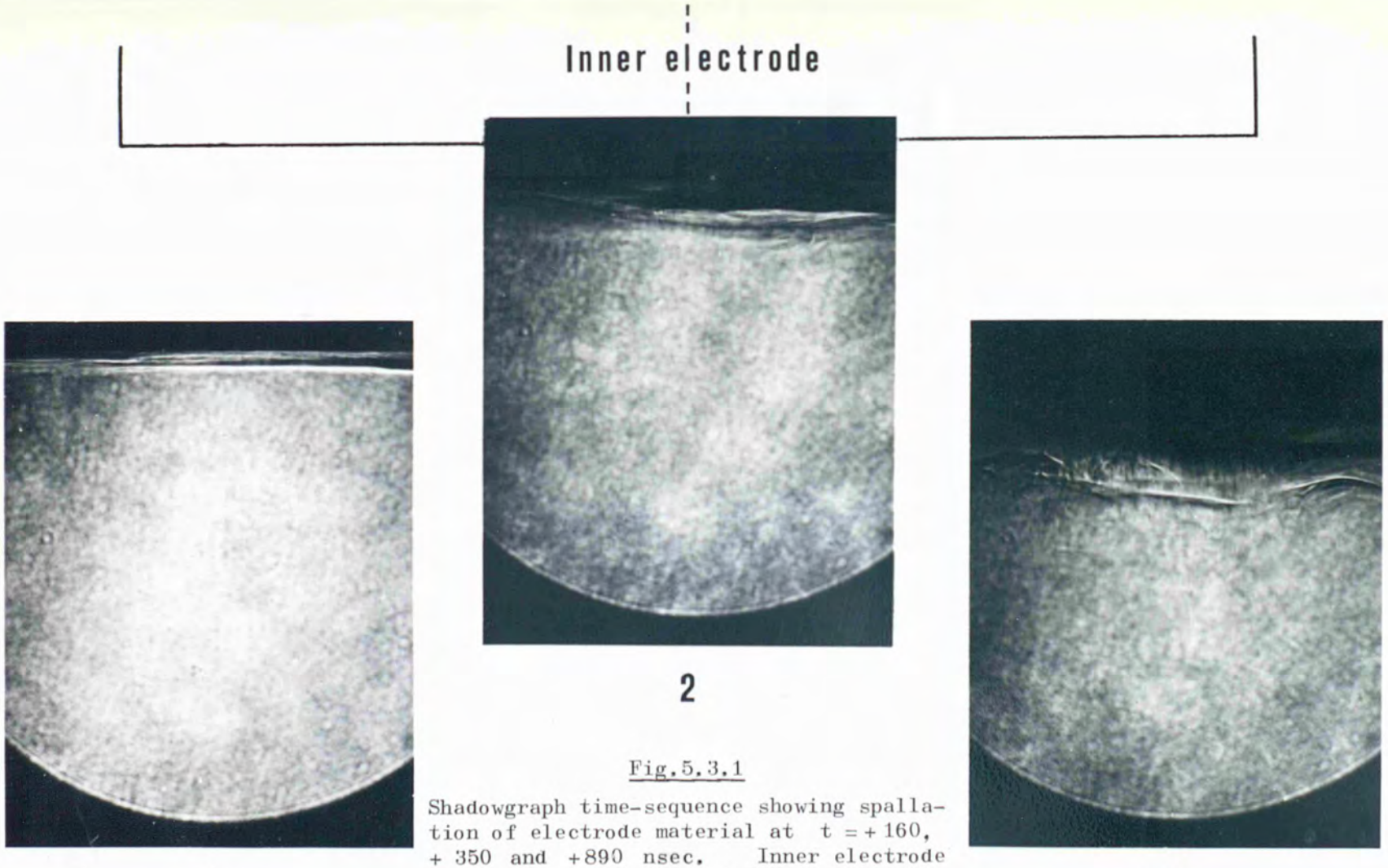

Fig.5.3.1

Shadowgraph time-sequence showing spallation of electrode material at t = + 160, + 350 and +890 nsec. Inner electrode diameter 5 cm. Initial conditions V = 30 kV, p_o = 2.5 torr (D_2 + 4% Ar)

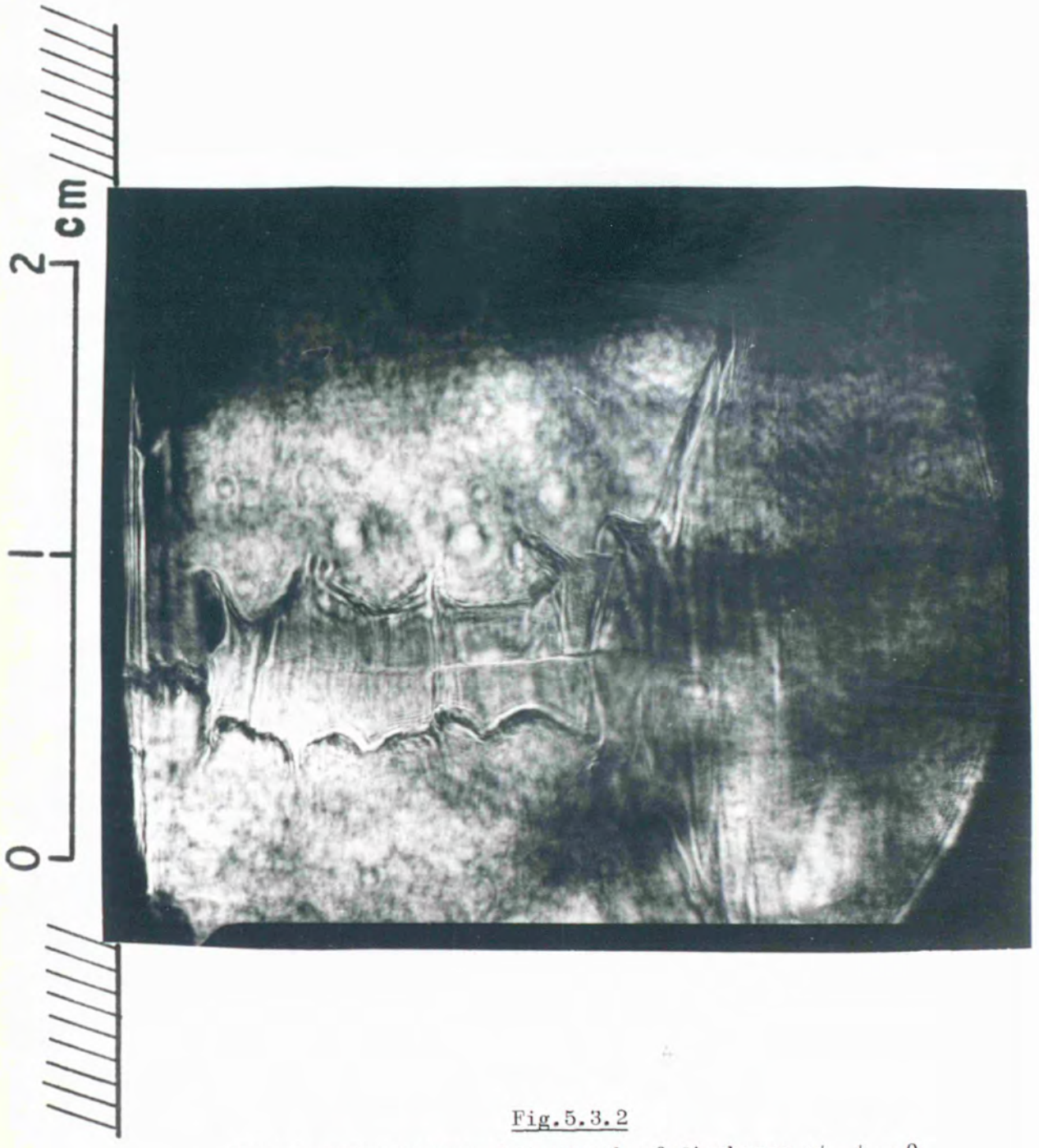

Fig.5.3.2

Nanosecond-exposure shadowgraph of discharge at $t = 0$.
Initial conditions $V = 30\,kV$, $p_o = 2.5\,torr$ $(D_2 + 4\%\ Ar)$

time, to be made during a single discharge , as described in section 4.3.1.

A time sequence taken during the collapse and pinch phases of a discharge, with a 15nsec interval between frames, is shown in Fig.5.3.3. The growth of acceleration-driven or Rayleigh-Taylor instabilities at the plasma-vacuum boundary during the collapse phase can be seen by comparing frames 1 and 2. Such time-sequences enabled the velocity and acceleration of the collapsing current-sheet to be calculated. Furthermore, the growth of instabilities could be directly measured.

Figure 5.3.4 shows a time sequence of shadowgrams during the dense pinch phase , with a time interval of 6.5nsec between frames. It is evident that, even on this rapid time-scale, there is considerable change in the boundary and structure of the pinch between frames. Such time-sequences during the dense-pinch phase were used to study the life history of the highly-compressed plasma regions.

Many shadowgram sequences were obtained at different times during the discharge, for a number of different voltages on the capacitor bank. A few good sequences were obtained using a filling of pure deuterium but, as in the interferometric studies, the shot-to-shot jitter generally proved troublesome.

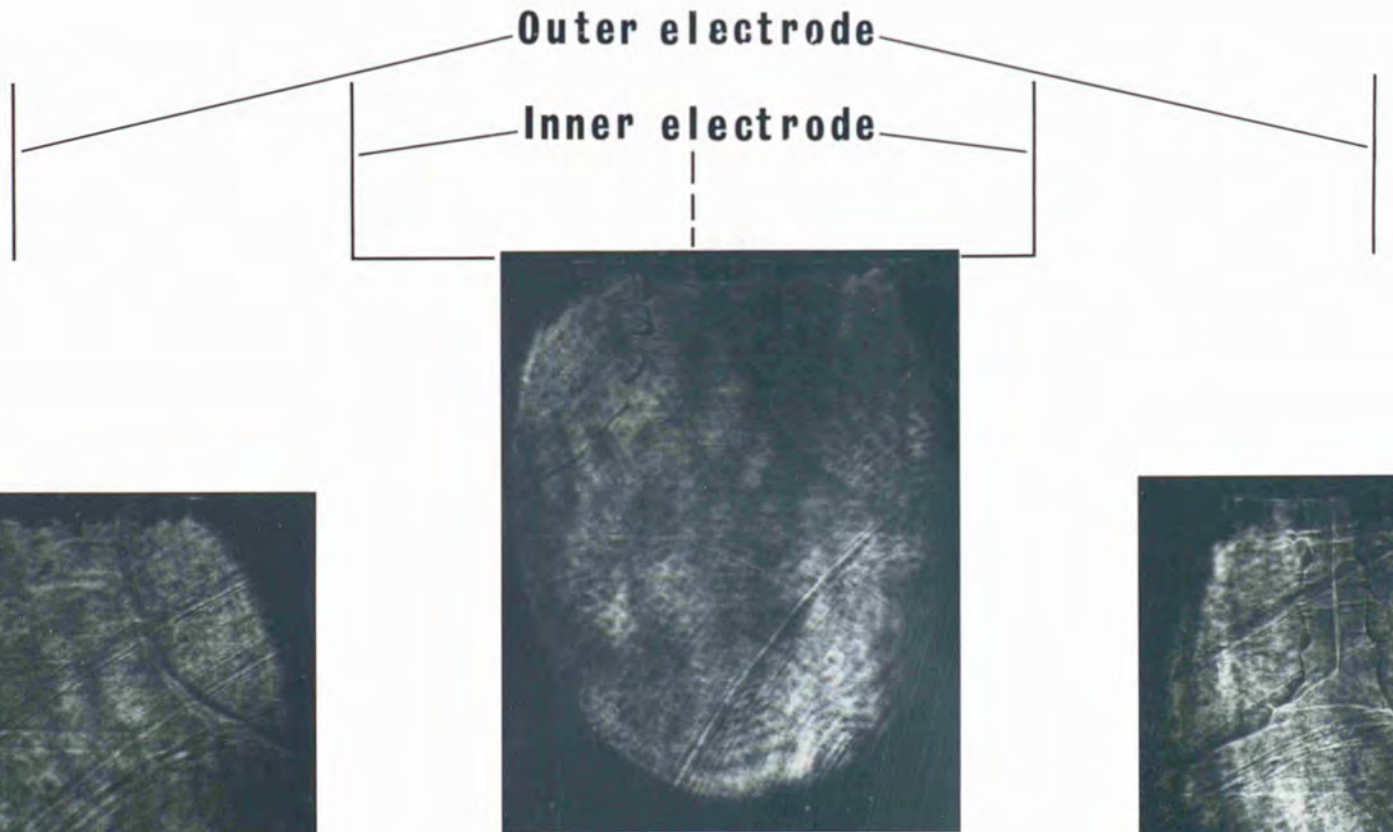

1

2

3

Fig.5.3.3

Shadowgram time-sequence during collapse and pinch phases. 15 nsec interval between frames. Inner electrode diameter 5 cm. Initial conditions V = 30 kV, p_o = 2.5 torr (D_2 + 4% Ar)

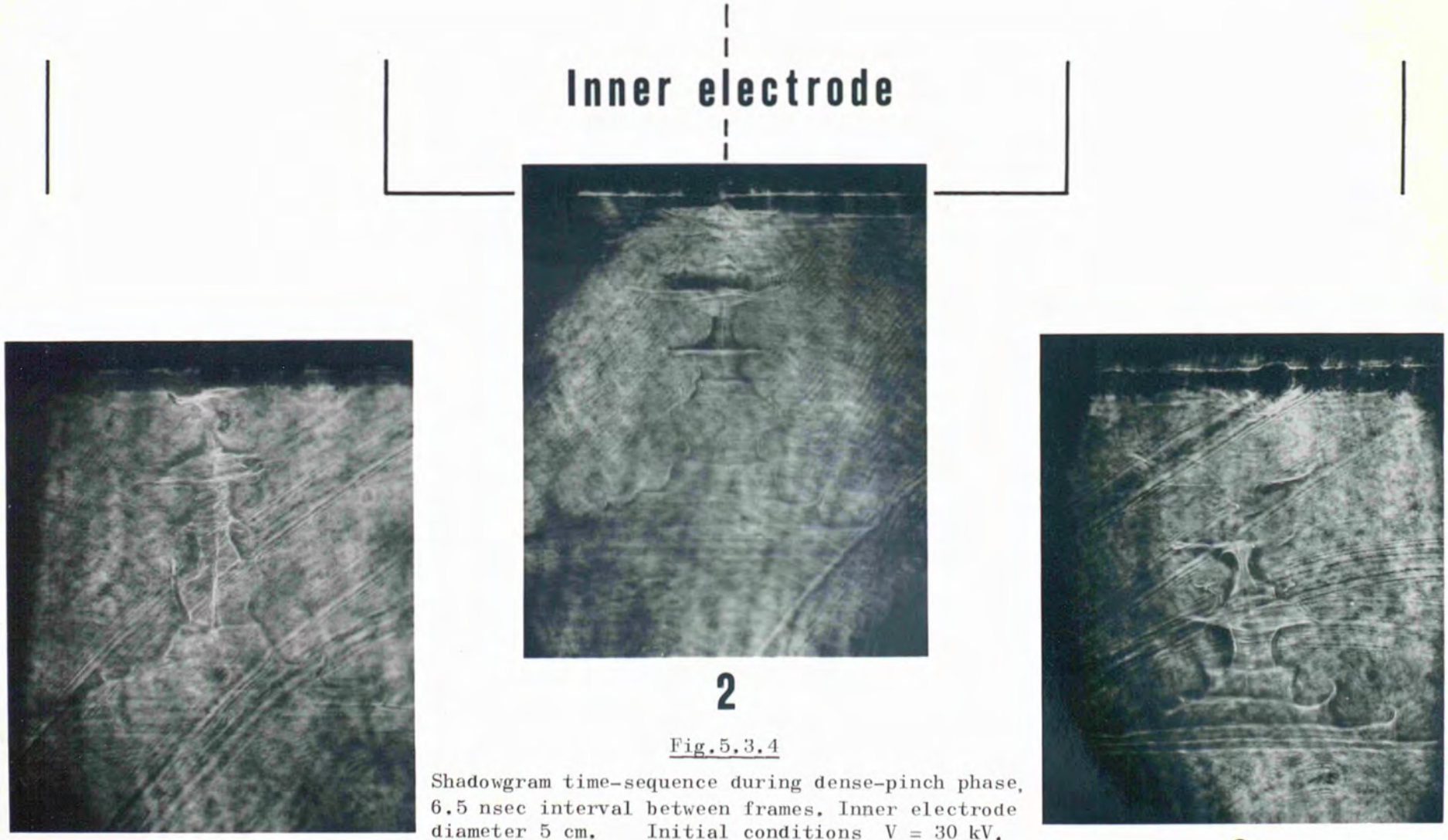

Fig.5.3.4

Shadowgram time-sequence during dense-pinch phase, 6.5 nsec interval between frames. Inner electrode diameter 5 cm. Initial conditions V = 30 kV, p_o = 2.5 torr (D_2 + 4% Ar)

CHAPTER VI

ANALYSIS OF RESULTS, INTERPRETATION AND DISCUSSION

The results presented in Chapter V are analysed in detail, their significance is discussed and they are compared with results from other studies. The chapter is divided into schlieren, interferometric and shadowgraph analyses.

6.1 ANALYSIS OF SCHLIEREN RESULTS

6.1.1 Results from Early Studies

When a mode-locked laser was used as light source, as described in section 5.1.1, many schlieren images, each produced by a separate pulse from the mode-locked train, were superimposed on every record obtained. Clearly, it was impossible to determine the density gradients on such records by measuring the light intensity changes, as given by equation (3.3.10). However, from the observed values of maximum beam deflection by the plasma, estimates of the peak electron density in the plasma were made.

It is assumed that the plasma is azimuthally symmetric, i.e. in cylindrical coordinates $n_e = \text{func}(r,z)$, and that $dn_e/dr \gg dn_e/dz$. Hence, when the schlieren obstacles of larger diameter were used, the light recorded on the film was due to the radial density gradients only. (The validity of this assumption is later confirmed by interferometric measurements.) The problem is now reduced to one of deflections in planes normal to the plasma axis.

Consider such a plane through the plasma at a distance z below the anode surface. An incident laser beam is parallel to the y axis of a Cartesian coordinate system, Fig.6.1.1, and strikes the plasma a distance x from its axis. From equation (3.3.9), the deviation of the laser light due to the component of refractive index gradient in the x direction is

$$\alpha_x = 2 \int_0^y \frac{\partial}{\partial x} \ell n\, n(x,y)\, dy$$

where $2y$ is the path length through the plasma at position x. Taking the variable $r^2 = x^2 + y^2$, the above equation is transformed to give deflections in terms of the radial density gradient, i.e.

$$\alpha_x = 2x \int_x^R \frac{1}{n(r)} \frac{dn(r)}{dr} \frac{dr}{\sqrt{r^2-x^2}} ,$$

where R is the plasma radius at the axial position considered. Now, the electron density $n_e(r)$ may be related to $n(r)$ using equation (3.2.3).

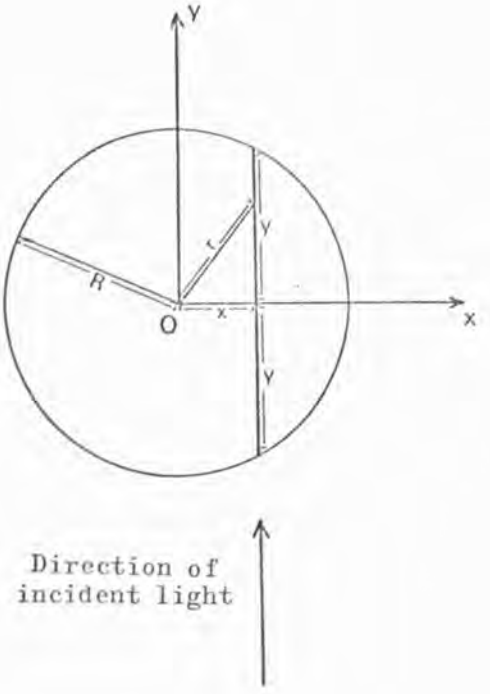

Fig.6.1.1
Schematic diagram representing the illumination of an azimuthally-symmetric plasma in a plane normal to its axis

Substituting this equation into the above equation, at $\lambda = 6943\text{Å}$,

$$\alpha_x = -\, 4.32 \times 10^{-22}\, x \int_x^R \frac{dn_e(r)}{dr} \frac{dr}{\sqrt{r^2 - x^2}} \quad \ldots \quad (6.1.1)$$

In the above, $n(r) \approx 1$ for $n_e(r) \leqslant 10^{20}\ \text{cm}^{-3}$.

Choosing an arbitrary electron density profile, i.e. $n_e = \text{func}(r)$ where the function is arbitrary, equation (6.1.1) may be integrated to yield values of α_x equal to those observed, allowing estimates of $n_e(r)$ to be made. The equation may either be integrated analytically or numerically, depending upon the form of the profile chosen.

The method is illustrated for the case of a parabolic radial distribution of n_e, i.e.

$$n_e(r) = \hat{n}_e(1 - r^2/R^2) ,$$

where $\hat{n}_e$ is the electron density on axis. Combining this equation with equation (6.1.1):

$$\alpha_x = K \int_x^R \frac{r\,dr}{\sqrt{r^2 - x^2}} ,$$

where $K = 8.64 \times 10^{-22}\ \hat{n}_e\ x/R^2$. The above integral may be evaluated on making the substitution $r = x \sec\theta$. Hence,

$$K \int = K x \Big[\tan\theta\Big]_0^{\sec^{-1}(R/x)} ,$$

$$\alpha_x = K R \sqrt{R^2 - x^2} .$$

If x is expressed as a fraction f of R, i.e. $x = f R$,

$$\alpha_x = 8.64 \times 10^{-22}\ \hat{n}_e\ f\sqrt{1 - f^2} . \qquad \ldots (6.1.2)$$

The above equation is independent of R. Thus, the deflection due to the radial electron-density gradient in an azimuthally-symmetric plasma, with a parabolic radial distribution of n_e, is independent of the plasma radius and depends only on $\hat{n}_e$ and f. Fig.6.1.2 shows a plot of α_x against f for three values of $\hat{n}_e$, such as would be found during the dense-pinch phase. Each curve has a maximum at $f \approx 0.7$, i.e. for a given value of $\hat{n}_e$, the maximum deflection of the light beam occurs for those rays which are incident on the plasma a distance $x \approx 0.7\,R$ from the axis.

More precisely, α_x is a maximum for a given value of $\hat{n}_e$ when $d\alpha_x/df = 0$ in equation (6.1.2), i.e.

$$d\alpha_x/df = 0 = 8.64 \times 10^{-22}\ \hat{n}_e \Big[(1 - f^2)^{\frac{1}{2}} - f^2(1 - f^2)^{-\frac{1}{2}}\Big] .$$

This occurs when $f = 1/\sqrt{2}$, giving $\alpha_x(\max) = 4.32 \times 10^{-22}\ \hat{n}_e$. Hence,

$$\hat{n}_e = \alpha_x(\max)/4.32 \times 10^{-22} . \qquad \ldots (6.1.3)$$

Other electron-density profiles may be chosen, and used in equation (6.1.1) to yield an expression for $\hat{n}_e$. Using a linear distribution, i.e. $n_e(r) = \hat{n}_e(1 - r/R)$, and proceeding in the same manner as previously, we obtain

$$\alpha_x = 4.32 \times 10^{-22}\ \hat{n}_e\ f\,\ell n\Big[(1 + \sqrt{1 - f^2})/f\Big] ,$$

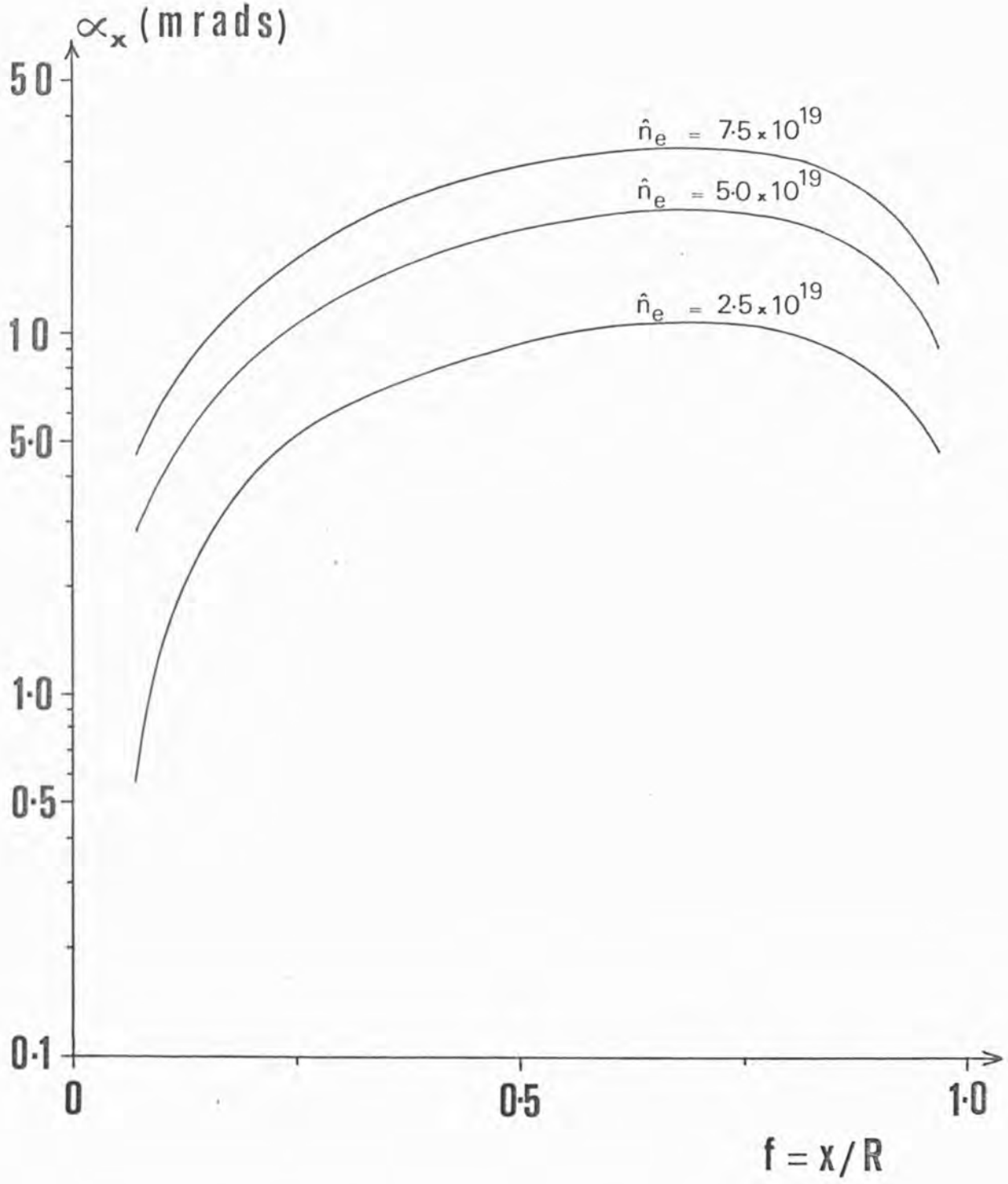

Fig.6.1.2

Deflection of a light beam passing through an azimuthally-symmetric plasma. See text for significance of parameters

giving

$$\hat{n}_e = \alpha_x(\max)/2.86 \times 10^{-22} \ . \qquad \ldots (6.1.4)$$

Choosing a Gaussian profile $n_e(r) = \hat{n}_e \exp(-Cr^2/R^2)$, where the factor C is chosen so that $n_e(R) = 10^{-5}\,\hat{n}_e$, equation (6.1.1) is integrated numerically. Using a range of values of $\hat{n}_e$ and f, a combination of the two is found which gives a value of α_x equal to the observed value, with $d\alpha_x/df = 0$.

Referring to the results shown in Fig.5.1.2, the three frames were obtained at t = 0 using schlieren obstacles of diameter, d, 0.32, 0.64 and 1.27 cm, respectively, at the focus of a lens of focal length f = 50 cm. The minimum angle through which any light ray could be deflected and still be recorded on the film was $\alpha_x = d/2f$. Hence, using the values of α_x corresponding to the different obstacle diameters, the minimum peak-density for each of the three frames could be estimated, for the three density distributions considered. Also, the maximum value of $\hat{n}_e$ in the dense pinch could be estimated from the observations that a faint image was obtained with an obstacle of diameter 2.54 cm, but no image was obtained using an obstacle of diameter 2.86 cm. The results may be tabulated:

Table 6.1.1

d (cm)	α_x (mrad)	Was Image Observed at t = 0?	Calculated $\hat{n}_e(cm^{-3})$ at r = 0		
			Parabolic	Linear	Gaussian
0.32	$\geq$ 3.2	yes	$\geq 7.3\times10^{18}$	$\geq 1.1\times10^{19}$	$\geq 9.7\times10^{18}$
0.64	$\geq$ 6.4	yes	$\geq 1.5\times10^{19}$	$\geq 2.2\times10^{19}$	$\geq 1.9\times10^{19}$
1.27	$\geq$ 12.7	yes	$\geq 2.9\times10^{19}$	$\geq 4.4\times10^{19}$	$\geq 3.9\times10^{19}$
2.54	$\geq$ 25.4	yes	$\geq 5.9\times10^{19}$	$\geq 8.9\times10^{19}$	$\geq 7.8\times10^{19}$
2.86	< 28.6	no	$< 6.6\times10^{19}$	$< 1.0\times10^{20}$	$< 8.8\times10^{19}$

Thus, for example, considering frame 3 of Fig.5.1.2, which was obtained using an obstacle of diameter 1.27 cm, since images of the plasma were produced, the electron density on axis must have been at least 2.9×10^{19},

4.4×10^{19} or 3.9×10^{19} cm^{-3} for the case of a parabolic, linear or Gaussian density distribution, respectively.

For any of the above obstacle diameters, there is a maximum difference of $\sim 32\%$ between the highest and lowest values of $\hat{n}_e$ calculated using the three radial profiles. Thus, the calculated value of $\hat{n}_e$ is not unduly sensitive to the profile chosen. At maximum compression in the pinch, the average value of $\hat{n}_e$ was $\sim 8 \times 10^{19}$ cm^{-3}.

Mather (1965b) has applied a schlieren technique, similar to that described in section 4.3.2, to the Plasma Focus. The main difference was that a laser pulse duration of ~ 100 nsec was used, resulting in poor temporal resolution. From the observed deflections, and assuming a rod-shaped plasma with a linear electron-density profile, a minimum value of n_e on axis of $\sim 10^{19}$ cm^{-3} was estimated at maximum compression, in a device for which $C = 90$ μF, $V = 20$ kV and $p_o \simeq 2.0$ torr D_2. A maximum value of $\hat{n}_e$ was not determined.

The values of n_e derived in this section cannot be regarded as more than estimates of the peak densities attained during the dense-pinch phase, because of the models used to derive these values. Nevertheless, for a first attempt at measuring n_e during a Plasma Focus discharge, the schlieren technique has proved useful.

6.1.2 Results Obtained with the Nanosecond Light Source

It is possible to determine values of electron density from schlieren records obtained using a spherical or circular obstacle, provided the density gradient in one direction in a plane in the plasma transverse to the illuminating beam is much larger than the gradient in any other direction in that plane.

Consider a schlieren system in which a circular light source is used, whose undisturbed image of radius r_s, at the focus of the schlieren lens,

is covered by a circular opaque stop of radius r_o, where $r_o > r_s$. Thus, the system transmits no light to the recording film. However, any shift of the source image by an amount $h > (r_o - r_s)$ will produce an illumination whose intensity, I, is proportional to $r_s[h - (r_o - r_s)]$. In the case of the test object being an azimuthally-symmetric plasma with $dn_e/dr \gg dn_e/dz$, and for the same illuminating geometry as given in Fig. 6.1.1, the illumination on the film is

$$I(x) \propto r_s f \alpha_x - r_s(r_o - r_s) ,$$

where f is the focal length of the schlieren lens and α_x is the deflection of the light by the plasma, i.e. $h = f \alpha_x$. Combining the above with equation (6.1.1)

$$I(x) = -4.32 \times 10^{-22} r_s f x K \int_x^R \frac{dn_e(r)}{dr} \frac{dr}{\sqrt{r^2 - x^2}} - K r_s(r_o - r_s).$$

In the above equation, K relates the light intensity reaching the film to the radial density gradient in the plasma, for a given obstacle diameter and incident beam power. K is determined experimentally by calibrating the film using a number of known refractive-index gradients. The above equation may then be inverted by applying Abel's integral transform, and the resulting equation is integrated numerically to yield the radial electron-density distribution from the absolute intensity on the schlieren records, Weyl (1955). However, the absolute electron density at one point in the plasma must first of all be known. This value would usually be determined by an interferometric measurement.

The schlieren technique was found to be valuable in determining the location of steep electron-density gradients in the Plasma Focus discharge. However, to obtain quantitative values of density the interferometric technique was preferable as it measures n_e directly.

6.2 INTERFEROMETRIC RESULTS

6.2.1 Analysis of Fringe Shifts

The inteferograms obtained at various times during the discharge, section 5.2, were analysed using enlarged prints having a real space magnification of 12–15. From a study of interferograms taken using the maximum possible field-of-view, it was found that the fringe pattern obtained with a static gas filling in the discharge chamber was not measureably different to the pattern obtained outside the plasma volume during a discharge. Thus, the latter fringes were used as undisturbed reference fringes when evaluating the fringe shifts due to the plasma.

A fringe-shift distribution was obtained by selecting an undisturbed reference fringe at a certain location on an interferogram, equivalent to a distance z from the anode, and drawing a line through the region of disturbance as a continuation of the fringe. This line was normal to the gun axis and it cut the displaced fringes at varying intervals. The position, x, of the fringes at the points of intersection, relative to the axis, could be measured, together with the displacement, s , of the fringes from their undisturbed positions. In Fig.6.2.1, a sequence of three fringe-shift distributions, obtained during the collapse, dense-pinch and break-up phases at - 70, 0 and + 20 nsec, respectively, is shown.

To obtain the radial electron-density profile from a fringe-shift distribution, a modified form of equation (3.3.21) must be solved. The plasma produced during a Plasma Focus discharge is, to a good approximation, azimuthally symmetric, i.e. $n_e = \text{func}(r,z)$. Consider a plane through the plasma normal to the gun axis, at a distance z below the anode. Laser light is incident in the y direction, as shown in Fig.6.1.1. The fringe shift caused by light traversing the plasma at any position x is from equation (3.3.21)

$$s(x) = - \frac{2}{3.2\times10^{17}} \int_0^y n_e(x,y)\, dy \ ,$$

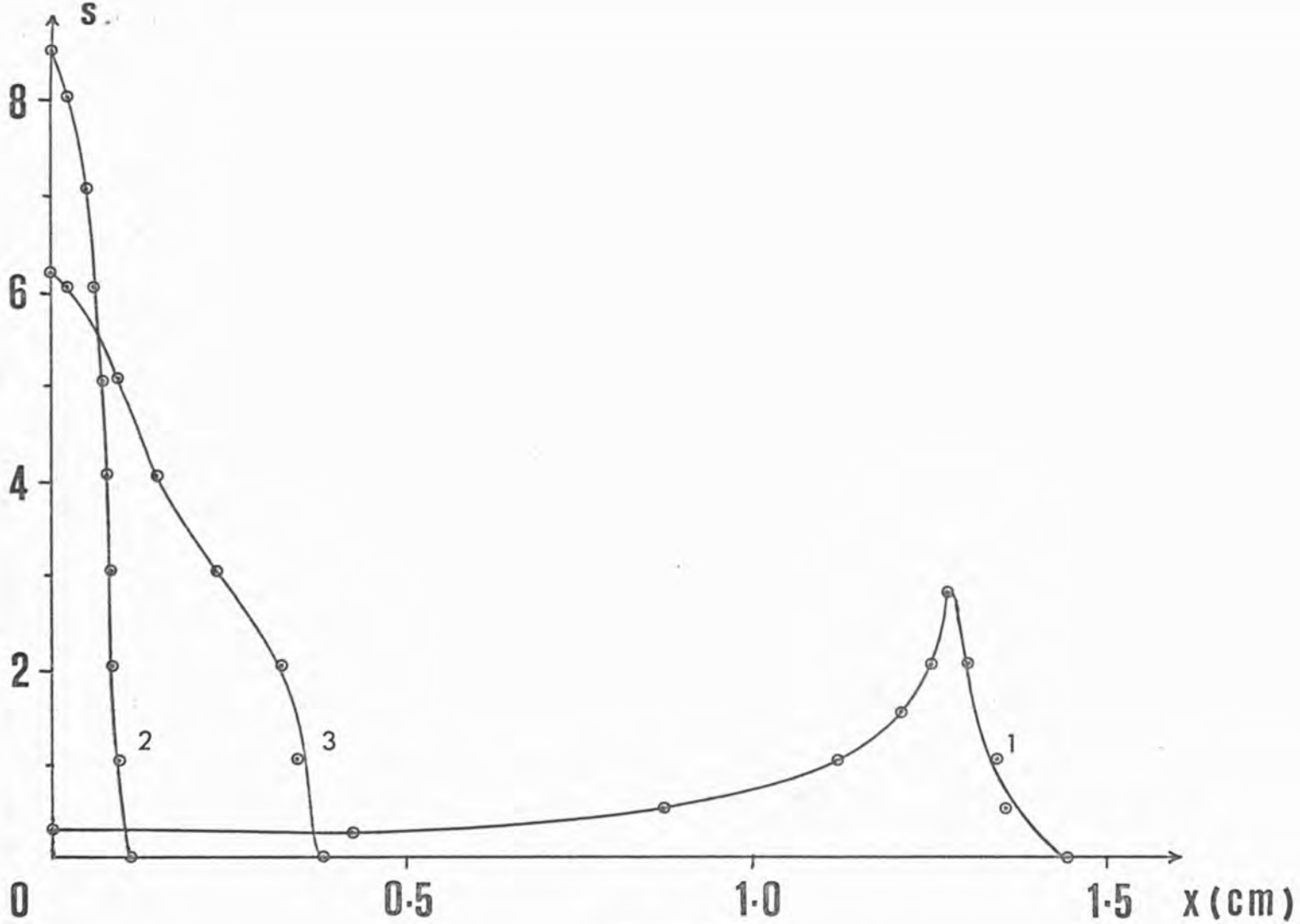

Fig.6.2.1

Fringe-shift distributions during the collapse (1), dense-pinch (2) and break-up (3) phases of a discharge, at $z \sim 0.5$ cm. Initial conditions V = 30 kV, p_o = 2.5 torr (D_2 + 4% Ar)

where $2y$ is the path length through the plasma. Expressing the electron density in cylindrical coordinates by using the variable $r^2 = x^2 + y^2$,

$$s(x) = -\frac{2}{3.2\times10^{17}} \int_x^R n_e(r) \frac{r\,dr}{\sqrt{r^2 - x^2}} . \qquad \ldots (6.2.1)$$

To obtain the radial electron-density profile, $n_e(r)$ versus r, the above equation is inverted using the Abel integral transform, Bennett et al (1952). Thus,

$$n_e(r) = \frac{3.2\times10^{17}}{\pi} \int_r^R \frac{ds(x)}{dx} \frac{dx}{\sqrt{x^2 - r^2}} . \qquad \ldots (6.2.2)$$

Except in cases where $s(x)$ is a simple analytic function, equation (6.2.2) cannot in general be solved analytically. The integral may be evaluated numerically using the method of Bockasten (1961). A fringe-shift distribution, $s(x)$ versus x, consists of a number of points through which a best-fit curve may be drawn. From this curve, a sequence of values s_k may be taken for equidistant x values, $x_k = kR/n$ $(k = 0, 1, 2, \ldots, n-1)$ where R is the plasma column radius at axial position z. From these s_k values, a number of values of $n_e(r)$, designated $(n_e)_j$ and corresponding to $r_j = j\,R/n$ $(j = 0, 1, 2, \ldots, n-1)$, may be calculated using the formula

$$(n_e)_j = R^{-1} \sum_k a_{jk}\, s_k , \qquad \ldots (6.2.3)$$

where a_{jk} are certain tabulated coefficients. Bockasten gives tables of coefficients for $n = 10$, $n = 20$ and $n = 40$ $(j \geq 30)$, the last set enabling accurate evaluations at the edge of the distribution to be made.

Using this numerical method, the fringe-shift distributions obtained from the interferograms were analysed to yield radial electron-density profiles.

Figure 6.2.2 shows an isometric projection of radial electron-density profiles during the collapse, dense-pinch and break-up phases of the discharge. The Plasma Focus was operated under the initial conditions $V = 30\,kV$ and $p_o = 2.5\,torr$ $(D_2 + 4\%\ Ar)$. There is a small spread of

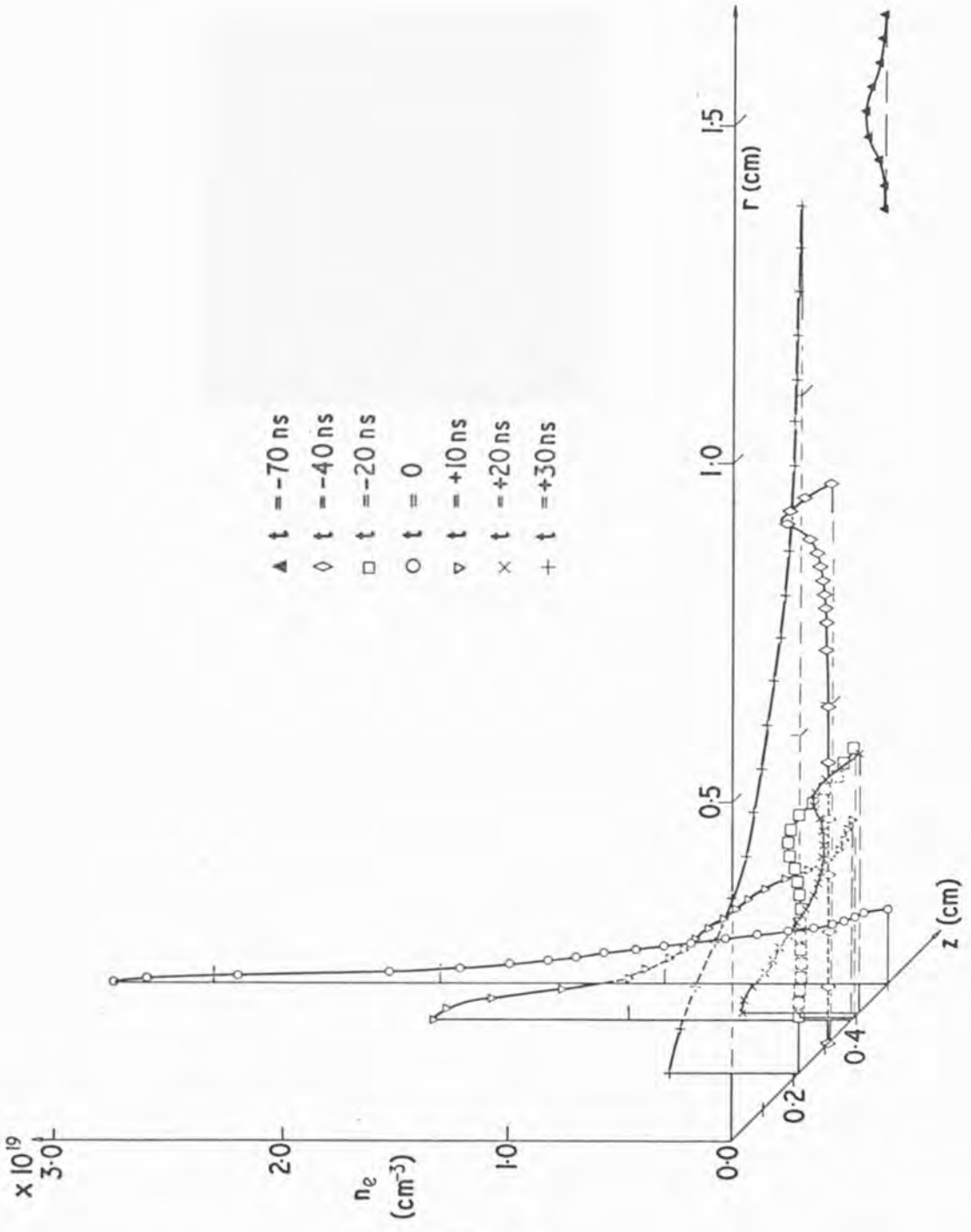

Fig.6.2.2

Radial electron-density profiles at various times during a discharge. Initial conditions V = 30 kV, p_o = 2.5 torr (D_2 + 4% Ar)

~ 0.3 cm in the axial position of the profiles because, on the corresponding interferograms, regions of plasma column unaffected by instabilities were chosen for analysis.

Firstly, the profiles at -70, -40 and -20 nsec, during the collapse phase, are examined. The inwardly-collapsing current-sheet at $t = -70$ nsec is sharply defined, with peak electron density $\sim 9 \times 10^{17}$ cm^{-3}. At this early stage, no electron concentration is detectable within the volume enclosed by the current sheet, of radius ~ 1.4 cm. In the profile at $t = -40$ nsec, the imploding shock is still well defined, with peak density $\sim 2 \times 10^{18}$ cm^{-3}, but a small electron concentration ($\sim 4 \times 10^{16}$ cm^{-3}) can now be detected within the enclosed volume. At $t = -20$ nsec, the profile shows that n_e on axis has increased to almost equal the peak value, $\sim 3 \times 10^{18}$ cm^{-3}, occurring at the plasma-vacuum boundary. In these three profiles, the peak electron density at the plasma-vacuum boundary varies rather slowly with time, increasing by a factor of ~ 3.4 in 50 nsec. On the other hand, on axis there is a rapid increase in n_e during this period. Over the 20 nsec interval between the last two profiles, n_e increases by a factor of ~ 75.

When the implosion reaches the axis of symmetry at $t = 0$, the profile is no longer hollow, i.e. the peak electron density of $\sim 3.4 \times 10^{19}$ cm^{-3} is on axis. The steepest density gradient in the dense pinch, of diameter ~ 0.2 cm, is adjacent to the axis.

The remaining profiles of Fig.6.2.2 are during the break-up phase. The pinched column rapidly expands in a few tens of nanoseconds, e.g. the profile at $+30$ nsec shows a very diffuse plasma-vacuum boundary, the column radius being ~ 1.3 cm. However, after the dense-pinch phase the radial density-profiles show much less shot-to-shot reproducibility, at a given axial location, than before the dense pinch. This is due to the

presence of long-wavelength MHD instabilities, principally of sausage (or $m=0$) type, which grow with a randomness in space and time, disrupting the dense pinch. Thus, two very different profiles can be obtained at the same position z from successive shots if, on one shot, the 'neck' of an instability occurs at that position and, on the other, the 'shoulder' occurs. This explains the apparent extreme velocity with which the plasma column has expanded in the ten nanosecond interval between the last two profiles.

In Fig.6.2.3, an isometric projection of radial-density profiles obtained from different axial positions on the same interferogram is shown. The interferogram was taken at $t=0$, with the initial conditions $V=30\,kV$ and $p_o = 2.5\,torr$ $(D_2 + 4\%\ Ar)$. In each profile the peak electron density occurs at the axis. The maximum on-axis density, $\sim 3.4 \times 10^{19}\ cm^{-3}$, occurs in the profile of smallest radius, and the minimum on-axis density, $\sim 1.0 \times 10^{19}\ cm^{-3}$, is found in the profile of largest radius, i.e. in general, the smaller the radius of the plasma column the higher its compression. Furthermore, the radial electron-density gradients are much steeper than those in the axial direction. The steepest radial gradient is $\sim 1.2 \times 10^{21}\ cm^{-4}$, while the steepest axial gradient is $\sim 3.2 \times 10^{19}\ cm^{-4}$. Thus, in the evaluation of the schlieren results (section 6.1.1), the assumption that the axial gradients of n_e could be neglected in comparison with the radial gradients was justified.

As discussed in section 5.2, a few interferograms were obtained using a pure deuterium filling of pressure 3.4 torr with a bank voltage of 30 kV. This deuterium filling had the same specific gravity as the D_2/Ar mixture more usually used, giving the same run-down time during a discharge. Because of the shot-to-shot jitter, few good interferograms were obtained. Fig.6.2.4 shows an isometric projection of radial profiles of n_e, obtained at different axial positions on the same interferogram at $t=0$. The

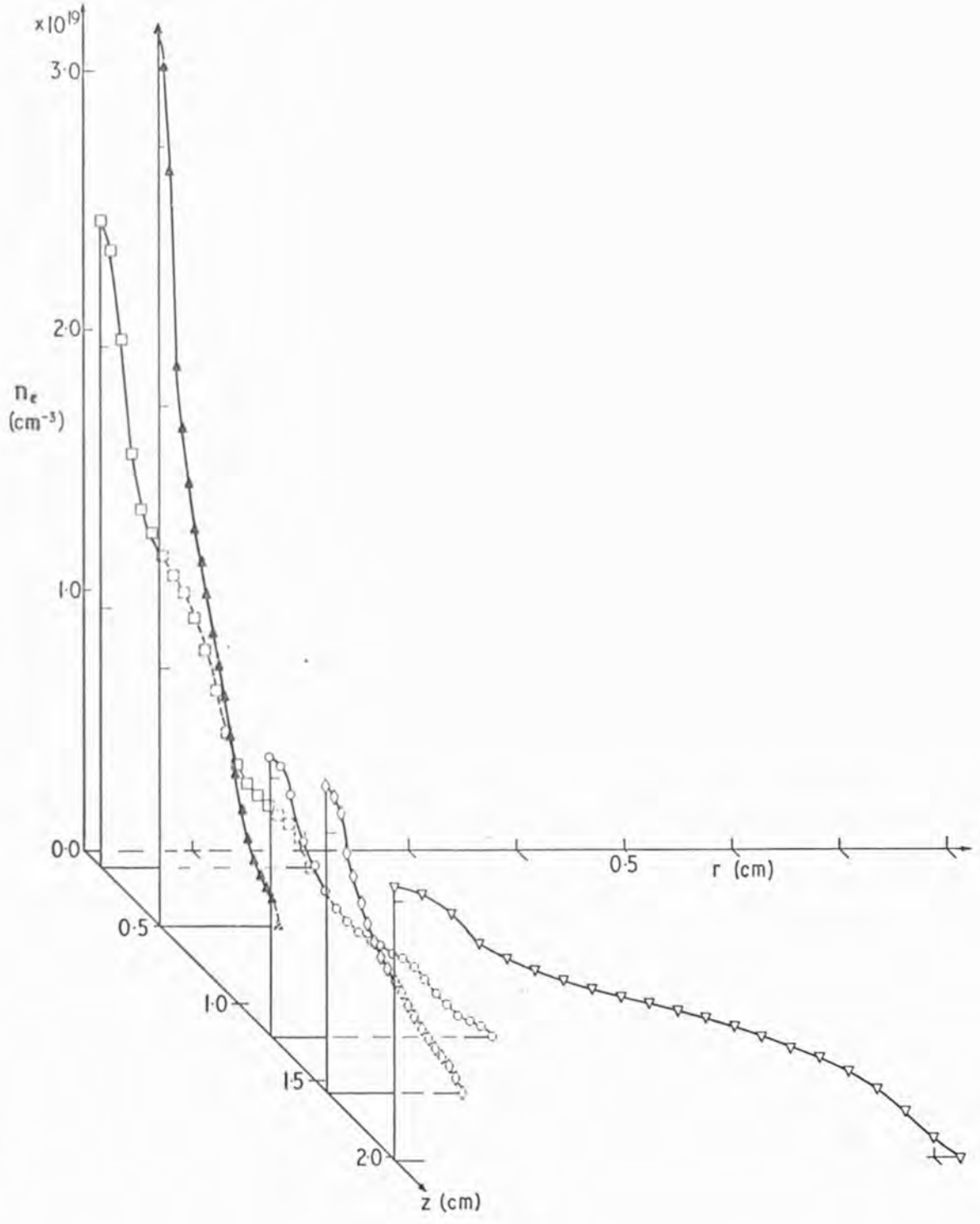

Fig.6.2.3

Radial electron-density profiles at $t = 0$, showing dependence on axial position. Initial conditions $V = 30\,kV$, $p_o = 2.5\,torr$ ($D_2 + 4\%\ Ar$)

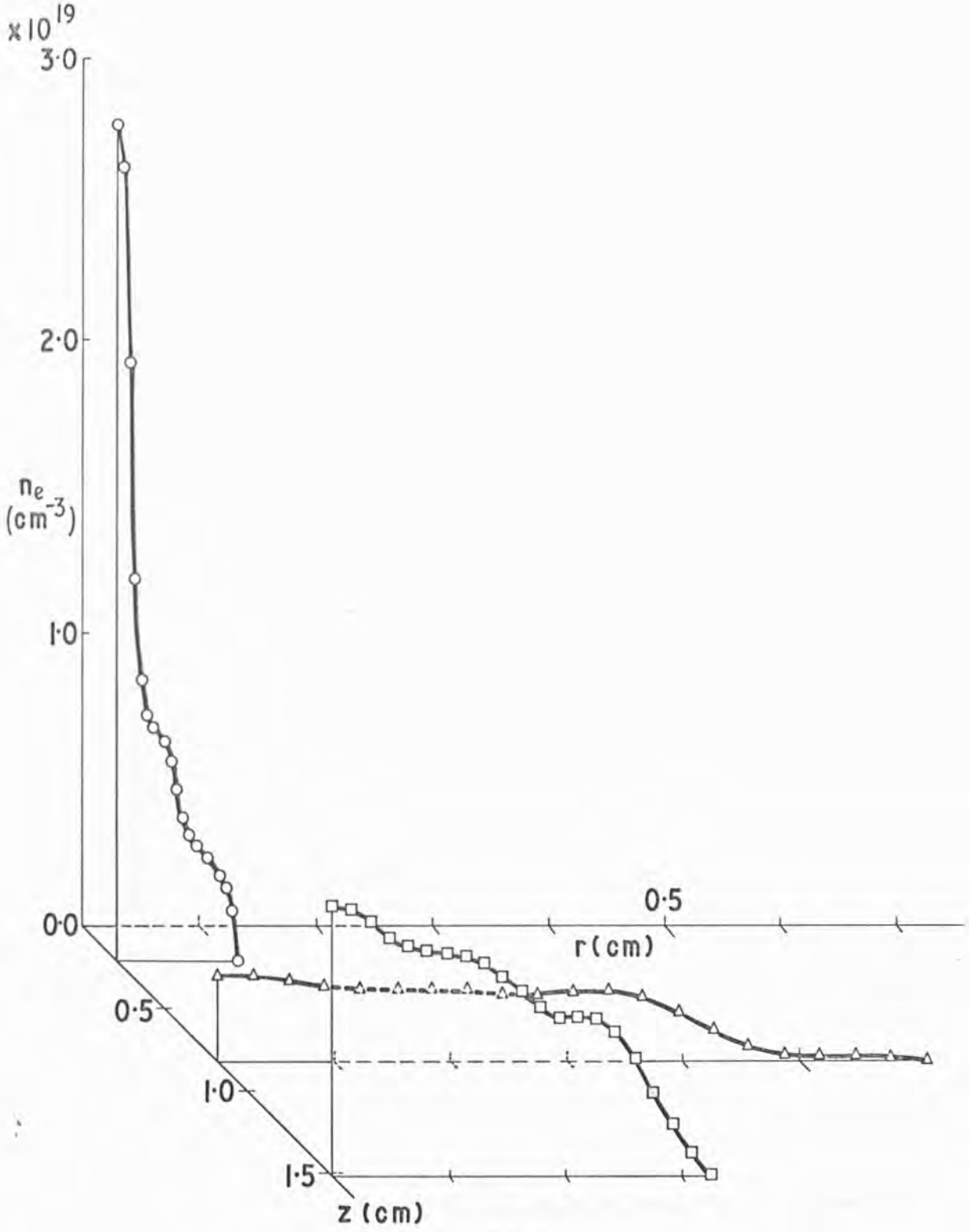

Fig.6.2.4

Radial electron-density profiles at $t = 0$, showing dependence on axial position. Initial conditions $V = 30\,kV$, $p_o = 3.4$ torr D_2

profile having the smallest radius, ~0.1 cm, has a dense central core rising to a peak density of $\sim 3 \times 10^{19}$ cm^{-3}, with the outer 2/3 of the column being more diffuse. The general form of the profiles is similar to that of the profiles obtained using the D_2/Ar mixture.

6.2.2 Assessment of Errors

The values of electron density obtained from the interferograms were, of course, subject to a variety of errors. These errors may be divided into six classes:

(a) Errors in the fringe shifts obtained from the interferograms, due to inaccuracies in measuring the fringe positions.

(b) Errors in the fringe shifts due to optical imperfections in the system causing spurious shifts.

(c) Errors in the fringe shifts due to displacement of the background fringes as a result of the laser beam traversing the return current-sheet to the outer electrode.

(d) Errors in the fringe shifts caused by non-electron refractivity in the plasma.

(e) Errors in the fringe shifts due to distortions caused by refractive index gradients in the plasma.

(f) Errors in the calculated values of $n_e(r)$ caused by inaccuracies in the numerical method of analysis.

These errors are considered in turn:

(a) When using prints of the interferograms giving a real space magnification of 12-15, the position of a fringe centre could be determined with a standard deviation of 0.025 cm. With the background fringe spacing employed, this represents a standard deviation σ_1 of 0.04 of a fringe.

(b) To assess the effects of optical imperfections in the system, an interferogram of background fringes only was used. Choosing five fringes at equal intervals over the whole interferogram, the deviation of each

fringe centre from linearity was measured at six points, separated by equal intervals, along the fringe. The standard deviation was 0.075 cm, i.e. $\sigma_2 = 0.12$ of a fringe.

(c) On every interferogram of the discharge, the fringe shifts are the result of the test beam having passed through the plasma column and, in addition, twice through the return current-sheet to the outer electrode end. The maximum width of the field of view being 4.3 cm, it was impossible to record the background fringes at a radial distance of 6 cm from the gun axis, i.e. outside the outer electrode (10 cm diameter) where the test beam would not traverse the return sheet. Referring to the fringe-shift distribution at $t = -70$ nsec in Fig.6.2.1, over the inner third of the distribution the fringe shift is constant at ~ 0.25. It is reasonable to suppose that the fringe-shift distribution due to the return current-sheet is similar to that of the collapsing current-sheet at early times, but of extent 5 cm in the x direction. Hence, on every interferogram, over the entire width of the field of view (normally 2.7 cm) extending axially from the anode end to the leading edge of the current sheet, the effect of the double traversal of the return current-sheet is to produce a uniform fringe-shift of 0.1 - 0.2 of a fringe. Because the fringe shift is uniform over the whole width of the plasma region, for reference and shifted fringes alike, the effect of the fringe shift is neglected.

(d) The refractivity due to non-electron species is discussed in section 3.2.3. It is shown that, of all non-electron species present in any plasma, the neutrals dominate. With reference to Fig.6.2.2, during a Plasma Focus discharge from $t \approx -30$ nsec onwards all deuterium particles present in the plasma will be ionized. The refractivity of excited argon ions can be neglected because of their low concentration. Thus, from $t \simeq -30$ nsec onwards no correction is necessary due to non-electron refractivity. However, at earlier times there are unionized deuterium and argon

atoms within the plasma volume enclosed by the collapsing current-sheet; their effect must be evaluated.

Using a field of view 2.7 cm wide, the maximum diameter of current sheet that could be accommodated on an interferogram was ~ 2.3 cm, allowing space for background fringes at the edges. Thus, on such interferograms, on axis the test beam has traversed a path of length $\ell = 2.3$ cm through the unionized atoms, while at the edge of the column this path length is zero. From Table 3.2.1, at $\lambda = 6943$ Å the specific refractivities of deuterium and argon atoms are $K_D = 4.24 \times 10^{-24}$ and $K_{Ar} = 1.05 \times 10^{-23} cm^3$. Assuming the same number density as given by the initial filling of 2.5 torr (D_2 + 4% Ar), then $n_D = 1.7 \times 10^{17}$ cm^{-3} and $n_{Ar} = 3.5 \times 10^{15}$ cm^{-3}. The refractive index of the mixture is given by $n - 1 = \Delta n = \sum_j n_j K_j = 7.2 \times 10^{-7}$. The fringe shift produced by this refractive mixture is $s = \ell \cdot \Delta n/\lambda = 0.025$. This is the maximum value, the minimum is zero. Thus, for profiles obtained for times before $t = -30$ nsec, the standard deviation is set to half this value, i.e. $\sigma_3 = 0.013$. For profiles obtained at times after this time, $\sigma_3 = 0$.

(e) For precise interpretation of the interferograms, the distortions to the fringe patterns due to angular deflections by electron-density gradients must be considered. From equations (3.3.24) and (3.2.3), the fringe shift caused by a transverse gradient of n_e is

$$\delta = - \frac{L^3 \lambda^3}{6} \left(4.48 \times 10^{-14} \frac{\partial n_e}{\partial x} \right)^2 .$$

Referring to Fig.6.2.2, at $t = 0$ the peak electron density on axis is $\sim 3.4 \times 10^{19}$ cm^{-3} in a column of radius $r = 0.1$ cm. Thus $\overline{\frac{\partial n_e}{\partial r}} = 3.4 \times 10^{20}$ cm^{-4}. For $\lambda = 6943$ Å and putting $L = 1.5\,r = 0.15$ cm, $\delta = 0.044$. At $t = +30$ nsec, the peak electron density on axis is $\sim 5.9 \times 10^{18} cm^{-3}$ in a column of radius $r \sim 1.3$ cm. Thus $\overline{\frac{\partial n_e}{\partial r}} = 4.6 \times 10^{18} cm^{-4}$. For $\lambda = 6943$ Å and putting $L = 1.5\,r = 1.9$ cm, $\delta = 0.016$. From these two

extremes, the average value of $\delta = 0.03$. Thus, we set $\sigma_4 = 0.03$ of a fringe.

(f) To assess the accuracy of the numerical method in evaluating the fringe-shift distributions, a parabolic fringe-shift distribution was assumed, i.e. $s(x) = \hat{s}(1 - x^2/R^2)$ with $\hat{s}$ and R having values typical of those observed. Using this distribution in equation (6.2.2), the equation may be integrated analytically to give

$$n_e(r) = \frac{6.4 \times 10^{17} \hat{s}}{\pi R} \left(1 - r^2/R^2\right)^{\frac{1}{2}} . \qquad \ldots (6.2.4)$$

Values of $s(x)$ at 20 equal intervals over the radius, calculated from the parabolic expression, were used as data for the numerical method, equation (6.2.3), to calculate twenty values of $n_e(r)$. These values were compared with those at corresponding positions r calculated using the same values of $s(x)$ in equation (6.2.4). The largest difference was less than 1 in 5,000. Thus, the error introduced by the numerical method can be neglected in comparison with the other errors.

The standard deviation in the measured value of any fringe shift is obtained by compounding the standard deviations evaluated above, i.e. $\sigma = (\sigma_1^2 + \sigma_2^2 + \sigma_3^2 + \sigma_4^2)^{\frac{1}{2}} \simeq 0.13$ of a fringe for all times considered. The effect of this uncertainty in the fringe-shift values, on the calculated values of electron density, was assessed numerically. A fringe-shift distribution from an interferogram was processed, in the usual manner, by dividing the radius into twenty equal intervals, giving twenty-one values of $s(x)$. Using the numerical method, the corresponding values of $n_e(r)$ were calculated. Then, a certain number of the twenty-one values of $s(x)$ were either increased or decreased by an amount σ, and the numerical method was used again to recalculate the values of $n_e(r)$. This was repeated, for each distribution, perturbing from one to six values of $s(x)$, in various combinations of position and spacing, from the centre to the edge of the distribution. The values of $n_e(r)$ from the perturbed

distributions were compared with the values from the unperturbed distributions.

Figure 6.2.5 shows three radial electron-density profiles, at - 40, 0 and + 30 nsec, with the assessed errors inserted at various points in the profiles. Error bars are drawn at the edge and centre of each profile and also at the axis, but at low values of density these error bars are difficult to see. In general, the errors on axis are ~ 10%, falling quickly over four or five intervals of radius to ~ 4%. This magnitude of error is maintained along the profile until four or five intervals from the edge, when the errors rise steeply to ~ 20% at the edge. Of course, the errors differ from profile to profile, but this is the general trend.

6.2.3 Further Analysis and Interpretation

It is instructive to calculate the electron line density, N_e, i.e. the total number of electrons per unit length of plasma column, at various times during the discharge to assess the gain or loss of particles during the different phases. The line density is obtained by integrating the radial electron-density profile, i.e.

$$N_e = 2\pi \int_0^R n_e(r)\, r\, dr \,. \qquad \ldots (6.2.5)$$

A numerical integrating procedure such as Simpson's rule gives sufficient accuracy.

The radial electron-density profiles shown in Fig.6.2.2 were integrated to give the electron line-densities shown in Fig.6.2.6. During the collapse phase, from t = - 70 to - 20 nsec, the line density is remarkably constant, at $\sim 9 \times 10^{17}$ cm^{-1}, in spite of the imploding shock sweeping up the particles in its path. Thus, an equilibrium is established between particle loss by flow parallel to and along the current sheet, away from the gun, and particle gain by the snow-ploughing action of the shock. The axial loss of particles is caused by the obliquity of the

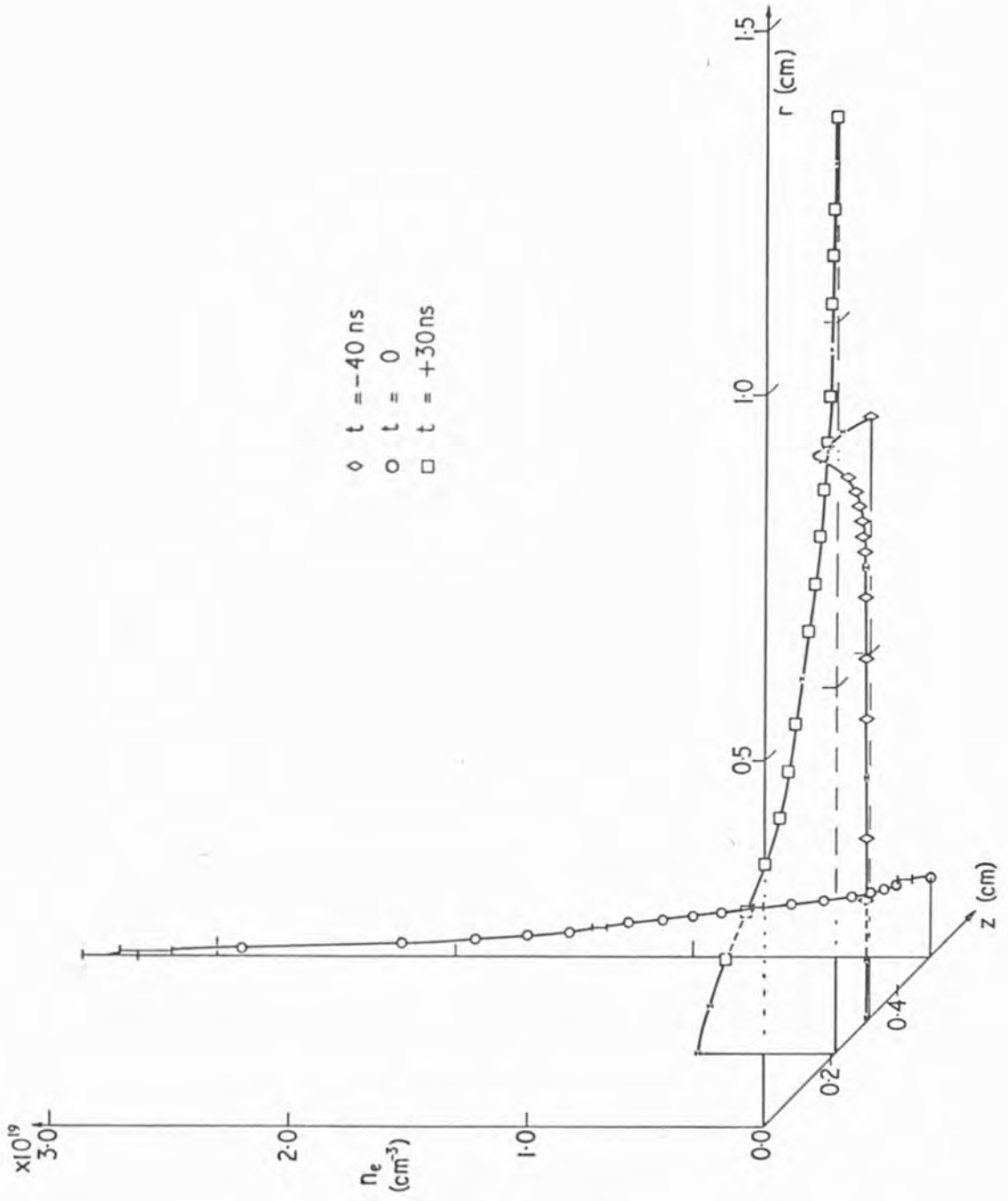

Fig.6.2.5

Radial electron-density profiles at various times during a discharge, showing distribution of assessed errors. Initial conditions V = 30 kV, p_o = 2.5 torr (D_2 + 4% Ar)

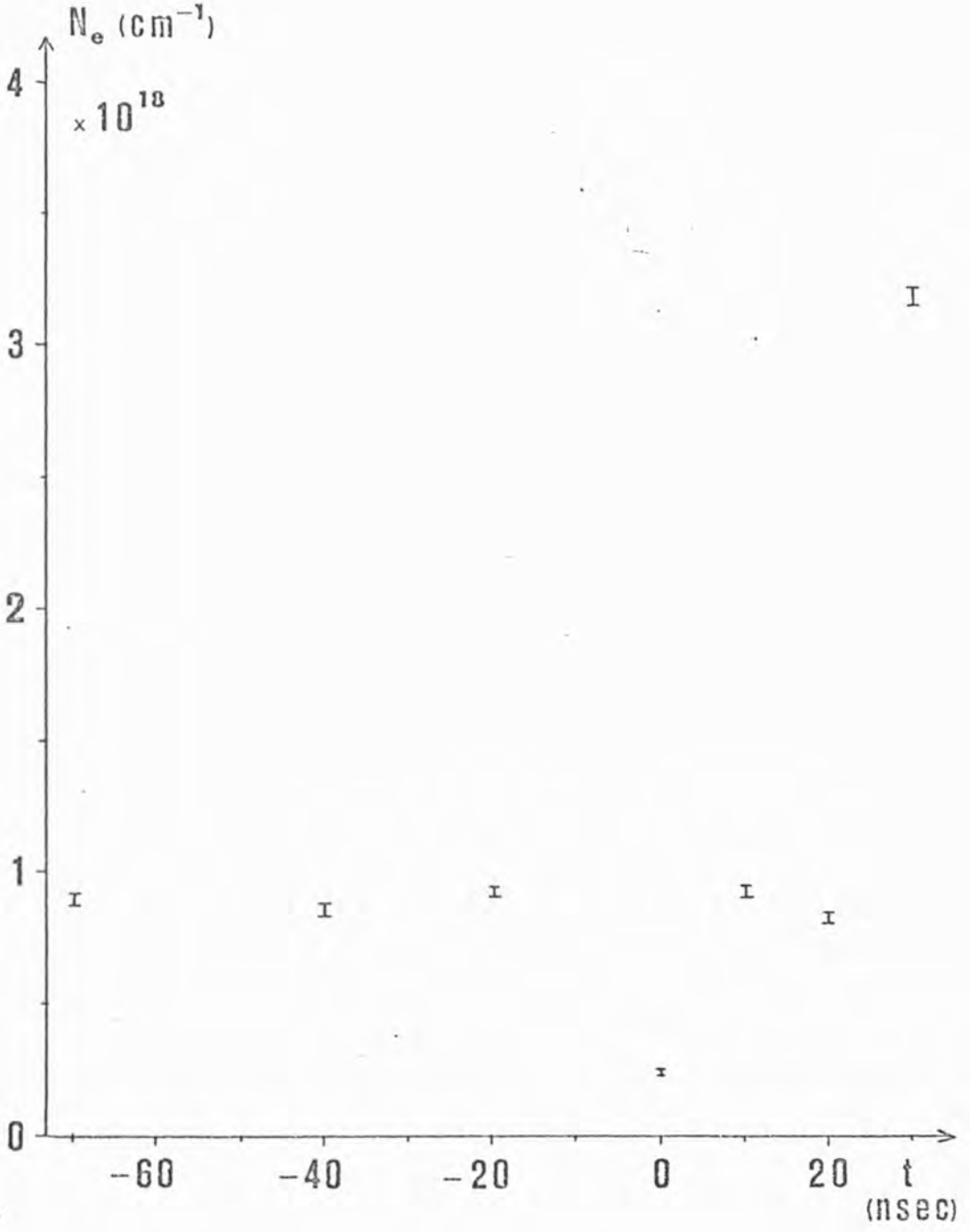

Fig.6.2.6

Electron line-density at various times during a discharge.
Initial conditions V = 30 kV, p_o = 2.5 torr (D_2 + 4% Ar)

imploding current-sheet, the radius of which increases with increasing axial distance from the anode. Fig.5.3.3 clearly illustrates this obliquity. At $t = 0$, in Fig.6.2.6, N_e has dropped by a factor of ~ 4 due to further incompressibility of the plasma, the line density increasing at adjacent positions both upstream and downstream of the local compression through axial plasma flow. This flow accounts for the recovery of the line density at $t = +10$ and $+20$ nsec, the start of the break-up phase. Finally, the pinch is severely disrupted by sausage-type instabilities and breaks up into regions where no electron concentration can be detected (the interferogram fringes assume a uniform pattern similar to that of the background - frame 3 of Fig.5.2.1) and into regions of a few centimetres' diameter containing many particles. The line density at $t = +30$ nsec is for such a region as the latter; N_e having increased to $\sim 3.2 \times 10^{18}$ cm^{-1}.

In a similar manner, the radial electron-density profiles of Fig.6.2.3 were integrated, yielding the electron line-densities at $t = 0$ for different axial locations, Fig.6.2.7. Near the electrode surface, N_e is $\sim 5.6 \times 10^{17}$ cm^{-1}. From $z \sim 0.4 - 1.6$ cm, the line density has dropped to $\sim 2 \times 10^{17}$ cm^{-1} in the regions of high compression. Finally, at $z \sim 2.1$ cm, N_e has risen sharply to $\sim 3.9 \times 10^{18}$ cm^{-1}. This high value of line density is due to axial plasma flow causing an aggregation near the open end of the imploding current-sheet.

The average electron density $\bar{n}_e$ may be obtained by dividing the electron line-density by the cross-sectional area of the plasma column, i.e.

$$\bar{n}_e = \left(2\pi \int_0^R n_e(r)\, r\, dr\right)/\pi R^2 .$$

A plot of $\bar{n}_e$ against time is shown in Fig.6.2.8. This figure corresponds to the profiles of $n_e(r)$ shown in Fig.6.2.2. In Fig.6.2.8, the average electron density increases relatively slowly initially, rises

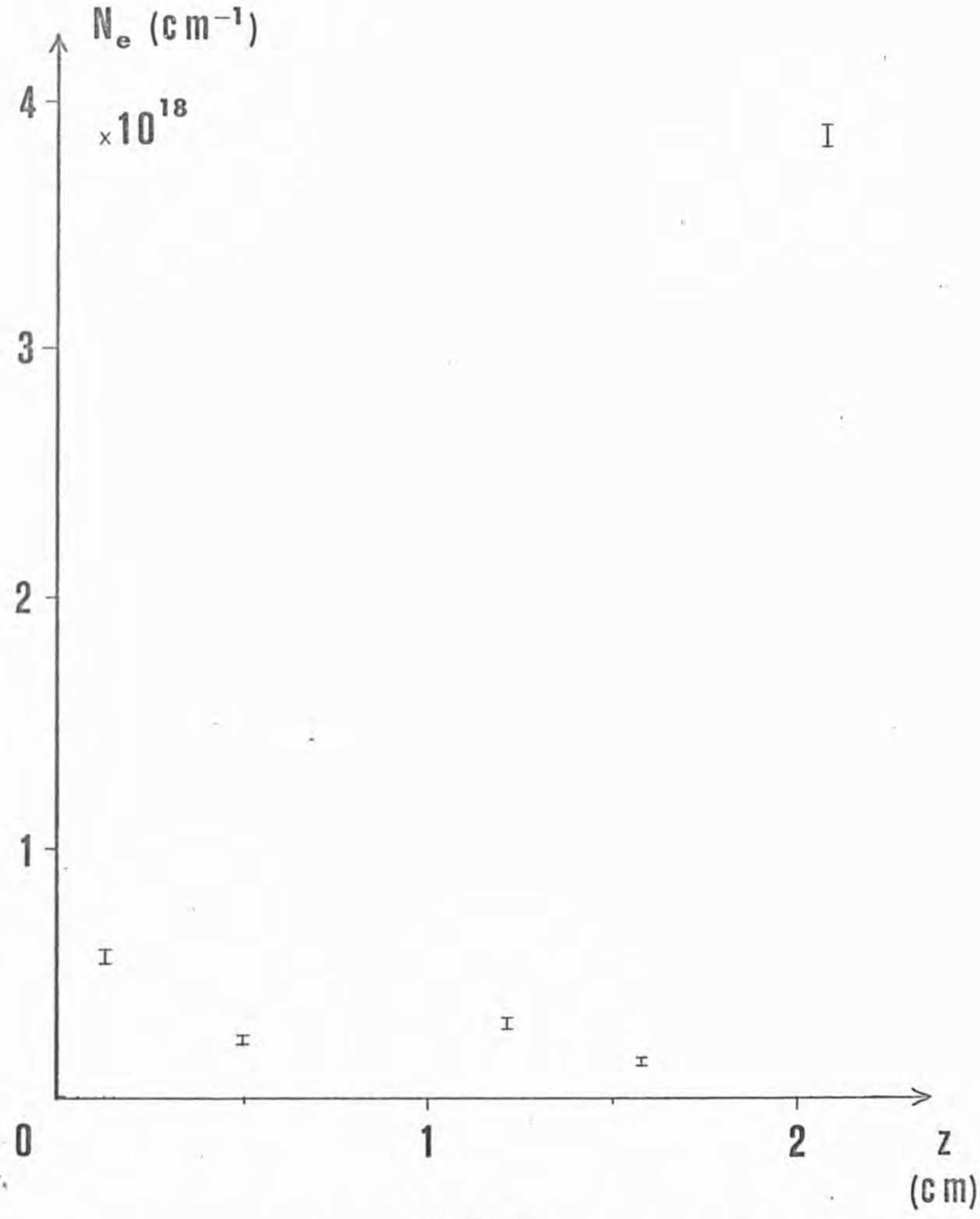

Fig.6.2.7
Electron line-density at $t = 0$ as a function of axial position.
Initial conditions $V = 30$ kV, $p_o = 2.5$ torr (D_2 + 4% Ar)

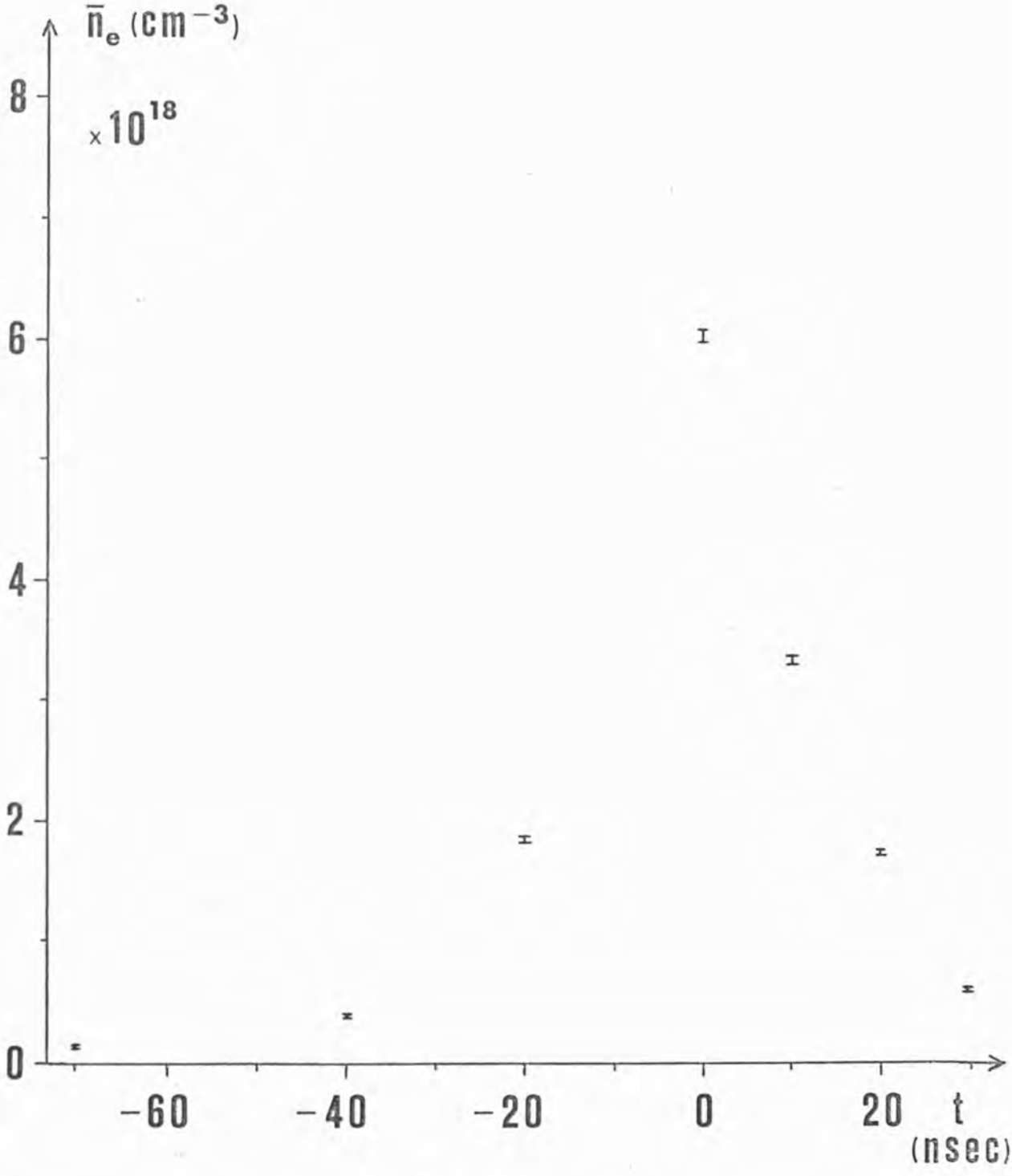

Fig.6.2.8

Average electron density at various times during a discharge.
Initial conditions V = 30 kV , p_o = 2.5 torr (D_2 + 4% Ar)

sharply to a maximum of $\sim 6 \times 10^{18}$ cm^{-3} at $t = 0$ and decreases abruptly during the break-up phase.

Using the derived values of line density, estimates of the efficiency of the focusing mechanism and of the particle loss rate may be made:

The collapse phase commences when the current-sheet spills off the inner electrode end and starts imploding radially inwards into the undisturbed gas. Suppose the current sheet sweeps up all atoms contained within a cylinder of radius equal to that of the inner electrode, R(2.5 cm), and length ℓ, and compresses them on axis to form a dense pinch. For a filling of 2.5 torr (D_2 + 4% Ar), the initial densities of deuterium and argon atoms is $n_D = 1.7 \times 10^{17}$ cm^{-3} and $n_{Ar} = 3.5 \times 10^{15}$ cm^{-3}. When all the atoms initially contained in the volume $\pi R^2 \ell$ are ionized, the resulting electron line-density is related to the initial densities by

$$N_e = \pi R^2 (n_D + Z n_{Ar}) , \qquad \ldots (6.2.6)$$

where Z is the argon ion charge. This is the maximum possible line-density and is arbitrarily used to define 100% focusing efficiency. During the dense-pinch phase, when $\bar{Z} = 14$, for 100% focusing efficiency N_e is $\sim 4.4 \times 10^{18}$ cm^{-1}. The value of $\bar{Z}$ was derived from spectroscopic measurements on the dense pinch, Peacock et al (1971). In the dense pinch, from Fig.6.2.6, at $t = 0$ N_e is $\sim 2.3 \times 10^{17}$ cm^{-1}. Thus, the efficiency of the focusing mechanism is $\sim 5\%$, i.e. $\sim 95\%$ of the atoms are lost by axial flow during the collapse of the current sheet to the axis.

With reference to Fig.6.2.2, during the collapse phase the plasma radius decreases from $R_1 \simeq 1.4$ cm to $R_2 \simeq 0.4$ cm in a time interval of 50 nsec; an average shock velocity of $\sim 2.1 \times 10^7$ cm sec^{-1}. The electron line-density during this time remains reasonably constant at $\sim 9 \times 10^{17}$ cm^{-1}, Fig.6.2.6. From these results, the particle loss rate is estimated.

During the collapse, a shock electron temperature of ~ 60 eV has been obtained from numerical computations, Potter (1971). At this temperature, a value of $\bar{Z} = 8$ can be derived for the argon ions in the shock, using the steady-state ionization curves of House (1963). With this value of $\bar{Z}$, for the case of 100% focusing efficiency, the number of electrons produced per unit length of column by the shock imploding from radius R_1 to R_2 may be obtained from equation (6.2.6), replacing R^2 by $(R_1^2 - R_2^2)$. This number, $\sim 1.2 \times 10^{18}$ cm^{-1}, is greater than the average line-density of $\sim 9 \times 10^{17}$ cm^{-1} over the same interval. Thus, $\sim 10^{18}$ atoms cm^{-1} are lost through axial flow during a 50 nsec time interval. This represents an average loss rate of $\sim 2 \times 10^{25}$ atoms cm^{-1} sec^{-1} during this part of the collapse.

Referring to Fig.6.2.7, at $t = 0$ the total number of electrons contained in the 2.1 cm length of plasma column adjacent to the anode may be obtained by integrating the electron line-density profile, i.e. $N = \int_0^L N_e(z)\, dz$. This number is $\sim 2.8 \times 10^{18}$. The portion of column between $z = 1.6$ cm and $z = 2.1$ cm contains $\sim 2.3 \times 10^{18}$ electrons, i.e. this part of the column adjacent to the open end of the 'funnel' contains $\sim$80% of the plasma in the whole column, due to axial flow from upstream.

Attempts to measure the electron density during the diffuse-pinch phase were largely unsuccessful, due apparently to the plasma being a low-density column of diameter greater than or equal to the width of the field of view. The fringes over the whole of this width showed a gradual shift, of up to 0.6 from edge to centre, and hence the edge of the column could not be determined with precision. However, it was possible to estimate the peak electron density at the axis, from the fringe shifts, by making a few assumptions.

Firstly, a parabolic fringe-shift distribution is assumed, i.e.

$$s(x) = -\hat{s}(1 - x^2/R^2) \ . \qquad \ldots (6.2.7)$$

Neither the peak fringe-shift $\hat{s}$ nor the plasma radius R could be determined from the interferograms, but it was observed that, in moving radially a distance d from the gun axis, a fringe shift of p occurred. The true fringe-shift at distance d is $-(\hat{s} - p)$, i.e.

$$-(\hat{s} - p) = -\hat{s}(1 - d^2/R^2) \ ,$$

or

$$\hat{s} = -p R^2/d^2 \ . \qquad \ldots (6.2.8)$$

Secondly, it is assumed that N_e during the diffuse-pinch phase is the same as during the collapse and break-up phases, i.e. plasma is conserved after break-up and forms a diffuse column. This value of N_e is $\sim 9 \times 10^{17}$ cm^{-1}.

The radial electron-density profile may be determined by substituting equation (6.2.7) into equation (6.2.2), and integrating analytically, i.e.

$$n_e(r) = -\frac{6.4 \times 10^{17} \hat{s}}{\pi R} (1 - r^2/R^2)^{\frac{1}{2}} \ .$$

The peak electron density, on axis, is thus

$$\hat{n}_e = -\frac{6.4 \times 10^{17} \hat{s}}{\pi R} \ . \qquad \ldots (6.2.9)$$

Substituting the above expression for the radial density profile into equation (6.2.5) and integrating, the electron line-density is

$$N_e = -12.8 \times 10^{17} \hat{s} R/3 \ ,$$

or

$$R = -3 N_e/(12.8 \times 10^{17} \hat{s}) \ .$$

Substituting equation (6.2.8) into the above

$$R = \left(\frac{3 d^2 N_e}{p \times 1.28 \times 10^{18}}\right)^{\frac{1}{3}} \ . \qquad \ldots (6.2.10)$$

Thus, having measured p and d on an interferogram, R and $\hat{s}$ were calculated using equations (6.2.10) and (6.2.8). These latter values were used in equation (6.2.9) to estimate $\hat{n}_e$. On most interferograms at t = + 200 nsec, it was observed that over regions extending axially from

$z \sim 0.5 - 2.5$ cm p was ≤ 0.6 for $d = 1.2$ cm. On a few interferograms, taken at the same time, no definite fringe-shifts could be observed. However, in all cases, the laser pulse used to obtain the interferograms had been synchronised with the peak of the soft X-ray emission associated with the diffuse pinch.

Using the above values of p and d, $\hat{s}$ and R are ~ 1.2 and ~ 1.7 cm, respectively. These values, in turn, lead to a value of $\sim 1.5 \times 10^{17}$ cm^{-3} for $\hat{n}_e$. Thus, at the time of peak soft X-ray emission during the diffuse-pinch phase, the plasma has expanded to diameter ~ 3.4 cm and has peak electron density $\sim 1.5 \times 10^{17}$ cm^{-3}.

6.2.4 Discussion and Summary

From the derived values of electron line-density and from a series of temperature measurements made on the discharge, values of beta and of the confining magnetic field may be calculated for the dense pinch. The parameter beta in a plasma is defined as the ratio of the kinetic energy to the sum of the kinetic and magnetic energies, i.e.

$$\beta = p/(p + B_i^2/8\pi) ,$$

where p is the plasma kinetic pressure and B_i is the internal magnetic field.

At maximum compression, the dense pinch is transiently in equilibrium with the confining azimuthal magnetic field. This may be expressed

$$p + \frac{B_i^2}{8\pi} = \frac{B_\theta^2}{8\pi} .$$

In the case of a discharge in a D_2/Ar mixture

$$p = k(n_e T_e + n_{iD} T_{iD} + n_{iAr} T_{iAr}) .$$

The strength of the external magnetic field may be related to the axial current flow through the pinch by

$$B_\theta = I/5R .$$

Combining the above four equations, we arrive at the Bennett relation for

a pinched plasma column in equilibrium

$$200\,k\,(N_e T_e + N_{iD} T_{iD} + N_{iAr} T_{iAr}) = \beta_\theta\, I^2 \,.$$

From the interferometric study, at $t = 0$ in a discharge produced at $V = 30\,kV$ and $p_o = 2.5$ torr (D_2 + 4% Ar), $N_e \simeq 2.3 \times 10^{17}$ cm^{-1}. The deuterium and argon line-densities may be obtained from N_e using the relationship $N_e = N_{iD} + \bar{Z}\, N_{iAr}$, where $\bar{Z}$ is the average argon ion charge, and from the initial filling conditions $N_{iD} = 48\, N_{iAr}$. In the dense pinch, $\bar{Z} = 14$ from spectroscopic studies, Peacock et al (1971). The current flowing in the discharge circuit at $t = 0$ was ~ 610 kA under the above operating conditions.

The electron temperature was determined by absorber-foil measurements on the soft X-ray flux, Peacock et al (1968), and spectroscopically from the ratio of the intensities of the He-like argon-ion resonance lines to the satellite-line intensities, Peacock and Hobby (1974). From these two methods, $T_e \sim 2.2$ keV. The argon ion temperature was obtained from the Doppler broadening of the He-like resonance lines due to ion thermal motion, Peacock et al (1971). T_{iAr} was found to be ~ 9.5 keV. Finally, T_{iD} was determined by cooperative scattering of ruby laser light, Peacock et al (1972). The experimentally-determined scatter profiles were compared with computed profiles which included the effects due to impurities. A best fit was found for $T_{iD} \sim 700$ eV at $t = 0$.

Using the above values in the Bennett relation, and assuming that all of the circuit current flowed through the discharge, then $\beta_\theta = 0.6 \pm 0.15$. The errors are primarily due to the uncertainties in the values of temperature and in the current flowing at peak compression. Thus, the plasma kinetic pressure is sufficiently high to be balanced by a confining magnetic field produced by between 67 and 87% of the total pinch current, in general agreement with the fluid code of Potter (1971). The external magnetic field,

$B_\theta = I/5R$, is ~ 1.2 MG for a column of radius 0.1 cm. For the dense pinch, the local instability time is seen to be ~ 5 nsec from the shadowgraph studies, section 6.3.2, which is longer than the self-collision time of each particle species present. Thus, from this point of view it is reasonable to assume that the pinch is transiently in equilibrium.

Apart from the interferometric study reported in this thesis, the only other detailed study of a Plasma Focus by interferometry, that has been reported, has been made by Filippov's group, Filippov et al (1971), Gribkov et al (1972) and Gribkov et al (1973). However, it is difficult to make a direct comparison between the two sets of results because the latter study was of a Filippov device. Detailed computations of the plasma parameters, throughout the discharge lifetime up to the break-up phase, have been made by Potter (1971). Results were obtained for an identical geometry to the device used in the present study, but with initial fillings of pure deuterium only.

The main results of the interferometric study are summarised, and the results of Filippov and Potter are compared with these where appropriate.

(a) During the collapse phase, the total number of ionized particles in the plasma column remains remarkably constant, because of an equilibrium between particle gain due to snowploughing by the imploding shock and particle loss due to mass flow parallel to and along the shock. The loss of $\sim 95\%$ of the particles during the collapse is the key to the working of the Plasma Focus, because the energy stored inductively behind the current sheet is concentrated into the relatively small number of particles compressed at the axis, in the dense pinch. The features observed during the collapse are in good agreement with the computations of Potter and in fair agreement with Filippov's results. The compression in the shock, $\hat{n}_e/(n_D + 8\ n_{Ar})$, at $t = -40$ nsec is ~ 10 above the initial filling density.

(b) In the dense pinch, peak electron densities of $\sim 3.4 \times 10^{19}$ cm^{-3} have been measured for a pinch radius of 0.1 cm. This represents an average electron density of $\sim 6 \times 10^{18}$ cm^{-3} over the pinch radius. The compression in the pinch, $\hat{n}_e / (n_D + 14\ n_{Ar})$, is ~ 150 above the initial filling density. Potter's computations are in good agreement with the experimental results, but, because of the discrete space-lattice employed in the computations, the pinch is partially diffused. This gives values of $\hat{n}_e$ which are a little low, $\sim 10^{19}$ cm^{-3}. Filippov has not measured n_e for the dense pinch but at t = - 100 nsec obtains a value of $\sim 4.5 \times 10^{19}$ cm^{-3} on axis for a pinch of radius 1.3 cm. This suggests that, during the dense-pinch phase, values of $\hat{n}_e \geqslant 10^{20}$ cm^{-3} are attained. The efficiency of the focusing mechanism has been estimated as being $\sim 5\%$ in the present study. Potter calculates that $\sim 15\%$ of the plasma initially at the end of the inner electrode is finally collected into the dense pinch.

(c) Some 200 nsec after the dense-pinch phase, a pulse of soft X-rays and of neutrons are emitted from a low density plasma of radius a few centimetres. The peak electron density of this plasma has been estimated at 1.5×10^{17} cm^{-3}. Gribkov et al (1972) has measured peak electron densities of $\sim 2 \times 10^{18}$ cm^{-3} during the diffuse-pinch phase. Morgan et al (1973) have measured peak densities of $\sim 3 \times 10^{17}$ cm^{-3} in a plasma of radius ~ 2 cm, at the peak of the diffuse-pinch neutron pulse in a Filippov device. The fluid code of Potter does not indicate further soft X-ray or neutron emission after the break-up of the dense pinch.

6.3 ANALYSIS OF SHADOWGRAPH RESULTS

6.3.1 Velocity and Acceleration of Collapsing Current-Sheet

During the collapse phase, by measuring the diameter of the imploding shock at the same relative position on the three successive frames of a time sequence, the distances travelled by the shock in the intervals between exposures were found. Thus, at any axial location, two values of radial velocity and one of radial acceleration were obtained, from each time sequence. Also, by measuring the distances of a particular disturbance on the current sheet from the anode end, the axial velocity of the sheet was obtained.

The variation of radial velocity with axial position is shown in Fig.6.3.1. The two curves were obtained from two different time-sequences - one obtained with initial conditions $V = 28.3\,kV$ and $p_o = 2.5\,torr\ (D_2 + 4\%\ Ar)$ and the other with $V = 24.3\,kV$ and $p_o = 2.5\,torr\ (D_2 + 4\%\ Ar)$. Each value of velocity is averaged over a 6.5 nsec interval. Considering the velocities for $V = 24.3\,kV$, the error associated with the highest velocity value is $\pm 0.15 \times 10^7\ cm\ sec^{-1}$ and that associated with the lowest value is $\pm 0.14 \times 10^7\ cm\ sec^{-1}$. It can be seen that the radial velocity decreases with increasing axial distance from the inner electrode end. This is because the driving pressure of the azimuthal magnetic field is inversely proportional to the square of the plasma column radius, $P = I^2/200\pi R^2$, and the radius of the shock increases with increasing axial distance.

However, as the current sheet implodes so the internal plasma pressure increases. In the absence of axial plasma loss, the plasma pressure varies inversely with R^2 and directly with temperature. Thus, at sufficiently small radii there is a rapidly-increasing pressure within the plasma column, as it implodes radially, which opposes the compressing action of the external field. In Fig.6.3.2, the radial velocity of the

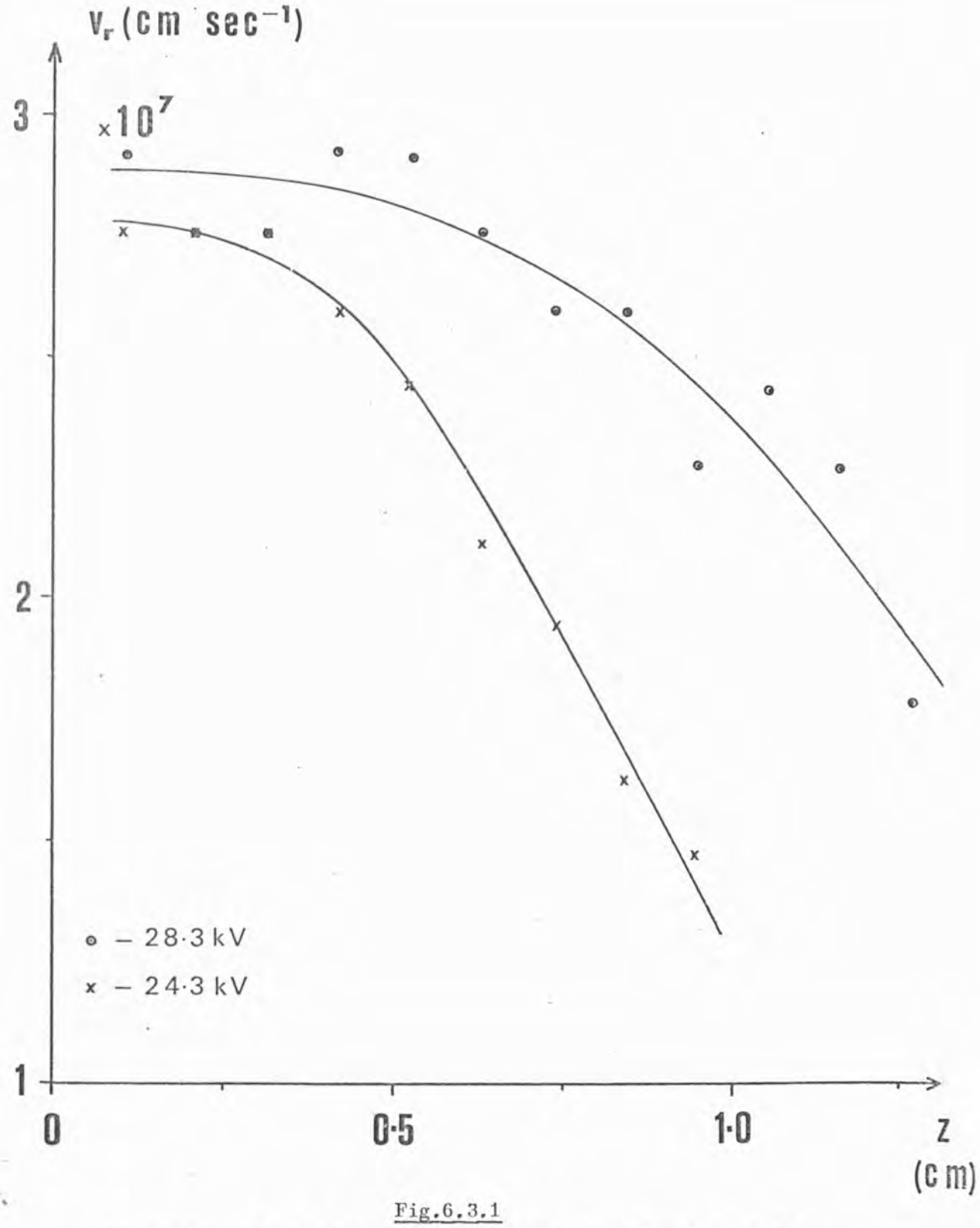

Fig.6.3.1

Variation of radial velocity with axial position during the collapse phase. Initial condition $p_o = 2.5$ torr (D_2 + 4% Ar)

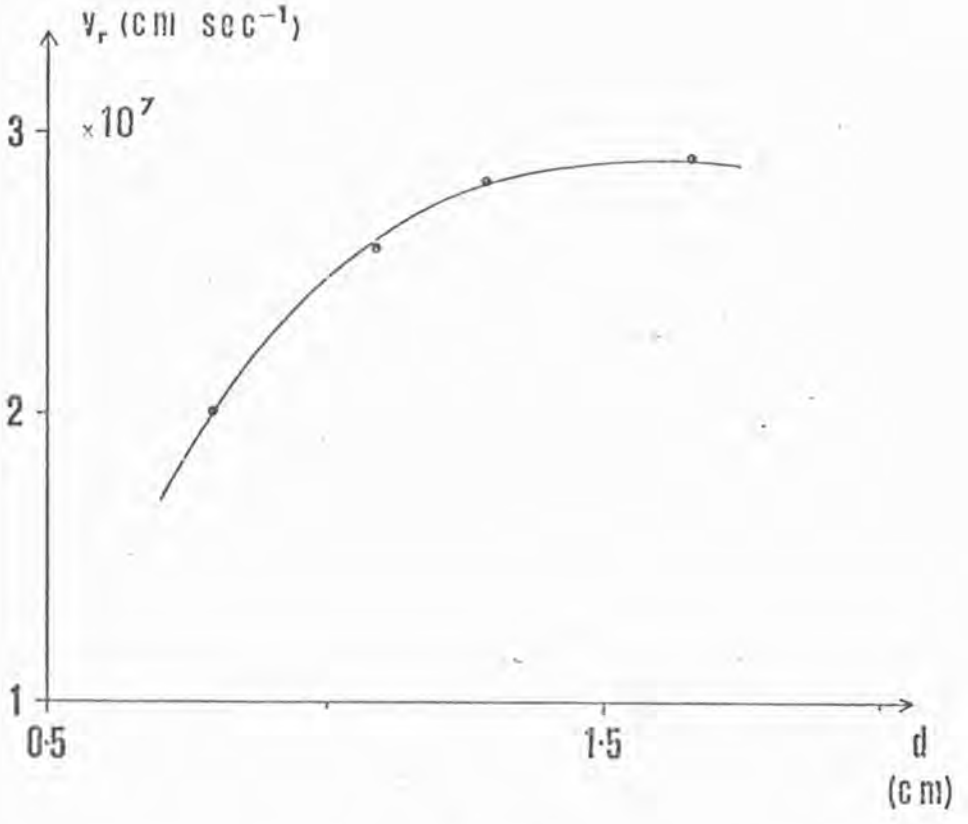

Fig.6.3.2

Variation of radial velocity with current-sheet diameter during the collapse phase, at $z \sim 0.4$ cm. Initial conditions $V = 28.3$ kV, $p_o = 2.5$ torr (D_2 + 4% Ar)

imploding shock at $z \sim 0.4$ cm is plotted as a function of the shock diameter, showing this effect. The initial conditions were $V = 28.3$ kV and $p_o = 2.5$ torr (D_2 + 4% Ar). It can be seen that the radial velocity decreases with decreasing diameter, at sufficiently small diameters.

The above effect is also shown in Fig.6.3.3, where the radial acceleration of the imploding shock is plotted against axial distance. The results were obtained from two separate time-sequences - one obtained with initial conditions $V = 26.3$ kV and $p_o = 2.5$ torr (D_2 + 4% Ar), and the other with $V = 24.3$ kV and $p_o = 2.5$ torr (D_2 + 4% Ar). In both sequences the interval between frames was 6.5 nsec. At small values of z the shock is decelerating, but for $z \geq 0.7$ cm the shock is accelerating because of the lower plasma pressure at these axial locations. It is noted that at small

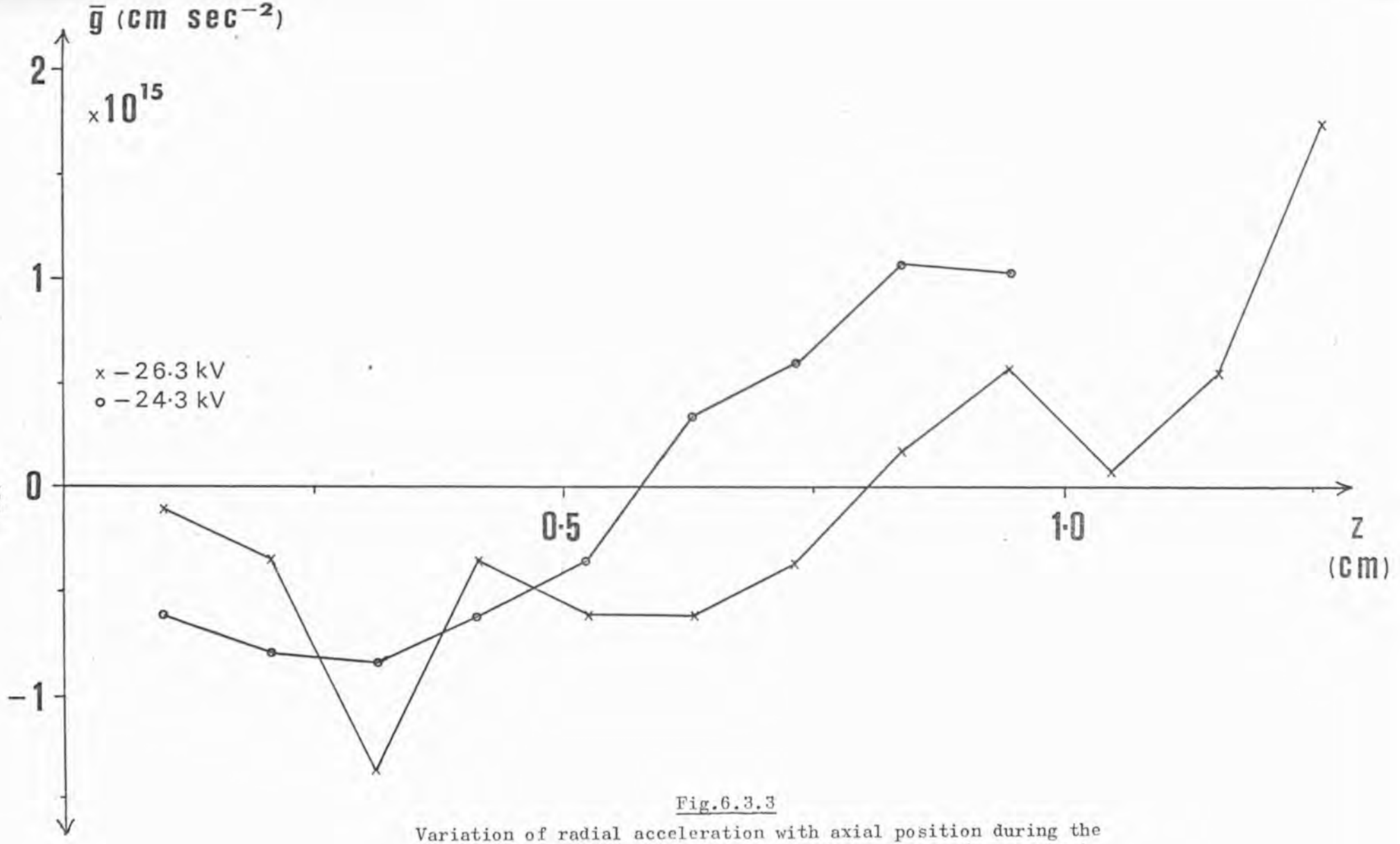

Fig.6.3.3

Variation of radial acceleration with axial position during the collapse phase. Initial condition $p_o = 2.5$ torr (D_2 + 4% Ar)

values of z the acceleration initially decreases with increasing axial distance, before increasing and eventually becoming positive at larger distances. This may be interpreted as the cool anode end-face cooling the plasma adjacent to itself, thereby reducing the plasma pressure.

The highest measured radial velocity was $\sim 4.2 \times 10^7$ cm sec^{-1} and the highest measured radial acceleration was $\sim 4.2 \times 10^{15}$ cm sec^{-2}, both at the operating conditions $V = 30$ kV and $p_o = 2.5$ torr ($D_2 + 4\%$ Ar). Axial velocities of the current sheet in the range $4.9 - 9.7 \times 10^6$ cm sec^{-1} were measured over the voltage range 25 - 30 kV.

6.3.2 Lifetime of Dense Pinch

Shadowgram sequences taken during the dense-pinch phase have been used to study the lifetime of the highly-compressed plasma. Fig.5.3.4 is one such time sequence, taken with $V = 30$ kV and $p_o = 2.5$ torr ($D_2 + 4\%$ Ar). The first frame shows that the maximum compression of the plasma column, to a radius of ~ 0.1 cm, occurs at an axial position of $z \sim 0.4$ cm. In the second frame, taken 6.5 nsec later, the column at this position has broken up, and the region of maximum compression occurs further away from the anode, at $z = 0.8$ cm. Finally, in the third frame, which was taken 13 nsec after the first, the region of maximum compression has again moved further downstream to $z = 1.3$ cm. The previous region of maximum compression has been completely disrupted.

Thus, the dense-pinch phase consists of a successive series of compressions and disruptions of the plasma column, the locality of the compression moving progressively downstream with time. On this basis, it is evident that the dense pinch lasts for a maximum of 40 - 50 nsec, i.e. during this time a local region of highly-compressed plasma is always present. However, the lifetime of any one such region is not longer than ~ 5 nsec.

The dense pinch is broken up mainly by sausage-type instabilities, Fig.5.3.4. These grow exponentially in amplitude as time progresses. The amplitude increase is given by, Jeffrey and Taniuti (1966),

$$a_t = a_o \exp(\omega t) , \qquad \ldots (6.3.1)$$

where a_o is the initial amplitude and ω is the growth rate. The latter, in turn, is given by $\omega \simeq v_s/R$, where $v_s = \sqrt{\gamma p/\rho}$ is the velocity of sound in the pinch of radius R. Taking typical values for the dense pinch, sections 6.2.3 and 6.2.4; $\bar{n}_e = 6.0 \times 10^{18}$ cm^{-3}, $T_e = 2.2$ keV, $T_{iD} = 0.7$ keV, $T_{iAr} = 9.0$ keV and $\bar{Z} = 14$. Setting γ, the specific heat ratio, to 5/3, the sound speed $v_s \simeq 4.5 \times 10^7$ cm sec^{-1}. In a column of radius 0.1 cm, $\omega \simeq 4.5 \times 10^8$ sec^{-1}. Thus, the time required for the amplitude of the instability to increase by a factor e is $\tau = \omega^{-1} \simeq 2.2$ nsec. This is approximately the lifetime of a dense plasma region as observed in the shadowgraph studies.

6.3.3 Study of Rayleigh-Taylor Instabilities

(a) Theory of the instability

The instability of an accelerated fluid interface was first studied by Rayleigh (1899) and the theory was subsequently developed by Taylor (1950). Consider the interface between two infinite plane fluid layers; ρ_1 and ρ_2 being the densities of the upper and lower fluids, respectively. If an acceleration g is applied normal to the interface, directed from the lower fluid to the upper, then an initial disturbance of amplitude a_o and wave number $k = 2\pi/\lambda$, where λ is the disturbance wavelength, grows exponentially with time according to equation (6.3.1). The growth rate is given by, Appendix 3,

$$\omega = \left[g\, k \left(\frac{\rho_1 - \rho_2}{\rho_1 + \rho_2} \right) \right]^{\frac{1}{2}} .$$

The interface is unstable only when $\rho_1 > \rho_2$, i.e. when the acceleration is

directed from the lighter to the heavier fluid. This is the classical Rayleigh-Taylor instability. The expression for ω, which ignores such effects as surface tension and viscosity, shows that the growth rate increases indefinitely with decreasing wavelength.

Kruskal and Swartzschild (1954) were the first to discuss Rayleigh-Taylor instabilities in an accelerated interface between an electrically conducting fluid and a magnetic field. They described in detail the way in which the inertial forces produce charge separation and particle drift, which drive the instability. It was shown that, even though in this instance electromagnetic fields produce the plasma motions, the instability growth-rate is exactly the same as in the purely hydrodynamic case. For the case of a plasma accelerated by a magnetic field, the density, electrical conductivity and viscosity of the lower fluid are set to zero. Thus, the growth rate of the instability is

$$\omega = \sqrt{g k} \quad . \qquad \ldots (6.3.2)$$

Harris (1962) has considered the growth of Rayleigh-Taylor instabilities at a plasma-vacuum boundary for the case of cylindrical geometry. Harris considered a cylindrical plasma shell accelerated radially inwards by an azimuthal magnetic field produced by an axial current flow in the shell. The analysis follows the same lines as that in Appendix 3, with pressure terms added to the equation of motion to account for the magnetic field. The growth rate of the most unstable mode is given by

$$\omega^2 = g\left\{\frac{1}{2R} + \left[\left(\frac{1}{2R}\right)^2 + k^2\right]^{\frac{1}{2}}\right\} , \qquad \ldots (6.3.3)$$

where R is the radius of the plasma column which, over a sufficiently-short time interval, may be regarded as constant. The wave number k defines the spatial periodicity of the instability parallel to the cylinder axis. For maximum growth-rate the azimuthal wavelength is infinite, i.e. $m = 2\pi/\lambda_r = 0$. In the limit of infinity large R, the growthrate reduces to that given by equation (6.3.2).

The above treatments consider the fluids as being perfect, resulting in growth rates which increase indefinitely with decreasing wavelength. In practice, the effects of viscosity and resistivity in a plasma are to damp out the shorter wavelengths, producing a wavenumber k_m of maximum instability. For example, the effect of viscosity increases with decreasing wavelength because the shearing forces increase. In essence, the wavelength λ_m of maximum instability is the wavelength at which the rate of doing work by the inertial forces is balanced by the rate of dissipation of energy due to the viscous forces. A Rayleigh-Taylor instability of dominant wavelength λ_m has been observed in a z-pinch plasma, Curzon et al (1960), and in a θ-pinch plasma, Green and Niblett (1960).

Zadoff and Begun (1968) have considered the effects of plasma resistivity and viscosity on the growth of Rayleigh-Taylor instabilities. The plasma was treated as an incompressible homogeneous fluid accelerated by a uniform magnetic field at a plane plasma-vacuum boundary. Two general results were found: firstly, the original instability is modified due to dissipative processes and, secondly, new modes of instability, not otherwise present, appear. It was demonstrated that when the wave vector of the growing Rayleigh-Taylor instability is normal to the direction of the magnetic field, i.e. $\underline{k} \cdot \underline{B} = 0$, the wavelength of the instability is determined as a function of viscosity and acceleration only. The plasma resistivity plays no part in damping the growing instability, since it does not deform the magnetic-field lines in the process. Under this condition, the observed Rayleigh-Taylor instability is the fastest growing of all the modes. The wavelength of the mode of maximum instability is

$$\lambda_m = 12.8\, g^{-\frac{1}{3}} \nu^{\frac{2}{3}} , \qquad \ldots (6.3.4)$$

where ν is the plasma kinematic viscosity. The corresponding growth-rate is

$$\omega_m = \left(\frac{\pi g}{1.16\, \lambda_m} \right)^{\frac{1}{2}} . \qquad \ldots (6.3.5)$$

Since the classic kinematic viscosity of a plasma is proportional to $T_i^{\frac{5}{2}} n_i^{-1}$, knowing the ion density, the plasma ion temperature may be estimated by observing the wavelength of maximum instability and measuring the acceleration of the interface.

In the shadowgraph studies described in this thesis, the azimuthal periodicity of any instability occurring could not be observed, due to the optical layout used. Only the instability periodicities in a plane which contained the gun axis could be observed, for which $\underline{k} . \underline{B} = 0$. Thus, the fastest-growing mode of Rayleigh-Taylor instability was always observed. Under this condition, the new modes of the instability reported by Zadoff and Begun (1968) need not be considered further.

Finally, all theories concerning Rayleigh-Taylor instabilities are based on small amplitude perturbations to the fluid interface, i.e. $a \ll \lambda$. It is pertinent to enquire up to what perturbation amplitude can linear analysis be used. Birkhoff (1954) has shown that in classical fluids the growth of the instability is exponential with time up to an amplitude $a \sim 0.4\lambda$. For $a \gtrsim 0.4\lambda$, the growth is no longer exponential.

(b) Experimental data

The growth of Rayleigh-Taylor instabilities in the current sheet during the collapse phase was observed in many shadowgram time-sequences, e.g. Fig.5.3.3. However, in the majority of cases the instabilities were not observed to grow beyond the second frame of such a sequence, because the current sheet was decelerating by this stage. Furthermore, the amplitude of the instabilities tended to be $\sim 0.5\lambda$ at this stage. Thus, since the growth of the instabilities was not exponential over the time interval for which the acceleration was determined, these time-sequences were rejected.

Because of the field-of-view limitation due to the output aperture of the discharge chamber, the current sheet could not be observed at larger diameters, where it would still be accelerating and the instability amplitude would be small. It was not practical to use a much shorter time interval than 6.5 nsec between exposures, because the increase in amplitude from frame-to-frame was bearly measurable. However, from the many time-sequences obtained, in a small number of these the instability growth was exponential between the three exposures.

Consider the data from a shadowgram time-sequence, with a real-space magnification of 4.75, obtained in a discharge under the initial conditions $V = 30\,kV$ and $p_o = 2.5\,torr$ $(D_2 + 4\%\ Ar)$. At the beginning, midpoint and end of a 13 nsec interval, the shock diameters were $d_1 = 11.63$ cm, $d_2 = 10.75$ cm and $d_3 = 9.78$ cm, respectively, at an axial position $z \sim 7.0$ cm. The instability wavelength at this axial position was $\lambda_m = 1.60$ cm, with the instability amplitude at the three times being $a_1 = 0.23$ cm, $a_2 = 0.30$ cm and $a_3 = 0.38$ cm, respectively. During the 13 nsec interval, the shock travelled axially ~ 0.1 cm. The circuit current flowing at this stage of the collapse was $I \approx 6.1 \times 10^5$ A.

(c) Analysis and interpretation of data

From the above data, the amplitude ratios $a_2/a_1 = 1.30$ and $a_3/a_2 = 1.27$ are almost equal, indicating that the instability growth is exponential, to a good approximation. Furthermore, the ratio $a_3/\lambda = 0.24$. Thus, linear theory can be applied to an analysis of the data, since $a/\lambda < 0.5$.

Using the measured values of shock diameter, and instability amplitude and wavelength, the following real values were calculated over the 13 nsec interval :

the radial acceleration	$g_r \sim 2.2 \times 10^{14}$ cm sec^{-2}
the radial velocity	$v_r \sim 1.5 \times 10^{7}$ cm sec^{-1}
the initial shock radius	$R_i \sim 1.22$ cm
the final shock radius	$R_f \sim 1.03$ cm
the instability wavelength	$\lambda_m \sim 0.34$ cm
the instability wave number	$k_m = 2\pi/\lambda_m \sim 18.6$ cm^{-1}
the instability growth rate	$\omega_m = \ell n(a_3/a_1)/1.3\times10^{-8} \sim 3.9\times10^{7}$ sec^{-1}

Ignoring for the present the effects of viscous damping, the growth rate of a Rayleigh-Taylor instability of wave number k_m at a plane infinite plasma-vacuum boundary under a constant acceleration g_r is, using the above values in equation (6.3.2), $\omega_i \simeq 6.40 \times 10^{7}$ sec^{-1}. For a cylindrical plasma-vacuum interface of radius $(R_i + R_f)/2$, under the above conditions the growth rate of the instability is, from equation (6.3.3), $\omega_c \simeq 6.47 \times 10^{7}$ sec^{-1}. The difference between ω_i and ω_c is $\sim 1\%$. Thus, the effect of the curvature of the interface is negligible, and formulae derived for the case of a plane infinite interface may be applied to an analysis of the collapsing current-sheet in the Plasma Focus, provided $R_f \geq 0.5$ cm. This may be confirmed by calculating the growth rate of a viscously-damped instability of wave number k_m at a plane interface, using the above data in equation (6.3.5). The calculated value of ω_m of $\sim 4.2 \times 10^{7}$ sec^{-1} is in good agreement with the observed value of $\sim 3.9 \times 10^{7}$ sec^{-1}.

The temperature of the deuterium ions in the collapsing shock is now estimated from the Rayleigh-Taylor instability growth rate.

In the absence of an internal magnetic field, the coefficient of dynamic viscosity of a plasma is, from Spitzer (1962),

$$\mu = \frac{0.41\ m_i^{\frac{1}{2}}\ (kT_i)^{\frac{5}{2}}}{Z^4\ e^4\ \ell n \Lambda_{ii}}\ , \qquad \ldots (6.3.6)$$

where

$$\Lambda_{ii} = \frac{3}{2\,e^3 Z^2}\left(\frac{k^3 T_e\, T_i}{\pi n_e}\right)^{\frac{1}{2}} \qquad T \text{ is in } {}^{\circ}K\ .$$

The coefficient of kinematic viscosity ν is related to that of dynamic viscosity by

$$\nu = \mu / n_i m_i . \qquad \ldots (6.3.7)$$

Thus, using the values of g_r and λ_m determined from the shadowgraph studies in equation (6.3.4), a value of ν can be derived. Using the above two equations, a value of T_i may be estimated from the value of ν, since the ion density n_i during the collapse phase is known from interferometry, section 6.2.1. Because $\ell n \Lambda_{ii}$ is a slowly-varying function of T_i and T_e, in the absence of a value for the latter it may be set equal to the former, without causing a significant error.

However, an internal magnetic field of strength B_i in a plasma reduces the ion viscosities in a direction orthogonal to the field lines, due to ion cyclotron orbiting effects. Kaufman (1960) quotes

$$\mu_\perp = \mu / (1 + 4(\omega_{ci} \tau_{ii})^2) . \qquad \ldots (6.3.8)$$

In the above

$$\omega_{ci} = Z e B_i / m_i c$$

is the ion cyclotron frequency, and

$$\tau_{ii} = \frac{m_i^{\frac{1}{2}} (3kT_i)^{\frac{3}{2}}}{8 \times 0.714 \pi n_i e^4 Z^4 \ell n \Lambda_{ii}}$$

is the self-collision time for ions, Spitzer (1962). Thus, it is necessary to know the magnitude of B_i before any estimate of T_i can be made from measurements on the Rayleigh-Taylor instabilities. An estimate of B_i may be made from momentum-conservation considerations of the collapsing current-sheet.

However, firstly the parameters which determine the kinematic viscosities of the deuterium and argon ions are compared to see if the presence of the latter in the plasma can be ignored. During the collapse phase, it is reasonable to assume that $T_{iD} \simeq T_{iAr}$ and that $\Lambda_{iiD} = \Lambda_{iiAr}$. In this case, the only parameters which can cause each ion species to have

a different value of ν are n_i, Z and m_i, i.e. $\nu \propto 1/n_i\, Z^4\, m_i^{\frac{1}{2}}$ and $\omega_{ci}\,\tau_{ii} \propto 1/n_i\, Z^3\, m_i^{\frac{1}{2}}$. From the initial conditions that $p_o = 2.5$ torr $(D_2 + 4\%\ Ar)$, $n_{iD} \simeq 50\, n_{iAr}$. During the collapse phase, the estimated argon ion charge is ~ 8, section 6.2.3. Finally, the mass of an argon ion is approximately 20 times that of a deuterium ion. Hence, $\nu_D \simeq 366\, \nu_{Ar}$ and $(\omega_{ci}\,\tau_{ii})_D \simeq 46 (\omega_{ci}\,\tau_{ii})_{Ar}$. Thus, provided $(\omega_{ci}\,\tau_{ii})_D \leq 1$ we have $\nu_{\perp Ar} \leq \frac{1}{70}\ \nu_{\perp D}$. Under this condition, the contribution of the argon ions to the plasma kinematic viscosity in the collapsing current-sheet is negligible.

As stated previously, B_i may be estimated from considerations of momentum conservation. The imploding current-sheet is accelerated inwards by the azimuthal magntic field, of strength $B_\theta = I/5R$, against opposing forces due to the plasma internal magnetic field and the plasma kinetic pressure. In addition, energy is given to the particles which are encountered by the current sheet during its collapse and which are lost from the pinch by axial flow. The rate of momentum change of the plasma, the pressure of the internal magnetic field, the energy per unit volume expended in removing the particles within the current sheet, and the plasma kinetic pressure are balanced against the external magnetic pressure. Thus, at any time during the collapse

$$\frac{I^2}{200\,\pi R^2} = \frac{d}{dt}\left(\frac{\sum_i N_i\, m_i}{2\pi R}\,\frac{dR}{dt}\right) + \frac{\rho}{2}\left(\frac{dR}{dt}\right)^2 + \frac{B_i^2}{8\pi} + \sum_{e,i} nkT, \qquad \ldots\ (6.3.9)$$

where ρ is the initial filling density in the discharge chamber, and the symbols e and i in the summations denote electrons and all ions.

From the initial filling pressure of 2.5 torr $(D_2 + 4\%\ Ar)$, the density ρ is $\sim 8 \times 10^{-7}$ gm cm^{-3}. Using the results of interferometry, section 6.2.3, during the collapse phase $N_e \simeq 8.8 \times 10^{17}$ cm^{-1} and in the shock $\bar{n}_e \simeq 1.1 \times 10^{18}$ cm^{-3}. The average argon-ion charge during the

collapse is $Z \sim 8$, section 6.2.3, and thus the ion densities and line densities may be calculated using the relations $n_e = n_{iD} + Z\, n_{iAr}$ and $N_e = N_{iD} + Z\, N_{iAr}$.

T_{iD} may now be estimated by an interative process. In the first instance, the internal magnetic field is assumed to be zero and a value of T_{iD} (minimum value) is obtained from equations (6.3.4), (6.3.6) and (6.3.7), using the appropriate values of g_r, λ_m, n_e and n_{iD}. Inserting this value of T_{iD} into equation (6.3.9), and assuming that $T_{iAr} = T_e = T_{iD}$, the equation is solved to yield a value of B_i. Because of the uncertainties already present in the estimate of T_{iD}, no significant additional error will be introduced by equating T_e and T_{iAr} with T_{iD} during the collapse. Using the calculated value of B_i and of $(T_{iD})_{min}$, $\omega_{ci}\tau_{ii}$ is determined. This enables a better value of T_{iD} to be obtained using equations (6.3.4), (6.3.7) and (6.3.8). This better value of T_{iD} is then used in equation (6.3.9), and so on. The steps are repeated until the values of T_{iD} obtained converge.

In this manner, from the data given, the estimated value of T_{iD} is ~ 74 eV with an associated $\omega_{ci}\tau_{ii}$ of ~ 0.2. For the case of zero internal magnetic field, i.e. $\omega\tau \to 0$, T_{iD} is ~ 70 eV. It is difficult to assess the accuracy of this value of T_{iD}, since the theory used in the analysis was derived for an incompressible fluid, under a constant acceleration and for a plane infinite interface; all of these conditions are violated during the collapse phase in the Plasma Focus. There are no published values of T_{iD} which have been measured during this phase. However, the computations of Potter (1971) are in fair agreement with this estimate; a value of ~ 30 eV being calculated for T_i during the collapse, under the initial conditions $C = 40\ \mu F$, $V = 40$ kV and $p_o = 0.26$ torr D_2.

6.3.4 Discussion and Summary

There are no published results of other shadowgraph studies of a Plasma Focus with which to compare the results of this study. However, a comparison may be made with the results obtain by Patou et al (1967) using an image-converter framing camera giving exposures of 1 nsec duration. Also, a comparison may be made with the results of the fluid code of Potter (1971).

The main features of the shadowgraph results are summarised :

(a) During the collapse phase, radial velocities in the range 9.7×10^{6} - 4.2×10^{7} cm sec^{-1} have been measured for the incoming current-sheet, for a range of capacitor bank voltages from 24.3 - 30.0 kV . Radial accelerations in the range -1.6×10^{15} to 4.2×10^{15} cm sec^{-2} have also been measured. The radial acceleration at any time during the collapse increases with increasing axial distance from the anode. The values of radial velocity are in good agreement with the results of Potter. Patou et al (1967), using a Mather device under initial conditions C = 90 μF, V = 18 kV and p_o = 2.5 torr D_2, measured radial velocities from $1-3\times10^{7}$ cm sec^{-1} during the collapse.

(b) During that part of the collapse phase when the current sheet is being accelerated, Rayleigh-Taylor instabilities grow at the plasma-vacuum boundary. From observations on the growth of the instability of dominant wavelength, a deuterium ion temperature of ~70 eV has been estimated. Bernard et al (1973), using a non-cylindrical z-pinch, have estimated electron temperatures of ~30 eV by similar means. During the collapse phase, the instabilities do not grow to such amplitude that the current sheet is severely perturbed, because of their low growth-rate. However, the perturbations that are produced develop subsequently, during the dense-pinch phase, into sausage-type instabilities. The fluid code of Potter does not predict the development of Rayleigh-Taylor instabilities

during the collapse. For the initial conditions $C = 40\,\mu F$, $V = 40\,kV$ and $p_o = 0.26$ torr D_2, an ion temperature of about 30 eV is calculated by Potter, for the shock.

(c) The total lifetime of the dense pinch is about 40 nsec. The pinch is not formed simultaneously over its whole length, but consists of a succession of local regions of dense plasma produced at the gun axis. Each region is a few millimetres in axial extent and is produced progressively further away from the anode than the preceding dense plasma region. Such regions have a lifetime of about 5 nsec, which is the same order as the growth time of a sausage-type instability in the dense plasma. In contrast, the results of Potter's computations indicate that the whole pinched column is stable for about 50 nsec, before being disrupted by sausage-type instabilities.

CHAPTER VII

CONCLUSIONS

7.1 GENERAL DISCUSSION

The application of schlieren photography, interferometry and shadowgraphy, using a light pulse of about one nanosecond's duration, to study the Plasma Focus has provided significant additions to our knowledge of this type of plasma.

The schlieren technique was found to be valuable in distinguishing electron-density gradients in the Plasma Focus discharge. However, for a detailed study of the dynamics of the discharge and for obtaining quantitative values of electron density, shadowgraphy and interferometry, respectively, were preferable.

The interferometric technique used in these studies had a high temporal and spatial resolution. This enabled the plasma electron-density profile to be determined unambiguously through the various phases of the discharge and at a variety of axial locations - a hitherto unaccomplished task. From these density profiles, the plasma line-density has been calculated so that the absolute number of particles in a unit length of plasma column is known. This is a necessary parameter in calculating, for example, the thermonuclear reaction rate in the dense pinch and the absolute level of density fluctuations in the plasma, at any time, due to ion thermal motion. Thus, comparisons may be made with experimentally-determined neutron fluxes and with the level of density fluctuations measured in light scattering experiments, leading to a better understanding of the micro processes in the plasma. Finally, the overall rate of loss or gain of particles by the plasma through the various phases of the discharge has been determined, giving an insight into the mechanisms responsible for the creation of the hot dense pinch.

By using a shadowgraph technique which permitted three time-separated exposures to be made during a single discharge, the behaviour of the plasma-vacuum boundary has been studied with far greater clarity than had previously been attained. This enabled the dynamics of the formation and disruption of the dense pinch to be established. Accurate values of the velocity and acceleration of the plasma-vacuum boundary have been obtained, especially during the collapse of the current-carrying sheet to the gun axis. Also, the growth of plasma instabilities during different phases of the discharge has been investigated, and the overall lifetime of the dense pinch measured. From observations on the growth of acceleration-driven instabilities during the collapse phase, the deuterium ion temperature has been estimated.

It has been difficult to compare the results of these optical studies with those of other groups operating Plasma Focus devices, for two reasons: Firstly, the majority of the results presented in these studies are new, and up to the present there have been few other experimental measurements with which to make a comparison. Secondly, because no two devices are of the same geometrical construction nor are they operated under the same initial conditions, even where similar measurements to those reported here have been made, a detailed comparison is usually not meaningful. However, the results obtained using a numerical two-dimensional fluid code, Potter (1971), to simulate a Plasma Focus discharge, have been compared with the present results. The code was written for a Focus device of identical geometry to the one used here, and good agreement between theory and experiment has been obtained.

7.2 LIMITATIONS IN THE EXPERIMENTAL METHODS, AND SUGGESTIONS FOR FUTURE OPTICAL STUDIES

The results obtained from the optical studies were subject to a number of limitations in the experimental methods. These limitations are considered in turn and suggestions are made for improvements.

(i) In the interferometric study, each electron-density profile in the time sequences produced was obtained for a separate discharge, since only one interferogram could be obtained per discharge, as in section 5.2. If at least three time-separated interferograms were obtained during each discharge, the temporal variation of electron density could be followed more precisely. It would be impossible to achieve this by using a Mach-Zehnder interferometer with an optical time-delay system similar to that described in section 4.3.1, since the strict conditions for interference could only be satisfied for one out of the three sets of beams. However, the technique of holographic interferometry, Jahoda and Sawyer (1971), could be used with such a time-delay system to produce multiple interferograms during a discharge.

(ii) It was not possible to observe phenomena over a radial distance greater than 4.3 cm, because of the field-of-view limitation imposed by the input and output apertures of the Plasma Focus discharge chamber. Thus, the behaviour and form of the return current-sheet to the outer electrode, of diameter 10 cm, was not known precisely. This caused some difficulty in interpreting results, since in all the optical studies the probing laser beam passed twice through the return current-sheet. However, intuitively this current sheet should be similar in form to the radially-imploding current sheet at early times during the collapse phase. In addition, because of the narrow field-of-view, it was only possible to observe the diffuse-pinch phase with difficulty, and to observe the later stages of the collapse phase. A discharge chamber with ports sufficiently

large to give a field of view wider than the outer electrode diameter would be a very useful facility. Then, in interferometric studies, the undisturbed background fringes outside the Focus gun could be recorded and used as an unambiguous reference. Also, during the diffuse-pinch phase, the whole extent of the broad plasma column could be observed. Finally, the collapse phase could be followed completely from beginning to end.

(iii) To eliminate the effect of non-electronic refractivity in interferometric measurements made during the collapse phase, when unionized atoms are trapped within the collapsing current-sheet, it is necessary to take simultaneous interferograms of the plasma at two different wavelengths, Alcock and Ramsden (1966). Also, the effect of the non-electronic species at other times during the discharge could then be checked. Referring to section 3.2, the refractivity of an electron gas varies as λ^2, all other factors remaining constant, while the refractivities of the dominant non-electronic species are only dependent on λ to the second order. Thus, the contribution of the latter species to the total refractivity could be evaluated. Two wavelengths with sufficient separation can be obtained simultaneously when using a Q-switched ruby laser by converting about 15% of its output to the second harmonic of the fundamental at 6943 Å. This is achieved by illuminating a uniaxial crystal, such as ADP or KDP, with the output of the laser, Wang and Racette (1965) and Pressley (1971).

(iv) On interferograms obtained during the dense-pinch phase, it was not always possible to resolve the fringe shifts in regions of high compression. This was due to one or more of the following reasons:

(a) Motion of these plasma regions during the 1 nsec exposure.

(b) Deflections of the test beam by steep gradients of n_e in these regions.

(c) Fringe crowding due to n_e being very high.

The time resolution could be improved by approximately a maximum of four by careful optimisation of the pulse-clipping circuit used with the laser, as discussed by Morgan and Peacock (1971).

The effects due to laser beam deflections and to fringe crowding could be simultaneously reduced by using light of a shorter wavelength than 6943 Å. Referring to sections 3.3.1 and 3.3.3, the beam deflection $\theta \propto \lambda^2$ and the fringe shift $s \propto \lambda$, all other factors being unchanged. By using a suitable uniaxial crystal, the second harmonic of the ruby laser output could be generated. By means of two such crystals in series, the fourth harmonic could be generated, i.e. $\lambda = 1736$ Å, but the conversion efficiency would be about 2%.

(v) During the diffuse-pinch phase, at the peak of the soft X-ray emission, the plasma was found to be approximately 4 cm in radial extent and had a peak electron density of about 10^{17} cm^{-3}. Such a plasma was difficult to detect with precision by interferometry because of the small fringe shifts involved, $s \sim 1$. By using radiation of wavelength longer than the 6943 Å used, increased sensitivity could be obtained since $s \propto \lambda$. A pulsed carbon dioxide laser working at 10.6 μm would be a suitable radiation source, because such a laser can produce a pulse of several hundred MW power and of duration a few nanoseconds. Using a CO_2 laser would give an increase in sensitivity of about 15. However, detection of 10.6 μm radiation is not as simple as detection of optical wavelengths, because photographic emulsions do not respond at this long wavelength. The most common approach to recording fringe patterns at infra-red wavelengths is to use films of Bi, Sb or Cd, of about 100 Å thickness, deposited on a glass substrate, Braun (1972). Detection is by local evaporation of the film. Sensitivities of about 0.5J cm^{-2} and resolutions of about 150 lines/mm have been achieved, the latter being sufficient for holographic purposes.

(vi) In the shadowgraph study, it would have been advantageous to have increased the number of exposures per discharge from three to five or six. This would have permitted a more detailed study of the dynamics of the discharge.

Optical diagnostic techniques incorporating the improvements suggested above would form a sound basis for future detailed studies of the Plasma Focus. In particular, much of the current effort on Plasma Focus is concentrated on the diffuse-pinch phase, the present understanding of which is superficial only, and it is here that the application of optical techniques is likely to prove very fruitful.

7.3 SUMMARY OF CONCLUSIONS FROM OPTICAL STUDIES

The main conclusions derived from the optical studies are now summarised :

(i) During the collapse phase, when the current-carrying plasma sheet is imploding radially inwards at a velocity which may be as great as 4×10^7 cm sec^{-1}, the particle line-density in the plasma remains remarkably constant. This is due to an equilibrium being established between the gain of particles by the snow-ploughing action of the imploding sheet, on the one hand, and the loss of particles by mass flow in an axial direction, on the other. Only about 5% of the particles that are initially enclosed by the collapsing current-sheet are compressed into the dense pinch. The loss of the majority of the particles during the collapse is an important mechanism. It results in the energy present in the driving azimuthal magnetic field being fed into the relatively small number of residual particles, with the attainment of high temperatures and densities in the pinch which is formed.

(ii) Acceleration-driven (or Rayleigh-Taylor) instabilities form at the plasma-vacuum boundary during the collapse phase, when the plasma is

accelerated towards the axis at up to 4×10^{15} cm sec^{-2}. The effect of the plasma viscosity is to damp out the instabilities of shortest wavelengths, and as a result an instability of a certain critical wavelength has the highest growth rate. From observations on the growth of this instability of dominant wavelength, a deuterium ion temperature of about 70 eV has been estimated. The instabilities have too slow a growth rate to cause serious disruptions to the current sheet. However, the resulting perturbations develop into sausage-type instabilities as the dense-pinch is formed.

(iii) In the dense pinch, peak electron densities of about 3.4×10^{19} cm^{-3} have been determined for a pinch of radius about 0.1 cm. This represents an increase in density of about 150 above the initial density of atoms in the gas filling.

(iv) The dense pinch is not formed simultaneously over its whole length, but consists of a succession of local regions of dense plasma produced, initially adjacent to the anode, at the axis. Each region is a few millimetres in axial extent, and is produced progressively further away from the anode than the preceding region. The lifetime of any one such region is about 5 nsec. This is the same magnitude as the growth time of a sausage-type instability in the dense plasma. Such instabilities cause the disruption of the regions of dense plasma.

(v) After a delay of about 200 nsec from the start of the dense-pinch phase, a pulse of soft X-rays and a pulse of neutrons are emitted. Then, the plasma is so rarefied that it is barely detectable using optical systems optimised to study the dense pinch. From interferometry, the peak density in this diffuse plasma has been estimated as 1.5×10^{17} cm^{-3}, with a radius of 2 cm.

APPENDIX 1

THE NOTATION

The symbols used in the text are defined. CGS (e.s.u.) units are used throughout, unless otherwise stated.

a	Amplitude
B	Magnetic field
c	Velocity of light
C	Capacitance
d	Diameter
e	Electronic charge
E	Electric field
f	Focal length
g	Acceleration
I	Current; intensity
j,J	Current density
k	Boltzmann constant; wave number
K	Specific refractivity
ℓ,L	Length
L	Inductance
m	Particle mass
n	Particle density; refractive index
N	Particle line density
p	Pressure
p_o	Initial pressure
P	Power
r,R	Radius
s	Fringe shift
t	Time
T	Temperature
v	Velocity
v_d	Drift velocity, $\underline{E}\times\underline{B}/cB^2$
v_m	Centre of mass velocity
v_s	Sound speed, $(\gamma p/\rho)^{\frac{1}{2}}$
v_{te}	Electron thermal velocity, $(kT_e/m_e)^{\frac{1}{2}}$
V	Voltage
W	Energy
Z	Charge

β	Beta, $p/(p + B_i^2/8\pi)$
γ	Ratio of specific heats
λ	Wavelength
μ	Coefficient of dynamic viscosity
ν	Coefficient of kinematic viscosity
ρ	Mass density
σ	Standard deviation
τ	Characteristic time; growth time
τ_{ei}	Electron-ion collision time
τ_{ii}	Ion-ion collision time
ω	Angular frequency
ω_{ce}	Electron cyclotron frequency, $eB/m_e c$
ω_{ci}	Ion cyclotron frequency, $ZeB/m_i c$
ω_{pe}	Electron plasma frequency, $(4\pi n_e e^2/m_e)^{\frac{1}{2}}$
ω_{pi}	Ion plasma frequency, $(4\pi n_i Z^2 e^2/m_i)^{\frac{1}{2}}$

Subscripts

e	Electron; external to the plasma
i	Ion; internal (inside the plasma)
r, θ, z	Components in cylindrical coordinates
x, y, z	Components in Cartesian coordinates

APPENDIX 2

DERIVATION OF THE DISPERSION RELATION FOR AN E.M. WAVE PROPAGATING THROUGH A FULLY-IONIZED PLASMA

Consider the propagation, in the z direction in a Cartesian coordinate system, of a transverse electromagnetic wave of small amplitude through an infinite homogeneous fully-ionized plasma, in which collision processes are dominant. A steady magnetic field is applied in the direction of propagation.

The e.m. wave exerts a force on the electrons and ions as it propagates through the plasma. This force gives rise to accelerations of the charges which in turn modify the time-varying e.m. field components of the wave, thereby altering its characteristics. In general, the magnetic forces exerted by an e.m. wave are much weaker than the electric forces, and in the following derivation the magnetic field of the wave is neglected.

Self-consistent solutions for the e.m. wave in the plasma can be obtained by solving Maxwell's equations, together with the Lorentz force equation of motion for charged particles in an e.m. field under the influence of a steady magnetic field. The plane wave solutions for the electric field propagating in the z direction are of the form

$$\underline{E}(z,t) = \underline{E}_0 \exp\left[i(kz - \omega t)\right] , \qquad \ldots (A2.1)$$

where the real part of $\underline{E}$ represents the physical quantity. The wave number $k = 2\pi/\lambda$ defines the space periodicity or wavelength λ, and ω is the wave angular frequency.

The first step in deriving the dispersion relation is to derive the general wave equation for the electric field from Maxwell's equations. Since it is convenient to treat all charges and currents explicitly, Maxwell's equations may be written in terms of total charges and currents:

$$\underline{\nabla} \times \underline{E} = - \frac{1}{c} \frac{\partial \underline{B}}{\partial t} \qquad \ldots (A2.2)$$

$$\underline{\nabla} \times \underline{B} = \frac{1}{c}\left(4\pi \underline{J} + \frac{\partial \underline{E}}{\partial t}\right) \qquad \ldots (A2.3)$$

$$\underline{\nabla} \cdot \underline{E} = 4\pi \rho \qquad \ldots (A2.4)$$

$$\underline{\nabla} \cdot \underline{B} = 0 \ , \qquad \ldots (A2.5)$$

where ρ and $\underline{J}$ refer, respectively, to the total charge and current densities.

Taking the curl of both sides of equation (A2.2) and substituting for $\underline{\nabla}\times\underline{B}$ from equation (A2.3)

$$\underline{\nabla} \times (\underline{\nabla}\times\underline{E}) = - \frac{1}{c^2}\left(4\pi \frac{\partial \underline{J}}{\partial t} + \frac{\partial^2 \underline{E}}{\partial t^2}\right) .$$

Using the vector identity $\underline{\nabla} \times (\underline{\nabla}\times\underline{E}) = \underline{\nabla}(\underline{\nabla} \cdot \underline{E}) - \underline{\nabla}^2\underline{E}$ and substituting for $\underline{\nabla} \cdot \underline{E}$ from equation (A2.4), the above equation may be written

$$\underline{\nabla}^2\underline{E} - 4\pi\underline{\nabla}\rho - \frac{4\pi}{c^2} \frac{\partial \underline{J}}{\partial t} - \frac{1}{c^2} \frac{\partial^2 \underline{E}}{\partial t^2} = 0 \ ,$$

which is the general wave equation. For the case of a transverse e.m. wave $\underline{k} \cdot \underline{E} = 0$, and hence combining equations (A2.1) and (A2.4) it is seen that $\rho = 0$. The wave equation is then

$$\underline{\nabla}^2\underline{E} - \frac{4\pi}{c^2} \frac{\partial \underline{J}}{\partial t} - \frac{1}{c^2} \frac{\partial^2 \underline{E}}{\partial t^2} = 0 \ . \qquad \ldots (A2.6)$$

Before the above equation can be solved, it is necessary to establish the relationship between $\underline{J}$ and $\underline{E}$. Ignoring for the moment the presence of the external magnetic field and the effect of particle collisions, the forces exerted on the electrons and ions, respectively, are

$$m_e \dot{\underline{v}}_e = - e\underline{E} \ , \qquad \ldots (A2.7)$$

$$m_i \dot{\underline{v}}_i = - Ze\underline{E} \ . \qquad \ldots (A2.8)$$

The total current density is

$$\underline{J} = e(n_i Z \underline{v}_i - n_e \underline{v}_e) \ .$$

Thus,

$$\frac{\partial \underline{J}}{\partial t} = e(n_i Z \dot{\underline{v}}_i - n_e \dot{\underline{v}}_e) \ .$$

Substituting equations (A2.7) and (A2.8) into the above

$$\frac{\partial \underline{J}}{\partial t} = e^2\left(\frac{n_i Z^2}{m_i} + \frac{n_e}{m_e}\right)\underline{E} = n_e e^2\left(\frac{Z}{m_i} + \frac{1}{m_e}\right)\underline{E} ,$$

since $n_i Z = n_e$. Because $m_i/Z \gg m_e$ we may write

$$\frac{\partial \underline{J}}{\partial t} = \frac{n_e e^2}{m_e}\underline{E} ,$$

i.e. the ion contribution can be ignored in determining a relationship between $\underline{J}$ and $\underline{E}$, because of the large disparity between the electron and ion masses.

Returning to the case of a plasma with an applied static magnetic field of strength B_o in the z direction, and considering the effect of collisions between the electrons and ions, characterised by a frequency ν, the equation of motion of the electrons is

$$m_e \dot{\underline{v}}_e = -e\left[\underline{E}(t) + \frac{1}{c}\left(\underline{v}_e \times \underline{B}_o\right)\right] - \nu m_e \underline{v}_e .$$

As above, the ion contribution can be neglected. Consequently, the subscript e may be dropped. For an oscillating electric field $\underline{E}$ varying as $\exp(-i\omega t)$, the electron velocity $\underline{v}$ will have the same time dependence as $\underline{E}$, i.e.

$$\underline{v} = \underline{v}_o \exp(-i\omega t)$$
$$\dot{\underline{v}} = -i\omega \underline{v} . \qquad \ldots (A2.9)$$

Substituting equation (A2.9) into the electron equation of motion, the latter equation may be written explicitly in terms of three scalar equations.

$$\left.\begin{aligned} (\nu - i\omega)\, v_x + \left(\frac{eB_o}{mc}\right) v_y &= -\frac{e}{m} E_x , \quad \ldots a \\ (\nu - i\omega)\, v_y - \left(\frac{eB_o}{mc}\right) v_x &= -\frac{e}{m} E_y , \quad \ldots b \\ (\nu - i\omega)\, v_z &= -\frac{e}{m} E_z . \quad \ldots c \end{aligned}\right\} \qquad \ldots (A2.10)$$

The third equation in set (A2.10) is not concerned with the transverse effects of the field $\underline{E}$. Since this equation is decoupled from the other two, it may be ignored. The quantity eB_o/mc is the electron

cyclotron frequency ω_{ce}. Multiplying equation b by i and adding to a

$$(\nu - i\omega)(v_x + i v_y) - i\,\omega_{ce}(v_x + i v_y) = -\frac{e}{m}(E_x + i E_y) .$$

Multiplying equation b by i and subtracting from a

$$(\nu - i\omega)(v_x - i v_y) + i\,\omega_{ce}(v_x - i v_y) = -\frac{e}{m}(E_x - i E_y) .$$

The above two equations may be combined by adopting the following notation: $v_+ = v_x + i v_y$, $v_- = v_x - i v_y$, $E_+ = E_x + i E_y$ and $E_- = E_x - i E_y$. Hence,

$$(\nu - i\,\omega \mp i\,\omega_{ce})\, v_\pm = -\frac{e}{m} E_\pm$$

and

$$v_\pm = -\frac{e}{m} E_\pm / (\nu - i(\omega \pm \omega_{ce})) . \qquad \ldots (A2.11)$$

The complex current due to the electrons is

$$J_\pm = -n_e e v_\pm = n_e e^2 E_\pm / m\,(\nu - i(\omega \pm \omega_{ce})) .$$

Substituting the above equation into equation (A2.6)

$$\underline{\nabla}^2 E_\pm - \frac{4\pi n_e e^2}{mc^2(\nu - i(\omega \pm \omega_{ce}))} \frac{\partial E_\pm}{\partial t} - \frac{1}{c^2} \frac{\partial^2 E_\pm}{\partial t^2} = 0 . \qquad \ldots (A2.12)$$

Substituting equation (A2.1), which represents the time and space variation of the electric field, into equation (A2.12) and denoting the quantity $4\pi n_e e^2/m$ by ω_{pe}^2, the electron plasma frequency, we obtain

$$-k^2 - \frac{\omega_{pe}^2}{c^2} \frac{i\omega}{(\nu - i(\omega \pm \omega_{ce}))} + \frac{\omega^2}{c^2} = 0 .$$

Hence

$$k^2 - \frac{\omega^2}{c^2}\left[1 - \frac{\omega_{pe}^2/\omega}{\omega \pm \omega_{ce} + i\nu}\right] = 0 . \qquad \ldots (A2.13)$$

The above equation is of the form

$$k^2 - \frac{\omega^2}{c^2}\,\epsilon'(\omega) = 0 .$$

This is the dispersion relation, the equation relating the wave frequency and the wave number in terms of the complex dielectric constant $\epsilon'(\omega)$. Hence, from equation (A2.13)

$$\epsilon' = 1 - \frac{\omega_{pe}^2}{\omega} \cdot \frac{\omega \pm \omega_{ce} - i\nu}{(\omega \pm \omega_{ce})^2 + \nu^2} . \qquad \ldots (A2.14)$$

The refractive index is related to the complex dielectric constant by

$$n = \Re e\ (\epsilon')^{\frac{1}{2}} .$$

If $\epsilon' = \alpha + i\beta$, then

$$n = \Re e\ (\alpha + i\beta)^{\frac{1}{2}} = \left(\tfrac{1}{2}\alpha + \tfrac{1}{2}(\alpha^2 + \beta^2)^{\frac{1}{2}}\right)^{\frac{1}{2}} .$$

Hence, from equation (A2.14)

$$n = \Re e\left[1 - \frac{\omega_{pe}^2}{\omega} \cdot \frac{\omega \pm \omega_{ce}}{(\omega \pm \omega_{ce})^2 + \nu^2} + i\,\frac{\omega_{pe}^2}{\omega} \cdot \frac{\nu}{(\omega \pm \omega_{ce})^2 + \nu^2}\right]^{\frac{1}{2}} ,$$

i.e.

$$n = \left\{\tfrac{1}{2}\left(1 - \frac{\omega_{pe}^2}{\omega} \cdot \frac{\omega \pm \omega_{ce}}{(\omega \pm \omega_{ce})^2 + \nu^2}\right) + \tfrac{1}{2}\left(\left[1 - \frac{\omega_{pe}^2}{\omega} \cdot \frac{\omega \pm \omega_{ce}}{(\omega \pm \omega_{ce})^2 + \nu^2}\right]^2 + \left[\frac{\omega_{pe}^2}{\omega} \cdot \frac{\nu}{(\omega \pm \omega_{ce})^2 + \nu^2}\right]^2\right)^{\frac{1}{2}}\right\}^{\frac{1}{2}} .$$

This is the refractive index of a fully-ionized collision-dominated plasma for an e.m. wave propagating parallel to an applied steady magnetic field.

APPENDIX 3

DERIVATION OF THE GROWTH RATE OF THE CLASSICAL RAYLEIGH-TAYLOR INSTABILITY

Consider a fluid in a Cartesian coordinate system. Let $\underline{v}$ be the velocity of the fluid at the point (x,y,z) and the time t, and let p be the pressure, ρ the density and $\underline{F}$ the external force per unit mass, at the same position and instant of time. The equation of motion of the fluid is

$$\left(\frac{\partial}{\partial t} + \underline{v} \cdot \underline{\nabla}\right) \underline{v} = \underline{F} - \frac{1}{\rho} \underline{\nabla} p \ .$$

The equation of continuity is

$$\left(\frac{\partial}{\partial t} + \underline{v} \cdot \underline{\nabla}\right) \rho + \rho \underline{\nabla} \cdot \underline{v} = 0 \ .$$

Suppose the external force has a potential Ω such that $\underline{F} = - \underline{\nabla} \Omega$. The potential Ω denotes the potential energy, per unit mass, at the point (x,y,z), in respect of the force acting at a distance. Furthermore, if the velocity of the fluid can be expressed in terms of a velocity potential φ, i.e. $\underline{v} = - \underline{\nabla} \varphi$, then for the case of constant fluid density, or the density being a definite function of pressure, the equation of motion may be integrated, Lamb (1962), to give:

$$\frac{\partial \varphi}{\partial t} = p/\rho + \Omega + \tfrac{1}{2} v^2 \ . \qquad \ldots \ (A3.1)$$

In the case of an incompressible fluid, the equation of continuity reduces to

$$\underline{\nabla} \cdot \underline{v} = - \underline{\nabla} \cdot \underline{\nabla} \varphi = 0 \ ,$$

i.e.

$$\underline{\nabla}^2 \varphi = 0 \ . \qquad \ldots \ (A3.2)$$

We next consider perturbations of the horizontal boundary between two incompressible nonviscous fluids, which are otherwise unlimited, acted on by a gravitational field, g, which is perpendicular to the interface. Consider a rectangular frame of reference such that the interface lies along the xy plane at $z = 0$, with the gravitational field acting in the $-z$ direction. The densities of the two fluids are ρ_1 and ρ_2, the

subscript 1 referring to the upper fluid, and conversely. The fluids are constrained to move in two dimensions only, the y and z directions.

Let the interface be subjected to a periodic perturbation such that, if η denotes the elevation of the surface above the point $(y,0)$ at any time t, the equation of the disturbed surface is

$$\eta = a \exp i\,(ky - \omega t) \; . \qquad \ldots \text{(A3.3)}$$

The wave number $k = 2\pi/\lambda$ defines the space periodicity or wavelength λ in the y direction, and ω is the frequency of the disturbance. Setting the potential $\Omega = g z$ in equation (A3.1), and assuming the amplitude a of the disturbance is sufficiently small to be able to neglect the term in v^2, we obtain for the two fluids

$$\begin{aligned} p/\rho_1 &= \frac{\partial \varphi_1}{\partial t} - g z \\ p/\rho_2 &= \frac{\partial \varphi_2}{\partial t} - g z \end{aligned} \; . \qquad \ldots \text{(A3.4)}$$

At the interface, the normal component of the fluids' velocities must be equal to the normal velocity of the surface itself. Thus, with sufficient accuracy,

$$\frac{\partial \eta}{\partial t} = - \left[\frac{\partial \varphi_1}{\partial z}\right]_{z=o} = - \left[\frac{\partial \varphi_2}{\partial z}\right]_{z=0} \; . \qquad \ldots \text{(A3.5)}$$

Also, equation (A3.2) must be satisfied in the y and z directions for the two fluids, i.e.

$$\frac{\partial^2 \varphi}{\partial y^2} + \frac{\partial^2 \varphi}{\partial z^2} = 0 \; .$$

We choose potentials for the two fluids which satisfy the above equation, i.e.

$$\begin{aligned} \varphi_1 &= C_1 \exp(-k z + i(k y - \omega t)) \\ \varphi_2 &= C_2 \exp(k z + i(k y - \omega t)) \end{aligned} \; , \qquad \ldots \text{(A3.6)}$$

and which vanish at $z = +\infty$ and $z = -\infty$, respectively.

Substituting for φ_1 and φ_2 from equation (A3.6) and for η from equation (A3.3) into equations (A3.5),

$$- a i \omega = C_1 k = - C_2 k . \qquad \ldots (A3.7)$$

At the interface there is continuity of pressure. Thus, equating the two halves of equation (A3.4)

$$\rho_1 \left\{ \frac{\partial \varphi_1}{\partial t} - g z \right\} = \rho_2 \left\{ \frac{\partial \varphi_2}{\partial t} - g z \right\} .$$

Substituting for φ_1 and φ_2 from equation (A3.6) into the above, and in the limit of small perturbations $a \simeq z = 0$

$$\rho_1 \left\{ - C_1 i \omega - g a \right\} = \rho_2 \left\{ - C_2 i \omega - g a \right\} .$$

Substituting the values of C_1 and C_2 from equation (A3.7) into the above, we have

$$\rho_1 \frac{\omega^2}{k} + \rho_1 g = - \rho_2 \frac{\omega^2}{k} + \rho_2 g .$$

Hence,

$$\omega^2 = g k \frac{(\rho_2 - \rho_1)}{(\rho_2 + \rho_1)} . \qquad \ldots (A3.8)$$

In the above equation, if $\rho_1 > \rho_2$ then $\sqrt{\omega^2}$ is imaginary and is equal to $i \omega$, say. Then, the amplitude of the disturbance grows exponentially in time as $\eta = a \exp(\omega t)$. This is the classical Rayleigh-Taylor instability at the interface of two infinitely-extended fluids, when the system is undergoing a constant acceleration directed from the lighter towards the heavier fluid, Taylor (1950).

REFERENCES

AGAFONOV, V.I., GOLUB, G.V., GOLUBCHIKOV, L.G., DYACHENKO, V.F., IVANOV, V.D., IMSHENNIK, V.S., KOLESNIKOV, Yu.A., SVIRSKII, E.B., FILIPPOV, N.V. and FILIPPOVA, T.I., (1968). 3rd IAEA Conference on Plasma Physics and Controlled Nuclear Fusion Research, Novosibirsk. Proceedings, 2, pp.21-37.

ALCOCK, A.J. and RAMSDEN, S.A., (1966). Appl. Phys. Lett., 8, (8), pp.187-188.

ALCOCK, A.J. and RICHARDSON, M.C., (1968). Phys. Rev. Lett., 21, (10), pp.667-670.

ALCOCK, A.J., DeMICHELIS, C. and HAMAL, K., (1968). Appl. Phys. Lett., 12, (4), pp.148-150.

ALCOCK, A.J. and RICHARDSON, M.C., (1970). Opt. Commun., 2, (2), pp.65-68.

ALLEN, C.W., (1963). 'Astrophysical Quantities'. Athlone Press (2nd ed.).

ANDRIANOV, A.M., BAZILEVSKAYA, O.A. and PROKHOROVA, Yu.G., (1960). 'Plasma Physics and the Problem of Controlled Thermonuclear Reactions', 4, pp.213-235. Editor M.A. Leontovich. Pergamon Press.

ASCOLI-BARTOLI, U. and MARTELLUCCI, S., (1963). Nuovo Cimento, 27, (2), pp.475-496.

ASCOLI-BARTOLI, U., MARTELLUCCI, S. and MAZZUCATO, E., (1963). 6th Int. Conf. on Ionization Phenomena in Gases, Paris. Proceedings, 4, pp.97-103.

ASCOLI-BARTOLI, U., MARTELLUCCI, S. and MAZZUCATO, E., (1964). Nuovo Cimento, 32, (2), pp.298-316.

BASOV, N.G., KROKHIN, O.N. and SKLIZKOV, G.V., (1967). Appl. Opt., 6, (11), 1814-1817.

BEAMS, J.W., (1955). 'Shadow and Schlieren Methods'. High Speed Aerodynamics and Jet Propulsion, 9, (Physical Measurements in Gas Dynamics and Combustion), pp.26-46. Editors R.W. Ladenburg, B. Lewis, R.N. Pease and H.S. Taylor. Oxford University Press.

BENNETT, F.D., CARTER, W.C. and BERGDOLT, V.E., (1952). J. Appl. Phys., 23, (4), pp.453-469.

BERNARD, A., COUDEVILLE, A. and WATTEAU, J.P., (1970). Phys. Lett., 33A, (8), pp.477-478.

BERNARD, A., CESARI, G., COUDEVILLE, A., JOLAS, A., de MASCUREAU, J. and WATTEAU, J.P., (1971). 4th IAEA Conference on Plasma Physics and Controlled Nuclear Fusion Research, Madison. Proceedings, 1, pp.553-560.

BERNARD, A., COUDEVILLE, A., DURANTET, J., JOLAS, A., LAUNSPACH, J., de MASCUREAU, J. and WATTEAU, J.P., (1972). 2nd Topical Conference on Pulsed High-Beta Plasmas, Garching. Proceedings, pp.147-150. (Max-Planck-Institut für Plasmaphysik Report IPP 1/127).

BERNARD, A., JOLAS, A., LAUNSPACH, J. and WATTEAU, J.P., (1973). Plasma Physics, 15, (10), pp.1019-1030.

BERNSTEIN, M.J., (1970). Phys. Fluids, 13, (11), pp.2858-2866.

BIRKHOFF, G., (1954). 'Taylor Instability and Laminar Mixing'. Los Alamos Scientific Laboratory Report LA-1862.

BOCKASTEN, K., (1961). J. Opt. Soc. Amer., 51, (9), pp.943-947.

BORN, M. and WOLF, E., (1970). 'Principles of Optics'. Pergamon Press (4th edition).

BOSTICK, W.H., GRUNBERGER, L. and PRIOR, W., (1969). 3rd European Conference on Controlled Fusion and Plasma Physics, Utrecht. Proceedings, p.120.

BOTTOMS, P.J., CARPENTER, J.P., MATHER, J.W., WARE, K.D. and WILLIAMS, A.H., (1968). 3rd I A E A Conference on Plasma Physics and Controlled Nuclear Fusion Research, Novosibirsk. Proceedings, 2, pp.67-75.

BRADLEY, D.J., HIGGINS, J.F., KEY, M.H. and MAJUMDAR, S., (1969). Opto-Electronics, 1, (1), pp.62-64.

BRAUN, W., (1972). 5th European Conference on Controlled Fusion and Plasma Physics, Grenoble. Proceedings, 1, p.56.

CARMAN, R.L., REINTJES, J. and FURUMOTO, H., (1970). I E E E J. Quantum Electron., QE-6, (11), pp.751-752.

CURZON, F.L., FOLKIERSKI, A., LATHAM, R. and NATION, J.A., (1960). Proc. Roy. Soc. London, 257A, pp.386-401.

DYACHENKO, V.F. and IMSHENNIK, V.S., (1969). Soviet Physics - JETP, 29, (5), pp.947-953.

FILIPPOV, N.V., FILIPPOVA, T.I. and VINOGRADOV, V.P., (1962). Nuclear Fusion, suppl. pt.2, pp.577-587.

FILIPPOV, N.V. and FILIPPOVA, T.I., (1965). 2nd I A E A Conference on Plasma Physics and Controlled Nuclear Fusion Research, Culham. Proceedings, 2, pp.405-416.

FILIPPOV, N.V., AGAFONOV, V.I., BELYAEVA, I.F., VIKHREV, V.V., GRIBKOV, V.A., GOLUBCHIKOV, L.G., DYACHENKO, V.F., IMSHENNIK, V.S., IVANOV, V.D., KROKHIN, O.N., MOISEEVA, M.P., SKLIZKOV, G.V. and FILIPPOVA, T.I., (1971). 4th I A E A Conference on Plasma Physics and Controlled Nuclear Fusion Research, Madison. Proceedings, 1, pp.573-600.

FORREST, M.J., NORTON, B.A. and PEACOCK, N.J., (1973). 6th European Conference on Controlled Fusion and Plasma Physics, Moscow. Proceedings, 1, pp.363-366.

GLASSTONE, S. and LOVBERG, R.H., (1960). 'Controlled Thermonuclear Reactions'. Van Nostrand.

GRATREAU, P., LUZZI, G., MAISONNIER, Ch., PECORELLA, F., RAGER, J.P., ROBOUCH, B.V. and SAMUELLI, M., (1971). 4th IAEA Conference on Plasma Physics and Controlled Nuclear Fusion Research, Madison. Proceedings, 1, pp.511-521.

GREEN, T.S. and NIBLETT, G.B.F., (1960). Nuclear Fusion, 1, (1), pp.42-46.

GRIBKOV, V.A., KORZHAVIN, V.M., KROKHIN, O.N., SKLIZKOV, G.V., FILIPPOV, N.V. and FILIPPOVA, T.I., (1972). Soviet Physics - JETP Lett., 15, (6), pp.232-234.

GRIBKOV, V.A., KROKHIN, O.N., SKLIZKOV, G.V., FILIPPOV, N.V. and FILIPPOVA, T.I., (1973). Pisma v Zh. Eksp. Teor. Fiz., 18, (1), pp.11-15.

HARRIS, E.G., (1962). Phys. Fluids, 5, (9), pp.1057-1062.

HOOK, W.R., HILBERG, R.P. and DISHINGTON, R.H., (1966). Proc. IEEE, 54, (12), pp.1954-1955.

HOUSE, L.L., (1963). Astrophys. J., suppl. series, 8, pp.307-328.

JAHODA, F.C., LITTLE, E.M., QUINN, W.E., RIBE, F.L. and SAWYER, G.A., (1964). J. Appl. Phys., 35, (8), pp.2351-2363.

JAHODA, F.C. and SAWYER, G.A., (1971). 'Optical Refractivity of Plasmas'. Methods of Experimental Physics, 9, pt.B, pp.1-48. Editors H.R. Griem and R.H. Lovberg. Academic Press.

JEFFREY, A. and TANIUTI, T., (1966). 'Magnetohydrodynamic Stability and Thermonuclear Containment'. Academic Press.

KAUFMAN, A.N., (1960). Phys. Fluids, 3, (4), pp.610-616.

KINDER, W., (1946). Optik, 1, (6), pp.413-448.

KOLESNIKOV, Yu.A., FILIPPOV, N.V. and FILIPPOVA, T.I., (1966). 'Dynamics of the Plasma Envelope of a Non-Cylindrical Z-Pinch up to the Instant of Implosion'. I.V. Kurchatov Institute Report 18/904.

KRUSKAL, M. and SCHWARZSCHILD, M., (1954). Proc. Roy. Soc. Lond., 223A, pp.348-360.

LADENBURG, R. and BERSHADER, D., (1955). 'Interferometry'. High Speed Aerodynamics and Jet Propulsion, 9, (Physical Measurements in Gas Dynamics and Combustion), pp.47-78. Editors R.W. Ladenburg, B. Lewis, R.N. Pease and H.S. Taylor. Oxford University Press.

LAFFERTY, D.L., GATES, D.C. and HINRICHS, C.K., (1968). Bull. Amer. Phys. Soc., 13, (11), p.1544.

LAMB, H., (1962). 'Hydrodynamics'. Cambridge University Press (6th edition).

LASHMORE-DAVIES, C.N. and MARTIN, T.J., (1973). Nucl. Fusion, 13, (2), pp.193-203.

LIEPMANN, H.W. and ROSHKO, A., (1957). 'Elements of Gasdynamics'. Wiley and Sons.

LONG, J.W., PEACOCK, N.J. and WILCOCK, P.D., (1967). APS Topical Conference on Pulsed High-Density Plasmas, Los Alamos. Proceedings, pp.C5-1 - C5-6. (Los Alamos Scientific Laboratory Report LA-3770).

MAISONNIER, Ch., GOURLAN, C., LUZZI, G., PAPAGNO, L., PECORELLA, F., RAGER, J.P., ROBUCH, B.V. and SAMUELLI, M., (1971). 4th IAEA Conference on Plasma Physics and Controlled Nuclear Fusion Research, Madison. Proceedings, 1, pp.523-532.

MAISONNIER, Ch., PECORELLA, F., RAGER, J.P. and SAMUELLI, M., (1972). 5th European Conference on Controlled Fusion and Plasma Physics, Grenoble. Proceedings, 2, pp.183-194.

MARSHALL, J., (1960). Phys. Fluids, 3, (1), pp.134-135.

MARTELLUCCI, S., (1967). Nuovo Cimento, suppl. 5, pp.642-679.

MATHER, J.W., (1964). Phys. Fluids, suppl., pp.S28 - S34.

MATHER, J.W., (1965a). Phys. Fluids, 8, (2), pp.366-377.

MATHER, J.W., (1965b). 2nd IAEA Conference on Plasma Physics and Controlled Nuclear Fusion Research, Culham. Proceedings, 2, pp.389-404.

MATHER, J.W. and WILLIAMS, A.H., (1966). Phys. Fluids, 9, (10), pp.2080-2082.

MATHER, J.W. and BOTTOMS, P.J., (1968). Phys. Fluids, 11, (3), pp.611-618.

MATHER, J.W., BOTTOMS, P.J., CARPENTER, J.P., WARE, K.D. and WILLIAMS, A.H., (1971). 4th IAEA Conference on Plasma Physics and Controlled Nuclear Fusion Research, Madison. Proceedings, 1, pp.561-570.

MESKAN, D.A., van PAASSEN, H.L. and COMISAR, G.G., (1967). APS Topical Conference on Pulsed High-Density Plasmas, Los Alamos. Proceedings, pp.C6-1 - C6-7. (Los Alamos Scientific Laboratory Report LA-3770).

MICHON, M., GUILLET, H., LE GOFF, D. and RAYNAUD, S., (1969). Rev. Sci. Instrum., 40, (2), pp.263-265.

MOCKER, H.W. and COLLINS, R.J., (1965). Appl. Phys. Lett., 7, (10), pp.270-273.

MORGAN, P.D., PEACOCK, N.J. and POTTER, D.E., (1969). 3rd European Conference on Controlled Fusion and Plasma Physics, Utrecht. Proceedings, p.118.

MORGAN, P.D. and PEACOCK, N.J., (1971). J. Phys. E : Sci. Instrum., 4, pp.677-680.

MORGAN, P.D. and PEACOCK, N.J., (1972). 2nd Topical Conference on Pulsed High-Beta Plasmas, Garching. Proceedings, pp.179-182. (Max-Planck-Institut für Plasmaphysik Report IPP 1/127).

MORGAN, P.D., PEACOCK, N.J., CLOTH, P., CONRADS, H., MAISONNIER, Ch., PECORELLA, F., RAGER, J.P. and SAMUELLI, M., (1973). 6th European Conference on Controlled Fusion and Plasma Physics, Moscow. Proceedings, pp.359-362.

PATOU, C., SIMMONET, A. and WATTEAU, J.P., (1967). APS Topical Conference on Pulsed High-Density Plasmas, Los Alamos. Proceedings, pp.C2-1 - C2-6. (Los Alamos Scientific Laboratory Report LA-3770).

PATOU, C., SIMONNET, A. and WATTEAU, J.P., (1969). Phys. Lett., 29A, (1), pp.1-2.

PEACOCK, N.J., WILCOCK, P.D., SPEER, R.J. and MORGAN, P.D., (1968). 3rd IAEA Conference on Plasma Physics and Controlled Nuclear Fusion Research, Novosibirsk. Proceedings, 2, pp.51-65.

PEACOCK, N.J., HOBBY, M.G. and MORGAN, P.D., (1971). 4th IAEA Conference on Plasma Physics and Controlled Nuclear Fusion Research, Madison. Proceedings, 1, pp.537-551.

PEACOCK, N.J., FORREST, M.J., HOBBY, M.G. and MORGAN, P.D., (1972). 5th European Conference on Controlled Fusion and Plasma Physics, Grenoble. Proceedings, 1, p.66.

PEACOCK, N.J. and HOBBY, M.G., (1974). To be published.

PETROV, D.P., FILIPPOV, N.V., FILIPPOVA, T.I. and KHRABROV, V.A., (1960). 'Plasma Physics and the Problem of Controlled Thermonuclear Reactions', 4, pp.198-212. Editor M.A. Leontovich. Pergamon Press.

POTTER, D.E., (1971). Phys. Fluids, 14, (9), pp.1911-1924.

POTTER, D.E. and HAINES, M.G., (1971). 4th IAEA Conference on Plasma Physics and Controlled Nuclear Fusion Research, Madison. Proceedings, 1, pp.611-620.

PRESSLEY, R.J., (1971). 'Handbook of Lasers with Selected Data on Optical Technology'. The Chemical Rubber Co. Press.

RAYLEIGH, Lord, (1899). 'Collected Papers', 2, pp.200-207, Cambridge University Press.

ROBERTS, K.V. and POTTER, D.E., (1970). 'Magnetohydrodynamic Calculations'. Methods in Computational Physics, 9, pp.339-420. Editors B. Alder, S. Fernbach and M. Rotenberg. Academic Press.

ROSENBLUTH, M., ROSENBLUTH, A. and GARWIN, R., (1954). 'Infinite Conductivity Theory of the Pinch'. Los Alamos Scientific Laboratory Report LA-1850.

SPITZER, L., (1962). 'Physics of Fully Ionized Gases'. Interscience (2nd edition).

TAYLOR, G., (1950). Proc. Roy. Soc. Lond., 201A, pp.192-196.

TSYTOVICH, V.N., (1966). Soviet Phys. - Uspekhi, 9, (9), pp.370-404.

VUYLSTEKE, A.A., (1963). J. Appl. Phys., 34, (6), pp.1615-1622.

WANG, C.C. and RACETTE, G.W., (1965). J. Appl. Phys., 36, (10), pp.3281-3284.

WEINBERG, F.J., (1963). 'Optics of Flames'. Butterworths.

WEYL, F.J., (1955). 'Analysis of Optical Methods'. High Speed Aerodynamics and Jet Propulsion, 9, (Physical Measurements in Gas Dynamics and Combustion.), pp.1-25. Editors R.W. Ladenburg, B. Lewis, R.N. Pease and H.S. Taylor. Oxford University Press.

WILKINSON, K.J.R., (1946). J. IEE, 93, pt.3A, (6), pp.1090-1112.

WONG, H.V., (1970). Phys. Fluids, 13, (3), pp.757-760.

ZADOFF, L.N. and BEGUN, M., (1968). Phys. Fluids, 11, (6), pp.1238-1244.

Reprint from

"PLASMA PHYSICS AND CONTROLLED NUCLEAR FUSION RESEARCH"

VOL. II

INTERNATIONAL ATOMIC ENERGY AGENCY
VIENNA, 1969

PROPERTIES OF THE DENSE PLASMA PRODUCED IN PLASMA FOCUS

N.J. PEACOCK, P.D. WILCOCK, R.J. SPEER* AND P.D. MORGAN**
UKAEA, CULHAM LABORATORY, ABINGDON, BERKS,
UNITED KINGDOM

Abstract

PROPERTIES OF THE DENSE PLASMA PRODUCED IN PLASMA FOCUS. The plasma produced by the focus or quasi-cylindrical magnetic compression which occurs at the open end of a metal-walled, coaxial plasma gun has been studied, using the electrical waveforms and the electromagnetic and reaction particle emission. The electromagnetic radiation in the XUV region of the spectrum has previously been briefly reported, and the present paper describes further more detailed analyses of the line emission at wavelengths shorter than 10 Å when impurities are added to the gas filling. The emission is characteristic of a plasma with a temperature of a few keV and a density greater than 10^{19} cm^{-3}, while the appearance of optical transitions in highly stripped ions, e.g. A XVIII, gives a measure of the thermalization in the plasma.

The stored electrical energy has been doubled and the scaling of the neutron emission with the applied voltage and the initial particle density is presented. The duration of the neutron and X-ray emission is considerably longer than the observed instability growth time in the plasma filament. Calculations of the mode of heating and the confinement of the plasma are compared with experimental observations.

1. INTRODUCTION

Filippov et al[2] and Mather[3] have described different versions of a metal-walled coaxial plasma gun which produces a dense pinch when operated in deuterium gas at about 1 torr pressure or higher. The pinch is accompanied by the emission of a high flux (about 10^{17} sec^{-1}) of neutrons from D-D reactions and by an intense burst of X-rays both for a duration of 10^{-7} sec.

The electron temperature obtained from measurements of the hardness of the X-ray spectrum is thought to be a few keV[2] while density estimates are of the order of 10^{19} cm^{-3} [4] to 2×10^{20} cm^{-3} [5] in a plasma volume of about 10^{-2} cm^{-3}. Measurements of the total plasma energy [5] indicate equally energetic ions. There exists, therefore, the possibility that the neutron flux may arise from collisions between ions at thermal energies characteristic of a temperature of a few keV, and indeed Filippov and Filipova [5] point out that a thermal blob of plasma moving with a velocity 2×10^{7} cm/sec may best account for the observed energy spectrum and intensity distribution of the neutrons. In similar devices however, the neutron emission has been attributed to non-thermal acceleration of ions in the plasma (e.g. Meskan et al. [6] and it has been suggested that the ion and electron energy distributions are uncoupled (Beckner [7]).

The present paper discusses thermalisation between ions and electrons from the appearance of optical transitions in highly-stripped ion stages and from the total flux of energy in the X-ray region of the spectrum. Macroscopic confinement of the plasma has been studied

---

* Imperial College, London.

** Royal Holloway College, London.

with an image converter framing camera, while the dynamic state of the focus and scale of the density gradients have been investigated using pulsed-laser shadowgrams.

2. APPARATUS

The dimensions of the discharge chamber and the coaxial electrodes are shown in Fig.1. The 5 cm diameter inner electrode (the anode) is shrouded by an outer current return 10 cm diameter with a perforated section for viewing the discharge. The energy source is a 94 μF capacitor bank which with a source inductance of 26 nH and operated at 30 kV will deliver 1.5 mA peak current into a short circuit with a rise time of 2.45 μsec. Previous results [1] have been reported with half this bank capacitance (48 μF). A radial implosion or 'focus' at the open end of the gun can be produced with a static pressure filling in the range 0.25 to greater than 30 torr D_2 and over the operating voltage range of the bank from 23 kV to 40 kV.

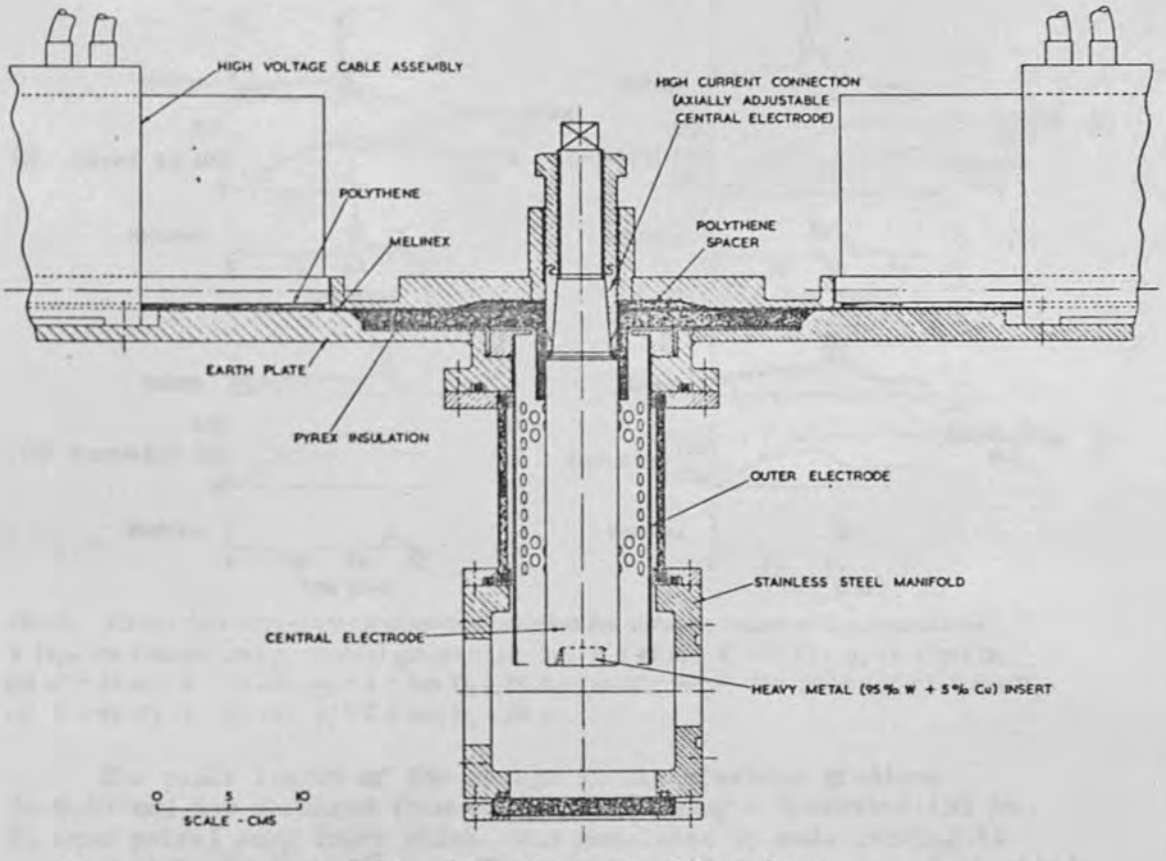

FIG.1. Schematic diagram of plasma focus.

3. FOCUS CHARACTERISTICS

The circuit waveforms are shown for the 48 μF bank in Fig.2(a,b) and in Fig.2(c,d) for the 94 μF bank. During the time τ_o to τ_c the current sheath is driven by the $j_r \times B_\theta$ force between the electrodes and reaches an axial speed, v_z, which varied from 2.1×10^7 cm sec^{-1} to 7×10^6 cm sec^{-1}. The axial speed varies with applied voltage and gas pressure as predicted by a snowplough compression. At time τ_c the current sheath collapses radially introducing a high voltage

$\sim I_c\, dL/dt$ into the circuit, where I_c is the current at 'collapse'. The electric fields generated internally by the radially imploding sheath, $E_s = \frac{2v_r}{c} \cdot \frac{I}{r}$, show as spikes at $t \gtrsim \tau_c$ in Fig.2 and are responsible for the intense fluxes of hard X-rays with mean energy equal to the characteristic K-shell radiation of tungsten from the W/Cu alloy anode.

The neutron pulse, Fig.2, depends on the operating conditions and capacitor source. Typically a sharp spike is produced in pure D_2 with the 48 μF bank Fig.2(a), while multiple bursts were more normal with added impurity Fig.2(b), and in all conditions of purity with the 94 μF bank Fig.2(c,d). The single sharp spike is associated with recovery of the current after collapse; when multiple spikes occurred the current after collapse tended to remain near half its peak value. No visible light could be seen on the image-converter pictures during these later spikes which suggests that the neutrons were emitted from lower density plasma than at the first collapse.

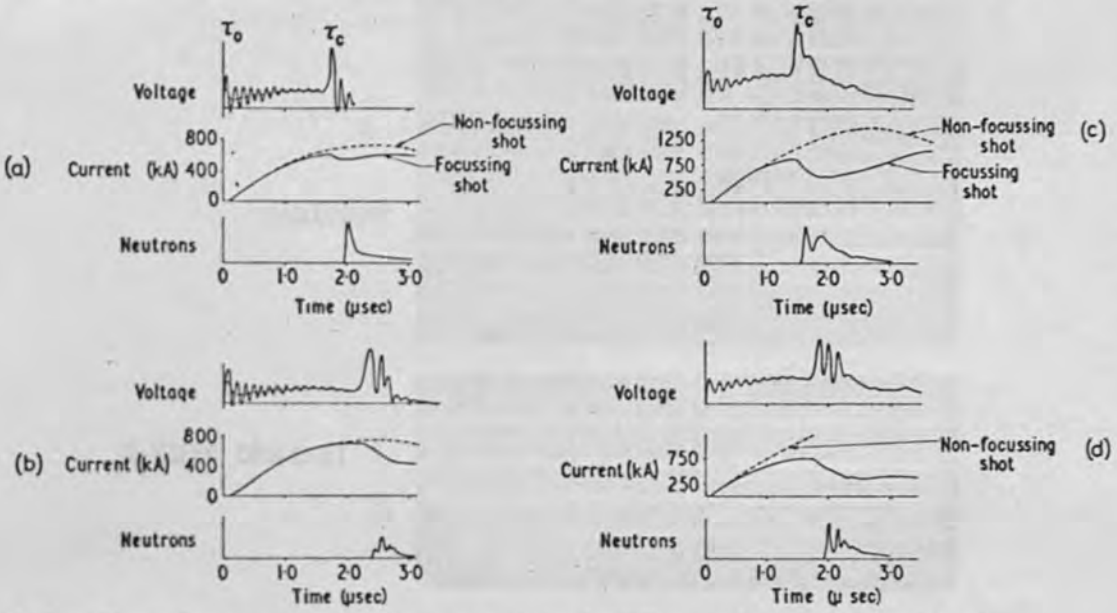

FIG.2. Plasma focus waveforms and neutron emission for different values of C (capacitance), V (applied voltage) and p_0, (initial gas pressure): (a) C = 48 μF; V = 30 kV; p_0 = 0.8 torr D_2; (b) C = 48 μF; V = 30 kV; p_0 = 1.1 torr D_2 + 2% A; (c) C = 96 μF; V = 30 kV; p_0 = 0.5 torr D_2; (d) C = 96 μF; V = 25 kV; p_0 = 0.8 torr D_2 + 3% A.

The scale length of the change in the electron gradient ($\simeq$ 0.01 cm) was measured from shadowgrams using a Q-spoiled (35 to 25 nsec pulse) ruby laser which was modulated by mode-locking to give a resolution $< 10^{-9}$ sec. The presence of a dense jet of electrode material visible on these shadowgrams at a time 0.2 μsec later than τ_c is thought to be the cause of the non-recovery of the current, Fig.2(b,c,d).

A mode of operation which occurred irregularly before the electrodes became conditioned by repeated discharges is also shown in Fig.2 and is termed 'non-focus'. The current in such a discharge approximates to that for a short-circuit, so a major fraction must continue to flow across the insulator, Fig.1. In this 'inactive mode' image converter pictures show a delayed and slowly (5×10^5 cm/sec) imploding current sheath but no neutrons or soft X-rays from the plasma volume, or hard X-rays from the anode, are emitted.

4.1 RADIATION MEASUREMENTS - EXPERIMENTAL TECHNIQUES

A further characteristic of the compressed plasma after collapse is the flux of radiation in the XUV region i.e. from 1 Å to about 20 Å. Surface barrier detectors with a known electrical conversion efficiency, placed in the image planes of 2 pinhole cameras, and viewing the same volume of plasma, were used to measure the relative transmission through thin foils and also the absolute intensity of the emission. The X-rays from the anode were screened from the image plane by a 5 mm thick lead sheet. Fig.3 shows the time of the emission across a 2 cm diameter field of view relative to the voltage spike. The D_2 plasma in these experiments was doped with a few percent argon by volume in order to enhance the emission and to render the plasma volume and position more reproduceable from shot to shot.

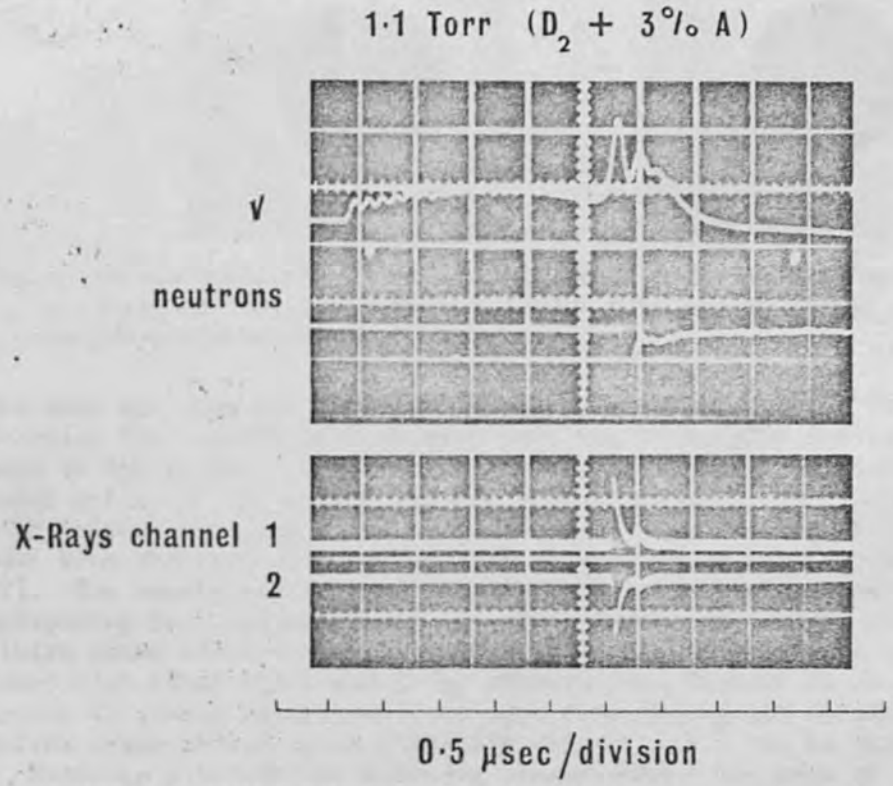

FIG.3. Neutron and emission in X-ray region from plasma focus

C = 48 μF; V = 30 kV; p_0 = 1.1 torr D_2 + 3% A

Both X-ray image channels screened with 2.68 mg/cm² Al. p-n junction (S_1O_2-Si) surface barrier detectors with 80 μ depletion layer.

Pinhole images of the plasma in its own XUV light are shown in Fig.4. Although in Fig.4 the D_2 is doped with heavier gases and the spatial resolution is limited by the finite (1 mm) size of the pinhole, the images clearly show the radial ejection of plasma from the column due to localised compression and instabilities (referred to in section 6.1). With much improved spatial resolution and in pure D_2 the minimum diameter of the plasma column was 0.5 mm with a minimum volume of 10^{-3} cm^{-3}. Since the filament retains an axial velocity of $\gtrsim 10^7$ cm sec^{-1} across the field of view the pinhole images have an inherent time-resolution of 50 nsec, about the half-width of the emission in Fig.3.

4.2 THE OBSERVED EMISSION SPECTRUM

Fig.5 shows the emission spectrum from an argon-doped D_2 plasma at wavelengths shorter than 10 Å. The top spectrum is recorded using a plane-grating with a high efficiency in the X-ray region [8]. The resolution is limited by the entrance collimation to 0.2 Å. The intense feature at 3.9 ± 0.1 Å is due mainly to the first resonance optical transition to the ground level of He-like argon. The weaker feature at 3.3 ± 1 Å includes the higher members of this series and free-bound continuum into the He-like ion.

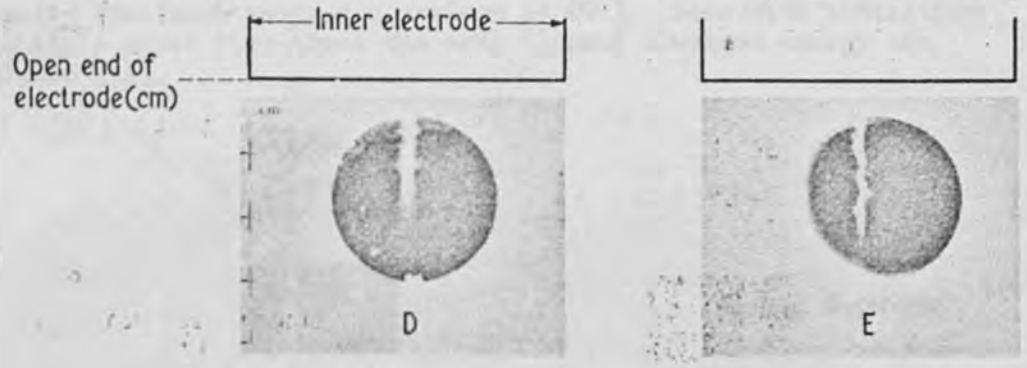

FIG.4. Pin-hole images in X-ray light from plasma focus: (D) C = 48 μF; V = 30 kV; p_0 = 1.1 torr D_2 + 40% HE; (E) C = 48 μF; V = 30 kV; p_0 = 1.2 torr D_2 + 10% Xe. (visible light screened by 268 mg/cm^2 Al)

The same spectrum was obtained in higher resolution, Fig.5 (below), by diffraction from a mica crystal bent into the de Broglie configuration [9] convex to the source. The resolution, 0.01 Å, is now determined by the lateral motion of the source and the 'window function' of the mica. Lyman-α of H-like argon and the series $1s^2\ {}^1S_0$ - $1snp\ {}^1P_1$ in He-like argon have been observed with n up to 5 (i.e. with an excitation of 3.95 keV). The wavelength scale of the crystal instrument was calibrated by superimposing Ne X optical resonance lines from a neon-doped plasma on the third order argon lines so that these optical transitions cannot be confused with inner shell and X-ray transitions, Peacock et al [10]. The presence of a weak background continuum from free-bound recombination into Li-like argon showed as an intensity step at 7.9 Å due to the Aℓ filter. Moreover although the emitting plasma volume was free of optical Cu lines, X-ray Cu lines were observed at and within about a mm from the anode. These energetic optical transitions establish that the electron temperature is of the order of 1 keV. Further, the transient stripping time to reach charge Z, τ_z (Z = 17 for a hydrogenic ion with an ionization potential equal to AXVII) must not be longer than the confinement time of the plasma τ_p; i.e.

$$\sum_{z=1}^{z=17} (\sigma v)^{-1}_{\text{ionization}} < n_e \tau_z < n_e \tau_p, \quad \text{for } Z = 17,$$

this gives a lower limit of $n_e\tau_z = 10^{11}\,\text{cm}^{-3}\,\text{sec}$. If now τ_z is equated to the duration of the X-ray emission pulse (~ 50 nsec) we find $n_e > 10^{18}\,\text{cm}^{-3}$. The results of more detailed calculations of the transient ion populations, including radiative recombination, in Fig.6, show that for the He-like and H-like ions to dominate the spectrum within 50 nsec, $n_e > 10^{19}\ \text{cm}^{-3}$. The coronal balance used here between electron impact ionization and radiative recombination is justified [11]

for ionization potentials of 4 keV at this density. It is deduced (section 4.5) from an analysis of the total X-ray flux that n_e cannot exceed $10^{20}\,cm^{-3}$.

4.3 COMPARISON WITH LASER-PRODUCED PLASMAS

Supporting evidence for the above plasma parameters is obtained by comparing the spectrum of Plasma Focus with that from laser irradiation of a solid target [12]. In the laser-produced plasma the density is high enough for a steady state ion population to be approached in the plasma formation phase. The electron temperature is 100 eV and the emission continuum reaches a maximum at 80 Å. Ions with ionization potentials about five times the mean thermal electron energy are produced [12].

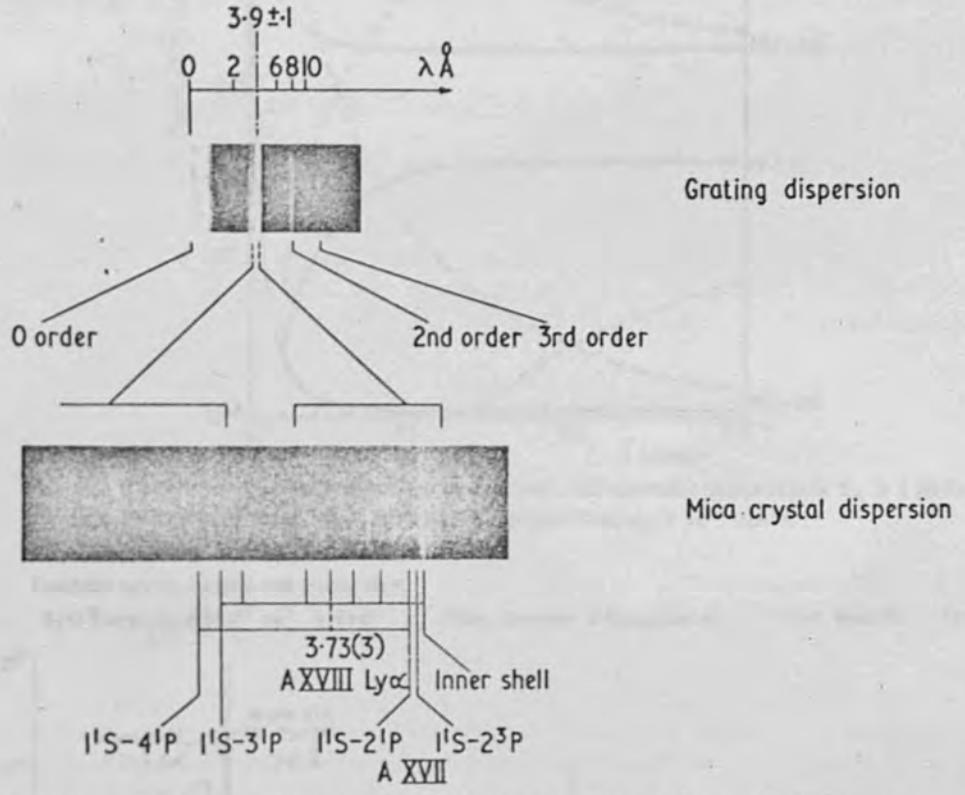

FIG.5. Crystal and grating dispersion of spectrum from plasma focus with initial gas pressure 1.3 torr D_2 + 8% A.

Above Etched grating 300 lines/mm, at 10 arc minutes grazing angle and 2 arc minutes collimation of source.

Below Mica crystal bent convex to plasma with radius of 3.8 cm.

In the Plasma Focus on the other hand, the continuum intensity increases monotonically to energies above the K-edge of Al, as expected for an electron temperature of 1 keV. The observed ionization potentials (~ 4 keV) are correspondingly more energetic.

4.4 MEASUREMENT OF ELECTRON TEMPERATURE

From the observed spectral features described in section 4.2 and using the steady state approximation, the transmission through thin foils can be computed, to give for example, the spectra plotted in Fig.7.

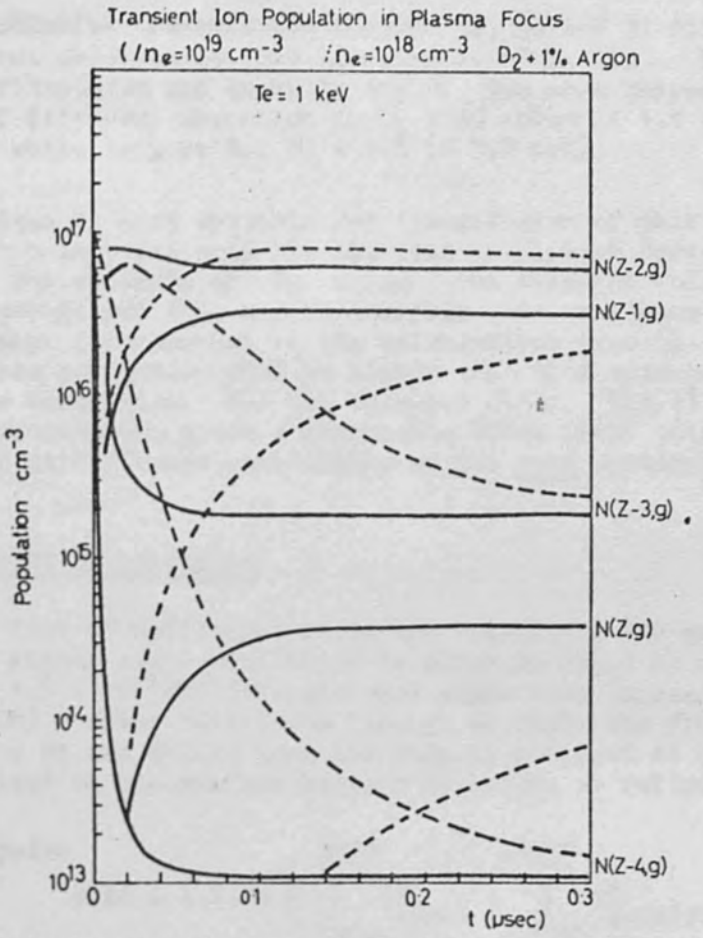

FIG.6. Calculated transient argon ion population; the electron temperature T_e is 1 keV; electron density (full line), $n_e = 10^{19}$ cm^{-3}; (dotted line) $n_e = 10^{18}$ cm^{-3}.

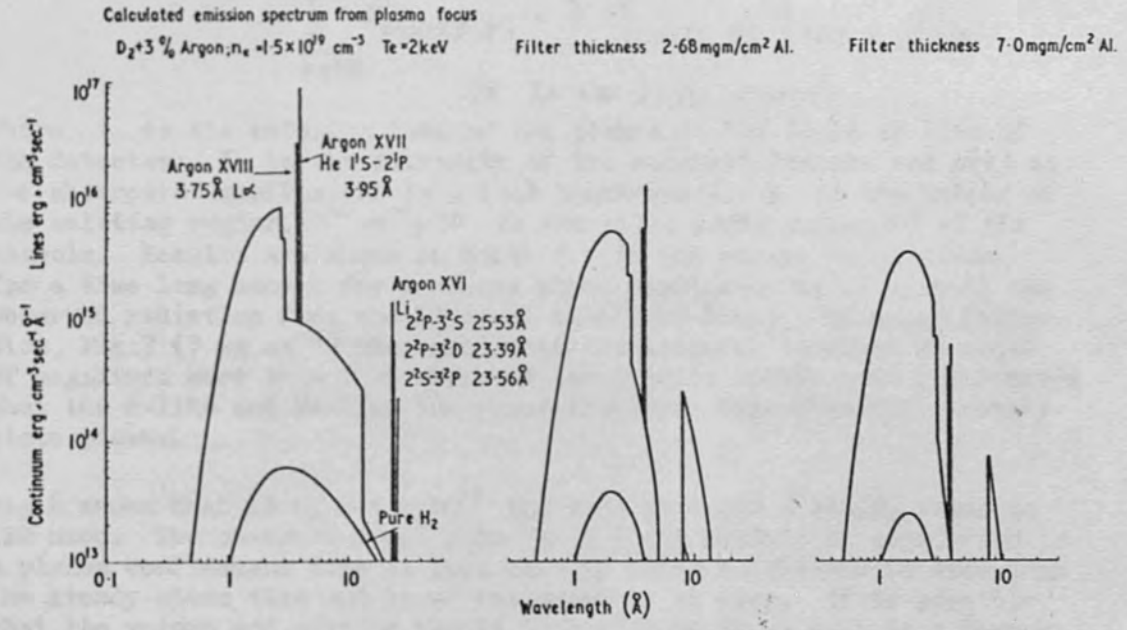

FIG.7. Calculated emission spectrum from plasma focus in D_2 + 3% A through various thickness of aluminium filters
electron density, $n_e = 1.5 \times 10^{19}$ cm^{-3}
electron temperature, $T_e = 2$ keV.

The calculated relative transmission through Aℓ, Be and Ni foils is compared with that observed to give an estimate of T_e [13]. Typical results for Aℓ filtration are shown in Fig.8. The mean temperature over a number of different absorbers in D_2 + 3% argon at 1.1 torr is 1.8 (± 0.6 keV) while in pure D_2, T_e = 2.5 (± 0.8 keV).

The technique is most reliable for transmission of that part of the spectrum which includes only the shortest wavelength free-bound recombination. The estimate of T_e using the thinnest foils (Fig.8) is lower than average and this can be attributed to continuum and line radiation not taken into account in the calculations from Li- and Be-like ions whose population will be higher than that calculated for steady state conditions. For the thickest foils (Fig.7) the steady state approximation gives a reasonable value since only the relative intensities at different wavelengths on the same continuum are involved.

4.5 ABSOLUTE FLUX OF RADIATION

The total flux of unfiltered radiation calculated for an argon-doped plasma in steady state conditions is shown in Fig.9 as a function of T_e, for $n_e = 1.5 \times 10^{19}$ cm^{-3} (the stripped argon ions increase the initial n_e by 50%). After filtration through Aℓ foils the flux is mainly due to the He and H-like ions and this is compared to the total charge, ϕ, received on the surface barrier detectors as follows:

$$5.76 \times 10^{-12} \int_0^{\tau_{pulse}} \phi.dt = \tau.V.d\Omega \left\{ \sum_{z=17}^{z=15} I^A_{lines} + \sum_{z=18}^{z=16} I^A_{cont(f-b)} + \sum_{z=18}^{z=16} I^A_{cont(f-f)} + \sum^{z=1} I^D_{cont(f-f)} \right\} \exp - \mu(\nu)x$$

(z is the ionic charge)

where τ is the emission time of the plasma in the field of view of the detector; I is the intensity of the spectral feature and $\mu(\nu)$ is the absorption coefficient in a foil thickness x. V is the volume of the emitting region, 10^{-3} cm^{-3}; $d\Omega$ is the solid angle subtended at the pinhole. Results are shown in Table I. If the plasma is confined for a time long enough for a steady state population to be reached the observed radiation flux should equal that calculated. At heavy filtration, Fig.7 (7 mg cm^{-2}) the calculated transmission is about an order of magnitude more than that observed and this is interpreted as evidence that the H-like and He-like ion populations are less than for a steady-state plasma.

Fig.6 shows that at $n_e = 1 \times 10^{19}$ the time to reach a steady state is 120 nsec. The observed results in Table I can readily be attributed to a plasma confinement time at this density which is limited to less than the steady-state time and is of the order of 40 nsec. It is possible that the volume and density should be scaled up by as much as a factor of 10; however, both these factors would increase the discrepancy between the calculated and observed fluxes, implying that the ion population is even further from a steady-state. The emission time in these circumstances would be much shorter than observed.

TABLE I

Comparison of observed and calculated transmission from a D_2 + 3% argon plasma with $n_e = 1.5 \times 10^{19}$ cm^{-3}

Al filter	I_o(observed intensity Ergs cm^{-3} sec^{-1}	I_c(calculated intensity Ergs cm^{-1} sec^{-1}		
		1.0 keV	1.5 keV	2.0 keV
0 mg/cm^2	9.85×10^{15}	7×10^{16}	1.2×10^{17}	1.5×10^{17}
4.36 "	5.4×10^{14}	3.2×10^{15}	8.5×10^{15}	1.4×10^{16}
7.0 "	2.7×10^{14}	8.9×10^{14}	3.2×10^{15}	6.8×10^{15}

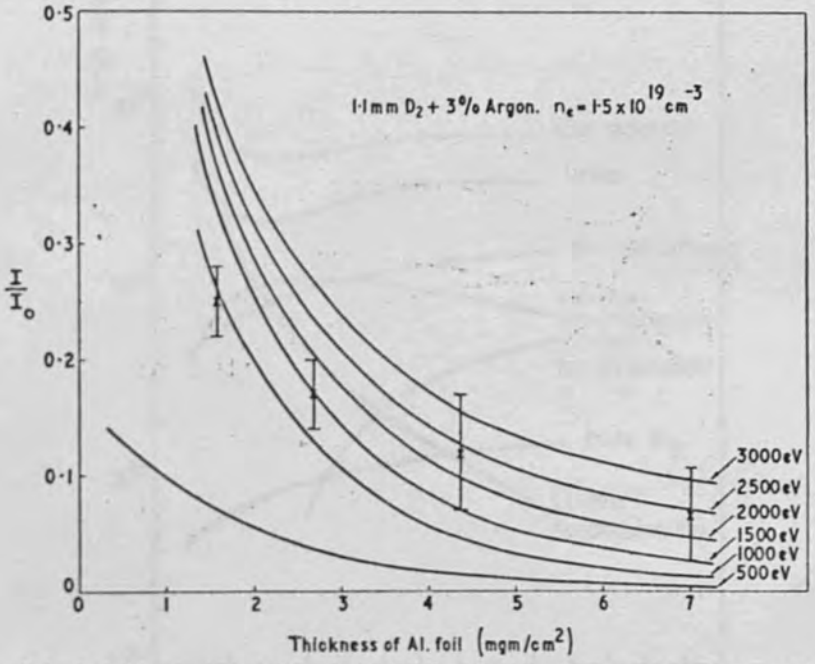

FIG.8. Calculated transmission through Al foil for varying plasma temperatures compared with experimental values (initial gas pressure, p_0 = 1.1 torr + 3% A).

Thus it is concluded from the observed spectrum, and from the duration and intensity of the E.M. radiation that a steady-state is approached, but not achieved, probably because the plasma is in a compressed state (at a density $\sim 10^{19}$ cm^{-3}) for only a limited period $\lesssim$ 40 nsec.

5. EQUIPARTITION BETWEEN IONS AND ELECTRONS

The relaxation times for the charged particles in the plasma focus are sufficiently short at densities of about 10^{19} cm^{-2} to ensure a thermal distribution of both ions and electrons. Equipartition between the energy distributions of the deuterium ions and electrons is given by

$$n_e \tau_{ie} \simeq 1.1 \times 10^{12}, \text{ for a 1 keV temperature.}$$

In addition, the time necesaary to reach a steady-state ion population (McWhirter [11]) is

$$n_e \tau \text{ (steady-state)} \sim 1 \times 10^{12}$$

and this criterion applies over a wide range of T_e. Since it has been shown (section 4.5) that a steady-state ion population is approached, the containment time cannot be much shorter than the equipartition time.

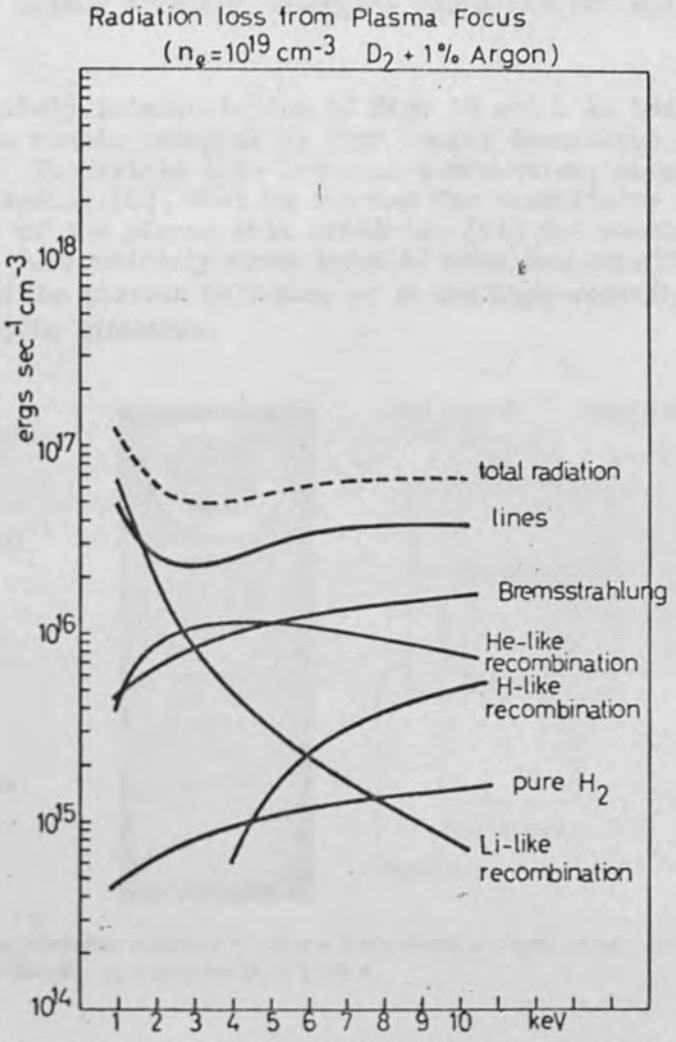

FIG.9. Calculated radiation loss versus electron temperature in D_2 + 1% A, plasma electron density, $n_e = 1.5 \times 10^{19}$.

6.1 STABILITY

Interchange instabilities are to be expected in the highly-pinched filament such as exists in Plasma Focus. In particular, the m = 0 instability having the shortest wavelength $(k)^{-1}$ should grow at a rate $\omega = (v_r^2\, k/r)^{\frac{1}{2}}$; with a plasma diameter of 0.5 mm and equal ion and electron temperatures the growth time $\tau_g \sim 10^{-9}$ seconds.

Image converter photographs as illustrated in Fig.10, show that the quasi-cylindrical compression produces a 'fountain' of plasma which travels axially away from the electrodes with a velocity $\sim 10^7$ cm sec^{-1}. Both sausage- and kink-type instabilities grow in the plasma column with $\tau_g << 5 \times 10^{-8}$ sec. They occur preferentially at the most compressed part of the column or filament, which at any time is nearest the centre electrode.[1] The radial ejection of plasma due to these instabilities is also

[1] Schlieren pictures taken in Q-spoiled ruby laser light and for the same plasma conditions as in Fig. 10 confirm the radial fluting.

discernible on the X-ray images, Fig.4. The instabilities do not disrupt the circuit current however, since further compressed regions appear as the filament travels axially away from the electrode. The pulsed laser shadowgrams reveal that during the collapse phase and afterwards the plasma boundary undergoes rapid ($<< 10^{-8}$ sec) radial oscillations.

A less likely interpretation of Figs 10 and 4 is that the dense blobs of plasma remain integral as they travel downstream with the plasma column. To sustain this argument a mechanism, possibly due to finite larmor radius [4], must be invoked for stabilising the blobs. At the surface of the plasma this criterion [14] for stabilisation is not satisfied. Alternatively some form of stabilisation either due to the bouncing of the plasma boundary or to the high-velocity axial flow of the ions may be effective.

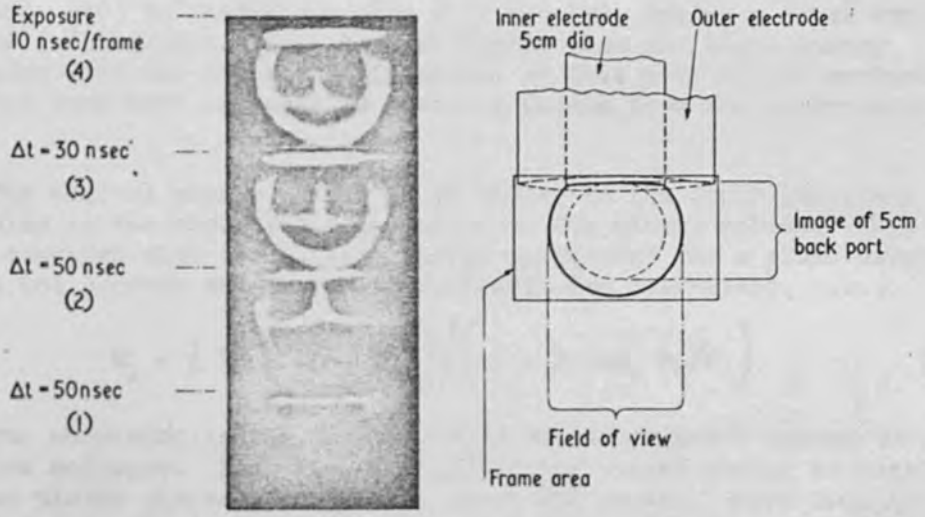

FIG.10. Image converter sequence of plasma focus during collapse phase. 10 ns exposure/frame: C = 48 μF; V = 28 kV; p_0 = 1.1 torr D_2 + 1.5% A.

6.2 ENERGY LOSS PROCESSES

Radiation in the XUV region, see Table I, can be seen to cool the plasma (with 3% added argon) with a time constant $nkT/I_o \approx 0.2$ μsec. In a pure D_2 plasma this cooling time is at least two orders of magnitude longer and can be neglected.

A more serious loss is that of particles whose axial flow is unrestricted. For a plasma in equilibrium the time constant for ion loss out of the ends is $\ell_p/(2v_i) = 50$ nsec, where ℓ_p is the length of the plasma column. However, the ion loss to the anode will be suppressed, because the axial velocity of the filament is of the order of the thermal velocity, and in the laboratory frame of reference the ions smear out only "downstream".

Again, assuming the plasma and the confining field to be in equilibrium after the radial compression the time constant for heat loss given by $\ell_p^2/v_e \lambda_{ee}$ is so short (3 nsec) that the plasma cannot remain in thermal contact with the electrode.

7. ENERGY CONVERSION IN PLASMA FOCUS

A solution of the circuit equations [15] with

$$\dot{L} = 2v_z \log_e R_1/R_2 = 1.8 \times 10^{-2}\ \Omega$$

where R_1, R_2 are the radii of the electrodes, shows that 40% of the electrostatic bank energy is stored as magnetic energy behind the current sheath at $\tau = \tau_c$. The part of this energy used to do mechanical work on the current sheath during collapse is

$$\int_{\tau_c}^{\tau > \tau_c} I^2 \left[(\log R_1/r)\, \dot{\ell}_p - \ell_p\, \dot{r}/r \right] dt$$

and this amounts to 2.5 kjoules at peak current. Ohmic heating is estimated [16] to contribute also 0.15 kjoules, making a total energy input of 2.65 kjoules. This is much higher than the total energy associated with the compressed filament, so that most of the mechanical work must have been expended in removing plasma from the compression region.

The thermal energy, 2VnkT is 10 joules in the lower limit and 100 joules in the upper limit depending on the plasma volume. This can be compared with the kinetic energy calculated for a pinch carrying all the current and in equilibrium with its self-field, viz.,

$$E_k = \tfrac{1}{2} L_1 \left(I_1^2 - I_2^2 \right) \Big/ \left(1 + 2 \log_e R_1/r \right) \qquad (1)$$

where the numerator is the difference in stored magnetic energy before and after collapse. For $I_2 = I_1/2$, 7/8 of the stored energy is available for plasma thermal energy i.e. about 850 joules. More usually E_k amounted to 500 joules indicating that over half the energy in the pinch is associated with non-thermal effects such as shocks and mass motion in axial flow and radial oscillations. Again equating the thermal energy to E_k, T should scale as I_1^2 and the neutron yield as I_1^8 (for constant pinch radius and particle density). Fig.11 shows a plot of the neutron yield as a function of constant pressure, Fig.11(a), and constant voltage, Fig.11(b). The interpretation is complicated as it is not known how the kinetic energy in the compressed plasma is shared between the density of the particle and their thermal energy as I_1 is varied. It is apparent however that as the stored magnetic energy and I_1, is increased the neutron output increases and scales approximately as I_1^5 from the curves in Fig.11.

8. CONCLUSIONS

Energetic (4 keV) optical transitions in highly-stripped ions are produced in Plasma Focus. From the total flux of energy in these transitions and their time of emission it is concluded that there is considerable coupling between the electron and ion distributions; the confinement time of the plasma is only a factor of about 3 too short for complete equipartition. At 1.1 torr in D_2 the electron temperature from absorber foil techniques is 2.5 ± 0.8 keV; the plasma volume varies from 10^{-3} cm^{-3} upwards to almost 10^{-2} cm^{-3} and the electron density is from 1 to 2×10^{-19} cm^{-3}.

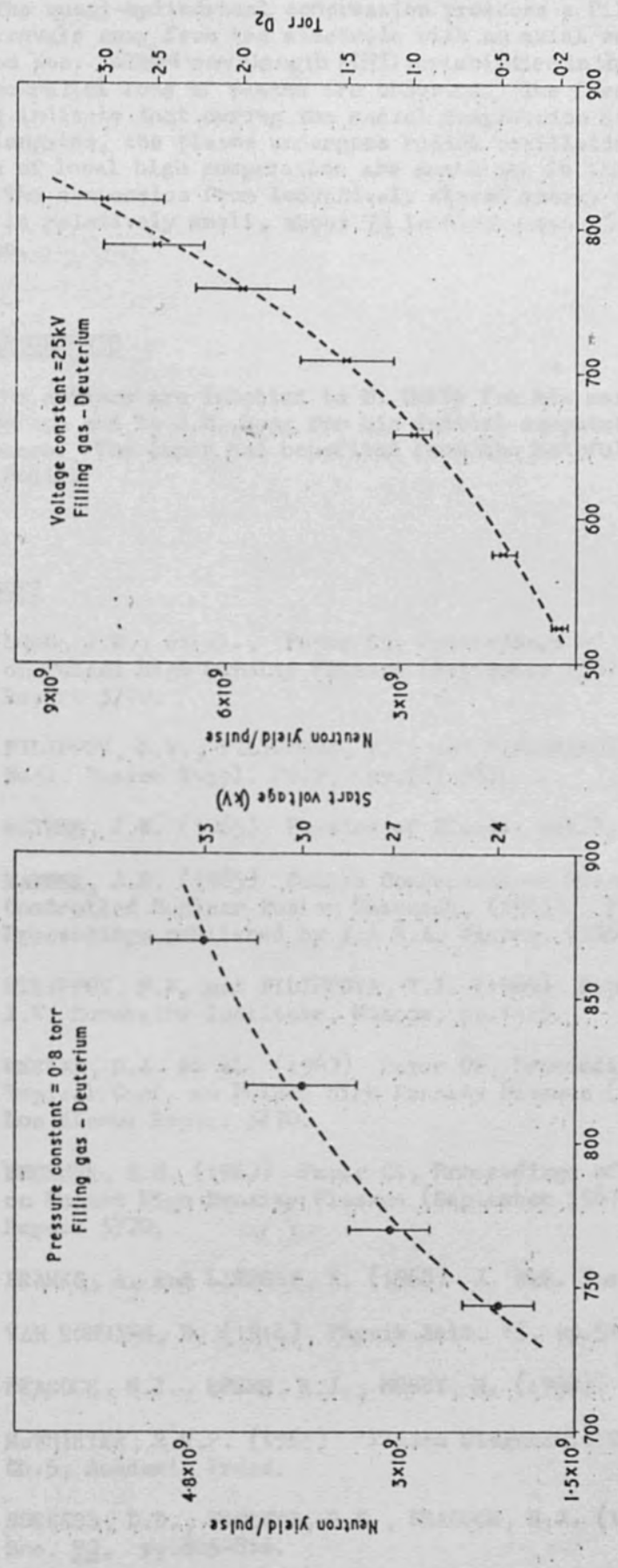

Neutron yield/collapse current.

FIG.11. Neutron yield versus current at collapse onset (A) with ambient pressure constant, p_0 = 0.8 torr D_2 and applied voltage, V, in range, 24 kV to 33 kV. (B) V constant, = 25 kV and p_0 in range 0.2 torr to 3 torr.

The quasi-cylindrical compression produces a filament of plasma which travels away from the electrode with an axial velocity $\sim 10^7$ cm sec. Short wavelength MHD instabilities in the plasma column, and some radial loss of plasma are observed. The foregoing experimental results indicate that during the radial compression and while the filament elongates, the plasma undergoes radial oscillations and that regions of local high compression are sustained in the moving filament. The conversion from inductively stored energy to plasma thermal energy is relatively small, about 7% in theory and 1% maximum in practice.

ACKNOWLEDGEMENTS

The authors are indebted to M. Hobby for his work with the crystal spectrograph and to J.W. Long for his initial computation of the radiation losses. The paper has benefited from the helpful comments of H.A.B. Bodin.

REFERENCES

[1] LONG, J.W., et al., Paper C5, Proceedings of APS Topical Conf. on Pulsed High Density Plasmas (September 1967), Los Alamos Report 3770.

[2] FILIPPOV, N.V., FILIPPOVA, T.I. and VINOGRADOV, V.P. (1962) Nucl. Fusion Suppl. Pt.2, pp.577-587.

[3] MATHER, J.W. (1965) Physics of Fluids, vol.8, no.2, pp.366-377.

[4] MATHER, J.W. (1965) Culham Conference on Plasma Physics and Controlled Nuclear Fusion Research, (1965). Paper Cn-21/80. 2, 389 Proceedings published by I.A E.A. Vienna, (1966).

[5] FILIPPOV, N.V. and FILIPPOVA, T.I. (1965) Report I.A.E.913, I.V. Kurchatov Institute, Moscow, pp.1-15.

[6] MESKAN, D.A.. et al. (1967) Paper C6, Proceedings of APS Topical Conf. on Pulsed High Density Plasmas (September 1967), Los Alamos Report 3770.

[7] BECKNER, E.H. (1967) Paper C4, Proceedings of APS Topical Conf. on Pulsed High Density Plasmas (September 1967), Los Alamos Report 3770.

[8] FRANKS, A. and LINDSEY, K. (1968) J. Sci. Instr. 1, 144.

[9] VAN ROHMANN, H. (1914) Physik Zeit. 15, pp.510-512.

[10] PEACOCK, N.J., SPEER, R.J., HOBBY, M. (1968). To be published.

[11] McWHIRTER, R.W.P. (1965) 'Plasma Diagnostic Techniques', Ch.5, Academic Press.

[12] BURGESS, D.D., FAWCETT, B.C., PEACOCK, N.J. (1967), Proc. Phys. Soc. 92, pp.805-816.

[13] STRATTON, T.F. (1965) 'Plasma Diagnostic Techniques', Ch.8, Academic Press.

[14] ROSENBLUTH, M.N., KRALL, N.A., ROSTOKER, N. (1962), Nuclear Fusion Supplement, Part I, pp.143-150.

[15] BAKER, D. Los Alamos (1968) Private communication.

[16] MATHER, J.W. and BOTTOMS P.J. (1968) Phys. Fluids, 11, pp.611-618.

Paper submitted to 3rd European Conference on Plasma Physics and Controlled Fusion, Utrecht - June 23rd-27th, 1969

COMPARISON OF A TWO-DIMENSIONAL MAGNETOHYDRODYNAMIC NUMERICAL MODEL WITH THE DENSE PLASMA FOCUS EXPERIMENT

by

P.D. MORGAN*, N.J. PEACOCK/ and D.E. POTTER/Ø

*Royal Holloway College, Englefield Green, Surrey, England.
/The Culham Laboratory, Abingdon, Berkshire, England.
ØImperial College, London, S.W.7, England.

ABSTRACT

A two-dimensional numerical fluid model of the implosion phase of the dense Plasma Focus [1,2] is compared with experiment. The plasma parameters are determined from radiation measurements, while the plasma dynamics are established by image converter and pulsed laser Schlieren photography. The theoretical model assumes a fully-ionized two-fluid plasma. Transport processes include electron and ion heat conduction, ion viscosity, resistive and Hall electric fields. Variable coefficients are used to describe both collisionless and collision-dominated regimes.

Such a thermal fluid model is shown to describe the dynamical formation and high kinetic energy densities of the plasma focus. A magnetic trap on the anode acts as a plasma source for flow through the pinch. Short wavelength instabilities are stabilised by ion viscosity. Non-linear effects repinch long wavelength $m = 0$ type instabilities (growth rate $\sim$ 40 nsec) and a double pinch effect (double neutron peak, voltage spike) results. A total sustainment time of $\sim$ 150 nsec is demonstrated.

EXPERIMENTAL RESULTS

The Plasma Focus device and its operating conditions relevant to this paper are described in [3]. Values of electron temperature and density have been obtained from the shape of the emission spectrum and from the absolute radiation flux in the soft X-ray region. At an initial gas pressure of 1·1 torr (D_2 + 3% A) $T_e \sim 1{\cdot}8 \pm 0{\cdot}6$ keV and $n_e \sim 1{\cdot}5 \times 10^{19}$ cm^{-3}. The ion confinement time is $\sim$ 40 nsec [3].

Image converter photographs of the focus show that the compression is sustained for $\sim$ 70 nsec by the radial collapse of the axially-travelling current sheath [3]. The pinch diameter from X-ray pinhole photographs is

CR69-115

~ 0·7 mm at peak compression, and the total volume of hot (~ 2 keV) plasma varies between 10^{-3} and 10^{-2} cm^{-3} [3]. The spatial definition of the plasma boundary in the image converter photographs is limited by the 10 nsec exposure.

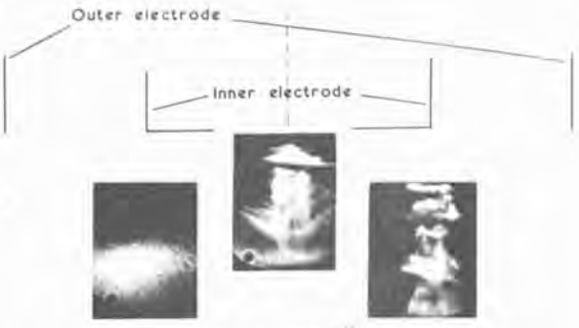

$t - 9 \times 10^{-8}$ secs $t + 1 \times 10^{-8}$ secs $t + 6 \times 10^{-8}$ secs

Fig.1
Pulsed laser Schlieren photographs of focus

Shorter exposures were obtained by using a cryptocyanine dye cell to mode-lock a ruby laser pulse and using the train of irregularly spaced light pulses of ~ 1 nsec duration as a source for Schlieren photography. Fig.1 shows a Schlieren time sequence of the focus using a spherical Schlieren obstacle and an initial gas filling of 2·5 torr (D_2 + 5% A). Frame 1 shows an ionization front 90 nsec before peak density is attained, frame 2 shows the detailed structure of the pinch and frame 3 shows its subsequent break up. The characteristic length (~ 0·1 mm) of the density gradients is smaller than the plasma radius measured from X-ray photographs. Also the prominent flutes in frame 2 Fig.1 are absent in the image converter photographs.

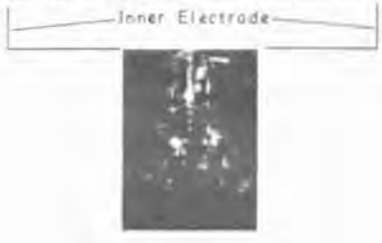

Fig.2 Dense pinch region

If a sufficiently large Schlieren obstacle is used, only the denser pinch regions are recorded, Fig.2. Assuming an electron density distribution of the form $n_e = \hat{n}_e \left(1 - \frac{x^2}{r^2}\right)$, r is the pinch radius, enables a minimum density value of $3{\cdot}8 \times 10^{19}$ cm^{-3} to be derived from Fig.2. Increasing the obstacle size until all the refracted light is just eliminated yields a maximum density value of 8×10^{19} cm^{-3}. The above values are several times the maximum obtained from X-ray measurements. These however give the mean value throughout the plasma volume.

A laser operating in the pulsed transmission mode is at present being used to obtain ~ 6 nsec exposure Schlieren photographs.

TWO-DIMENSIONAL MHD MODEL

A two-fluid electron-ion fully-ionized plasma is assumed. The equations are written in conservation form, in cylindrical co-ordinates assuming azimuthal symmetry, with the magnetic field restricted to the θ-direction. The

set of six dependent variables satisfies the equations of continuity, conservation of axial and radial momentum, Faraday's law (with the generalised Ohm's law), conservation of electron pressure and total energy [4]. The equations are integrated in time using the two-step Lax-Wendroff method [5] on an Eulerian mesh, and are coupled with an external L-C circuit.

Results are given for an anode length of 10 cm, initial filling pressure of 1 torr D_2 and an initial capacitor voltage of 40 kV.

In the collapse to the axis, Fig.3, momentum flow parallel to the current sheet removes 90% of the plasma initially at the end of the centre electrode. Adiabatic compression is thus permitted to raise the remaining plasma to thermonuclear temperatures.

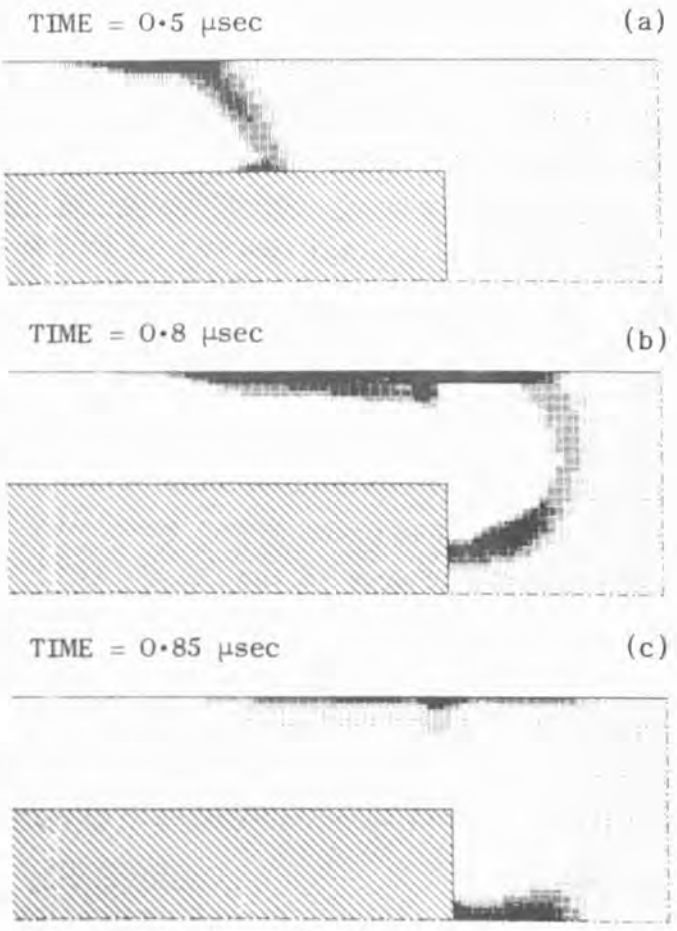

Fig.3
Distribution of plasma density $\rho = \rho(r,z)$.
(a) Run down phase. (b) Collapse phase.
(c) Dense pinch phase. (The scale in (c) is a factor 10 greater than in (a,b)).

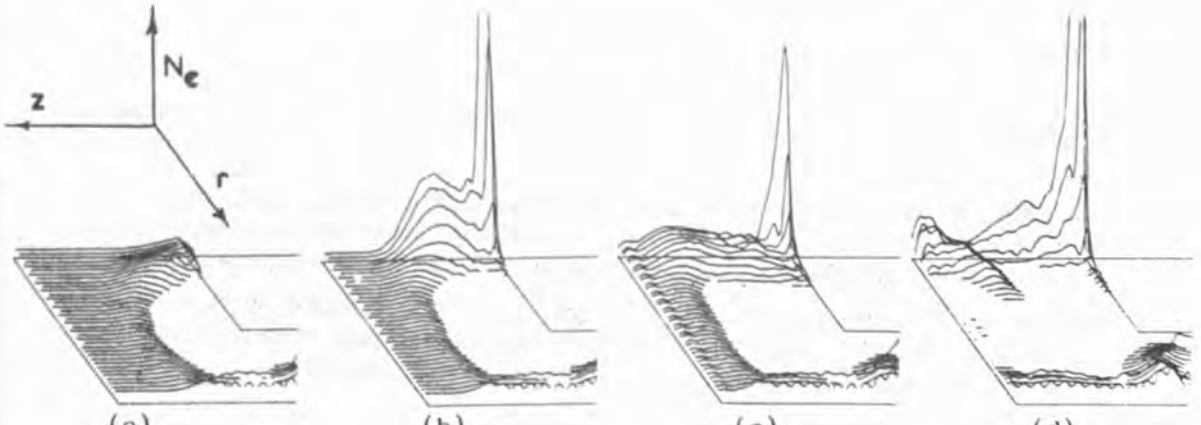

Fig.4
Plasma density in the R-Z plane in the dense pinch phase. The series shows the collapse, (a) to the axis, the dense pinch (b), partial break up (c), and repinch (d).

A near equilibrium magnetic trap is established on the anode, by the removal of thermal energy through electron heat conduction and the resultant resistive diffusion of field. The trap sustains the pinch by axial flow ($V_z \sim 4 \times 10^7$ cm sec^{-1}) Short wavelength fast hydromagnetic instabilities are damped by the large ion viscosity. The break-up of the pinch through a long wavelength (m = 0) mode is observed in Fig.4, with a growth rate of 40 nsec. Fig.4d shows a non-linear effect on the instability causing a 're-pinch'. This double pinch effect manifests itself in the interruption of the characteristic drop in the 'focus-shot' current curve, Fig.5.

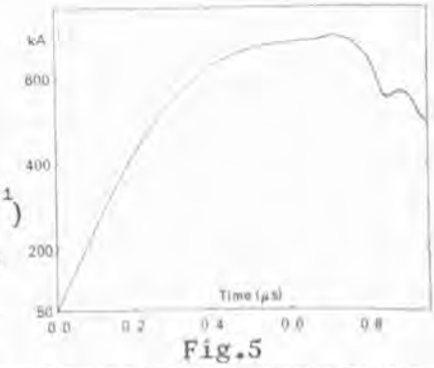

Fig.5
Theoretical curve of the current against time

Typical values for the plasma parameters in the pinch are $T_i \sim 2$ keV, $T_e \sim 1$ keV, $n_e \sim 4 \times 10^{18}$ cm^{-3}. Although these values are in qualitative agreement with experiment more accurate values are obtained on a fine scale mesh (switched in at the focus stage) in which the pinch relaxes to a radius $\sim 0{\cdot}6$ mm and electron densities $n_e \sim 10^{19}$ cm^{-3} are obtained.

DISCUSSION

Qualitative agreement with experiment for the dense pinch phase (pinch radius, electron density, electron temperature, sustainment time) demonstrates that the essential features of the plasma focus can be described in terms of a thermal fluid model.

The duration of the pinch is enhanced by two effects: ion viscous stabilisation of short wavelength hydromagnetic instabilities and the non-linear repinch of the slower modes; and a sustainment of the pinch through axial flow.

REFERENCES

[1]. FILIPPOV, N.V., FILIPPOVA, T.I. and VINOGRADOV, V.P. Nucl. Fusion Suppl. Pt.2, pp.577-587, (1962).

[2]. BOTTOMS, P.J., CARPENTER, J.P., MATHER, J.W., WARE, K.D. and WILLIAMS, A.H. Paper CN-24/G-5. IAEA Third Conference on Plasma Physics and Controlled Nuclear Fusion Research, Novosibirsk, Aug.1968.

[3]. PEACOCK, N.J., WILCOCK, P.D., SPEER, R.J. and MORGAN, P.D. Paper CN-24/G-4. IAEA Third Conference on Plasma Physics and Controlled Nuclear Fusion Research, Novosibirsk, Aug.1968.

[4]. POTTER, D.E. and ROBERTS, K.V. Methods of Computational Physics, vol.9, Academic Press (To be published).

[5]. RICHTMYER, R.D. and MORTON, K.W. Difference Methods for Initial-Value Problems, Interscience, (1967).

INTERNATIONAL ATOMIC ENERGY AGENCY

CN-28/D-3

FOURTH CONFERENCE ON PLASMA PHYSICS AND CONTROLLED NUCLEAR FUSION RESEARCH

Madison, Wisconsin, U S A 17 - 23 June 1971

Measurements of the Plasma Confinement and Ion Energy in the Dense Plasma Focus

N.J. Peacock[o], M.G. Hobby[+] and P.D. Morgan*

[o] The Culham Laboratory

[+] Leicester University

* Royal Holloway College, London

ABSTRACT
(revised)

The structure and velocity of the plasma boundary during the implosion phase of the dense Plasma Focus has been studied using repetitively-pulsed, 1 nanosecond exposure, transmission photography with spatial resolution of 100 microns. Both acceleration and deceleration of the plasma boundary are observed by shadowgram and schlieren photography. Long-wavelength, Rayleigh-Taylor instabilities grow on the boundary during its acceleration. On subsequent deceleration, a singularly-steep density gradient is observed transiently on the axis of symmetry and has dimensions smaller than any other plasma parameter except the collision-free skin depth. The density distribution, which is approximately parabolic with a maximum on the axis of symmetry when the pinch is well developed, is derived directly from interferograms. Local break-up of the pinch takes place, often due to m = 0 and, less commonly, m = 1 instabilities. The sustainment time of the pinched plasma is not more than 50 nanoseconds and corresponds directly with the initial burst of thermal X-rays.

No correlation of the refractive index gradients could be found with the later, double and triple pulses of soft X-rays (and neutrons), which in some instances are emitted 200 nanoseconds after the first pulse, and this implies the existence of a more tenuous plasma ($n_e < 8 \times 10^{18}$ cm^{-3}) at this time.

The ion energy distributions, transverse to the axis of symmetry, of several ion species of argon and neon have been measured using high resolution, X-ray spectroscopic techniques. The ions have a thermal energy distribution with a mean energy of about 9 keV. These results, in addition to the deuterium ion temperature estimated from the neutron

emission, are interpreted as giving a scaling law for the transverse energy $E_{Z/M} = T_0(1 + Z^2/M)$, where T_0 results from compression and resistive heating and the remainder may be due to weak turbulence.

Dielectronic recombination is responsible for the Li-like ion satellites and has to be taken into account to explain the intensity and the time of appearance of the line emission.

1. INTRODUCTION

In contrast to much of the research on the dense Plasma Focus which is aimed at providing an explanation for the characteristics of the intense neutron emission [1,2], the authors' programme attempts to relate the particle heating and confinement to the observed dynamics and structure in the collapse phase. An important feature of this programme has been the development of a 2-dimensional (r,z,t), 2-fluid MHD numerical code to describe the Focus, [3], and its comparison with the experimental observations, [4].

The present paper extends the experimental observations on the dynamics and structure of the focus [5, hereinafter referred to as Paper 1] using improved time and spatial resolution, and examines the role of instabilities in the plasma. The object of the experiments is to derive a more detailed description of the plasma dynamics and of the electron density distribution which then may be compared with the code. The dimensions of the electrodes and the discharge chamber and the parameters of the electrical circuit are identical to those described previously, [Paper 1,6].

In addition, the spectroscopic study of the ion energies and the ion confinement reported in the earlier Paper 1 has been extended. Profiles of line emission from heavy gases seeded into the deuterium and viewed transverse to the axis of symmetry give information on the mean transverse ion energy as a function of mass and charge of the ion, and enable us to propose a mechanism for the ion heating.

Since any comprehensive model of the neutron emission [2] is likely to involve anisotropic ion energies in the directions transverse and parallel to the axis of symmetry (i.e. $E_r \neq E_z$), it is clearly desirable to measure both components. The present paper discusses only the transverse energy.

2. DYNAMICS OF THE FOCUS

2.1 Experimental Arrangement - Nanosecond Transmission Photography

Measurements of the plasma refractive index and its gradients across the plasma boundary are conveniently made by interferometric, shadowgraph and schlieren photography using a pulsed ruby laser as an external light source. In order to study the fine structure ($< 0{\cdot}1$ mm) in the focus a time resolution of 1 nanosecond is required. This is achieved by clipping the output from the conventionally Q-switched laser with an extra-cavity, electro-optic shutter, [7].

In the shadowgraph and schlieren photography, a time-sequence of typically three exposures is obtained by splitting the laser pulse and illuminating the same discharge at variable time intervals using optical-delay techniques, [8]. In the schlieren technique a spherical obstacle is used to record density gradients in the plasma in all directions in the plane orthogonal to the incident laser beam. By varying the obstacle diameter it has been ascertained that deviations of the laser light of up to ~ 30 milliradians are introduced by plasma refraction. This sets a lower limit to the maximum density and its gradient.

The density itself is measured by fringe-shift interferometry using a parallel-plate Mach-Zehnder, arranged so that single-plate control is possible, [9].

2.2 Results of Shadowgraph and Schlieren Photography - Motion of the Plasma Boundary, Dimensions of the Plasma and Fine Structure

Figure 1 shows a sequence of shadowgrams taken during the implosion of the current sheath, the time between exposures, Δt, being in this case 15 nanoseconds. Figure 2 shows a sequence, later in time, during the dense pinch phase where $\Delta t = 6{\cdot}5$ nanoseconds, and it is evident that there is considerable change in the boundary and structure of the focus even on this rapid time scale. From these and similar records, values of the velocity and acceleration of the boundary can be derived particularly since instabilities at the boundary serve as local identification tags. The change in the refractive gradient at the boundary is quite sharp $\delta\left(\frac{\partial ne}{\partial r}\right) \lesssim 1$ mm and does not change appreciably during the implosion. The non-cylindrical nature of the plasma compression is thus readily followed. The velocity of the boundary is initially greatest close to the anode where, due to the cusped shape, figure 3, the plasma pressure is highest. As pressure balance is approached the boundary close to the anode decelerates as illustrated in figure 4. Boundary velocities up to a maximum of 4×10^7 cm sec^{-1} have been measured, corresponding to the highest voltages (30 kV) and with filling pressures of 3 torr D_2. A few percent of argon added to even lower deuterium pressures is sufficient to slow down the implosion. All of the subsequent analysis pertains to 2·5 torr D_2 + 4% Ar doping. At the time the plasma has reached a maximum compression the boundary is fluted (figure 2) due to the Rayleigh-Taylor instabilities, which have grown earlier during the implosion phase (figure 1). However local break up of the pinch then proceeds through the growth of $m = 0$ and, less often, $m = 1$ instabilities (figure 2). Over a field of view ($z \times 2r$) of 3·8 cm × 2·7 cm covered by the transmission photography, the total duration of the quasi-cylindrical implosion, of the formation of the dense pinch and its break-up is no greater than 100 nanoseconds. After this time no features are observed with $\hat{n}_e > 8 \times 10^{18}$ cm^{-3} (see also section 2.4).

At a distance z below the anode where locally the boundary decelerates to almost zero velocity, there appears transiently, along the axis of symmetry, a singularity in the density gradient (see figures 2,6). The dimension of $\delta\left(\frac{\partial ne}{\partial r}\right) \lesssim 100$ microns and is smaller than all characteristic plasma dimensions except the collisionless skin depth c/ω_{pe}. This may be interpreted as damping of a collision-free shock arriving on the axis of symmetry.

The regions of the plasma, with refractive index n, which result in maximum laser beam refraction $2\int_{\ell=0}^{r} \frac{1}{n}\frac{\partial n}{\partial r}\, d\ell$, are readily determined by inserting a large obstacle in the schlieren optics and resorting to a long (unclipped) Q-spoiled laser pulse of width about equal to the duration of the dense-pinch phase. A schlieren photograph, figure 5, shows the region of the steepest density gradients and highest density to be on the axis. The fine structure occurs within an envelope 1 mm in diameter. This region also corresponds, figure 5, to the

locality of intense line emission due to collisions of thermal (2 keV) electrons with ions, [Paper 1]. A lower limit for the peak density in this region can be derived from the refraction and is $7{\cdot}5 \times 10^{19}$ cm^{-3}. The average density across the plasma is however less, (section 2.4 and also Paper 1) by at least a factor of two.

2.3 Instability Growth Rates

During the acceleration phase, Rayleigh-Taylor instabilities (R.T) develop in the plasma boundary. Direct measurements of ω, the growth rate, g, the acceleration and k, the wave number are taken from the shadowgrams (figure 1). Dissipative processes such as viscosity ν and resistivity (σ^{-1}) will damp out the fastest growing (large k) disturbances, and there will be some value of ω (i.e. ω_m) where the inertial forces are just balanced by the rate of energy dissipation, [10]. The corresponding wave-length k_m^{-1} will then dominate the instability spectrum.

Assuming resistive damping as the dominant mechanism, the observed R.T. wavelength could be explained by a resistivity which is anomalously higher than the zero-field value by a factor approaching 100 or, as is more likely, by the effects of a few percent Li-like argon ions in the plasma. If, on the other hand, viscous damping was dominant, a consideration of the figures in Table 1 shows that the observed wavelength can be accounted for provided $\omega_{ci}\tau_{ii} \approx 2$, an entirely reasonable situation. For either damping mechanisms (e.g. Table 1) ω (observed) $< \omega_m$ (calculated). A plane boundary approximation has however been used in these preliminary calculations.

Table 1

[Rayleigh-Taylor growth for mean plasma radius r_p = 9 mm, $g = 2{\cdot}1 \times 10^{15}$ cm sec^{-2}, V_b = 26·3 kV, p_0 = 2·5 torr (D_2 + 4% Ar), Te = 100 eV and Ti = 250 eV (from the computations [3]), $n_e = 2 \times 10^{18}$ cm^{-3} (from interferometry, section 2.4), $\omega_{ci}\tau_{ii} \approx 2$]

ω (observed)	λ (observed)	$\sqrt{gk}$	λ_m	$\sqrt{gk_m/2}$
$3{\cdot}3 \times 10^7$ sec^{-1}	3·2 mm	2×10^8 sec^{-1}	3·2 mm	$1{\cdot}3 \times 10^8$ sec^{-1}

In the pinch phase local break-up of the compressed plasma is due to m = 0 instabilities as seen in figure 2. The growth time and wavelength are derived and the former is in reasonable agreement with that estimated from $r_p/\sqrt{\gamma p/\rho}$ ($\approx$ 10 nsecs), where the square root factor is the sound speed. Kink (m = 1) instabilities are less commonly observed with much slower growth rates and these are less important in the break-up of the pinch.

2.4 Interferometry - Radial Density Distribution

The interferogram at peak compression in figure 6 shows well-developed m = 0 instabilities and an early-stage of an m = 1 instability. The fringe shifts along the section A A (figure 6) are plotted in figure 7 as a function of position r/a orthogonal to the axis of symmetry, where a is the radius of the column. An average value of density $\bar{n}_e(r/a)$, at position r/a, may be obtained by dividing $\int_0^\ell n_e dl$ at that position by the chord of length $2(a^2 - r^2)^{\frac{1}{2}}$. In figure 7, $\bar{n}_e(r/a)$ is plotted versus r/a and is in approximate

agreement with the parabolic function $\bar{n}_{em}(1 - (r/a)^2)$, where $\bar{n}_{em}$ is the maximum value of $\bar{n}_e(r/a)$. Thus it is also reasonable to propose a parabolic distribution for the actual density, $n_e(r/a)$, and thus obtain an estimate of the peak density on the axis, $\hat{n}_e$. For the section A A, a value of 8×10^{18} cm^{-3} is obtained for $\hat{n}_e$. Values of $\hat{n}_e$ up to 4×10^{19} cm^{-3} have been evaluated at other axial positions, closer to the anode, and are in good general agreement with those evaluated from the schlieren measurements (section 2.2) and from the soft X-ray intensity [Paper 1]. Relaxation of the sharp density front, observed during the implosion, to the parabolic distribution implies considerable penetration of the current finally into the pinch. Taking into account the effect of the impurities, the electrical conductivity temperature must be anomalously low by at least a factor of 10 to explain the field diffusion.

3.1 Line Emission Profiles in the X-ray Region

Line radiation between 3 and 14 Å from optical and inner-shell transitions in argon and neon seeded into the focus are observed from the pinched plasma, [Paper 1].

Doppler broadening of the lines due to thermal motion is,

$$\Delta\lambda_D = \lambda \cdot 2{\cdot}44 \times 10^{-3} \cdot \left(\frac{T}{M}\right)^{\frac{1}{2}} \text{(T in keV, M in a.m.u)} \quad (1)$$

For a complete profile analysis a resolution $\frac{\lambda}{\Delta\lambda_{inst}} > 10^3$ is required at temperatures of the order of 1 keV, and this was achieved using a focussing mica spectrometer [11] with an aperture W, of a few cms. Spectra from several discharges of the Plasma Focus (viewed orthogonal to the axis of symmetry and in 2·5 torr, D_2 + 4% Ar, Ne) were recorded in several orders on photographic emulsion placed round the Rowland circle. The Ar XVII lines shown in a microphotometer trace, figure 8, are considerably broadened relative to the characteristic X-ray lines of the anode material, e.g. $W_L\beta_1$.

The measured line profiles are subject to several instrumental broadening effects which must be removed before a true analysis can proceed. As well as the intrinsic broadening due to the dispersive crystal diffraction window there is an aperture-dependent geometrical aberration inherent in semi-focussing optics of the Johann type. There is also the broadening introduced by the finite emulsion thickness at oblique incidence. Overall corrections to the intensity profiles due to these effects are typically quite small, being 8% of FWHM for $W_L\beta_1$ in figure 8 and 3% of FWHM for the $^1S_0 - {}^1P_1$ Ar XVII line.

The corrected profiles e.g., figure 9, are found to be a good fit to a Voigt function. The dispersive component of the profiles can be accounted for in all orders and at all wavelengths by the crystal diffraction pattern and the remaining Gaussian component is the true source function.

3.2 Results

Figure 10 shows the component profiles of the Ar XVII 3·9492 Å line. The Gaussian component of 0·0046 ± 0·0006 Å, if interpreted as a thermal width, corresponds to an ion temperature of 9 ± 3 keV. A similar analysis for the same argon line in third order yields an equivalent ion temperature of 10 ± 1 keV, and for the Ne X line in first order 9 ± 1 keV. The results are shown in Table 2. The deuterium ion temperature has not been measured in this work but laser-beam

scattering experiments in a similar apparatus [13], the neutron emission assuming a moving thermal source [12] and numerical calculations [3], all indicate an ion temperature of about 1 keV or slightly more. There remains only the problem of explaining the Gaussian source function and in particular its scaling with ion charge, Z, and atomic mass, M.

Table 2

Ion	Transition	λ (Å)	Order n	$\Delta\lambda_{1/2}$ (Gaussian)	T_i(equiv)	Z	M
Ar XVII	$1s^2\ {}^1S_0 - 1s2p\,{}^1P_1$	3·9492	1st	0·0046	9 ± 3 keV	16	40
Ar XVII	$1s^2\ {}^1S_0 - 1s2p\,{}^1P_1$	3·9492	3rd	0·0048	10 ± 1 keV	16	40
Ar XVII	${}^1S_0 - {}^3P_1$	3·9689	1st	0·0047	9·4 ± 1 keV	16	40
Ne X	1s - 2p	12·134	1st	0·0203	9 ± 1 keV	10	20
DII					$\sim 1^{o} \rightarrow 2$ keV* <5 keV^{+}	1	2

^{o}[13], *[3], $^{+}$[12]

3.3 Interpretation of source function of lines

In summary, the spectroscopic results are (a) the source function $I_\lambda(d\lambda)$ is Gaussian, (b) $\frac{\lambda}{\Delta\lambda_{1/2}} \propto \sqrt{M}$, and (c) $\frac{\lambda}{\Delta\lambda_{1/2}} \sim 500$ to 1000 for the Neon and Argon lines. Resonance absorption broadening can be discounted on the grounds that the oscillator strength of the intercombination line is 10^5 times smaller than that of the allowed line of Ar XVII while the broadening of both lines is similar. Stark broadening at densities of $\sim 10^{19}$ cm^{-3} is also small relative to Doppler effects at these short wavelengths. For the Ne X Lyman series, the quasi-static effect is

$$\Delta\lambda_{\text{stark(cm)}} \simeq 0{\cdot}064\ \lambda^2\ n^2\ E \quad (E \text{ in kV/cm})$$

which is $\sim 8 \times 10^{-4}$ Å at approximately 10 Å for Lyα. This is likely to be an upper limit to Stark broadening for the spectral lines under consideration. Wavelength shifts corresponding to the observed plasma velocity (section 2.2) of $\leq 4 \times 10^7$ cm sec^{-1} can quantitatively account for the observed line broadening, $\Delta\lambda_{1/2}$. However, the source function $I(d\lambda)$ is strictly Gaussian and this requires the ion velocities to have, or imitate, a thermal distribution.

The spectroscopic data is consistent with an ion temperature $T_i \sim 9$ keV, common to all the ions in the plasma. In this case, however, the neutron emission from thermonuclear reactions would exceed the observed emission while the plasma kinetic energy would also exceed that predicted by pressure balance. It is more reasonable to propose that the deuterium ion temperature is closer to that observed by laser scattering [13] and is between 1 and 2 keV as predicted by the 2-dimensional MHD code [3]. It is, therefore, probable that each separate ion species has a characteristic ion temperature. This could arise for example when there are electric fields in the plasma due to current-driven ion acoustic waves [14] with characteristic frequency

$< \omega_{ip} = 1{\cdot}5 \times 10^{2}\ n_e^{\frac{1}{2}}$ c/s, (i.e. $< 7{\cdot}5 \times 10^{11}$ c/s). These waves will be damped by coulomb collisions, $\nu_{ei} \simeq 10^{11}$ c/s.

An estimate of the electric field, $\xi_o e^{i\omega t}$ due to these waves can be derived from the average particle energy, E,

$$E = \frac{e^2 \xi_o^2}{4(\omega_{ip}^2 + \nu_{ei}^2)} \frac{Z^2}{M} \qquad (2)$$

$\xi_o \simeq 5 \times 10^{4}$ V/cm, and this is still smaller than the interionic Stark field in the plasma.

It is clear that if one includes an estimated value for T_i, for deuterium, Table 2, the ion energies do not scale either with M or Z alone. However, a scaling with Z^2/M gives as a best fit to the results.

$$E_{Z/M} = T_o(1 + Z^2/M) \qquad (3)$$

with T_o the true thermal component equal to 1·4 keV. Since the ion-ion relaxation time is of the order of a few nanoseconds, it is somewhat difficult to explain the existence of a separate energy for the different ions. However, a similar situation is known to exist in the orthogonal pinch, [15].

We now consider whether current-driven turbulence could play a role in heating the ions. Certainly the critical field for run-away electrons

$$E_c = 2 \times 10^{12}\ n\ Z^2/Te \quad V/cm$$

can be exceeded in a magnetic field-free region by the inductive $\left(\frac{V \times B}{10^8}\right)$ V/cm field in the plasma column. The flux of hard (> 100 keV) X-rays are evidence that much higher electric fields can be generated during the plasma column break-up. However, the condition for relatively weak ion-acoustic turbulence, namely that the electron drift velocity should exceed the ion sound speed, is not satisfied unless a substantial fraction of the total current is confined to dimensions of the order of the filamentary structure observed with the nanosecond transmission photography and with the space resolved Ar XVII emission (see sections 2.2 and 3.4).

It has been pointed out recently [16, 17] that a two-component ion distribution with a non-thermal component accelerated along the axis of symmetry could suitably modify the moving thermal plasma concept proposed in [1] and [18] to explain the puzzling features of the neutron emission (the latter are the large equivalent centre of mass velocity of the ions, $> 10^{8}$ cm sec^{-1}, and the nearly isotropic neutron emission). The spectroscopic analysis in this paper is concerned only with the thermal component since the plasma is viewed orthogonal to the axis of symmetry and the results in no way discount the existence of two-component ion-energy distribution.

3.4 Source-Crystal Aspect (and Evidence for Fine Structure)

Also emerging from the study of line profiles obtained with various source-spectrometer configurations is the vital importance of geometrical matching of the source to the crystal and its plane of curvature for maximum use of the source-radiation. The bandwidth of the instrument is entirely determined by the angular width of the source. The effect of this is demonstrated in figure 10 where the limited bandwidth of $\sim$ 0·1 Å imposed by a source 1 cm long, 130 cms

from the crystal truncates the Ne X 1s - 2p line. Deliberately mismatching the source and crystal so that the bandwidth would be severely restricted for a very narrow source has, in fact, indicated the presence of thin, mobile filamentary structures in the pinch. Figure 11 shows the spectral intensity of the Ar XVII resonance line in third order when such a mismatch was effected. The 'structure' is consistent with emitting regions of the order of 100 μm in diameter. Filaments of the same dimensions are also evident in interferometric and shadowgram studies of the discharge, section 2.2.

3.5 Time-Resolution of Line Emission and Evidence for Dielectronic Recombination

In Paper 1, calculations of the ion confinement, estimated from the appearance time and relative intensities of the H and He-like argon ions, depended on the rate coefficients for ionisation and recombination. Following this, it is important to consider modifications to those rates due to dielectronic recombination, autoionisation and collisional step-wise excitation [19].

At most it would seem that the ionisation rates could be enhanced by a factor of 2 or 3 due to step-wise effects. Dielectronic recombination, on the other hand, could account for most of the recombination for highly-stripped ions. A consideration of the expression derived by Burgess, [20], indicates that for Ar XVII with $n_e = 2 \times 10^{19}$ cm^{-3} and Te = 2 keV, dielectronic recombination could be a factor of ten higher than collisional-radiative recombination, assumed in Paper 1. The effect of the low thermal limit ($n^* = 10$ for Ar XVII) which decreases the dielectronic recombination has been taken into account in this estimate.

The structure of the Li-like satellites ($1s^2 2s$ - $1s2s2p, 1s2p^2$) to the He-like resonance line ($1s^2\ ^1S_0$ - $1s2p\ ^1P_1$), shown in figure 8 for the Ar XVII ion, provides direct confirmation that dielectronic recombination is the dominant process for this ion. In the case where dielectronic recombination populates the upper levels of the satellite lines there will be typically two satellites, of equal intensity; this according to [21] should be ~ 20% of the resonance line intensity.

In the focus the two Li-like satellites, figure 8, have been identified previously, [6], and have an intensity which is 20% of the He-like resonance line intensity for neon, and 15% for argon. In the alternative case that the $1s2s2p, 1s2p^2$ levels are populated directly from the Li-like ion, only one component, that arising from the $1s2p^2\ ^2P^e$ level, would be in evidence. The other levels would lead preferentially to autoionization.

The effect of the enhanced recombination is to lower the degree of ionization which would exist in the steady-state at a given temperature. The intensity of H-like relative to He-like argon then indicates a closer approach to a steady state than in Paper 1.

In the analysis of ion energies it has been demonstrated [22] that it is important to compare ions which appear at the same time. Figure 12 shows typical time-histories of the inner-shell Li-like lines and the He-like resonance lines of argon measured with p-n junction surface barrier detectors [Paper 1]. These are compared with the neutron emission and the electrical waveforms. For all the plasma lines considered in this paper the time of emission was similar, though this result may be in error, since, except for the $1s^2$ - 1s2p transitions a relatively large continuum contribution was admitted with the line.

It is of interest to note that when the plasma meets the axis of symmetry (dI/dt (Minimum)) the peak of the soft X-rays follows some 20 nsecs or so later, and after a similar time interval the peak of the neutron emission follows. In many instances double and even triple, soft X-ray pulses have been seen, separated by 100 nsec or more. Corresponding multiple neutron pulses are also seen, with the later ones of low intensity. These later pulses of soft X-rays were synchronized with the laser pulse used in the optical studies but no refraction or shift of the background fringe pattern could be discerned.

4. CONCLUSIONS AND DISCUSSION

The nanosecond-exposure transmission photography confirms the following features of the plasma dynamics which are predicted by the 2-D two fluid code, [3]: (a) The cusped topology of the plasma boundary during the implosion phase results in a continuous axial flow of plasma from the compression volume so that only a small fraction ($\sim$ 5% is measured by the interferograms) of the original gas exists in the final pinch. (b) The width of the plasma boundary is $\lesssim$ 1 mm during the implosion, but at peak compression the density distribution relaxes to a parabolic form typical of a diffuse pinch.

Rayleigh-Taylor instabilities cause fluted distortions of the imploding sheath but since the boundary decelerates before maximum compression they do not contribute greatly to plasma loss. The most highly compressed region of the pinch, initially close to the anode, suffers break-up through $m = 0$ and, less often, $m = 1$ instabilities, the former having a growth time of 10 nanoseconds.

One feature not predicted by the fluid code is the fine (< 100 microns) filamentary structure within the envelope of the compressed plasma. This has been observed both in the optical study and in the X-ray spectroscopy.

The emission line profile analysis indicates a thermal energy distribution for each ion species, the transverse energy in each scaling as Z^2/M. The component of the ion energy along the axis has not been investigated. The importance of dielectronic recombination for these ions has been indicated.

Average values of the measured pinch parameters e.g. the deuterium ion temperature, the electron density and the electron temperature measured previously, [5], are in agreement within a factor of two with those predicted by the fluid code.

The scaling of temperature with Z^2/M suggests a method for transferring some of the directed energy in the implosion into thermal energy, namely the addition of a small percentage of heavy gas (less than that which would cause radiative cooling i.e., $\lesssim$ 5% argon). Finally the X-ray and neutron pulses which occur up to 200 nanoseconds later than the first pulses cannot be identified with any optical features of a dense focus. This is unlikely to be simply a field of view limitation, since this was extended to 6 cm below the centre electrode. It is more likely that the source of the later emission is a much more tenuous plasma with $\hat{n}_e \ll 8 \times 10^{18}$ cm^{-3}.

REFERENCES

[1] BOTTOMS, P.J., CARPENTER, J.P., MATHER, J.W., WARE, K.D. and WILLIAMS, A.H. Paper CN-24/G-5, Proc. of IAEA 3rd Conf. on Plasma Physics and Controlled Nuclear Fusion Research, Novosibirsk, (1968).

[2] POTTER, D.E. and HAINES, M.G. Proc. of IAEA 4th Conf. on Plasma Physics and Controlled Nuclear Fusion Research, Wisconsin, (1971).

[3] POTTER, D.E. Ph.D Thesis, University of London, (1970).

[4] MORGAN, P.D., PEACOCK, N.J. and POTTER, D.E. Proc. of 3rd European Conf. on Controlled Fusion and Plasma Physics, p.118, (1969).

[5] PEACOCK, N.J., WILCOCK, P.D., SPEER, R.J. and MORGAN, P.D. Paper CN-24/G-4, Proc. of IAEA 3rd Conf. on Plasma Physics and Controlled Nuclear Fusion Research, Novosibirsk, (1968).

[6] PEACOCK, N.J., SPEER, R.J. and HOBBY, M.G. J. Phys. B, 2, p.798-810, (1969).

[7] MORGAN, P.D. and PEACOCK, N.J. To be published, (1971).

[8] BASOV, N.G., KROKHIN, O.N. and SKLIZKOV, G.V. Appl. Opt., 6, p.1814-1817, (1967).

[9] KINDER, W. Optik, 1, p.413-448, (1946).

[10] GREEN, T.S. and NIBLETT, G.B.F. Nuclear Fusion, 1, p.42-46, (1960).

[11] JOHANN, H.H. Z. Phys., 69, p.185-206, (1931).

[12] PATOU, C. Journal de Physique, 31, p.339-349, (1970).

[13] BERNARD, A., CESARI, G., COUDEVILLE, A., JOLAS, A., de MASCUREAU, J. and WATTEAU, J.P. Proc. of IAEA 4th Conf. on Plasma Physics and Controlled Nuclear Fusion Research, Wisconsin, (1971).

[14] HAMBERGER, S.M. and JANCARIK, J. Phys. Rev. Lett., 25, p.999-1002, (1970).

[15] SAWYER, G.A., BEARDEN, A.J., HENINS, I., JAHODA, F.C. and RIBE, F.L. Phys. Rev., 131, p.1891-1897, (1963).

[16] POTTER, D.E. Proc. of 4th European Conf. on Controlled Fusion and Plasma Physics, p.116, (1970).

[17] BERNSTEIN, M.J. Phys. Fluids, 13, p.2858-2866, (1970).

[18] AGAFONOV, V.I., GOLUB, G.V., GOLUBCHIKOV, L.G., DYACHENKO, V.F., IVANOV, V.D., IMSHENNIK, V.S., KOLESNIKOV, Yu.A., SVIRSKY, E.B., FILIPPOV, N.V. and FILIPPOVA, T.I. Paper CN-24/G-2, Proc. of IAEA 3rd Conf. on Plasma Physics and Controlled Nuclear Fusion Research, Novosibirsk, (1968).

[19] JORDAN, C. Mon.Not. Roy. Astr. Soc., 142, p.501-521, (1969).

[20] BURGESS, A. Astrophys. J., 141, p.1588-1590, (1965).

[21] GABRIEL, A.H. and JORDAN, C. Case Studies in Atomic Collision Physics, vol.2, Editors McDowell and McDaniel, North Holland Press, (1971).

[22] JONES, B.B. and WILSON, R. Nucl. Fusion Supplement, pt.3, p.889-893, (1962).

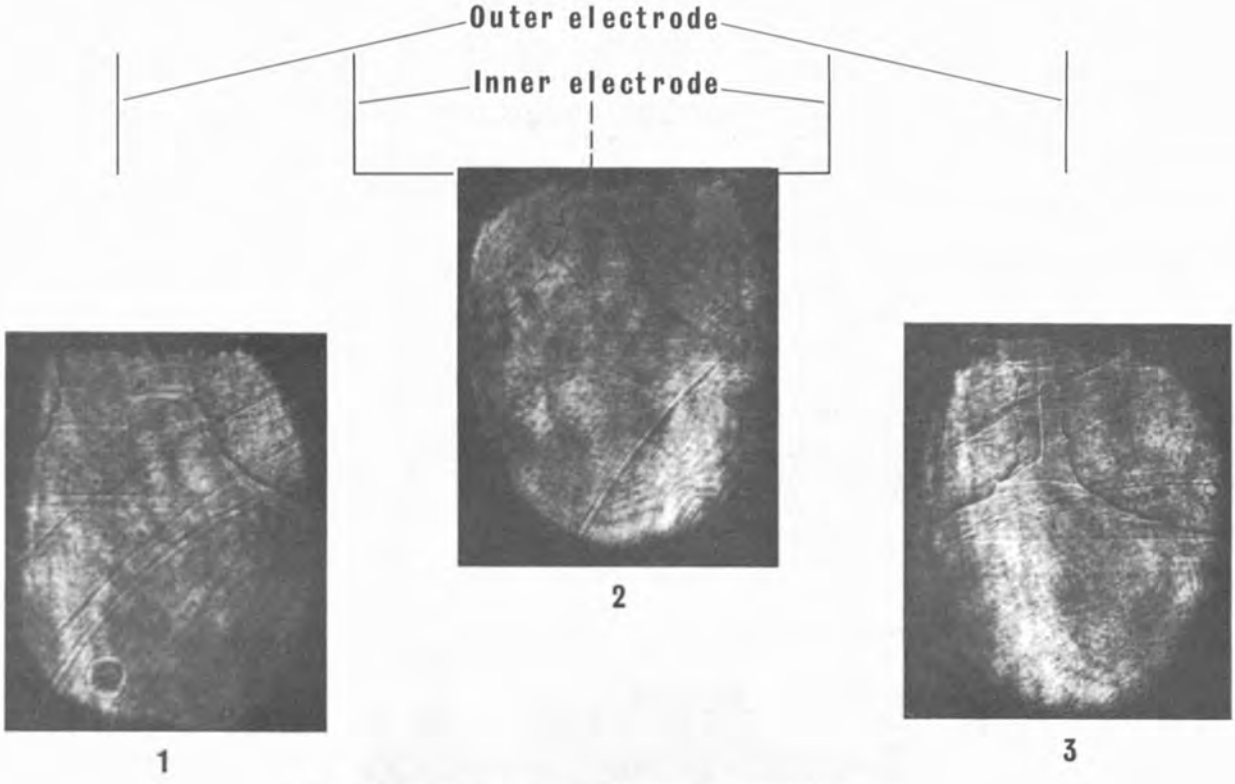

Figure 1 Shadowgram sequence during run-down and pinch stages; Time interval between frames = 15 nsec. Inner electrode diameter = 5 cm; V = 30 kV; p_o = 2·5 torr (D_2 + 4% Ar).

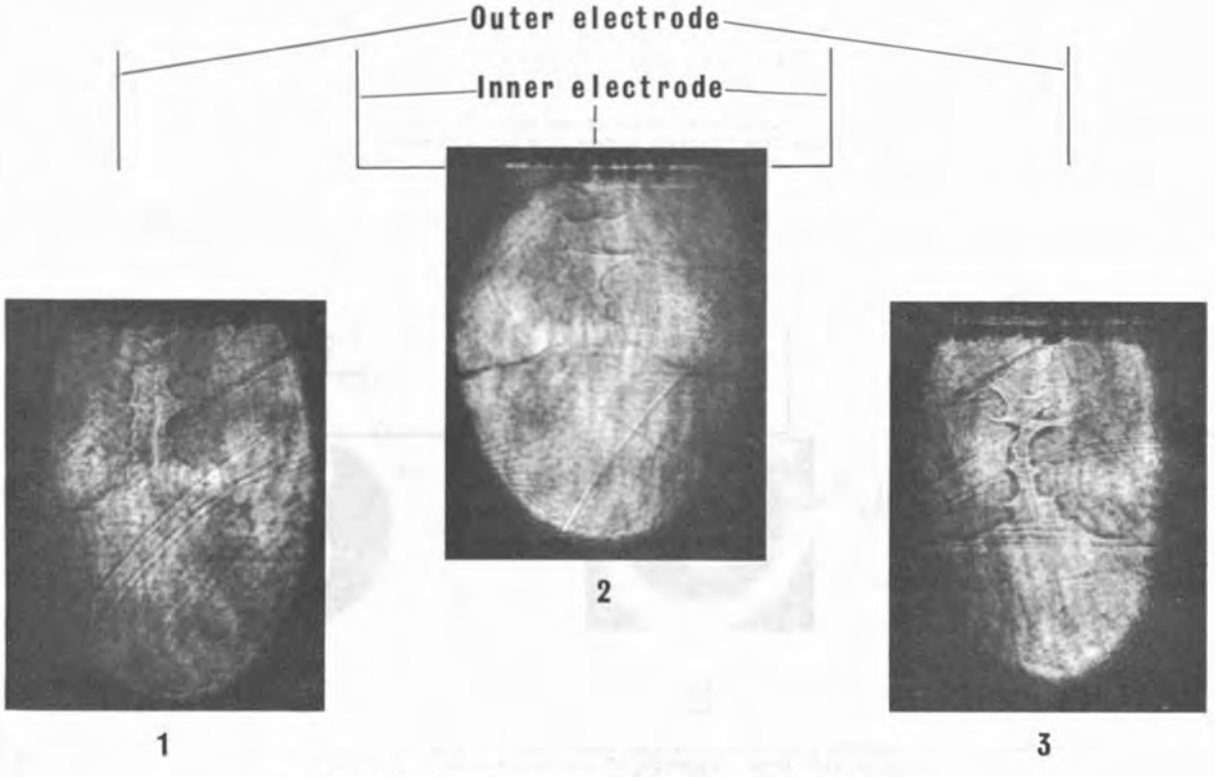

Figure 2 Shadowgram sequence during dense-pinch stage; Time interval between frames = 6·5 nsec. Inner electrode diameter = 5 cm; V = 30 kV; p_o = 2·5 torr (D_2 + 4% Ar).

CR 71 66

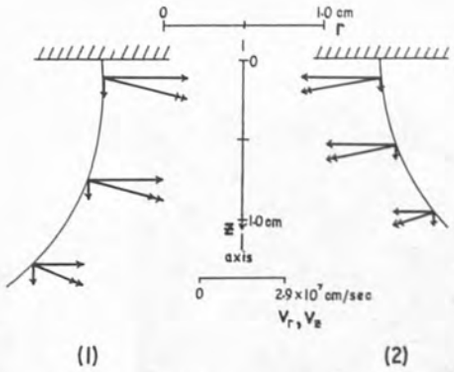

Figure 3 Variation of radial and axial velocity of the imploding sheath with distance from electrode surface; (1) V = 28·3 kV; (2) V = 24·3 kV; p_o = 2·5 torr (D_2 + 4% Ar).

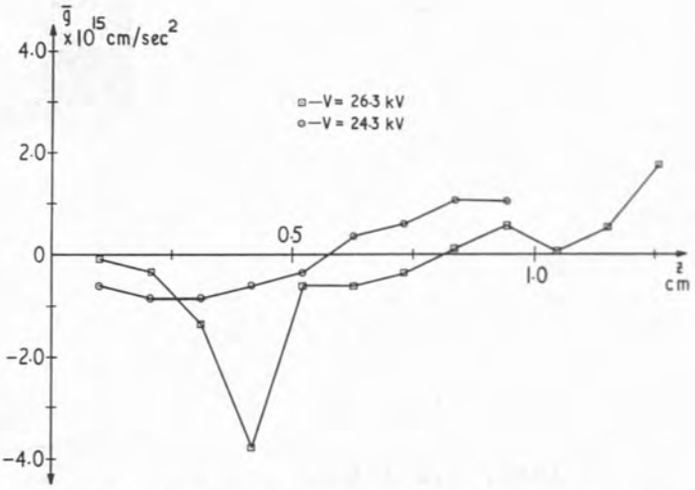

Figure 4 Variation of radial acceleration of the imploding sheath with distance from electrode surface, for two different charging voltages. Initial pinch diameter ~ 1·7 cm at z = 0·1 cm. p_o = 2·5 torr (D_2 + 4% Ar).

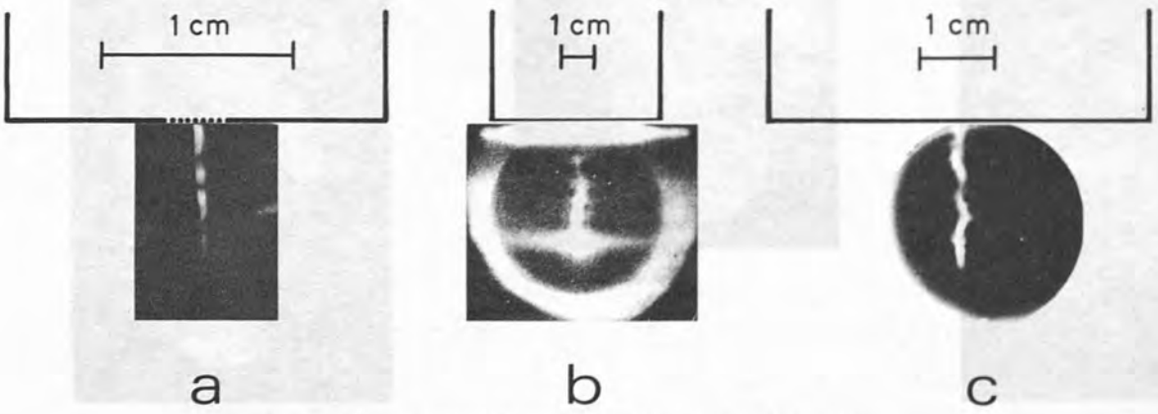

Figure 5 (a) schlieren, (b) image-converter camera and (c) time-integrated soft X-ray photographs of dense-pinch stage. V = 30 kV; p_o = 2·5 torr (D_2 + 4% Ar).

CR 7166

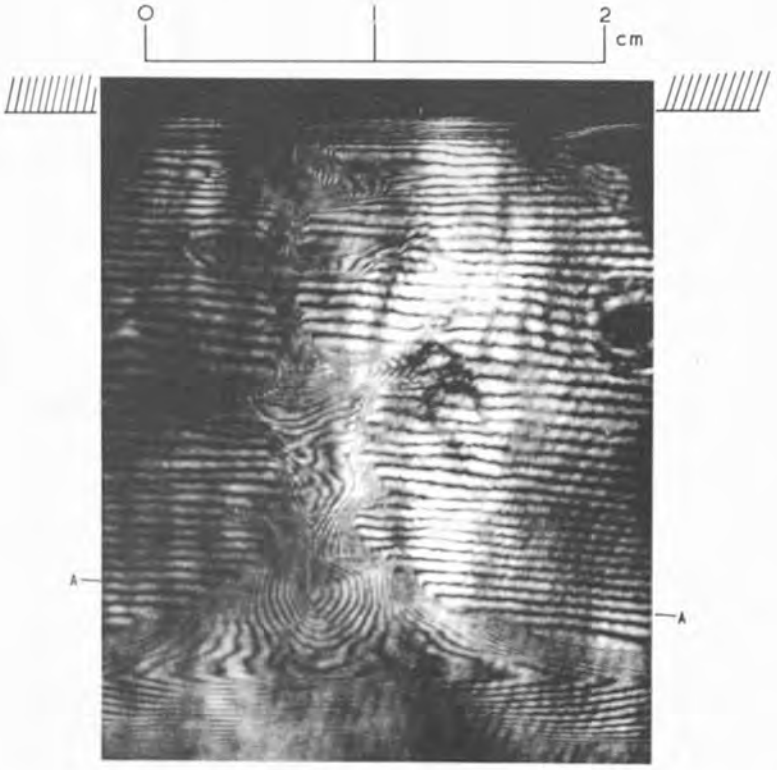

Figure 6 Mach-Zehnder interferogram of dense-pinch stage. V = 30 kV; p_o = 2·5 torr (D_2 + 4% Ar). [AA is section along which the fringe shifts have been analysed - see figure 7].

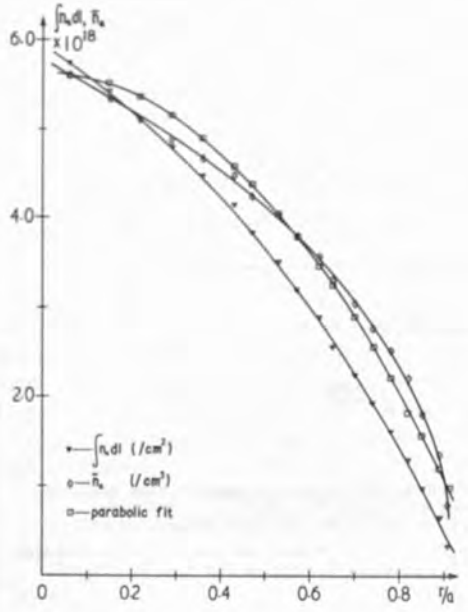

Figure 7
Variation of $\int_0^t n_e \, dt$ and $\bar{n}_e(r/a)$.

Analysis has been made along section AA of figure 6. A parabolic function $\bar{n}_{max}(1-(r/a)^2)$ is also shown.
V = 30 kV; p_o = 2·5 torr (D_2 + 4% Ar).

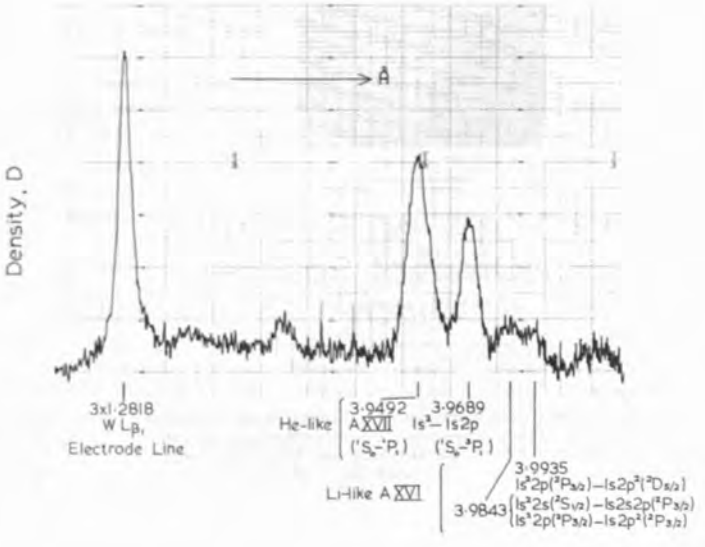

Figure 8
Concave curved mica spectrum of a Plasma Focus discharge;
V = 28 kV, p_o = 2·5 torr (D_2 + 4% Ar).

CR 71 66

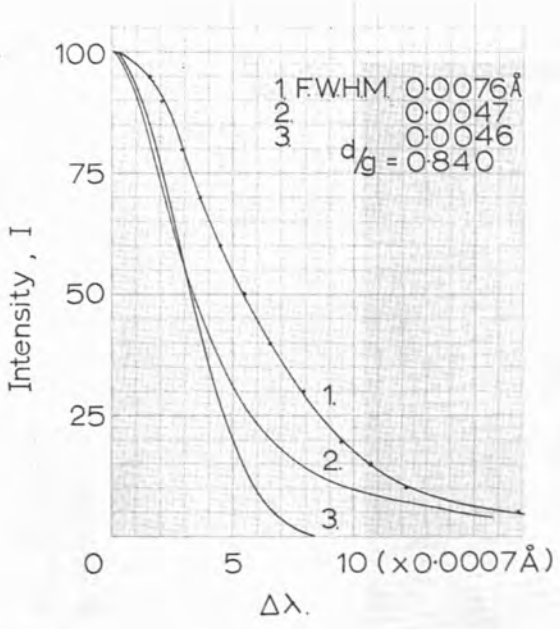

Figure 9
Measured Ar XVII profile 1 (Voigt), compared with instrumental 2 (Dispersive), and true 3 (Gaussian) profiles.

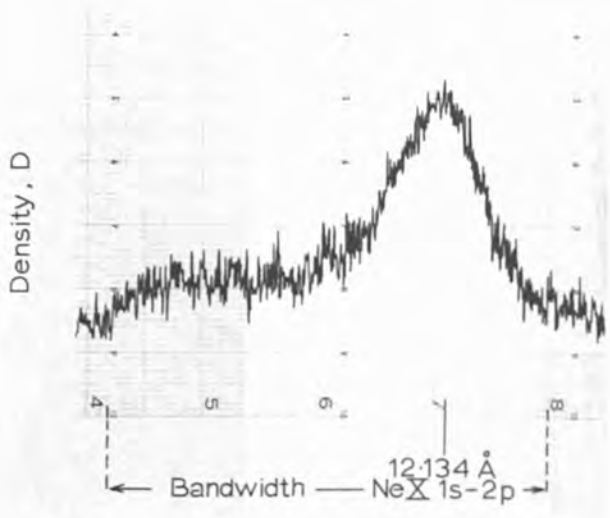

Figure 10
Concave curved mica spectrum of a Plasma Focus discharge showing the effect of limited bandwidth; V = 28 kV, p_o = 2·5 torr (D_2 + 6% Ne).

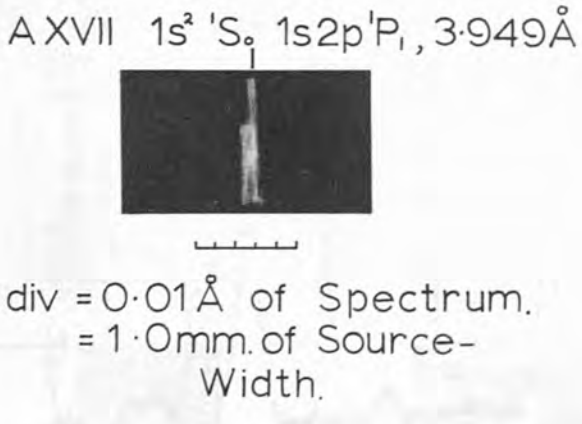

Figure 11
Concave curved mica spectrum of a Plasma Focus discharge showing the effect of source fine-structure and motion when the bandwidth is deliberately set less than the line-width; V = 28 kV, p_o = 2·5 torr (D_2 + 4% Ar).

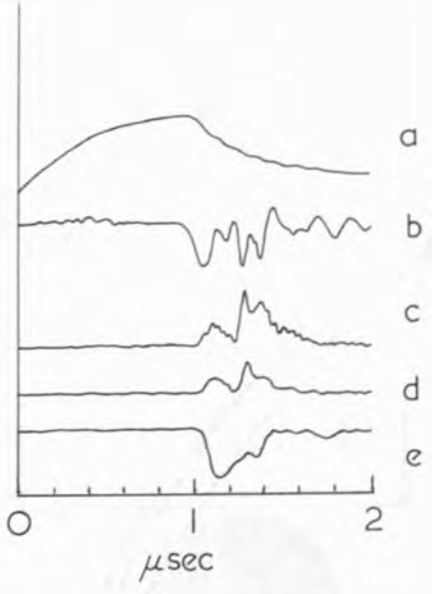

Figure 12
Electrical, soft X-ray and neutron diagnostic time sequences of a Plasma Focus discharge; V = 28 kV, p_o = 2·5 torr (D_2 + 4% Ar). (a) I, (b) dI/dt, (c) soft X-rays, Ar XVII He-like wavelength, (d) soft x-rays, Ar XVI Li-like wavelength and continuum, (e) neutrons (corrected for time of flight).

CR 71 66

Nanosecond laser pulse generation using an electro-optic shutter external to the Q-spoiled cavity

D Morgan† and N J Peacock‡
Department of Physics, Royal Holloway College, Englefield Green, Surrey
†Culham Laboratory, UKAEA, Abingdon, Berks.

Received 9 March 1971

Abstract An electro-optic switching circuit is described which will produce a pulse of duration 1 ns or less from a ruby laser. The switch, external to the *Q*-spoiled oscillator cavity, uses a KD*P Pockels cell which is driven by a full-wave voltage pulse. The laser pulse, after $\times 15$ amplification, has an energy of 3×10^{-2} J and is sufficiently coherent and free of jitter to find a ready application in the diagnostics of highly transient plasmas.

1 Introduction

The problem of producing a laser pulse of 1 ns duration or less is of importance in diagnostic measurements of transient high density plasmas produced, for example, in the plasma focus device (Peacock *et al.* 1969) or by irradiation of solid targets by high-powered lasers (Basov *et al.* 1968). The speed of the density fronts in these plasmas can be up to 0·4 mm ns^{-1} while the characteristic dimensions of the structure in the plasma are often less than 0·1 mm. For diagnostic purposes, e.g. refractive index measurements, pulses of high energy are not necessary, less than 0·01 J being adequate for single pulse illumination of the plasma, though for multiple exposure sequences (Basov *et al.* 1967) at least this energy per pulse is desirable. It is advantageous when making holographic or interferometric studies to have a coherence length of several centimetres and a beam divergence of a few milliradians. It is also desirable to have the pulse-to-pulse jitter considerably less than 10 ns, so as to be able to illuminate the plasma at the same time during its formation or decay on successive discharges.

Because of the fine-grained spatial structure of these transient phases it is not very practicable to illuminate the plasma with a long (~ 50 ns) laser pulse and shutter the exposure using recent developments in image converter cameras (Bradley *et al.* 1970). It is desirable therefore to employ laser pulses which have the required time resolution or shorter (i.e. $\lesssim 1$ ns). There are two well tried methods of producing pulses of shorter duration than those yielded by conventionally switched Q-spoiled lasers, namely the pulse-transmission mode laser (Hook *et al.* 1966) and the mode-locked laser (e.g. DeMaria *et al.* 1966). The duration of a light pulse produced by the former method is determined by the time required for light to travel twice the path between the reflectors of the oscillator cavity. In order to produce a pulse duration of 500–700 ps the overall oscillator cavity length has to be less than 7·5 cm and the switching of the electro-optic cell in the cavity has to be accomplished in approx. 200 ps. These requirements are difficult to meet. The mode-locked oscillator on the other hand lacks the coherence which is convenient for interferometric diagnostics. In order to produce clean, mode-locked pulses a saturable dye switch within the cavity is necessary, and the overall jitter between the start of the flashtube discharge and the appearance of the output pulse is typically of several microseconds.

The present paper describes the results of pulse-clipping the output pulse from a conventionally *Q*-switched cavity. This technique gives a pulse which fulfills all the requirements for the optical study of highly transient plasmas.

2 The experimental method

The use of an extra-cavity electro-optic shutter to shorten the output of a *Q*-switched laser is perhaps an obvious technique, but it has been employed only recently (e.g. Michon *et al.* 1969, Alcock and Richardson 1970). In these references the electro-optic shutter was switched from zero voltage corresponding to the condition for blocking the polarized oscillator beam to $V_{\frac{1}{2}\lambda}$ (the half-wave voltage) corresponding to full transmission, and then back to zero voltage. The half-width of the voltage pulse then determined the laser pulse width.

In the present arrangement, shown schematically in figure 1, the electro-optic shutter external to the cavity is a KD*P cell, which requires a relatively modest voltage, approximately 5 kV, to rotate the plane of polarization through 90° (the half-wave voltage). A laser-triggered spark gap (LTSG) similar to that described by Bradley *et al.* (1969) is used to generate the voltage pulse on the KD*P cell. Maximum energy in the transmitted pulse is gained by clipping the oscillator output at its peak intensity, using a Blumlein circuit (figure 1). Full-wave switching is employed; i.e. the transmission of the output from the ruby oscillator is allowed only over that part of the steep falling edge of the voltage pulse centred around the voltage $V_{\frac{1}{2}\lambda}$ as illustrated in figure 1. For identical circuit parameters, e.g. switching voltage, spark gap impedance, Pockels cell impedance and coaxial cable characteristics full-wave switching in this manner can yield shorter laser pulses than those reported previously.

3 Mode of operation

The Korad K1500 ruby laser system used for the short pulse generation is basically a conventionally *Q*-switched oscillator and an amplifier giving typically 10 J in a pulse whose half-width is of the order of 17 ns. When *Q*-switched the plane polarized output from the oscillator passes through the unbiased KD*P Pockels cell with no rotation of the plane of polarization. The Pockels cell is operated in the longitudinal

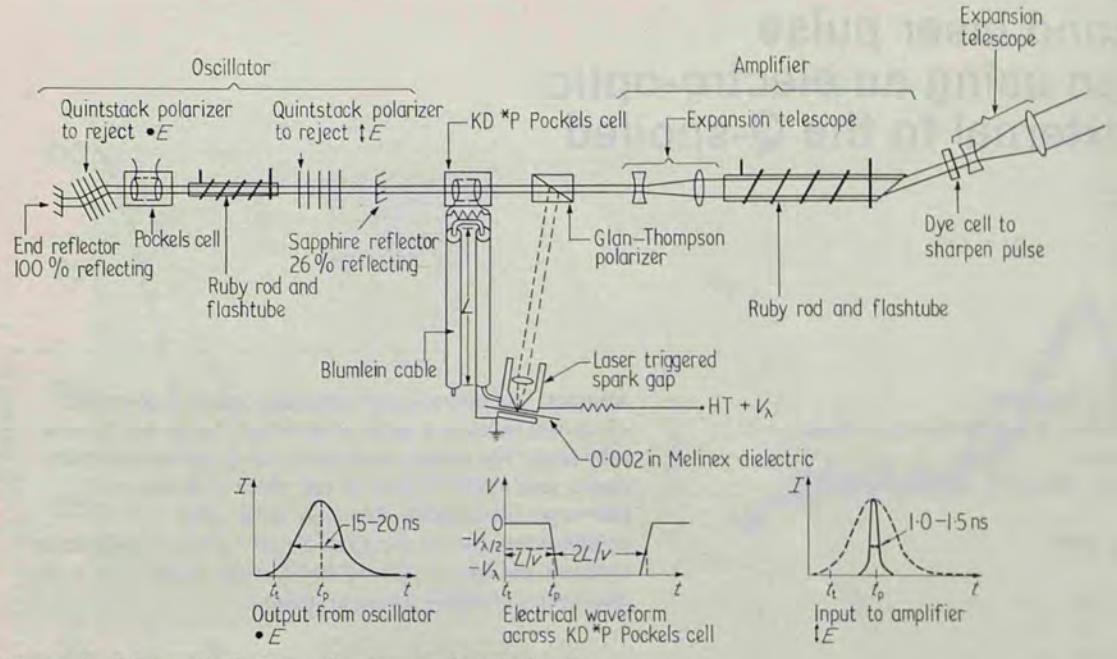

Figure 1 Schematic diagram of nanosecond optical pulse generator. KD*P Pockels cell fed from centre of Blumlein cable and shunted with $2Z_0$ impedance

mode and has an aperture of 1 cm. A Glan–Thompson polarizer prevents transmission through to the amplifier and deflects the beam on to the LTSG.

The LTSG consists of two brass electrodes, 100 μm apart and open to the atmosphere, with a Melinex sheet of thickness 50 μm separating the electrodes. A static voltage of about 14 kV is maintained across the gap. Triggering is achieved by puncturing the dielectric with the laser beam which is focused with a 5 cm focal length lens on to one electrode through a 1 mm hole in the other. The Melinex sheet is replaced after each shot. The LTSG is capable of switching voltages of the order of 15 kV with nanosecond rise-time and jitter. The delay in the gap breakdown is of the order of a few nanoseconds and depends on the incident laser power. With the present arrangement the threshold for breakdown occurs at a power level of approx. 1 MW.

One electrode of the LTSG is connected to the inner conductor at one end of the Blumlein cable (Wilkinson 1946), of half-length L, while the other electrode is connected to the outer conductor at the same end of the cable. Uniradio 67 cable is used with a characteristic impedance Z_0 of 50 Ω. The inner conductor of the Blumlein cable is charged to a voltage $+V_\lambda$, the outer conductor being earthed. The outer conductor has a short break in it at the midpoint of the Blumlein, and the load which is the Pockels cell in parallel with a $2Z_0$ resistance is connected across the break to the two sections of conductor. The other end of the Blumlein cable is an open circuit.

When the LTSG is triggered, at time t_t (figure 1), a voltage step of magnitude $-V_\lambda$ is launched into the cable in the direction of the load. At a time L/v after the gap breakdown (v denotes the velocity of propagation in the cable), a rectangular pulse of magnitude $-V_\lambda$, and duration $2L/v$ appears across the load. As the voltage across the Pockels cell decreases from zero to $-V_\lambda$ volts, during the leading edge of the pulse, so the plane of polarization of the laser light passing through the cell is rotated through a full 180°. The degree of rotation is proportional to the applied voltage. Thus, at a given voltage level $-V_{\frac{1}{2}\lambda}$ on the leading edge of the pulse, the plane of polarization at the output of the Pockels cell will have rotated through 90°. The oscillator light can now pass straight through the Glan–Thompson polarizer into the amplifier. However, the applied voltage continues to fall to $-V_\lambda$, corresponding to 180° of rotation, where again the oscillator output is rejected sideways at the Glan polarizer interface. The duration of the rectangular clipping pulse $2L/v$ is sufficiently long to block the remainder of the Q-spoiled pulse. Thus, the shutter only admits light through to the amplifier over a portion of the leading edge of the applied electrical pulse, centred around the point where the voltage is $-V_{\frac{1}{2}\lambda}$ (figure 1). By adjusting the flux of light on the LTSG and choosing a suitable length for the Blumlein cable, the time at which the voltage pulse arrives at the KD*P Pockels cell is arranged to coincide with the maximum of the Q-spoiled pulse ($t=t_p$). The shuttered pulse which is admitted to the amplifier is thus of maximum intensity. Because of mismatching and losses in the cable, the static voltage on the Blumlein has to be somewhat greater than the pulsed full-wave voltage of the Pockels cell. Also, because of losses within the Pockels cell, the applied pulse voltage is approx. 1 kV higher than the calculated pulsed full-wave voltage (10·4 kV).

4 Results and discussion

Figure 2 shows the waveform of the electrical pulse appearing across the Pockels cell. The pulse is monitored using a low-inductance resistive voltage divider coupled to a Tektronix 519 oscilloscope, the inherent rise-time of the measuring

Figure 2 Waveform of electrical pulse across Pockels cell. Horizontal scale, 10 ns per major division; vertical scale, 5·7 kV per major division

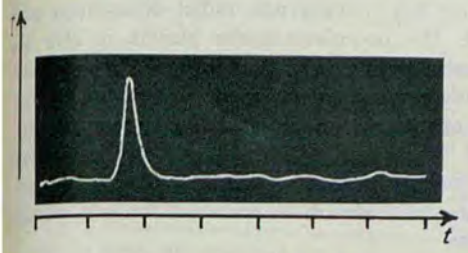

igure 3 Waveform of optical pulse after amplification touched for clarity). Time scale, 5 ns per division

stem being 0·9 ns. The rise-time between 10% and 90% of ak amplitude is 2·5 ns. This is approximately equal to 2τ, where τ is the 1/e time.

Figure 3 shows the waveform of the amplified optical pulse onitored using an ITL (HCBI) photodiode which with a 519 cilloscope has an inherent rise-time of 0·35 ns. The duration the optical pulse (HPFW) is 1·2 ns.

For an electro-optic cell operating in the longitudinal ode and mounted between crossed polarizers as in figure 1, e transmission I can be expressed as a function of the odulation voltage ratio $V/V_{\frac{1}{2}\lambda}$, i.e.

$$I_V/I_i = \sin^2\left(\tfrac{1}{2}\pi \frac{V}{V_{\frac{1}{2}\lambda}}\right) \qquad (1)$$

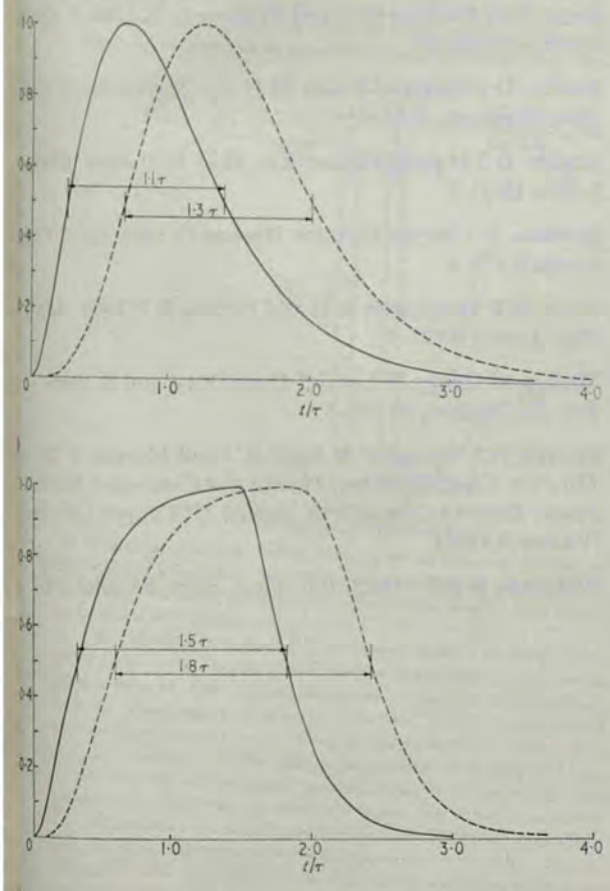

igure 4 (a) Computed optical waveform of pulse produced full-wave clipping. Full curve, $\tau_1 \gg$ or $\ll \tau_2$; broken rve, $\tau_1 = \tau_2$. (For definition of τ_1 and τ_2 see text).
) Computed optical waveform of pulse produced by lf-wave clipping. Full curve, $\tau_1 \gg$ or $\ll \tau_2$; broken curve, $= \tau_2$. (For definition of τ_1 and τ_2 see text)

where I_i is the incident light flux. For any voltage step the half-intensity points of the Pockels cell transmission correspond to 25% and 75% of the full amplitude of the switching voltage $-V_\lambda$ as given by equation (1). The time between these voltage levels is approx. 1·2 τ, as shown in figure 4(a). The measured optical pulse width (figure 3), is 1·2 ns and is in good agreement with this value. The rise-time of the optical pulse is 0·8 ns.

The fall time of the leading edge of the electrical pulse at the Pockels cell can be considered as the product of two exponentially decreasing voltages with characteristic times τ_1 and τ_2, where τ_1, the fall time due to the switch inductance L_s is L_s/Z_0, and τ_2, the fall time due to the Pockels cell capacitance C, is $2CZ_0$. With full-wave switching using a Blumlein circuit it can be shown that in general the open time of the electro-optic switch varies from 1·1 τ ($\tau = \tau_1 \gg \tau_2$ or $\tau = \tau_2 \gg \tau_1$) to 1·3 τ ($\tau_1 = \tau_2 = \tau$), see figure 4(a).

Similarly the half-wave switching procedure, e.g. Alcock and Richardson (1970), using a different circuit configuration can be shown to give transmission, reaching full intensity, for approximately 1·5 τ to 1·8 τ, figure 4(b).

Some improvement in narrowing the pulse can be achieved by (i) reducing the aperture (and hence capacitance) of the Pockels cell; (ii) using several cables in parallel in the Blumlein $Z_{\text{eff}} = Z_0/N$ and (iii) reducing the inductance of the LTSG. No special attempts were made to do so in the work described in this paper, and for example, a standard Pockels cell of aperture 1 cm was used. Taking the simple precautions above, however, it should be possible to produce a voltage pulse with a rise-time of the order of 1 ns across the Pockels cell and thus obtain an optical pulse of approx 500 ps duration.

After amplification (×15) and passage through a cryptocyanine cell to improve the peak-to-background contrast the energy in the shuttered pulse is 3×10^{-2} J, which is sufficient for many diagnostic purposes in plasma physics. The divergence of the clipped laser pulse was not measurably greater than that of the conventional Q-spoiled pulse, i.e. 3 mrad contained 90% of the beam energy.

A lower limit to the spectral width of the laser beam $\lambda^2/c\Delta t$, is set by the duration of the clipped pulse Δt. In the present experiments (with $\Delta t = 1{\cdot}2$ ns) a monochromatic continuous laser beam would be broadened to 0·013 Å. However, mode coupling in the oscillator cavity did not, in practice, allow linewidths of less than 0·075 Å so that no appreciable deterioration in linewidth, and therefore in coherence length, was introduced by the pulse clipping. A Fabry–Perot interferogram of the amplified pulse, taken with an etalon spacing of 1·0 cm, is shown in figure 5. The

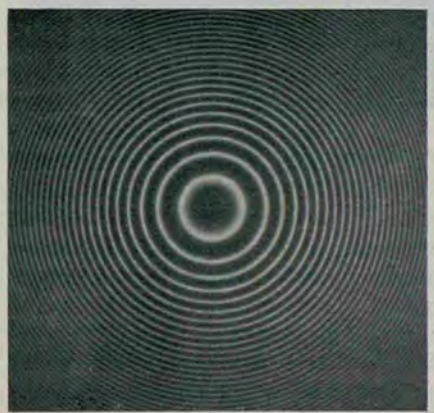

Figure 5 Fabry–Perot interferogram of light in amplified clipped pulse. Free spectral range, 0·24 Å

line-width, 0·075 Å, corresponds to a coherence length of 3·2 cm, which is sufficiently long for nanosecond exposure interferometry.

A 10 ns exposure photograph of the visible light from the dense plasma focus (Peacock *et al.* 1969) using an image converter camera is shown in figure 6(*a*). For comparison a 1 ns exposure shadowgraph of the same plasma using the ruby laser source with full-wave switching is shown in figure 6(*b*). It is readily appreciated that without the required spatial and temporal resolution many of the features of the plasma are overlaid and lost. Along the axis of symmetry of the device the shadowgram shows that there is a density gradient

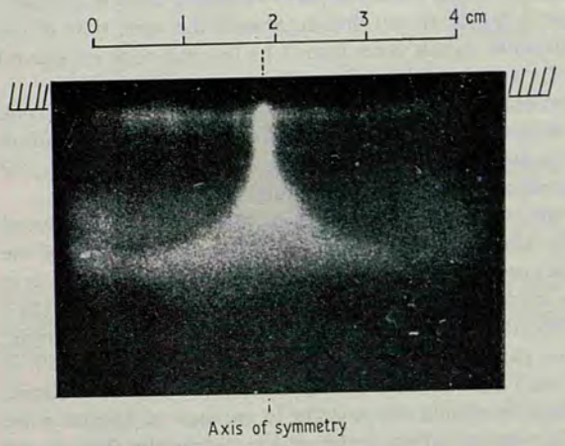

(*a*)

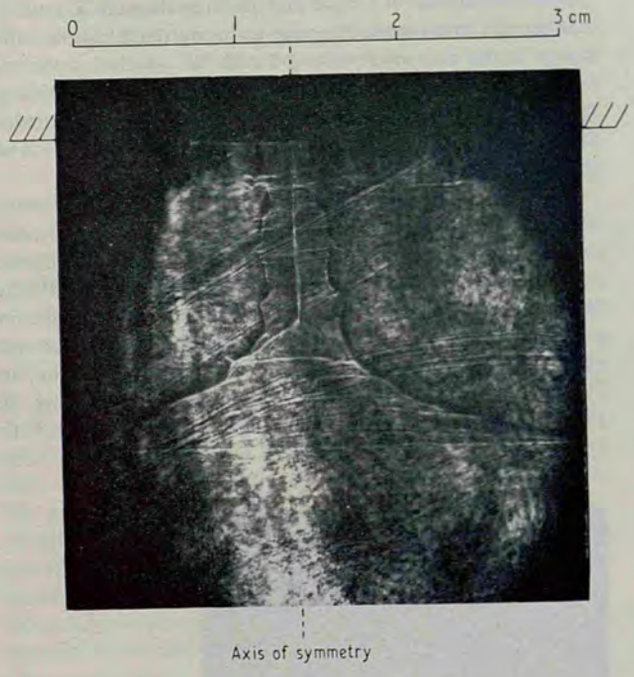

(*b*)

Figure 6 (*a*) 10 ns exposure of pinch stage of plasma focus device taken with image converter camera. The plasma is compressed into the form of a fountain by the axisymmetric magnetic field. The stem of the fountain is close to the anode surface. (*b*) Shadowgram of pinch stage of plasma focus device using amplified clipped pulse for illumination. The diagonal striations across the field are spurious and are due to nonuniformity of the illuminating laser beam

structure which has characteristic radial dimensions of less than 0·1 mm. The boundary of the plasma is also sharp and is scalloped by Rayleigh–Taylor instabilities. Multiple exposure shadowgrams show that these features change in their spatial positions in times considerably less than 10 ns. High spatial resolution ($>100\,\mathrm{l\,mm^{-1}}$) and nanosecond exposure is therefore necessary to study the growth rate of the instabilities and to identify the source of the axial structure.

5 Conclusions

An electro-optic shutter has been developed which is capable of giving nanosecond pulses from a ruby laser. The method used involves full-wave switching of a KD*P Pockels cell external to the oscillator cavity. The laser, with a ×15 amplifier, has adequate energy, 30 mJ, coherence length, 3·2 cm, and time resolution, 1 ns, to find immediate application in the diagnostics of dense, highly transient plasmas. It may also prove useful as a first stage of a multistage laser system for creating high temperature plasmas from a solid target when irradiated by the focused laser beam.

Acknowledgments

The authors would like to thank P D Wilcock for many helpful discussions on this problem.

References

Alcock A J and Richardson M C 1970 *Optics Commun.* **2** 65–8

Basov N G Krokhin O N and Sklizkov G V 1967 *Appl. Optics* **6** 1814–7

Basov N G Krokhin O N and Sklizkov G V 1968 *J. Quant. Electron.* **4** 988–91

Bradley D J Higgins J F Key M H and Majumdar S 1969 *Opto-Electronics* **1** 62–4

Bradley D J Higgins J F and Key M H 1970 *Appl. Phys. Letters* **16** 53–5

DeMaria A J Stetser D A and Heynau H 1966 *Appl. Phys. Letters* **8** 174–6

Hook W R Dishington R H and Hilberg R P 1966 *Appl. Phys. Letters* **9** 125–7

Michon M Guillet H Le Goff D and Raynaud S 1969 *Rev. Sci. Instrum.* **40** 263–5

Peacock N J Wilcock P D Speer R J and Morgan P D 1969 *Third Int. Conf. on Plasma Physics and Controlled Nuclear Fusion Research, Novosibirsk, August 1968* Paper CN-24/G4 (Vienna: IAEA)

Wilkinson K J R 1946 *J. Inst. Elect. Engrs* **93** 1090–112

5.3.11

NANOSECOND TRANSMISSION PHOTOGRAPHY OF A DENSE PLASMA USING A PULSE-CLIPPED Q-SWITCHED LASER

P. D. Morgan* and N. J. Peacock/

* Royal Holloway College, Englefield Green, Surrey, U.K.

/ The Culham Laboratory, Abingdon, Berkshire, U.K.

1. Introduction

The study of refractive index variations in plasmas of electron density, n_e, $\geq 10^{15}$ cm^{-3} using shadowgram, schlieren and interferometric techniques has yielded much useful information on the spatial and temporal variations in n_e, on the gross motion of the plasma, on the growth of instabilities at the plasma boundary and on plasma turbulence [1,2]. The properties of the light pulses from a Q-switched ruby laser, viz. short duration (~ 15 nsec), high intensity (~10^{13} watts cm^{-2} sterradian^{-1}), small beam divergence (~ 1 milliradian), long coherence length (~ 5 cm) and high degree of monochromaticity ($\Delta\lambda \sim 0.1$ Å), make it an invaluable light source for use with the above techniques in their application to the study of transient plasmas.

In order to obtain good time resolution of the high velocity (~3×10^7 cm sec^{-1}) shock fronts associated with dense, highly-transient plasmas (such as those produced in the Plasma Focus device [3] or by irradiation of solid targets by high-powered lasers [4]), light pulses of duration $\leq$ 1 nsec are necessary. A simple and reliable way of obtaining light pulses of suitable duration from any Q-switched ruby laser, without adversely affecting the other properties of the pulses, is to clip the pulse from the laser by means of an extra-cavity electro-optic shutter [5].

This paper describes the use of such a system as a light source for shadowgram, schlieren and interferometric studies of a dense, highly-transient plasma, and some of the results obtained are presented.

2. The Experimental Apparatus

The electro-optic shutter, shown schematically in Fig.1, used to clip the output from a Korad K-1500 laser system was situated between the oscillator and amplifier sections. An output pulse from the oscillator passes through 1, a Glan-Thompson polariser, and 2, an unbiased KD*P Pockels cell, and is incident on 3, another G-T polariser which is crossed with 1. This polariser rejects the laser light sideways at the interface onto 4, a laser-triggered spark gap (LTSG) [6].

The LTSG consists of two electrodes separated by a 50 μ melinex sheet, one electrode being at a voltage + V_λ (~ 12 kV) whilst the other electrode is earthed. A short focal length lens focuses the laser light onto one electrode through a small hole in the other, thereby puncturing the dielectric and triggering the gap. The inner conductor at one end of a coaxial cable, of length 2L and characteristic impedance Z_o, is connected to the positive electrode and the outer conductor is connected

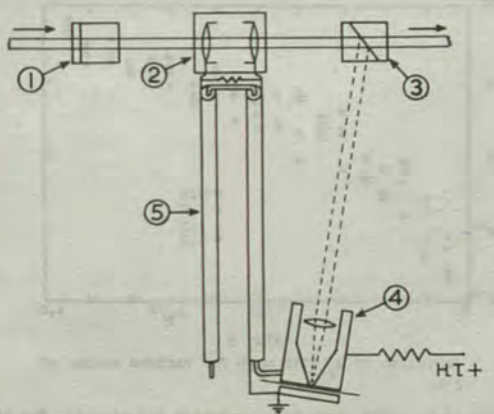

FIG. 1
The Electro-Optic Shutter

to the earthed electrode. At the midpoint of the cable the Pockels cell, in parallel with a 2 Z_o resistor, is connected as a load across a short break in the outer conductor. The other end of the cable is an open circuit. This cable arrangement, 5, is known as a Blumlein [7].

When the LTSG is triggered, a rectangular pulse of magnitude - V_λ and duration 2L/v, where v is the propagation velocity in the cable, appears across the load after a delay of L/v. The clipping action of the shutter is associated entirely with the leading edge of this pulse, in contrast to [5]. As the voltage across the load decreases from 0 to - V_λ, during the fall-time of the leading edge, so the plane of polarisation of the light passing through the Pockels cell is rotated further from its original plane, the full voltage - V_λ causing 180° rotation. In order for the light from the oscillator to pass with undiminished intensity through 3 to the amplifier its plane of polarisation must suffer 90° rotation by the Pockels cell, and this only occurs when the voltage across it is $-\frac{1}{2} V_\lambda$. The half-width of the optical pulse transmitted to the amplifier is defined by the fall-time of the electrical pulse from $-\frac{1}{4} V_\lambda$ to $-\frac{3}{4} V_\lambda$.

By adjusting the light flux incident on the LTSG and choosing a suitable length for the Blumlein, clipping is made to occur at peak light output from the oscillator. The duration of the electrical pulse is sufficiently long to block the remainder of the Q-switched pulse. After amplification the half-width of the clipped pulse was ~ 1.2 nsec and its energy content was ~ 30 millijoules. The beam divergence and line-width of the clipped pulse was essentially unchanged from that of the Q-switched pulses, being ~ 3 milliradians (90% energy) and ~ 0.08 Å respectively.

3. Applications and Results

Although quantitative values of n_e are usually difficult to obtain using the shadowgram technique, valuable information, such as shock velocities and instability growth rates, can be obtained about the formation and break-up processes of a transient plasma. To obtain meaningful information from irreproducible plasmas it is necessary to obtain any time sequence required from as few discharges as possible.

One method of achieving a multiple exposure time sequence from a single discharge [8] utilises semi-reflecting mirrors to split the short laser pulse into a number (3-5) of equal intensity pulses. Each pulse has its own path to the common plasma volume, and time separation is achieved by making each path length different. If the paths are inclined at small angles to each other, the shadowgrams produced can be recorded as separate images on a film. Fig.2 is an example from a time sequence of 3 focused shadowgrams taken during the collapse phase of the Plasma Focus device. The plasma-vacuum interface is clearly shown, with associated Rayleigh-Taylor and m = 0 instabilities. Collapse velocities of ~ 4×10^7 cm sec^{-1} have been recorded and instability growth rates obtained, ($\omega_{R-T} \sim 10^8$ sec^{-1}).

Interferometric studies of the collapse and dense pinch stages of the Plasma Focus device have been made using a Mach-Zehnder interferometer. Over the regions of highest electron density the fringe shifts were too large to be reliably traced. In regions of lower density, the fringe shifts could be counted, and densities of ~ 4×10^{19} cm^{-3} have been obtained.

In the schlieren technique, if instead of using a knife edge at the focus of the schlieren lens a circular obstacle is used, the density gradients in the plasma in all directions in the plane orthogonal to the incident laser beam can be recorded. By using an obstacle of sufficiently large diameter, only the plasma regions of high electron density and steep density gradients will be recorded. Fig.3 shows a schlieren photograph of the collapse phase of the Plasma Focus device Peak densities in excess of 7×10^{19} cm^{-3} have been evaluated using this technique. The presence of instabilities on the plasma-vacuum boundary is clearly shown.

4. Conclusions

An electro-optic shutter has been used to shorten the pulse from a Q-switched ruby laser to ~ 1 nsec duration. This system has been used as a light source for studying a dense, highly-transient plasma by shadowgram, schlieren and interferometric techniques. Values of electron density, shock front velocities and instability growth rates have been obtained.

FIG. 2
Nanosecond Exposure Shadowgram

FIG. 3
Nanosecond Exposure Schlieren Photograph

5. References

[1] F.C. JAHODA, E.M. LITTLE, W.E. QUINN, F.L. RIBE and G.A. SAWYER, J. Appl. Phys. 35, 2351-2363 (1964).

[2] U. ASCOLI-BARTOLI, S. MARTELLUCCI and E. MAZZUCATO, Proc. 6th Int. Conf. on Ionization Phenomena in Gases 4, 97-103 (1964).

[3] N.J. PEACOCK, P.D. WILCOCK, R.J. SPEER and P.D. MORGAN, Paper CN-24/G-5, IAEA 3rd Conf. on Plasma Physics and Controlled Nuclear Fusion Research, Novosibirsk (1968).

[4] N.G. BASOV, O.N. KROKHIN and G.V. SKLIZKOV, J. Quant. Elect. 4, 988-991 (1968).

[5] A.J. ALCOCK and M.C. RICHARDSON, Opt. Commun. 2, 65-68 (1970).

[6] D.J. BRADLEY, J.F. HIGGINS, M.H. KEY and S. MAJUMDAR, Opto-Electronics 1, 62-64 (1969).

[7] K.J.R. WILKINSON, J. Inst. E.E. 93 Pt. IIIA, 1090-1112 (1946).

[8] N.G. BASOV, O.N. KROKHIN and G.V. SKLIZKOV, Appl. Opt. 6, 1814-1817 (1967).

Proceedings of 10th International Conference on Phenomena in Ionized Gases, Oxford. 13-18 September 1971.

MEASUREMENT OF BETA IN A PLASMA FOCUS

by

P D Morgan* and N J Peacock

UKAEA, Culham Laboratory, Abingdon, Berks, England.

*Royal Holloway College, Englefield Green, Surrey, England.

Abstract: The electron and ion line-densities obtained by interferometry during the collapse, dense-pinch and break-up stages of a Plasma Focus discharge are reported. Using these values, together with previously reported values of the average temperatures of the particles, the Bennett relation, $I^2 \beta_\theta = 2 k \sum_{e,i} N\bar{T}$, is satisfied in the dense pinch for a value of β_θ (beta) ~ 0.6. This is consistent with a fluid model in which plasma is transiently in equilibrium with the self-magnetic field of the current in the pinch.

1. Introduction: In the Plasma Focus it is important to know the value of beta (β_θ), which for the transient, dense pinch can be defined by the Bennett relation:

$$I^2 \beta_\theta = 2 k \sum_{e,i} N\bar{T}$$

where I is the current flowing in the pinch and $N\bar{T}$ is the product of line density and average temperature for each of the particle species.

Two-dimensional, MHD computations based on a 2-fluid model using classical transport coefficients, [1], indicate that the dense pinch is transiently in equilibrium with the confining magnetic field, and has a β_θ of value unity. In the dense pinch, because of cyclotron-orbiting effects and collision lengths of the order of the plasma dimensions, it is not clear a priori that a fluid model is justified.

Up to the present no experimental value of β_θ has been reported. In this paper measured values of line densities, average temperatures and current are used in the Bennett relation, from which a value of β_θ is derived.

2. Experimental Method: Detailed descriptions of the Plasma Focus device used and its mode of operation are to be found in [2,3] . The operating conditions used for the work described in this paper were an initial gas filling of 2.5 torr (D_2 + 4% Ar) and a capacitor bank voltage of 30 kV (42 kJ stored energy).

Figure 1 shows an interferogram of the pinch taken at the onset of soft X-ray emission (t = 0), using a nanosecond light pulse from a ruby laser, [3,4] . The minimum radius of the pinched column is ~ 0.1 cm. In order to obtain the radial electron density profile, $n_e(r)$, the fringe-shift profiles obtained must be evaluated numerically using the Abel integral-transform, [5]. Figure 2 shows three radial density-profiles obtained during the collapse (t = -40 nsec), dense pinch (t = 0) and break-up (t = + 30 nsec) stages. The values of electron density

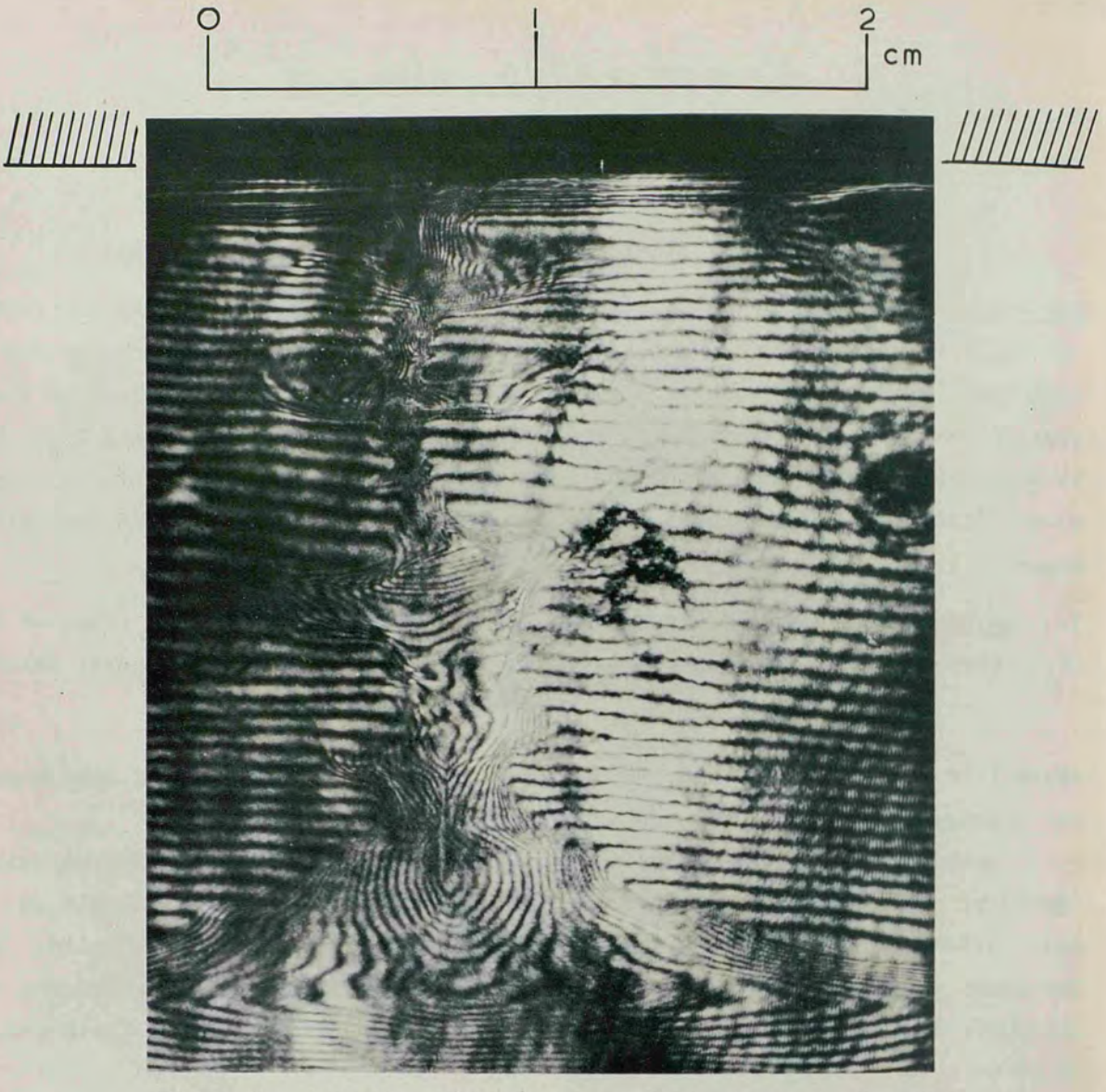

Figure 1: Interferogram of dense pinch at onset of soft X-ray emission (t=0). Exposure time ∿ 1 nsec.

obtained and the shapes of the profiles are in general agreement with the results of computations, [1] .

The electron line-density

$$N_e = 2\pi \int_0^R n_e(r) r \, dr \qquad cm^{-1}$$

where R is the radius of the pinch as determined by interferometry, has been evaluated. There is a sharp decrease in N_e at t=0, corresponding to the time when peak compression occurs, figure 3, due to axial flow from the compressed pinch, to a value $\sim 2.3 \times 10^{17}$ cm^{-1}. The deuterium and argon ion line-densities are obtained using the relation:

$$N_e = N_{i_D} + \bar{z} N_{i_A}$$

where $\bar{z}$ is the average argon ion charge.

From spectroscopic studies, [3], $\bar{z} = 12$ in the dense pinch, and allowing for the

dissociation of the deuterium, one obtains:

$$N_{i_D} = 0.8\ N_e \quad , \quad N_{i_A} = 0.017\ N_e$$

The plasma electron temperature has been determined by absorber-foil measurements on the soft X-ray flux, [2] , and spectroscopically from the ratio of the intensities of the He-like argon-ion resonance lines to the satellite-line intensities, [6] . The mean electron temperature by these two methods is $\sim$ 2.2 keV. The temperature of the argon ions has been determined as being $\sim$ 9.5 keV by measuring the Doppler-broadening, due to the ion thermal motion, of the He-like resonance lines, [3] . From cooperative scattering of ruby laser light, the deuterium ion temperature is $\sim$ 0.7 keV, [7] . Finally, the current in the discharge circuit was measured using a calibrated Rogowskii coil coupled to an integrating circuit. At t = 0 a value of 610 kA is obtained.

3. Discussion: Assuming that all of the current in the discharge circuit flows through the pinch, (not an unreasonable assumption, [8]), and inserting the measured parameter values for the dense pinch into the Bennett relation, a value of $\beta_\theta = 0.6 \pm 0.15$ is obtained. The errors are due to the uncertainties in the values of the particle temperatures and of the current at maximum compression. This means that the plasma kinetic pressure is sufficiently high to be balanced by a confining magnetic field produced by between $\sim$ 67 and 87% of the total pinch current flowing, in general agreement with the fluid code, [1] . From optical studies there is evidence that the local instability time of the dense pinch is $\sim$ 5 nsec, [3] , which is still longer than the self-collision time of each of the particle species, the pinch being transiently in equilibrium is reasonable from this point of view.

The fact that β_θ is measured to be fractionally less than unity can be ascribed to losses not included in the fluid code, eg, anomalous heat conduction.

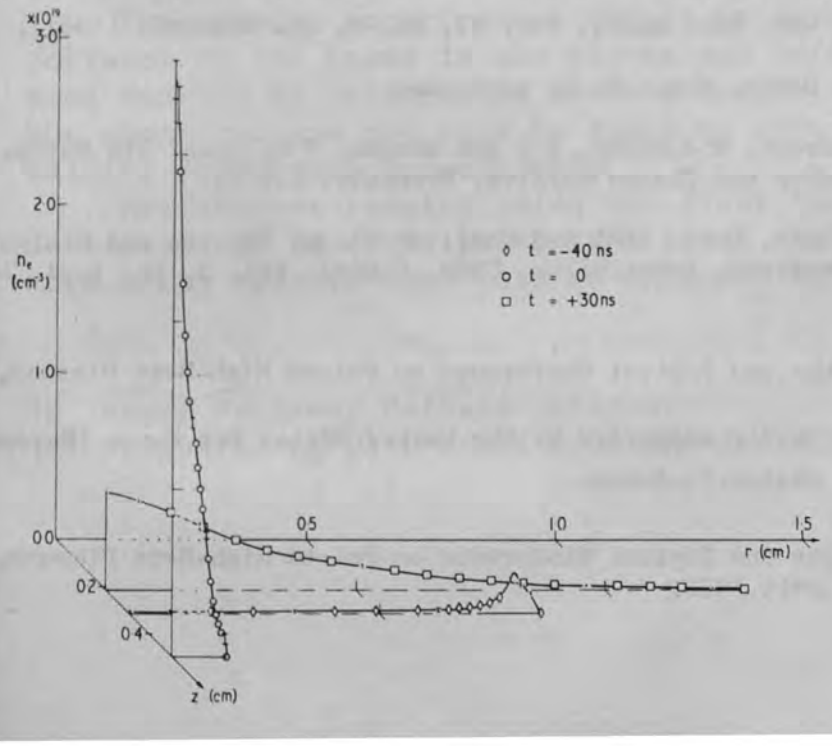

Figure 2:
Radial electron-density profiles during collapse at t = - 40 nsec, maximum compression at 5 mm from anode (t = 0) and at t = + 30 nsec.

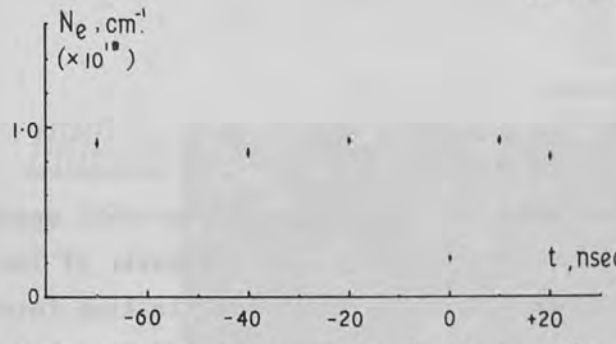

Figure 3:
Electron line-density at different times before, during and after the dense-pinch stage (t = 0).

An alternative explanation is that β_θ is indeed unity and that between ~ 13 and 33% of the curcuit current flows outside the pinch region. However, there is no evidence from the electrical waveforms to support this possibility.

4. Conclusions: Measurements of the plasma kinetic pressure indicate that a high beta plasma exists in the dense-pinch phase of the Focus. The kinetic pressure is sufficiently high, that to be balanced by the self-magnetic field of the current, requires at least 67% flowing in the dense pinch. Using the Bennett relation, a value of $\beta_\theta = 0.6 \pm 0.15$ is derived, in agreement with a fluid model in which the plasma and self-magnetic field are transiently in equilibrium.

References:

1 Potter, D E, Phys. Fluids, Vol.14, No. 9, pp. 1911-1924, (1971).

2 Peacock, N J, Wilcock, P D, Speer, R J and Morgan, P D, Proc. IAEA 3rd Conf. on Plasma Physics and Controlled Nuclear Fusion Research, Novosibirsk, USSR, (1968), Vol. 2, pp. 51-65, IAEA, Vienna, (1969).

3 Peacock, N J, Hobby, M G and Morgan, P D, Proc. IAEA 4th Conf. on Plasma Physics and Controlled Nuclear Fusion Research, Madison, USA, (1971), Vol. 1, pp. 537-551, IAEA, Vienna, (1971).

4 Morgan, P D and Peacock, N J, J. Phys. E - Scient. Instrum., Vol. 4, No. 9, pp. 677-680, (1971).

5 Bockasten, K, J. Opt. Soc. Amer., Vol. 51, No. 4, pp. 943-947, (1961).

6 Peacock, N J and Hobby, M G. To be published.

7 Peacock, N J, Forrest, M J,Hobby, M G and Morgan, P D, Proc. 5th Europ. Conf. on Controlled Fusion and Plasma Physics, Grenoble, (1972).

8 Agafonov, V I et al., Proc. IAEA 3rd Conf. on Plasma Physics and Controlled Nuclear Fusion Research, Novosibirsk, USSR, (1968), Vol. 2, pp. 1-24, IAEA, Vienna, (1969).

This research is partly supported by the United States Air Force (European Office) under Contract F44620-71-C-0098.

Proceedings of the 2nd Topical Conference on Pulsed High-Beta Plasmas, Garching. 3-6 July 1972.

Sixth European Conference on Controlled Fusion and Plasma Physics
Moscow, USSR. 30 July - 2 August 1973

EVIDENCE FOR A BROAD AND UNIFORM NEUTRON-PRODUCING PLASMA COLUMN IN THE PLASMA FOCUS

Joint European Programme on Plasma Focus

P.D. Morgan (*, +), N.J. Peacock
The Culham Laboratory, Abingdon, Berks., U.K.

P. Cloth, H. Conrads
IPP-IRE, Ass. EURATOM-KFA, Jülich, Germany

Ch. Maisonnier, F. Pecorella, J.P. Rager, M. Samuelli
Laboratori Gas Ionizzati (Ass. EURATOM-CNEN), Frascati, Italy.

ABSTRACT

Holographic interferometry, time of flight measurements on the fusion reaction neutrons and time-resolved x-ray imagery have been used to specify some of the parameters of the plasma during the late-time history of the dense pinch in the 120 kJ Plasma Focus at Frascati. The measured parameters are in agreement with the model of a broad and uniform plasma column which is turbulently heated after the break-up of the pinch.

INTRODUCTION

One of the first goals of the Joint European effort on Plasma Focus is to check by direct measurements on the Frascati device / 1 / the validity of the model / 1 / proposed to account for the neutron emission. Following this model, most of the neutrons would be of thermonuclear origin, and a small fraction only would be produced at the time of maximum compression, whereas the bulk of neutron emission would originate later from a diffuse plasma of considerably larger dimensions, lower density, and higher temperature resulting from efficient turbulent heating during the radial expansion of the plasma column.

The present experimental effort is aimed at assessing the importance of ion beams in the plasma and defining the region of electron density by holographic interferometry. Also, the location of hot electrons and hot ions is found by soft-x-ray and by neutron imaging techniques respectively.

Preliminary results using the first three methods are given hereafter. It is anticipated that final density measurements and more x-ray measurements will be included in a supplement paper.

(*) *Royal Holloway College (London)*
(+) *Supported by USAF under contract F.44620-71-C-0098*

HIGH ENERGY IONS

The method for measuring the number of high-energy ions is based on the intensity of (D,Li^7) reactions. The method has been used successfully for tracing in a Focus device / 2 / the number of ions with energy exceeding 300 keV, where the reaction cross-section becomes substantial. Lithium deuteride is placed in the anode and lithium hydride in the cathode, both on axis. Three time-of-flight spectrometers are used for analysing the neutron spectrum and are placed at 8 m, 13 m, and 20 m respectively from the Focus. The arrangement has a threshold sensitivity for detecting neutrons from the (D,Li^7) reactions which is about 10^8 neutrons per discharge.

The neutron spectra recorded on the Frascati Focus show little evidence of ions having energies above 300 keV. Over more than 50 discharges with pressures varying between 0.5 and 2 Torr, only one case indicates the presence of a few (D,Li^7) neutrons above threshold. The bulk of neutrons are from (D,D) reactions. By contrast, on the Jülich Focus the (D,Li^7) reactions exceed the (D,D) reactions by a factor of five. The total neutron yield is about equal for both experiments ($\sim 2 \times 10^{10}$).

DENSITY MEASUREMENTS

Fig. 1 is a schematic diagram of the apparatus used for the holographic interferometry. 1 - ruby laser, / 3 /; 2,7-expansion telescopes; 3,5-pellicle beam splitters; 4-photo-diode; 6-mirror arrangement to equalise the scene and reference paths; 8-hollow wedge; 9-lens focusing plasma plane onto diffuser; 10-1mm pinhole; 11-camera; 12-diffuser; 13-lens to expand reference beam to fill film 14. The input apertures of the camera are closed by narrow-band interference filters.

The double-exposure holograms were recorded on Kodak SO-243 film. Background fringes were introduced by replacing the initial air filling in the hollow wedge with helium, between exposures. Electron-density profiles were obtained from the interferograms after an Abel-inversion, / 4 /.

In particular, the diffuse-pinch phase, during which maximum neutron emission occurs, has been investigated. Preliminary results show clearly the presence of a broad, well-defined column of plasma during this phase, with peak electron densities approximately two orders of magnitude lower than those in the dense pinch; there is evidence that the line density remains constant. Fig. 2 shows an electron density profile obtained at the maximum intensity of neutron emission, with an inset showing a typical neutron signal. The radius of the column is 1.9 cm and the peak electron density is $\sim 3.2 \times 10^{17}$ cm^{-3}. It can be seen that the plasma boundary is sharp and that the electron density within the column is, to a first approximation, constant. The line density, $N_e = 2\pi \int_0^r n_e(r)\, r\, dr$, is $\sim 2.7 \times 10^{18}$ cm^{-1} and the column length is ~ 3 cm. In order to account for the neutron yield of 4.8×10^{10}, observed on the discharge pertaining to the density profile, a deuterium ion temperature

of 8 keV is necessary for a thermal plasma with an emission time of 100 nsec. At even later times in the discharge, during the decay of the second neutron burst, the plasma expands to a diameter which is larger than the width of the field of view of 5.7 cm. For example, 60 - 100 nsec after peak neutron intensity, the recorded fringe shifts become assymmetric about the electrode axis and are irregular across the field of view. This indicates that during this phase the plasma column breaks up shortly after the peak neutron emission.

SOFT x-RAYS

Fig.3 is a 50 ns exposure, soft x-ray image centered on the maximum of the second neutron burst shown inset on Fig. 2.

Fig. 3 shows a diffuse plasma of much larger diameter than the 2 mm dimension of the plasma column at maximum compression, / 5 /. The latter appears in the picture as a black filament at the centre. This is due to early charge depletion of the x-ray intensifier (channel plate) by the much higher emissivity of the denser plasma. A systematic investigation of the spatial and temporal evolution of the x-ray emitting volume is in progress.

CONCLUSION

A well-defined, hot plasma column of about 4 cm in diameter with a mean density of 2.3×10^{17} cm^{-3} exists at the time of maximum neutron intensity. No gross density perturbations within the column are observed. There is no evidence of high energy ion beams in the plasma. These results are in agreement with the model previously proposed / 1 /.

REFERENCES

/ 1 / Ch. MAISONNIER, et al.: Proc. of Vth European Conf. on Controlled Fusion and Plasma Phys. Vol. II, p. 183 - Grenoble 1972.

/ 2 / H. CONRADS et al.: Phys. Fluids 15, 209 (1972).

/ 3 / P.D. MORGAN and N.J. PEACOCK: J. Phys. E: Sc. Instr. 4, 671 (1971).

/ 4 / K. BOCKASTEN: J. Opt. Soc. Am., 5, 943 (1961).

/ 5 / Ch. MAISONNIER et al.: Proc. Conf. Plasma Physics and Controlled Thermonuclear Research, Vol. I, p. 511 - Madison (1971).

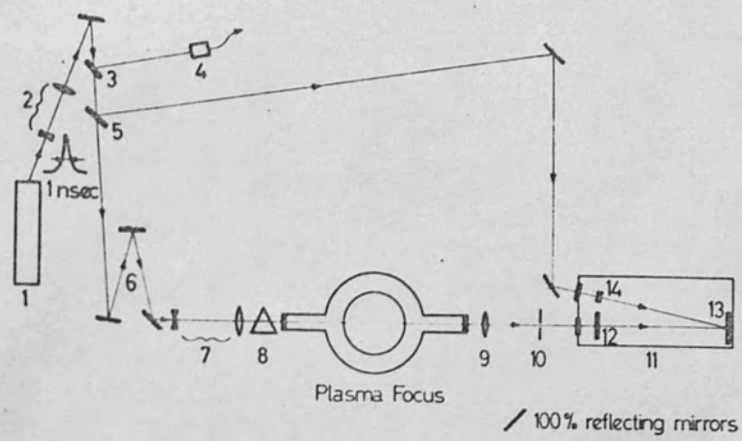

Fig. 1 - SCHEMATIC LAYOUT OF HOLOGRAPHIC OPTICS.

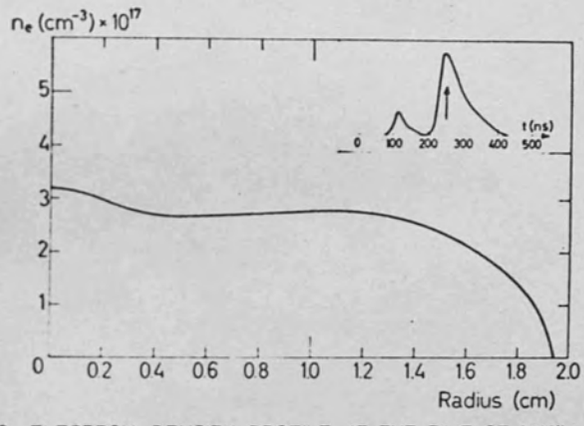

Fig 2 - ELECTRON DENSITY PROFILE AT THE TIME OF MAXIMUM NEUTRON EMISSION. INSET TYPICAL NEUTRON SIGNAL

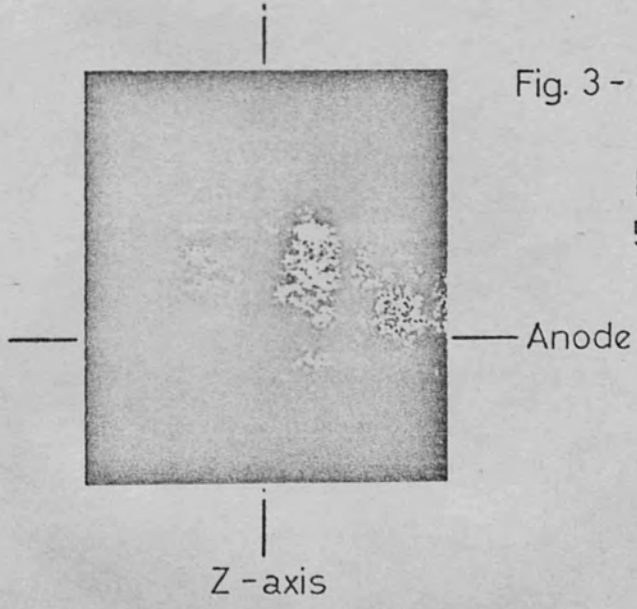

Fig. 3 - X-RAY IMAGE DURING THE SECOND NEUTRON EMISSION (EXPOSURE 50 ns).

ERRATA

Page	Line	Line Beginning	Correction
3	10	The principles of ..... should read	'showdowgraphy' 'shadowgraphy'
9	27	From a review ..... should read	'diffuse-pinch' 'break-up and diffuse-pinch'
21	20	Thus T_e	after 'Thus' insert ', in general,'
22	11	2.3.2 The	'Collpse' should read 'Collapse'
26	7	The overall lifetime ..... should read	'10-100 kJ cm^{-3}' '1-100 kJ cm^{-3}'
30	11	However, the	'be' should read 'by'
30	12	For an electron	after 'v_d' delete '$= \underline{E} \times \underline{B}/cB^2$'
42	14	Even in the	'ionized' should read 'stripped'
47	15	The intensity	'will be' should read 'will not be'
50	8	Occasionally, it	'necessary' should read 'desirable'
56	15	Combining the ..... $\frac{\partial}{\partial x} \ell n(x,y,z)\, dz$ (in equation (3.3.10)) should read	$\frac{\partial}{\partial x} \ell n\, n(x,y,z)\, dz$
91	10	With less	'that' should read 'than'
103	3	Operating a	'inceident' should read 'incident'
113	6	The interferometric ..... should read	'integerograms' 'interferograms'
118	19	From this	'maximu' should read 'maximum'
141	1	There is a	after 'because' insert 'where possible'
155	11	For a filling	'is' should read 'are'
168	28	In the limit	'infinity' should read 'infinitely'
171	6	It was not	'bearly' should read 'barely'
174	12	As stated	'magntic' should read 'magnetic'
175	4	T_{iD} may	'interative' should read 'iterative'
176	19	(b). During	'when' should read 'that'
185	31	v_d Drift	replace '$, \underline{E} \times \underline{B}/cB^2$' with 'of electrons relative to ions'
191	9	Hence, from	'$+ \left[\frac{\omega_{pe}^2}{\omega}\right.$' should read '$\left[\frac{\omega_{pe}^2}{\omega}\right.$'